THE EFFECTS OF FRICTION STIR WELDING ON THE MICROSTRUCTURE AND MECHANICAL BEHAVIOR OF ALUMINUM ALLOY AA2139-T8

By

Uchechi Chinaka Okeke

A DISSERTATION

Submitted to
Michigan State University
in partial fulfillment of the requirements
for the degree of

Materials Science and Engineering—Doctor of Philosophy

2021

ABSTRACT

THE EFFECTS OF FRICTION STIR WELDING ON THE MICROSTRUCTURE AND MECHANICAL BEHAVIOR OF ALUMINUM ALLOY AA2139-T8

By

Uchechi Chinaka Okeke

The demand for both high-strength and lightweight metals for structural applications to increase vehicle mobility has driven an increase in the research and development of lightweight alloys, including those based on aluminum (Al), to replace commonly-used steel. When alloyed copper (Cu), Al alloys can exhibit high tensile strengths. However, Al-Cu alloys are difficult to join using fusion welding processes due to solidification cracking. To circumvent the issues that arise with fusion welding, friction stir welding (FSW) can be employed.

FSW is a solid state joining method that utilizes friction generated heat between a rotating tool and two metal plates to create a joint without the use of additional material. FSW temperatures are lower than the melting point and are historically achieved by controlling the welding speed. The welding temperature has largely been both an uncontrolled and unmonitored variable, which presents an issue when trying to predict or explain the weld microstructures. In addition, most FSW investigations are performed on parts that are less than 12 mm thick. This limits the understanding of processing-microstructure-property relationships of thicker FSW plates. This dissertation studied the effect of FSW on the microstructure and mechanical behavior of 25 mm thick AA2139-T8, a precipitation strengthened Al-Cu-Mg-Ag alloy.

Processing-microstructure-property relationships were studied using both constant-speed (150 RPM and 50 mm/min) and constant-temperature FSW (performed at 490°C, 500°C, and 510°C). The microstructural evolution throughout the thickness of the weld was analyzed via optical microscopy, SEM, TEM, and XRD. The mechanical behavior was analyzed using tensile

and Vickers hardness experiments. The distribution of the different precipitates was plotted throughout the welded area for the constant-temperature FSW materials. The average matrix grain size decreased from the weld top to bottom, while the precipitate volume percent increased from the weld top to bottom. The stir zone (SZ) exhibited lower strengths and hardness than the base metal. In addition, the larger grains in the upper weld nugget (UWN) of the SZ had a higher hardness than the smaller grains in the lower weld nugget (LWN) of the SZ and this was explained by the dissolution of the precipitates during welding and the associated solid solution strengthening.

This study was the first to perform constant-temperature FSW on both an Al-Cu-Mg-Ag alloy and a 25 mm thick plate. Compared with the 500° and 510°C constant-temperature FSW, the 490°C constant-temperature FSW yielded the smallest average grain size and the highest precipitate volume percent through the SZ. The average grain size increased with welding temperature. The 510°C FSW exhibited the lowest room-temperature (RT) tensile YS, UTS, ε_f, and joint efficiency due to the void formation during the welding. The 490°C and 500°C FSWs failed at the interface between the SZ and the thermomechanically affected zone (TMAZ) and in the HAZ, respectively, which were the weakest links of the weld and dictated the tensile properties.

The work in this dissertation provided new insights into the effects of constant temperature FSW on the microstructural evolution and the mechanical properties through the weld thickness. The knowledge gained from this work will not only assist in determining optimal welding parameters for this alloy for targeted applications, but will also serve as a framework for future research targeted at understanding processing-microstructure-property relationships of a variety of metallic systems undergoing not only FSW under controlled conditions but also undergoing different controlled thermomechanical processing treatments.

Nke Chineke Pụrụ Ime Ihe Niile Nke Napụtara M.

ACKNOWLEDGMENTS

First and foremost, I give thanks to God who has given me the strength, wisdom, knowledge, and understanding to navigate this Ph.D. and to overcome all of its unique challenges. A Ph.D. is not earned by oneself, so I would like to acknowledge those who have contributed to my journey.

I would like to thank my advisor, Professor Carl Boehlert, for his guidance on the research and helping me to be a better experimentalist. I am also thankful for my co-chair, Professor Donald Morelli, who supported me and gave me his unbiased ear which changed the course of my Ph.D. I express my sincerest gratitude to my committee members Professor David Grummon, Professor Thomas Bieler, Dr. Tomoko Sano, and Professor Patrick Kwon for their patience, support, and guidance on the writing and the analysis.

I am thankful for Mr. Steven Thomas of AGEP who assisted with my transition to MSU. I thank Professor Seungik Baek who brought me into MSU and took me into his lab before my transition to Materials Science & Engineering. Thank you to Dr. Robert Ofoli for his guidance. I would like to thank Dr. Percy Pierre and Professor Shanelle Foster for their mentorship. I would like to acknowledge the students and professors of the Metals Research Group for the many learning opportunities. I am grateful to Dr. Per Askeland for training and assistance on the SEM in the Composite Materials and Structures Center. I couldn't have asked for better friends in Dr. Demetrice "Dee" Jordan and Dr. Aida Amroussia who emboldened and advocated for me. I also thank Dr. Kristen Mills, Dr Joyce Farley, Dr. Talesha Dokes for their friendship and encouragement.

This dissertation was made possible via the collaborations with the U.S. Army DEVCOM

GVSC, which started with Ms. Lisa Prokurat Franks who established the connection and encouraged me. I thank DEVCOM GVSC Materials Directorate and Mr. Matthew Rogers, Dr. Katie Sebeck, Mr. Martin McDonnell, Mr. Demetrios Tzelepis, Mr. Ian Toppler, Dr. Greg Hudas, and Dr. Ravi Thyagarajan for their invaluable support and discussions. I thank DEVCOM ARL for the materials used in this study. I thank the research staff at the Pacific Northwest National Laboratory, Dr. Scott Whalen, Mr. Ken Ross, Dr. Md. Reza E Rabby, and Dr. Piyush Upadhyay for their invaluable collaboration on the constant-temperature friction stir welds.

This research was supported by the National Science Foundation Division of Material Research (Grant Nos. DMR1107117 and DMR1607942). The TEM on the as-received material was performed under the National Science Foundation East Asia and Pacific Summer Institute Fellowship (Award No. 1515111) at the Institute of Materials Research (IMR) Tohoku University in Sendai, Japan. Acknowledgement is provided to Professor Mitsuo Niinomi and Dr. Huihong Liu of IMR Tohoku University for their support. Acknowledgement also goes to Dr. Makoto Nagasako and Shun Ito at the IMR Tohoku University for help with acquiring the TEM images. Use of the TEMs at the Center for Nanoscale Materials (CNM) at Argonne National Laboratory, an Office of Science user facility, was supported by the U.S. Department of Energy, Office of Science, Office of Basic Energy Sciences, under Contract No. DE-AC02-06CH11357. Thank you to Dr. Yuzi Liu, CNM, who assisted in acquiring the as-welded and deformed TEM images.

I am earnestly grateful for Pastors Dr. Emmanuel and Ethel Ayorinde, the members of Christ the King Miracle Church-Redford, and my family for their relentless prayers and words of encouragement. I am blessed to have a mother who has encouraged me without fail, raised four children all by herself, worked long hours, and obtained her BSN. Thank you Ozioma Okeke for recognizing early on that I don’t like dolls and buying me a microscope.

TABLE OF CONTENTS

LIST OF TABLES ..... **x**

LIST OF FIGURES ..... **xii**

KEY TO ABBREVIATIONS AND SYMBOLS ..... **xxvii**

CHAPTER 1 INTRODUCTION **1**
1.1 Rationale and Research Objective 1
1.2 Work Performed 4

CHAPTER 2 BACKGROUND **6**
2.1 Aluminum and Aluminum Alloys 6
2.1.1 Physical Metallurgy of Al and Al alloys 6
2.1.2 The Nomenclature and Tempering of Al and Al alloy 8
2.2 The Microstructure of 2xxx Aluminum Alloys 10
2.3 The Development of Aluminum Alloy AA2139 14
2.4 Friction Stir Welding 16
2.4.1 Introduction 16
2.4.2 Manufacturing Processes 19
2.4.3 Microstructural Zones 22
2.5 Summary 25

CHAPTER 3 EXPERIMENTAL METHODS **28**
3.1 Materials and Processing 28
3.1.1 AA2139-T8 28
3.1.2 Friction Stir Welding (FSW) 29
3.1.3 Metallurgical Preparation 39
3.1.4 Microscopy 40
3.1.5 X-ray Diffraction (XRD) 41
3.2 Mechanical Testing 44
3.2.1 Vickers hardness testing 44
3.2.2 Tensile Testing 46
3.3 Post-Weld Heat Treatment (PWHT) 49

CHAPTER 4 RESULTS AND DISCUSSION **52**
4.1 AA2139-T8 52
4.1.1 Microstructure 52
4.1.2 Hardness Behavior 63
4.1.3 Tensile Behavior 63
4.2 Effects of Constant-Speed Friction Stir Welding 64

4.2.1 Microstructure 65
4.2.2 Effects of FSW on the Microstructure 88
4.2.3 Mechanical Behavior 92
4.2.4 Effects of FSW on the Mechanical Behavior 96
4.2.5 Post Weld Heat Treatment 98
4.3 Effects of Constant-Temperature FSW 115
4.3.1 Microstructure 115
4.3.2 Effect of FSW Temperature on Microstructure Discussion 122
4.3.3 Hardness Behavior Results 124
4.3.4 Tensile Behavior Results 134
4.3.5 Effect of FSW Temperature on Mechanical Behavior 138
4.4 Precipitate Phase Plot of Constant-Temperature FSW 141
4.4.1 Construction of the Precipitate Phase Plot 141
4.4.2 Precipitate Phase Plot Analysis 150
4.4.3 Effect of FSW Processing on Microstructure to Mechanical Behavior 155

CHAPTER 5 SUMMARY, CONCLUSIONS, AND FUTURE WORK 159
5.1 Summary 159
5.2 Conclusions 159
5.2.1 Microstructure of Constant-Speed FSW 159
5.2.2 Mechanical Behavior of Constant-Speed FSW 160
5.2.3 Microstructure of Constant-Temperature FSW 161
5.2.4 Mechanical Behavior of Constant-Temperature FSW 161
5.2.5 Impact of Constant-Temperature FSW on Optimizing FSW Processing 162
5.3 Recommendations for Future Work 163

APPENDICES 166
APPENDIX A DARK FIELD TRANSMISSION ELECTRON MICROSCOPY 167
APPENDIX B SIMULATED SELECTED AREA DIFFRACTION PATTERNS 169
APPENDIX C *IN SITU* TENSILE BEHAVIOR FOR THE AS-RECEIVED AA2139-T8 176
APPENDIX D *IN SITU* TENSILE BEHAVIOR FOR THE CONSTANT-SPEED FSW 184
APPENDIX E CREEP 190
APPENDIX F XRD PEAKS COMPARING THE BASE METAL TO THE CONSTANT-TEMPERATURE FSW 213
APPENDIX G XRD PEAKS OF THE CONSTANT-TEMPERATURE FSW BY DISTANCE FROM THE WELD CENTER 215

BIBLIOGRAPHY 228

LIST OF TABLES

Table 2.1. Aluminum alloying designation system and temper designation system per the Aluminum Association [2]. 9

Table 2.2. Target compositions per the Aluminum Association, 2006 for alloys a) AA2039, and b) AA2139 (boxed elements are those that have been modified). 15

Table 2.3. Important benefits of friction stir welding [11]. 19

Table 2.4. A summary of the stir zone grain size in FSW/FSP aluminum alloys. Notice that only one alloy has a thickness of 25 mm [11]. The referred references are found within the work of Mishra and Ma [11]. 25

Table 3.1. Composition limits for AA2139 (top) and the measured composition for the plate received from CTC (bottom). Plates given to DEVCOM ARL were from CTC. 29

Table 3.2. Constant-speed welding parameters with tool dimensions [55]. 30

Table 3.3. Constant-temperature FSW parameters. 34

Table 4.1. Elemental wt.% based on the EDS measurements of selected areas in Figure 4.2a... 54

Table 4.2. Elemental wt.% based on the EDS measurements of selected areas in Figure 4.2b. . 54

Table 4.3. Summary of precipitate phases present during the XRD *in situ* heat treatments shown in Figure 4.6. 63

Table 4.4. List of precipitates identified through XRD analysis of AA2139-T8, which was naturally aged after heat treating at 409°C, 481°C, and 516°C. 63

Table 4.5. Measured average tensile properties of the base metal through the plate thickness. The standard deviation is provided in parentheses. 64

Table 4.6. Average grain size through the depth of the constant-speed FSW. 70

Table 4.7. Precipitate volume percent through the depth of the constant-speed FSW. 70

Table 4.8. Maximum Vickers hardness values through the depth of the SZ for the constant-speed FSW. 95

Table 4.9. Tensile properties of constant-speed FSW through the depth of the weld. It is noted that an extensometer was not used at 300°C and for this case the elongation to failure was estimated from the sample dimensions before and after the test and the E value was not measured. 96

Table 4.10. Maximum Vickers hardness values through the depth of the stir zone for the constant-speed as-welded and PWHT FSWs. 112

Table 4.11. Tensile properties of the as-welded and PWHT FSW samples. Samples were extracted from the middle of the weld. 113

Table 4.12. Average grain size through the depth of the FSWs. Constant-speed FSW is provided for comparison. 117

Table 4.13. Measured precipitate volume percent through the depth of the constant-temperature FSW materials. The constant-speed FSW measurements are provided for comparison. 118

Table 4.14. Maximum Vickers hardness values through the depth of the SZ for the constant-temperature and constant-speed FSWs. 134

Table 4.15. Tensile properties of constant-temperature FSW joints shown in Figures 4.63 through 4.65. Joint efficiency is defined as the ratio of the UTS of the FSW joint to the unwelded base metal. *Samples are listed in the same order as the legend in the stress-strain plot of Figure 4.62. 135

Table 4.16. Average of the constant-temperature FSW tensile property values listed Table 4.15. The standard deviation is in parentheses. Constant-temperature FSW at 510°C exhibited the lowest values due to voids in the SZ, which served crack initiation sites. 136

Table 5.1. AA2139-T8 base metal *in situ* tensile property comparison. 179

Table D.1. Tensile properties of the *in situ* tensile tested constant-speed FSW. 185

Table E.1. List of creep experiments performed in this dissertation. 194

Table E.2. Precipitate V_p of the creep tested samples and the center of the SZ through the depth of the weld. 203

LIST OF FIGURES

Figure 2.1. Al-Cu-Mg ternary system phase diagrams. The thin, vertically slanted shaded region represents the Mg concentrations in the AA2139 alloy. The horizontal shaded region represents the Cu concentrations in the AA2139 alloy. a) liquidus (estimated to be approximately 640-650°C, b) solidus (estimated to be approximately 527°C) [19]. 15

Figure 2.2. Al-Cu-Mg phase diagram at 190°C. The shaded region represents the Mg concentration in the AA2139 alloy. The thick solid line is the α/α+S phase boundary at 500°C [19]. The appropriate Cu concentration (4.5-5.5 wt%) for this alloy is just outside the range of this chart. 16

Figure 2.3. Illustration of the friction stir welding process and tool [11]. 18

Figure 2.4. Illustration of the FSW tool features [11]. 20

Figure 2.5. Scanning electron microscopy photomicrograph of the transverse cross section of a friction stir weld adapted from [77] with the labelled weld zones. The weld nugget is also referred to as the stir zone (SZ). UWN and LWN refer to the upper weld nugget and lower weld nugget, respectively. 23

Figure 3.1. Schematic depicting the friction stir welding (FSW) process and the transverse cross sectional view. Adapted from Mishra and Ma [11]. 30

Figure 3.2. Digital image of the FSW plate received from the DEVCOM ARL. The blue ruler is 305 mm long. 31

Figure 3.3. Digital image of the Transformation Technologies, Inc (TTI) FSW machine used to perform FSW at constant temperature. It is located at PNNL. 33

Figure 3.4. The Al-Cu binary phase diagram [80]. FSW temperatures were chosen below the eutectic temperature and the out of the Al+L phase region. For Al-Cu-Mg alloys, the liquidus and solidus temperatures range from 640-650°C and 510-527°C, respectively. 33

Figure 3.5. (a) Plunge depth versus displacement, (b) force versus displacement, (c) torque versus displacement, and (d) shoulder temperature and rotational speed versus displacement plots for the constant-temperature FSW at 490°C. 35

Figure 3.6. (a) Plunge depth versus displacement, (b) force versus displacement, (c) torque versus displacement, and (d) shoulder temperature versus displacement plots for the constant-temperature FSW at 500°C. 36

Figure 3.7. (a) Plunge depth versus displacement, (b) force versus displacement, (c) torque versus displacement, and (d) shoulder temperature versus displacement plots for the constant-temperature FSW at 510°C. 37

Figure 3.8. Comparison of the rotational speed (left) and torque (right) versus FSW tool displacement used to achieve and maintain the target temperatures at 490°C, 500°C, and 510°C. 38

Figure 3.9. Digital images of the FSW tool routed with the thermocouple used for the constant-temperature FSW. 38

Figure 3.10. Digital image of the FSW tool and plate. Extensive clamping was used to minimize plate separation and shifting. A pre-drilled countersink hole makes the plunge process easier by reducing the forces on the tool and extending tool life. 39

Figure 3.11. Digital images of the Rigaku XRD in situ heating stage. Left: uncovered with the platinum sample holder. Middle: higher magnification image of the heater assembly with the thermocouple inserted into the sample holder. Right: covered with the vacuum tube. 43

Figure 3.12. Digital image of the FSW sample with fiducial dots, separated by 10 mm, representing where the XRD scans were acquired at the top, middle, and bottom. As the sample was polished to a mirror finish but not etched, the weld cross section is not evident. 43

Figure 3.13. Schematic drawing of the transverse cross sectional area (shown in Figure 3.1 right) used for the Vickers hardness and XRD experiments. 44

Figure 3.14. a) Digital photograph of the where the Vickers hardness indentation arrays were acquired with respect to the weld. b-c) The distance of the edge of the array to the b) top and c) bottom rows of indents is indicated in the red markings. Neighboring indents were spaced 1 mm apart from each other. 45

Figure 3.15. Optical micrograph of the etched cross-section of a constant-speed FSW specimen, where the array of hardness indents are evident. 46

Figure 3.16. A digital image of one of the welded plates indicating where the samples were extracted for the mechanical behavior studies. Note that the central region (of light contrast) represents the welded region and to the right and left of that region represents the base metal regions. 47

Figure 3.17. (a) Schematic drawing representing the dogbone-shaped sample geometry used for the constant-speed FSW tensile experiments. The dimensions are in inches. (b) Schematic showing the orientation of the dogbone shaped sample with respect to the weld used for the RT tensile testing of the constant-speed FSW material. 48

Figure 3.18. Schematic drawing of the dogbone-shaped sample geometry used measuring the RT tensile properties of the constant-temperature FSW materials. Samples were machined so that the transverse cross section was on the largest face of the gage section (see Figure 3.19). The dimensions are in inches. 48

Figure 3.19 Schematic showing the orientation of the dogbone shaped sample with respect to the weld used for the RT tensile testing of the constant-temperature FSW materials. 49

Figure 3.20. Time-Temperature-Transformation (TTT) curve for Al-4Cu-1.7Mg wt.%. The letters A-F correspond to the properties provided in Figure 3.21 [19]. 50

Figure 3.21. The effects of aging on some of the properties of Al-4Cu-1.7Mg wt.%. The letters A-F correspond to the TTT curve provided in Figure 3.20 [19]. 51

Figure 4.1. (a) OM photomicrograph of the plan view and (b) SE SEM photomicrograph of the transverse section of the as-received AA2139-T8 microstructure. 53

Figure 4.2. SE SEM photomicrographs of the as-received AA2139-T8 microstructure. The marked spots represent where EDS measurements were taken. a) Such EDS measurements are listed in Table 4.1, b) Such EDS measurements are listed in Table 4.2. 54

Figure 4.3. X-ray diffraction intensity versus 2-theta plot for the as-received AA2139-T8. The orange peakbar with a 2θ angle of 34.64 degrees indicates a Cu K_β peak. 55

Figure 4.4. Bright field TEM photomicrographs along with the corresponding SADPs for the as received AA2139-T8 alloy; a) and b) <100>, c) and d) <110>, and e) and f) <111> zone axes. Aluminum matrix diffraction spots are indexed. Precipitate phases are indicated by streaks (d) and smaller diffraction spots (b, d, e). The scale bar in e) is 200 nm. 57

Figure 4.5. Indexed precipitate diffraction spots on the FCC Al-matrix SADPs in the a) <100>, b) <110>, and c) <111> zone axes. 58

Figure 4.6. XRD intensity versus 2-theta data of 2139-T8 a) as-received, b) *in situ* and post annealed at 409°C, c) *in situ* and post annealed at 481°C, and d) *in situ* and post solutionized at 516°C. Cu Ka radiation. Parallel beam/parallel slit analyzer (PB/PSA) was used for all of the annealed and solutionized experiments. The orange peakbar indicates Cu Kβ radiation. The XRD scan times took approximately 48 minutes. 61

Figure 4.7. Optical macrograph of the etched constant-speed FSW in the transverse cross section. The advancing side (AS) is on the left side and the retreating side (RS) is on the right side. 66

Figure 4.8. Optical macrograph of the etched constant-speed FSW in the transverse cross section. Small dots are indents from the Vickers hardness test which are 1 mm apart. The advancing side

(AS) is on the left side and the retreating side (RS) is on the right side. 66

Figure 4.9. EBSD orientation maps of the cross section of the constant-speed FSW 9 mm from the bottom edge of the sample. The green box indicates where the EBSD was acquired. The top row is a continuous montage of many individual scans, some of which are provided in higher magnification below in A) to C). A) The AS of the weld is shown. High magnification maps are shown of the HAZ, TMAZ, and SZ. B) The center of the SZ is shown. C) The RS of the weld is shown with high magnification maps of the SZ, TMAZ, and HAZ. The IPF color coded FCC unit triangle is based upon the sample normal direction. The advancing side (AS) is on the left side while the retreating side (RS) is on the right side. 68

Figure 4.10. Transverse cross section of the FSW with blue boxes indicating the positions of the top, middle top, middle, middle bottom, and bottom. The advancing side (AS) is on the left side while the retreating side (RS) is on the right side. 69

Figure 4.11. SE SEM photomicrographs of the microstructure through the depth of the stir zone for the constant-speed FSW. The welding direction is perpendicular to the page. 69

Figure 4.12. EBSD orientation maps showing the variation in grain size through the depth of the constant-speed FSW stir zone at the top, mid top, middle, mid bottom, and bottom. The scale bar is 15μm. The welding direction is parallel to the page. 70

Figure 4.13. Bright field (BF) TEM photomicrographs and the corresponding SADP in the SZ (<100> zone axis) of the top layer a) and c) and middle layer b) and d), mid bottom layer e) and g), and bottom layer f) and h) The welding direction is perpendicular to the page. Dark grains are the refracting grains and where the SADP was acquired. 72

Figure 4.14. Bright field TEM photomicrographs and diffraction patterns in the SZ (<110> zone axis). The welding direction is perpendicular to the page. Dark grains are the refracting grains and where the SADP was acquired. 74

Figure 4.15. Bright field (BF) TEM photomicrographs and diffraction patterns in the SZ (<111> zone axis). The welding direction is perpendicular to the page. Dark grains are the refracting grains and where the SADP was acquired. 76

Figure 4.16. Bright field TEM photomicrographs and SADP from the mid top, +10 mm (RS) from the center of the weld (<100> zone axis). The SADPs indicate that only the Ω precipitate phase remains. The welding direction is perpendicular to the page. 78

Figure 4.17. (a)-(d) Bright field and diffraction pattern from the mid top +10 mm (RS) from the center of the weld (<110> zone axis), (e) the respective SADP in the <110> zone axis. The welding direction is perpendicular to the page. Dislocations pinned down by precipitates can be seen in c) and d). e) SADP shows that the Ω precipitate remains and θ' is absent. 79

Figure 4.18. (a)-(b) Bright field TEM photomicrographs and diffraction pattern from the mid top, +10 mm (RS) from the center of the weld (<111> zone axis), (c) the respective SADP in the <111> zone axis. The welding direction is perpendicular to the page. 81

Figure 4.19. Dark field TEM photomicrographs with inset diffraction patterns in the SZ top (a) <100> zone axis, (b) <110> zone axis, and (c)-(d) <111> zone axis. The spot associated with the DF images is circled in purple. The welding direction is perpendicular to the page. 82

Figure 4.20. Dark field TEM photomicrographs with inset diffraction patterns from the mid top, +10 mm (RS) from the center of the weld. (a) <100> zone axis, (b)-(c) <110> zone axis, and (d) <111> zone axis. The spot associated with the DF images is circled in purple. The welding direction is perpendicular to the page. 83

Figure 4.21. (a) Bright field photomicrographs in the <110> zone axis and (b) dark field photomicrograph at the <110> zone axis with inset diffraction pattern taken from the middle at the center of the SZ. The welding direction is perpendicular to the page. 85

Figure 4.22. (a)-(b) Bright field TEM photomicrographs in the <110> zone axis and (c) dark field photomicrograph at the <110> zone axis with inset diffraction pattern taken from the mid bottom at the center of the SZ. The welding direction is perpendicular to the page. Dislocations can be seen in a). Precipitates pinning down grain boundaries can be seen in a) and b). The dark field TEM photomicrograph demonstrates that θ' and Ω are not present. 86

Figure 4.23. Dark field TEM photomicrograph with inset SADP of the constant-speed FSW top. The purple circle correlates to the diffraction spot to the illuminated secondary phases in the DF image. Elemental EDS measurements on the right correspond to the region circled in red. The welding direction is perpendicular to the page. 87

Figure 4.24. Dark field TEM photomicrograph with inset SADP of the constant-speed FSW mid bottom. The purple circle correlates to the diffraction spot to the illuminated secondary phases in the DF image. Elemental EDS measurements on the right correspond to the region circled in blue. The welding direction is perpendicular to the page. 87

Figure 4.25. Dark field TEM photomicrograph with inset SADP of the constant-speed FSW bottom. The purple circle correlates to the diffraction spot to the illuminated secondary phases in the DF images. EDS measurements on the right correspond to region in the DF image circled in purple. The welding direction is perpendicular to the page. 88

Figure 4.26. Schematic depiction of the cause of the thermal gradient throughout the thickness of the weld. 92

Figure 4.27. Demonstration of how the HV map overlays on the etched welds. The sample was welded via constant-speed FSW. 93

Figure 4.28. Vickers microhardness map across the transverse cross section of the constant-speed FSW. Each pixel represents an 1 mm x 1 mm area. 94

Figure 4.29. Vickers microhardness map overlaid on only the welded region. 94

Figure 4.30. Vickers hardness plot of the constant-speed FSW through the thickness of the weld. HV0.5 represents a 0.5 kg load used for indentation. 95

Figure 4.31. Stress-strain plot of the constant-speed FSW at the top, middle, and bottom of the stir zone. The sample tested at 300°C was machined near the middle region of the weld. The tensile axis of the samples were parallel to the weld direction. 96

Figure 4.32. SE SEM photomicrographs of the microstructure through the depth of the SZ of the constant-speed FSW PWHT heat treated at 200°C for 10 hrs. 101

Figure 4.33. SE SEM photomicrographs of the microstructure through the depth of the SZ of the constant-speed FSW PWHT heat treated at 247°C for 2 hrs. 102

Figure 4.34. EBSD orientation maps showing the variation in grain size through the depth of the 247°C/2h PWHT at the top, mid top, middle, mid bottom, and bottom. 103

Figure 4.35. EBSD orientation maps showing the variation in grain size through the depth of the 200°C/10h PWHT at the top, mid top, middle, mid bottom, and bottom. 103

Figure 4.36. Average grain size versus the depth of the as-welded and post weld heat treated FSWs. 104

Figure 4.37. Precipitate volume versus the depth of the as-welded and post weld heat treated FSWs. 104

Figure 4.38. EBSD orientation maps of the PWHT (200°C/10h) FSW cross section 10 mm from the bottom edge of the sample, as shown in the green box macroetched image. The top row is a continuous montage of many individual scans, some of which are provided in higher magnification below in A) to C). A) The AS of the weld is shown. High magnification maps are shown of the HAZ, TMAZ, and SZ. B) The center of the SZ is shown. C) The RS of the weld is shown with high magnification maps of the SZ, TMAZ, and HAZ. The IPF color coded FCC unit triangle is based upon the sample normal direction. 105

Figure 4.39. EBSD of the PWHT (247°C/2h) FSW cross section 9 mm from the bottom edge of the sample, as depicted in the macroetched image. The top row is a continuous montage of many individual scans, some of which are provided in higher magnification below in A) to C). A) The AS of the weld is shown. High magnification maps are shown of the TMAZ, and SZ. B) The center of the SZ is shown. C) The RS of the weld is shown with high magnification maps of the

TMAZ, and HAZ. The IPF color coded FCC unit triangle is based upon the sample normal direction. 106

Figure 4.40. Vickers hardness plot through the thickness for the constant-speed, as-welded FSW. Hardness data was acquired using a 0.1 kgf load (HV0.1). 109

Figure 4.41. Vickers hardness plot through the thickness of the weld for the constant-speed FSW PHWT at heat treated at 200°C for 10 hrs. 110

Figure 4.42. Vickers hardness plot through the thickness of the weld for the constant-speed FSW PHWT heat treated at 247°C for 0.5 hr. 110

Figure 4.43. Vickers hardness plot through the thickness of the weld for the constant-speed FSW PHWT heat treated at 247°C for 0.9 hr. 111

Figure 4.44. Vickers hardness plot through the thickness of the weld for the constant-speed FSW PHWT heat treated at 247°C for 2 hrs. 111

Figure 4.45. Room temperature engineering stress versus engineering strain curves of constant-speed FSW for as-welded and PWHT conditions. Samples were extracted from the middle of the weld. 113

Figure 4.46. Optical macrograph of the etched a) constant-speed FSW and constant-temperature FSWs at b) 490°C, c) 500°C, and d) 510°C in the transverse cross section. Small dots are indents from the Vickers hardness test. The advancing side is on the left. 117

Figure 4.47. Average grain size throughout the depth of the weld for the constant-temperature and constant-speed FSWs. 118

Figure 4.48. Average precipitate volume percent throughout the depth of the weld for the constant-temperature and constant-speed FSWs. 118

Figure 4.49. SE SEM photomicrographs of the microstructure through the depth of the SZ of the constant-temperature FSW at 490°C. 120

Figure 4.50. SE SEM photomicrographs of the microstructure through the depth of the SZ of the constant-temperature FSW at 500°C. 121

Figure 4.51. SE SEM photomicrographs of the microstructure through the depth of the SZ of the constant-temperature FSW at 510°C. 122

Figure 4.52. Summary of the cause of the grain growth observed in the 500°C constant-temperature FSW. 123

Figure 4.53. Vickers microhardness map across the transverse cross section of the constant-temperature FSWs. The scale bar is constant for all of the welds. Each pixel represents an 1 mm x 1 mm area. The advancing side is on the left. 125

Figure 4.54. Vickers microhardness map overlaid on only the welded region for the constant-temperature and constant-speed FSWs. The constant-speed weld is provided for comparison. Each pixel represents an 1 mm x 1 mm area. The advancing side is on the left. 126

Figure 4.55. OM photomicrograph of the top of the 490°C FSW with the overlaid HV map below it for the AS (left) and the RS (right). The Vickers hardness map is overlaid on the photomicrographs. The color map follows the ROYGBIV scale with red being the highest hardness. The rotated grains indicate the TMAZ. The shown SZ and the TMAZ have similar hardness values. The green pixels indicate the HAZ. Each pixel is 1 mm in width and height. 127

Figure 4.56. OM photomicrograph of the bottom of the 490°C FSW with the overlaid HV map below it for the AS (left) and the RS (right). The Vickers hardness map is overlaid on the photomicrographs. The color map follows the ROYGBIV scale with red being the highest hardness. The rotated grains indicate the TMAZ. The shown SZ and the TMAZ have similar hardness values. Each pixel is 1 mm in width and height. 128

Figure 4.57. OM photomicrograph of the top of the 500°C FSW with the overlaid HV map below it for the AS (left) and the RS (right). The Vickers hardness map is overlaid on the photomicrographs. The color map follows the ROYGBIV scale with red being the highest hardness. The rotated grains indicate the TMAZ. The shown SZ has a higher hardness than the TMAZ. Each pixel is 1 mm in width and height. 129

Figure 4.58. OM photomicrograph of the bottom of the 500°C FSW with the overlaid HV map below it for the AS (left) and the RS (right). The Vickers hardness map is overlaid on the photomicrographs. The color map follows the ROYGBIV scale with red being the highest hardness. The rotated grains indicate the TMAZ. The shown SZ has a higher hardness than the TMAZ. Each pixel is 1 mm in width and height. 130

Figure 4.59. OM photomicrograph of the top of the 510°C FSW with the overlaid HV map below it for the AS (left) and the RS (right). The Vickers hardness map is overlaid on the photomicrographs. The color map follows the ROYGBIV scale with red being the highest hardness. The rotated grains indicate the TMAZ. The shown SZ has a higher hardness than the TMAZ. Each pixel is 1 mm in width and height. 131

Figure 4.60. OM photomicrograph of the bottom of the 510°C friction stir weld with the overlaid HV map below it for the AS (left) and the RS (right). The Vickers hardness map is overlaid on the photomicrographs. The color map follows the ROYGBIV scale with red being the highest hardness. The rotated grains indicate the TMAZ. The shown SZ has a higher hardness than the TMAZ. Each pixel is 1 mm in width and height. 132

Figure 4.61. Vickers hardness (using a 0.5 kgf load) plot of the constant-temperature FSWs through the thickness of the weld. This data was acquired from the hardness maps in Figure 4.53. Localized hardness in the SZ increases with temperature. Voids in the 510°C sample led to sudden decreases in hardness. The negative values on the x-axis represent the advancing side of the weld, while the positive values represent the retreating side. Some images of the actual indents are provided in the plots for comparison. 133

Figure 4.62. Weld joint comparison of the constant-temperature FSW. The as-received, base metal AA2139-T8 stress-strain curve is also provided for comparison. Constant-temperature FSW tensile samples are shown in Figures 4.63 through 4.65. 135

Figure 4.63. Digital images of the RT tensile tested 490°C constant-temperature FSW samples. The advancing side is on the left for all samples and images. 136

Figure 4.64. Digital images of the RT tensile tested 500°C constant-temperature FSW samples. Yellow arrows indicate areas of additional necking. The advancing side is on the left for all samples and images. 137

Figure 4.65. Digital images of the RT tensile tested 510°C constant-temperature FSW samples. The advancing side is on the left for all samples and images. 138

Figure 4.66. Schematic depiction explaining the mechanical behavior exhibited by the constant-temperature FSWs. 141

Figure 4.67. XRD comparison of the constant-temperature FSWs -30 mm (advancing side) from the center of the weld. 143

Figure 4.68. XRD comparison of the constant-temperature FSWs -20 mm (advancing side) from the center of the weld. 144

Figure 4.69. XRD comparison of the constant-temperature FSWs -10 mm (advancing side) from the center of the weld. 145

Figure 4.70. XRD comparison of the constant-temperature FSWs at the center of the weld. 146

Figure 4.71. XRD comparison of the constant-temperature FSWs +10 mm (retreating side) from the center of the weld. 147

Figure 4.72. XRD comparison of the constant-temperature FSWs +20 mm (retreating side) from the center of the weld. 148

Figure 4.73. XRD comparison of the constant-temperature FSWs +30 mm (retreating side) from the center of the weld. 149

Figure 4.74. Phases present in the FSWs at the target weld temperatures: 490°C, 500°C, and 510°C according to their position in the weld. Negative distance is for the AS, while positive distance is for the RS. 150

Figure 4.75. Constant-temperature FSWs Vickers hardness maps with orange markers showing where the XRD data was acquired (i.e. at the top, middle, and bottom layers). Negative distances represent the AS, while positive distances represent the RS. 158

Figure A.1. TEM photomicrographs of the unwelded AA2139-T8 depicting the θ' and the Ω phases in the <110> zone axis. Dark field (DF) photomicrographs are indicated in the first four images, while the last photomicrograph indicates the BF photomicrograph. 167

Figure A.2. TEM photomicrographs of the unwelded AA2139-T8 depicting the θ' and the Ω phases in the <100> zone axis. Dark field (DF) photomicrographs are indicated in the first seven images, while the last photomicrograph indicates the BF photomicrograph. 168

Figure B.1. Simulated diffraction patterns of three <100> variants for the θ' precipitate phase. The θ' precipitate diffraction spots are labelled on the experimental selected area diffraction pattern for the <100> Al-matrix zone axis. 170

Figure B.2. Simulated diffraction patterns of three <110> variants for the θ' precipitate phase. The θ' precipitate diffraction spots are labelled on the experimental selected area diffraction pattern for the <110> Al-matrix zone axis. 171

Figure B.3. Simulated diffraction patterns of <111> orientations for the θ' precipitate phase. The θ' precipitate diffraction spots are labelled on the experimental selected area diffraction pattern for the <111> Al-matrix zone axis. 172

Figure B.4. Simulated diffraction patterns of three <100> variants for the Ω precipitate phase. The omega precipitate diffraction spots are labelled on the experimental selected area diffraction pattern for the <100> Al-matrix zone axis. 173

Figure B.5. Simulated diffraction patterns of three <110> variants for the Ω precipitate phase. The omega precipitate diffraction spots are labelled on the experimental selected area diffraction pattern for the <110> Al-matrix zone axis. 174

Figure B.6. Simulated diffraction patterns of the <111> variants for the Ω precipitate phase. The omega precipitate diffraction spots are labelled on the experimental selected area diffraction pattern for the <111> Al-matrix zone axis. 175

Figure C.1. Schematic representing the specimens used for the *in situ* tensile and creep experiments. 176

Figure C.2. Stress vs. displacement plot for the base metal tested at room temperature and 300C in the rolling direction (RD) and the transverse direction (TD). "X" indicates samples taken to failure. Displacement values include displacement in the sample grip. Sudden decreases in stress indicate where the testing was paused for imaging. 178

Figure C.3. Sequential SE SEM micrographs for AA2139-T8 *in situ* tensile tested at room temperature (RT) in the rolling direction (RD). Strain at time of loading is indicated below the photomicrograph. Numbered micrographs). The engineering strain is indicated below the photomicrograph. Numbered micrographs correspond to the numbers on the stress-displacement curve. The tensile axis is horizontal. 180

Figure C.4. Sequential SE SEM photomicrographs for AA2139-T8 *in situ* tensile tested at 300°C in the rolling direction (RD). The engineering strain is indicated below the photomicrograph. Numbered photomicrographs correspond to the numbers on the stress-displacement curve. The tensile axis is horizontal. 181

Figure C.5. Sequential SE SEM photomicrographs for AA2139-T8 *in situ* tensile tested at RT in the TD. The engineering strain is indicated below the micrograph. The numbered photomicrographs correspond to the numbers on the stress-displacement curve. The tensile axis is horizontal. 182

Figure C.6. Sequential SE SEM photomicrographs for AA2139-T8 *in situ* tensile tested at 300°C in the TD. The engineering strain is indicated below the photomicrograph. The numbered photomicrographs correspond to the numbers on the stress-displacement curve. The tensile axis is horizontal. 183

Figure D.1. Stress vs. displacement plot for the constant-speed friction stir welded samples tested at room temperature and 300°C in the RD and the TD. "X" indicates samples taken to failure. Displacement values include displacement in the sample grips. 184

Figure D.2. Sequential SE SEM photomicrographs for constant-speed FSW *in situ* tensile tested at RT in the RD. The engineering strain is indicated below the micrograph. The numbered photomicrographs correspond to the numbers in the stress-displacement curve. The tensile axis is horizontal. 186

Figure D.3. Sequential SE SEM photomicrographs for constant-speed FSW *in situ* tensile tested at RT in the TD. The engineering strain is indicated below the micrograph. The numbered photomicrographs correspond to the numbers on the stress-displacement curve. The tensile axis is horizontal. 187

Figure D.4. Sequential SE SEM photomicrographs for constant-speed FSW *in situ* tensile tested at 300°C in the RD. The engineering strain is indicated below the photomicrograph. The labelled numbers in each photomicrograph corresponds to those instress-displacement curve. The tensile axis is horizontal. 188

Figure D.5. Sequential SE SEM micrographs for constant-speed FSW *in situ* tensile tested at 300°C in the TD. The engineering strain is indicated below the photomicrograph. The numbered photomicrographs correspond to the numbers onthe stress-displacement curve. Tensile axis is horizontal. 189

Figure E.1. A schematic of the strain versus time plot typically obtained for high-temperature creep under constant load and temperature. The different stages of creep (primary, secondary, and tertiary) are labelled. [84,95,96] 191

Figure E.2. Creep rate versus time plots for the creep strain versus time plots in Figs. Polynomial functions were fit to derive the secondary creep rates. Plots a) and b) correspond to Figure E.3. Plots c) and d) correspond to Figure E.4. Plots e) and f) correspond to Figure E.8. 196

Figure E.3. (a) Creep strain versus time plot for SZ Mid Bottom-2 and HAZ samples at 225°C and stresses ranging between 50-75-100-125 MPa. BSE SEM photomicrographs for (b) SZ Mid Bottom-2 (0.75% creep strain) and (c) HAZ (0.95% creep strain). 198

Figure E.4. a) Creep strain versus time plot for SZ and HAZ samples at temperatures ranging between 250-275°C and at stress of 50 MPa. BSE SEM photomicrographs of the b) SZ Mid Bottom-1 (2.4% creep strain) and c) HAZ (0.25% creep strain). 199

Figure E.5. a-b) SE SEM photomicrographs of the fractured sample SZ Mid Bottom-2 creep tested at 225°C and 50-75 MPa. Lateral sides of the sample have dimples. c) Intergranular features were observed at the center. The creep strain to failure was 0.75%. 200

Figure E.6. SE SEM photomicrographs of the fractured sample HAZ creep tested at 225°C and 50-125 MPa. a) Left half (which contained dimples). b) Right half (which exhibited intergranular cracking. c) higher-magnification image showing cracking at triple junctions (arrows) and along GBs (boxed area). The creep strain-to-failure was 0.95%. 201

Figure E.7. a-b) SE SEM photomicrographs of fractured sample SZ Mid Bottom-1 which underwent a temperature increase creep test at 250-275°C and 50 MPa. c) Higher-magnification image of the boxed region in (b indicating intergranular cracking. The creep strain-to-failure was 2.4%. 202

Figure E.8. (a) Creep strain versus time plot of a stress-jump test for a sample tested at 250°C and at stresses ranging between 25-35-50 MPa. BSE SEM photomicrographs of b) SZ Bottom (2.4% creep strain) and c) SZ Mid Bottom-3 (1.6% creep strain). 204

Figure E.9. a-b) Low-magnification SE SEM photomicrographs of a fractured sample SZ Bottom which underwent a stress increase creep test at 250°C and 25-35-50 MPa. Dimples are present on the fracture surface are shown in greater detail in (c) and (d). (e) Cracks and voids are observed. The creep strain to failure was 2.4%. 205

Figure E.10. a-b) Low-magnification SE SEM photomicrographs of SZ Mid Bottom-3 creep tested at 250°C and 25-35-50 MPa. Lateral sides exhibited dimples as shown in (c). The center contains evidence of intergranular fracture shown in (d). The creep strain to failure was 1.6%. Higher magnification of worm-like features in (d) are shown in (e)-(g), which demonstrate that they are a part of the material and contain secondary phases. (g) is a high magnification image of the precipitates on the fracture surface. 206

Figure E.11. a-b) Bright field TEM photomicrographs and their associated <100> and <110> zone axes of SZ Bottom and c) SZ Mid Bottom-3 in the <110> (bottom) creep tested at a temperature of 250°C and stresses of 25-35-50 MPa. 208

Figure E.12. Dark field TEM photomicrograph and the associated <110> zone axis of the HAZ creep tested at a temperature of 225°C and stresses of 50-125 MPa showing the θ' and σ (cuboidal) phases. 209

Figure E.13. a) Dark field photomicrograph associated with the circle points represented in the <100> zone axis insert and b) bright field photomicrograph (with the <110> zone axis insert) of the SZ Mid Bottom-2 creep tested at a temperature of 225°C and stresses of 50-125 MPa. Stress increases were done in 25 MPa increments. The Ω and θ' phases coarsened during the creep experiment..... 210

Figure F.1. Comparison of the XRD intensity versus 2-theta peaks for the as-received base metal and the constant-temperature FSWs at 490°C, 500°C, and 510°C. 213

Figure G.1. XRD intensity versus 2-theta plots for constant-temperature FSW at 490°C at all distances from the center of the weld and throughout the depth of the weld. 215

Figure G.2. XRD intensity versus 2-theta plots for constant-temperature FSW at 490°C and at -30 mm (the advancing side) throughout the depth of the weld (top, middle, and bottom)..... 216

Figure G.3. XRD intensity versus 2-theta plots for constant-temperature FSW at 490°C and at -20 mm (the advancing side) throughout the depth of the weld (top, middle, and bottom)..... 216

Figure G.4. XRD intensity versus 2-theta plots for constant-temperature FSW at 490°C and at -10 mm (the advancing side) throughout the depth of the weld (top, middle, and bottom)..... 217

Figure G.5. XRD intensity versus 2-theta plots for constant-temperature FSW at 490°C and at 0 mm throughout the depth of the weld (top, middle, and bottom). 217

Figure G.6. XRD intensity versus 2-theta plots for constant-temperature FSW at 490°C and at +10 mm (the retreating side) throughout the depth of the weld (top, middle, and bottom)..... 218

Figure G.7. XRD intensity versus 2-theta plots for constant-temperature FSW at 490°C and at +20

mm (the retreating side) throughout the depth of the weld (top, middle, and bottom)..... 218

Figure G.8. XRD intensity versus 2-theta plots for constant-temperature FSW at 490°C and at +30 mm (the retreating side) throughout the depth of the weld (top, middle, and bottom)..... 219

Figure G.9. XRD intensity versus 2-theta plots for constant-temperature FSW at 500°C at all distances from the center of the weld and throughout the depth of the weld. 219

Figure G.10. XRD intensity versus 2-theta plots for constant-temperature FSW at 500°C and at -30 mm (the advancing side) throughout the depth of the weld (top, middle, and bottom)..... 220

Figure G.11. XRD intensity versus 2-theta plots for constant-temperature FSW at 500°C and at -20 mm (the advancing side) throughout the depth of the weld (top, middle, and bottom)..... 220

Figure G.12. XRD intensity versus 2-theta plots for constant-temperature FSW at 500°C and at -10 mm (the advancing side) throughout the depth of the weld (top, middle, and bottom)..... 221

Figure G.13. XRD intensity versus 2-theta plots for constant-temperature FSW at 500°C and at 0 mm throughout the depth of the weld (top, middle, and bottom). 221

Figure G.14. XRD intensity versus 2-theta plots for constant-temperature FSW at 500°C and at +10 mm (the retreating side) throughout the depth of the weld (top, middle, and bottom). 222

Figure G.15. XRD versus 2-theta plots for constant-temperature FSW at 500°C and at +20 mm (the retreating side) throughout the depth of the weld (top, middle, and bottom). 222

Figure G.16. XRD intensity versus 2-theta plots for constant-temperature FSW at 500°C and at +30 mm (the retreating side) throughout the depth of the weld (top, middle, and bottom). 223

Figure G.17. XRD versus 2-theta plots for constant-temperature FSW at 510°C at all distances from the center of the weld and throughout the depth of the weld. 223

Figure G.18. XRD intensity versus 2-theta plots for constant-temperature FSW at 510°C and at -30 mm (the advancing side) throughout the depth of the weld (top, middle, and bottom)..... 224

Figure G.19. XRD intensity versus 2-theta plots for constant-temperature FSW at 510°C and at -20 mm (the advancing side) throughout the depth of the weld (top, middle, and bottom)..... 224

Figure G.20. XRD intensity versus 2-theta plots for constant-temperature FSW at 510°C and at -10 mm (the advancing side) throughout the depth of the weld (top, middle, and bottom)..... 225

Figure G.21. XRD intensity versus 2-theta plots for constant-temperature FSW at 510°C and at 0

mm throughout the depth of the weld (top, middle, and bottom). 225

Figure G.22. XRD intensity versus 2-theta plots for constant-temperature FSW at 510°C and at +10 mm (the retreating side) throughout the depth of the weld (top, middle, and bottom). 226

Figure G.23. XRD intensity versus 2-theta plots for constant-temperature FSW at 510°C and at +20 mm (the retreating side) throughout the depth of the weld (top, middle, and bottom). 226

Figure G.24. XRD intensity versus 2-theta plots for constant-temperature FSW at 510°C and at +30 mm (the retreating side) throughout the depth of the weld (top, middle, and bottom). 227

KEY TO ABBREVIATIONS AND SYMBOLS

Ag	Silver
Al	Aluminum
AS	Advancing Side
BSE	Backscattered electron
BM	Base metal
C	Carbon
Cr	Chromium
Co	Cobalt
Cu	Copper
DRX	Dynamic recrystallization
EDM	Electrodischarge machining
EBSD	Electron backscattered diffraction
EDS	Energy Dispersive X-Ray Spectroscopy
FCC	Face-centered cubic
Fe	Iron
FSW	Friction stir welding
GB	Grain boundary
GBS	Grain boundary sliding
GP	Guinier-Preston
GPB	Guinier-Preston-Bagaryatsky
HAZ	Heat affected zone

IPF	Inverse Pole Figures
Li	Lithium
LWN	Lower Weld Nugget
Mg	Magnesium
Mn	Manganese
Ni	Nickel
OIM	Orientation Image Map
O	Oxygen
RD	Rolling direction
ROYGBIV	red-orange-yellow-green-blue-indigo-violet
RS	Retreating Side
RT	Room temperature
SEM	Scanning electron microscopy
SE	Secondary electron
Si	Silicon
SiC	Silicon Carbide
Ag	Silver
SZ	Stir zone
TD	transverse direction
TMAZ	Thermomechanically affected zone
Ti	Titanium
TEM	Transmission electron microscopy
TTI	Transformation Technologies, Inc.

TTT	time-temperature-transformation
UTS	Ultimate tensile strength
UWN	Upper Weld Nugget
V	Vanadium
wt.%	Weight percent
XRD	X-ray Diffraction
YS	Yield strength
Zn	Zinc
Zr	Zirconium
ε_f	Elongation-to-failure
ε_{tot}	Total strain
Ω	Omega phase
σ	Sigma phase
σ_a	Applied stress
θ	Theta phase
θ'	Theta prime phase

CHAPTER 1

INTRODUCTION

1.1 Rationale and Research Objective

The demand for the development of both high-strength and lightweight metals for structural applications to increase vehicle mobility has driven an increase in the research and development of lightweight alloys, including those based on aluminum (Al), magnesium (Mg), and titanium (Ti), to replace commonly-used steel. Although steels offer a wide range of yield strengths (YS) (ranging from 200 to 1650 MPa), their densities range from 7.65 to 8 g/cm^3, which is three times higher than that for Al [1]. Magnesium alloys have a density of approximately 1.8 g/cm^3 and YS values ranging between 97 to 220 MPa (depending on processing), however, they sometimes suffer from low corrosion resistance [1]. With a density of 4.5 g/cm^3 and a YS between 170 to 1100 MPa, Ti alloys are good candidates for lightweighting [1]. Primarily due to the processing required, Ti alloys suffer from high costs and welding sometimes requires specialized welders and welding techniques. Common Al alloys, which benefit from low-cost processing, good weldability using conventional welding techniques, and good corrosion resistance, have an average density of 2.7 g/cm^3 and a YS that ranges between 90 to 572 MPa (depending on processing) [1,2].

The excellent strength-to-weight ratio of Al alloys is desirable for use in structural applications within the transportation industry. The earliest successful industrial integration of Al involved the use of copper (Cu)-based Al alloys, otherwise known as Al-Cu alloys, in the engine of the Wright Flyer in the 1900s [3]. Lightweighting in the aerospace industry translates into increased revenue generated through increased range and payload capabilities [4]. The National Aeronautics and Space Administration (NASA) was able to shed 7,500 pounds from their 60,000

pound U.S. Space Shuttle Super Light Weight Tank by replacing the original AA2219, Al-5.8Cu-0.2Mn (wt.%)[1], with AA2195, Al-4Cu-1Li-0.4Mg-0.4Ag. This allowed them to increase the payload and reduce the number of trips needed to construct the International Space Station, which saved millions of dollars [4,5]. The National Highway and Safety Administration (NHTSA) issued a required fleet-wide fuel economy average of 40.3-41 miles per gallon by the 2021 model year for passenger cars and light trucks [6]. The Ford Motor Company replaced steel body panels with Al alloys on the 2015 F-150 pick-up truck in order to reduce the weight by 600 pounds and increase the fuel efficiency by 23% [7,8].

Aluminum is intentionally alloyed with elements to increase the YS, fatigue life, and fracture toughness. Common alloying elements for Al include Cu, Mn, Si, Mg, Mg+Si, and Zn+Mg, which correspond to the 2xxx, 3xxx, 4xxx, 5xxx, 6xxx, and 7xxx series, respectively. The Mn, Si, and Mg additions result in increased strength via solid-solution strengthening. The Cu, Mg+Si, and Zn+Mg additions create very fine precipitates that inhibit dislocation motion and grain boundary sliding (GBS). To further increase their mechanical strength, these precipitation-hardened alloys are tempered using a combination of cold or hot working and a sequence of heat treatments. Aluminum-copper alloys alloyed with Mg and Ag can exhibit higher ultimate tensile strengths (UTS) and fracture toughness values than most Al alloys, especially when tempered [9]. The Al alloys of choice for critical damage tolerance in aircraft applications are 2324-T39 (Al-4Cu-1Mg) and 7475-T7351 (Al-5.5Zn-1.9Mg-1.2Cu), while 2519 (Al-5.3Cu-0.1Mn-0.05Mg) is favored for armored vehicles [9]. Cho and Bes demonstrated that the newly-developed 2139-T8

[1]Hereafter, all alloy compositions are provided in weight percent.

(Al-5Cu-0.5Mg-.38Ag, nominal composition) exhibited greater fatigue life, fracture toughness, and ballistic performance compared to the above-mentioned alloys [9]. Nonetheless, Al-Cu alloys are difficult to join using fusion welding processes due to solidification cracking. To circumvent the difficulties that arise with fusion welding, friction stir welding (FSW) can be employed.

FSW is a solid-state joining method that utilizes friction generated heat between a rotating tool and two metal plates to create a joint. Additional material, such as a filler metal, is not needed to initiate or complete the weld. FSW employs process temperatures that are lower than the melting point. This solid state process yields three distinct microstructural zones in the welded area: the heat affected zone (HAZ), the thermomechanically affected zone (TMAZ), and the stir zone (SZ). The microstructure exhibited in each zone is a result of the level of interaction between the metal and the tool, which also influences the degree of thermal and mechanical processing. There is a lateral temperature gradient, where the SZ is the hottest zone and also undergoes dynamic recrystallization (DRX) [10,11]. In addition, the SZ exhibits a microstructural gradient through the weld thickness. This is due to the difference in cooling rates between the top of the weld, which is dominated by convection heat rejection, and the bottom of the weld, which is dominated by conduction heat rejection.

There has been great interest in understanding the grain refinement of the SZ and its effects on corresponding mechanical properties. For this reason, the effects of welding speed, strain rate, and cooling rate on the microstructure and mechanical behavior of the SZ (as well as the HAZ and TMAZ) are intensely studied. The welding temperature has largely been an uncontrolled and unmonitored variable. This presents an issue when trying to predict or explain the weld microstructures using equilibrium phase diagrams, time-temperature-transformation curves, and/or continuous cooling transformation curves. Recently, the ability to achieve and maintain

targeted FSW temperatures has been demonstrated by independently controlling the tool speed [12,13]. One of the primary objectives of this dissertation was to systematically study the effect of FSW temperature on the microstructural evolution in the welded region.

Much of the research on FSW has been conducted on Al alloy plates between 2-12 mm thick. There is limited information on military-grade alloys, which frequently utilize plate thicknesses of 25 mm and greater. Thus, there is a lack of clear understanding as to how FSW affects the processing-microstructure-property relationships of thick-plate Al alloys. Therefore, a systematic study relating the FSW process to the microstructure and mechanical properties of thick Al alloys is needed for the successful integration of FSW in military applications.

The principal goal of this dissertation was to understand how FSW affects the resulting microstructure and mechanical properties in a thick Al alloy when the welding temperature is kept constant. A secondary goal was to understand how FSW affects the resulting microstructure and mechanical properties in a thick Al alloy when the welding speed is kept constant. In this work, the matrix grain size and the evolution of the precipitate phases as a function of weld location and temperature were studied. Knowledge of FSW processing-microstructure-property relationships of thick Al-Cu alloys will aid in the prediction of the resulting microstructures and their mechanical behavior, optimization of the welding parameters, tool development, and understanding of dominant strengthening mechanisms in the specific weld zones. The microstructures and mechanical properties of constant-speed and constant-temperature FSW were compared using 25 mm thick AA2139-T8, an Al-Cu-Mg-Ag alloy.

1.2 Work Performed

The effects of constant-speed and constant-temperature FSW on the microstructural evolution and mechanical behavior of the welded region were studied for AA2139-T8. Novel aspects of this work were the large thickness (25 mm) of the welded plates and that constant-

temperature FSW was utilized.

In Chapter 2, a background of Al and Al alloys is provided, including the crystal structure, the effects of alloying elements, Al alloy nomenclature, temper classifications, and precipitation sequence. Emphasis is placed on precipitation-hardened alloys, and in particular, Cu-based alloys. A background on FSW, its effects on the microstructure, welding temperature ranges including current measurement techniques, and tool features are also provided.

In Chapter 3, the experimental methods used in this dissertation are detailed. The nominal and measured alloy compositions, heat treatments used, sample machining, and sample preparation are also provided. The methods used for the microstructural and mechanical property analysis are described. The FSW parameters and tooling are also detailed.

In Chapter 4, the results from the microstructural characterization, post weld heat treatments (PWHTs), Vickers hardness testing, and tensile testing are provided for the experimental control (as-received AA2139-T8) and constant-speed FSW material. The results from the microstructure characterization, Vickers hardness testing, and tensile tests are also provided for constant-temperature FSW material. The X-ray diffraction (XRD) results are also presented. The results are then discussed to relate the FSW processing to the resulting microstructures and its effect on the mechanical behavior.

In Chapter 5, the summary, conclusions, and recommended future work are presented.

CHAPTER 2

BACKGROUND

This chapter describes the justification for the use of Al alloys in the FSW process. A literature review on Al and Al alloys has been provided highlighting pertinent items related to the research performed in this dissertation. The fundamental Al physical metallurgy, the nomenclature, processing, and application are discussed, with emphasis on precipitation-hardened Al alloys. The history of FSW processing and its effect on the microstructure and mechanical properties of Al alloys—in particular Al-Cu, Al-Cu-Mg, and Al-Cu-Mg-Ag alloys, are provided. At the end of this chapter a critical assessment of some research gaps remaining for FSW of Al alloys is provided as well as how this dissertation work is intended to bridge some of these gaps.

2.1 Aluminum and Aluminum Alloys

Lightweight materials play a role in increasing the performance of vehicles and reducing their payload, which assists in increasing their fuel economy. Aluminum and its alloys have traditionally been considered as one of the primary materials of choice whenever a high strength-to-weight ratio is required for structural applications. Lightweight materials are critical in the aerospace industry due to the limited capabilities of the aircraft engines [4]. In the early 1900s, the Wright Flyer airframe was comprised of Al to decrease aircraft weight while maintaining structural integrity. Aircraft fuselage is also commonly constructed using Al alloys, usually from the 2xxx, 6xxx, and 7xxx series [9]. In addition, the incorporation of high-strength Al alloys is increasing in the Army [14]. For example, the Mg-based Al alloy 5083, has been used for lightweighting options in U.S. Army ground vehicles such as the Bradley [15].

2.1.1 Physical Metallurgy of Al and Al alloys

Aluminum is the 13th element listed in the periodic table. It makes up 8% of the Earth's

crust and is the third most abundant element in the Earth's crust after oxygen (O) and silicon (Si) [16,17]. Aluminum is especially reactive in humid and oxidative environments. Upon exposure to O at relatively low temperatures ($T \leq 573$ K), Al reacts to form a ceramic, passive, amorphous oxide film termed alumina or aluminum oxide (Al_2O_3), which can reach up to 1 nm in thickness [18]. At higher temperatures ($T \geq 673$ K), this oxide film can thicken up to 2.4 nm and it eventually becomes crystalline [18]. This oxide film protects the metal underneath from environmental degradation. Aluminum has a density approximately one-third that of steel (i.e. 2.7 g/cm^3) [1,19]. The thermal conductivity of Al is 237 W/m-K, which is greater than that for magnesium (Mg) (156 W/m-K) and less than that for copper (Cu) (386 W/m-K) [19–21]. The melting point of Al is 660°C [1,19,22]. Aluminum has a face-centered cubic (FCC) crystal structure with a lattice parameter of 4.0495 Å [1,19]. The Young's modulus (E) varies with the crystallographic orientation; the [100], [110], and [111] have an E values of 63.7, 72.6, and 76.1 GPa, respectively [1]. The tensile YS for pure Al is 26-117 MPa and the ultimate tensile strength (UTS) ranges between 50-125 MPa depending on the temper and the purity [1,19]. Alloying, along with tempering, can increase the YS to 505 MPa and the UTS to 572 MPa [1] .

Since pure Al lacks the strength needed for many structural applications, it is usually alloyed. An alloy is a pure metal that has been intentionally mixed with other elements to improve the mechanical, chemical, electronic, and thermal properties. Copper typically is added to improve the strength of Al through precipitation strengthening; however, Cu decreases the corrosion resistance in the annealed condition and it increases stress corrosion in the age hardened condition [19,22]. Through solid-solution strengthening, Mg additions increase the strength, elongation-to-failure, corrosion resistance, and weldability especially when combined with Zn additions such as in the Al-Zn-Mg alloy system [19,22]. Manganese (Mn) additions improve the hardness especially

in Al-Cu-Mn, Al-Mg-Mn, and Al-Zn-Mg-Mn alloy systems [19]. Silicon (Si) improves weldability, casting, and some mechanical properties [19,22]. Each primary alloying element is grouped into an alloy system, or series, and is named accordingly. The nomenclature of the Al alloy series is explained in the next section.

2.1.2 The Nomenclature and Tempering of Al and Al alloy

The Al alloy nomenclature designation system is set by the American National Standards Institute (ANSI) standard H35.1 [2]. The designation system includes the product form (wrought, casting, or ingot) and the respective temper (strain hardening and heat treatment) [2]. The designation systems for wrought and cast Al alloys is depicted in Table 2.1 [2]. Cast Al and Al alloys are designated by three digits before the decimal point and a fourth digit after the decimal point. Wrought Al and Al alloys use a four-digit numerical system without a decimal point. For both naming conventions, the first digit indicates the main alloying element. For example, the 2xxx alloys have Cu as their main alloying element while the 5xxx alloys have Mg as their main alloying element, see Table 2.1. As this dissertation research investigates a wrought 2xxx alloy, the focus is on the wrought designation system. The 1xxx series do not have an intentional alloying element. For the 1xxx series, the last two digits represent the purity of the Al [2,23]. For instance, Al with a purity of 99.5% is designated as Al 1050. A non-zero second digit in the 1xxx series indicates the special control of one or more impurities [2]. For example, Al 1150 has special control on Si, Fe, and Cu [2]. In the 2xxx to 8xxx series, the last two digits serves only as an alloy identifier and does not specify the sequence in alloy development or registration [2,23]. The second digit indicates there is a slightly different range of the alloying elements and Fe and Si impurities compared with the original target composition [2,23]. For example, AA2324 is the third modification of AA2024 and it contains 3.8-4.4%Cu and 1.2-1.8%Mg (the upper limit of Cu was modified) [2]. Alloying and heat treating enhance the mechanical properties (e.g. UTS, YS, and

hardness) of Al.

Table 2.1. Aluminum alloying designation system and temper designation system per the Aluminum Association [2].

Wrought Alloy Groups		Basic Temper Designations	
1xxx	Unalloyed 99% Al	F	As fabricated
2xxx	Copper is the principal alloying element: gives substantial increases in strength, permits precipitation hardening, reduces corrosion resistance, ductility and weldability	O	Annealed: there may be a suffix to indicate the specific heat treatment
3xxx	Manganese: increases strength through solid solution strengthening and improves work hardening	H	Strain hardened (cold worked): it is always followed by two or more digits to signify the amount of cold work and any heat treatments that have been carried out
4xxx	Silicon: increases strength and ductility, in combination with magnesium produces precipitation hardening	W	Solution heat treated: applied to alloys that precipitation harden at room temperature (natural aging) after a solution heat treatment. The designation is followed by a time indicating the natural aging period, e.g. W 1 h
5xxx	Magnesium: increases strength through solid solution strengthening and improves work hardening ability	T	Thermally aged: T1: cooled and naturally aged T2: cooled, cold worked, and naturally aged T3: solution heat treated, cold worked, and naturally aged T4: solution heat treated and naturally aged T5: cooled and artificially aged T6: solution heat treated and artificially aged T7: solution heat treated and overaged or stabilized T8: solution heat treated, cold worked, and artificially aged T9: solution heat treated, artificially aged, and cold worked
6xxx	Magnesium-Silicon		
7xxx	Zinc-Magnesium: substantially increases strength, enables precipitation hardening, can cause stress corrosion		
8xxx	Other elements - Li, for example, substantially increases strength and Young's modulus, provides precipitation hardening, decreases density		

Aluminum temper designations are standardized by the Aluminum Association. There are three temper groups: O, H, and T [2,24]. Each temper may be followed by a non-zero digit to further specify temper processing. The O designation means the alloy has been annealed. This results in a lower hardness than the non-heat treated alloy. The H designation means the alloy has been strain-hardened. T-type tempers indicate the alloy has been thermally aged. T- and H-tempers result in a higher hardness than the non-treated or annealed alloy. An alloy is tempered to achieve desirable mechanical, chemical, electrical, or machining properties for targeted production applications. Aluminum alloys are categorized by whether they are heat treatable or non-heat treatable [24]. Non-heat treatable alloys experience enhanced mechanical properties through cold or hot working and are generally strain hardened and undergo O- and H-type tempers [24]. Non-heat treatable Al alloys are the 1xxx, 3xxx, 4xxx, and 5xxx series [24]. Heat treatable alloys are those that can be precipitation hardened and generally undergo T-type tempers [24]. The Al alloy series that are heat treatable are the 2xxx, 6xxx, and 7xxx series [24]. Table 2.1 describes the O, T, and H tempers. The temperatures for each temper process are tailored to the

alloy. For instance, in heat-controlled procedures, the temperature is based on phase diagrams and time-temperature-transformation (TTT) curves. Although these temperatures vary among and within alloy systems, there are some generalities. Solutionizing is generally performed around 500-550°C. Artificial aging can range from 130-200°C. Hot working is generally performed around 200°C. These temperature ranges are generally associated with binary Al alloys. For tertiary, quaternary, and more complex systems, one needs to consider all the alloying components and their effects on the microstructure. The alloy investigated in this dissertation (AA2139) underwent the T8 temper. Therefore, emphasis is placed on T-type tempers. The T8 temper process consists of solutionizing, then cold working, and finally, artificially aging to facilitate increased precipitation.

For AA2139, the T8 temper intensifies the precipitation of the θ' and Ω phases and results in achieving a peak tensile strength [9]. Solutionizing dissolves the precipitates yielding a supersaturated solid solution. The cold working process—in this case rolling—reduces the thickness of the metal plate and creates numerous dislocations and dislocation subgrain structures. This puts the material in a high energy state as dislocations are energetically expensive [25]. They are line defects that distort the lattice and can cause strain misfits, vacancies, and local disorder. As a result, when the material is artificially aged, these dislocations act as diffusion pipes causing the solute atoms to diffuse to them. The high concentration of solute atoms then order themselves on these dislocations in order to reduce the Gibb's free energy and bring the bulk material closer to its equilibrium state [25].

2.2 The Microstructure of 2xxx Aluminum Alloys

Tempering Al-Cu alloys promotes a homogeneous distribution of the secondary phases. When tempered appropriately, the precipitation sequence in binary Al-Cu alloys is

$$\text{SSS} \rightarrow \text{GP I} \rightarrow \text{GP II } (\theta'') \rightarrow \theta' \rightarrow \theta \qquad [2]$$

where SSS stands for the supersaturated solid solution and GP stands for Guinier-Preston zones I and II [25]. The θ-type precipitates are the primary precipitate phases of the 2xxx series. The GP I, θ", and θ' precipitates are all thermally metastable transition phases [19,25–28]. Thermally metastable indicates that with time and temperature (and enough Cu-solute at their disposal), the precipitates will transform from their current phase to another phase that is more energetically favorable [25]. This involves reducing the lattice strains that arise due to the coherency between the matrix and the precipitate. The transformation reduces the coherency of the precipitate to the matrix from fully coherent (GP I), where all sides of the precipitate lattice are equivalent to the lattice of the matrix, to semicoherent (θ" and θ'), where one or more sides are equivalent to the matrix lattice, to incoherent (θ) [25]. The incoherent θ precipitate phase is regarded as the equilibrium phase as none of the sides are coherent with the matrix and no transformation is expected to occur afterwards. In addition, the equilibrium θ precipitates (Al_2Cu, body-centered tetragonal, a=4.0495 Å, c=5.80Å, I4/mcm) are coarse and therefore readily observed using a scanning electron microscopy (SEM) [25]. The thermally metastable precipitates are finer [25] and are usually characterized using transmission electron microscopy (TEM). The GP I precipitate forms as clusters of Cu-solutes on dislocation loops when artificially aged at 180°C for 15-30 s [28]. The GP I then transforms to an ordered and crystalline phase, θ", at 180°C and 30 s [28]. The θ" phase transforms into θ' when the Al-Cu-Mg and Al-Cu-Mg-Ag alloys are aged at 180°C for 2.5 hours [28]. After a treatment at 250°C and 2.5 hours, the equilibrium θ forms [25,27,28]. The θ-type precipitates typically nucleate on dislocations, grain boundaries, and at the precipitate-matrix interface. The more stable and strengthening of the metastable precipitates is θ' (Al_2Cu, tetragonal, a=4.0495Å, c=5.80Å, I-4m2) [26], due to its ability to withstand temperatures up to 400°C and dislocation shearing [29]. It forms as either a rectangular or octagonal platelet [27],

has a $\{100\}_\alpha$ habit plane, and has the following orientation relationship with the matrix: {001}a//{001}θ',{ 010}a//{010}θ', [001]α//[001]θ' [26,30].

Another precipitate phase that can be found in the 2xxx series is the S-type precipitates. This precipitate is usually found in the 2xxx series in which the Cu:Mg weight ratio is relatively low (approximately 1.5-4) [31–34]. The generally accepted precipitation sequence is

$$SSS \rightarrow GPB\ 1 \rightarrow GPB\ 2\ (S'') \rightarrow S' + \theta' \rightarrow S + \theta$$

where GPB is the Guinier-Preston-Bagaryatsky [27,28,31,32,35]. GPB is the GP zone equivalent for the S-type precipitates. The equilibrium S (Al_2CuMg, orthorhombic, a=4.96Å, b=8.59Å, c=8.48Å, Fmmm) [27,28,31,36–39] phase appears to be the most studied phase and therefore the most understood while the morphology, crystallography, and nucleation of the other transition phases in the Al-Cu-Mg and Al-Cu-Mg-Ag alloys are less understood [28,29,40–42].

The Al-Cu-Mg-Ag alloy systems have introduced another strengthening precipitate phase, Ω (Al_2Cu, orthorhombic, a=4.96, b=8.59 Å, c=8.48Å, Fmmm) [36,37,42]. The Ω phase has been the focus of much research due to its stability at high temperatures, added strengthening, and ability to precipitate at elevated artificial aging temperatures. With small additions of Ag (up to 0.4 wt%) the Ω phase can precipitate in the Al-Cu-Mg-Ag alloy [40]. However, Gable et al. demonstrated that Ω can also precipitate in Al-Cu-Mg alloys when the Si content is less than 0.1 wt% [43]. A Cu:Mg ratio of approximately 6 favors Ω precipitation over θ', while a ratio of approximately 10 favors θ' [29]. The Ω phase can precipitate at 180°C for aging times between 30 seconds to 2.5 hours, and it can coexist with the θ' precipitate [27,28,44]. The Ω phase is stable up to 250°C after which it is replaced by the equilibrium θ [27]. The Ω phase is also thermally stable in alloys with a Cu:Mg ratio of 13-14 when aged at relatively high temperatures ranging between 200-300°C [27]. It appears as a fine dispersion of hexagonal platelets that have a $\{111\}_\alpha$ habit plane and the

following orientation relationships with the α-matrix[2]: $\{111\}_\alpha//\{001\}_\Omega$, $[10\text{-}1]_\alpha//[010]_\Omega$, $[1\text{-}21]_\alpha//[100]_\Omega$ (edge on) [27,36]. Nucleation of the Ω phase is stimulated with the addition of Ag and Mg atoms through the clustering of Ag and Mg atoms on the $\{111\}_\alpha$ [44–46]. The Ag and Mg atoms are also present at the α-matrix/Ω interface [46,47]. Sun et al. determined that the Al atoms in the α-matrix bind to the Ag atoms which bind to the Mg atoms which bind to the Ω precipitate [48]. The Ω phase can be detected after the precipitation of the θ" [46], thus the precipitation sequence is

$$SSS \rightarrow GP\ 1 \rightarrow \theta" \rightarrow \Omega \qquad [47]$$

Ringer et al. demonstrated that the θ' phase is a competing precipitate [49]. When an Al-Cu-Mg-Ag alloy with up to 6 wt% Cu is cold worked before artificial aging, the density of the Ω phase is reduced while that of the θ' phase is increased [29,49]. The cold working creates dislocations that move through the matrix, which disrupts the Mg and Ag clustering and the vacancies that attract these solutes. This results in a reduced hardness.

As aforementioned, the Ω phase improves the mechanical properties of Al-Cu-Mg-Ag alloys. The creep resistance is improved up to 200°C, indicating that Ω is stable at elevated temperatures for prolonged times [40]. It also improves the high-temperature strength and hardness over alloys without the Ω phase and with no Mg and Ag additions [40].

The θ', Ω, and S precipitates govern the strength and elongation-to-failure of the age hardenable alloys and do so based on their size, distribution, and nucleation/habit planes (e.g. dislocations, grain boundaries, misfit strains, etc.). Tempering encourages precipitation by

[2] α is the symbol that represents the matrix.

facilitating the diffusion of Cu, Mg, and Ag solutes to high energy sites (e.g. dislocations and grain boundaries) where, with time and temperature, the clusters become ordered phases. The generally accepted precipitation sequence of Al-Cu-Mg and Al-Cu-Mg-Ag alloys is

$$SSS \rightarrow GP\ 1 \rightarrow \theta'' \rightarrow \theta'+\Omega \rightarrow \theta'+S' \rightarrow S+\theta \qquad [9,29,50]$$

2.3 The Development of Aluminum Alloy AA2139

AA2139 was developed by ALCAN and in 2010 the U.S. Army RDECOM[3] Acquisition Center contracted ALCAN to supply them with AA2139-T8 plates for research on damage tolerance [9,51]. The Army Research Laboratory (ARL) studied this alloy via this contract. In addition to damage tolerance, the U.S. Army investigated this alloy for unibody applications [52].

AA2139 is a 2xxx series precipitation-strengthened alloy. Per the naming system described in the previous section, it is the first modification of AA2039 (Al-4.5%Cu-0.2%Mg-0.15%Ag) and is the 39th alloy group within the 2xxx series. Some of the modifications in AA2139 tighten the range of allowable Mg and broaden the range of Ag additions. The target composition of alloys 2039 and 2139 are listed in Table 2.2.

The ternary phase diagrams for the Al-Cu-Mg system are presented in Figure 2.1 and Figure 2.2. The shaded regions on the phase diagrams represent the wt% for Cu and Mg in AA2139. The liquidus temperature (approximated from Figure 2.1a) lies between 640-650°C. The solidus temperature (approximated from Figure 2.1b) is approximately 527°C. The strengthening precipitates of this alloy are the θ' and Ω-phases. The S-phase is also expected to

[3] RDECOM underwent reorganization and is now called the Combat Capabilities Development Command (DEVCOM).

be a strengthening precipitate in this alloy per the Al-Cu-Mg solidus phase diagram, see Figure 2.2.

Table 2.2. Target compositions per the Aluminum Association, 2006 for alloys a) AA2039, and b) AA2139 (boxed elements are those that have been modified).

AA2039

a)

Al	Cu	Mg	Ag	Mn	Si	Fe	Cr	Zn	Ti	V
Bal	4.5-5.5	0.2-0.8	0.15-0.16	0.2-0.6	0.10	0.15	0.05	0.25	0.15	0.05

AA2139

b)

Al	Cu	Mg	Ag	Mn	Si	Fe	Cr	Zn	Zr	Ti	V
Bal	4.5-5.5	0.4-0.8	0.05-0.50	0.2-0.5	≤0.20	≤0.30	≤0.05	--	0.10-0.25	≤0.15	--

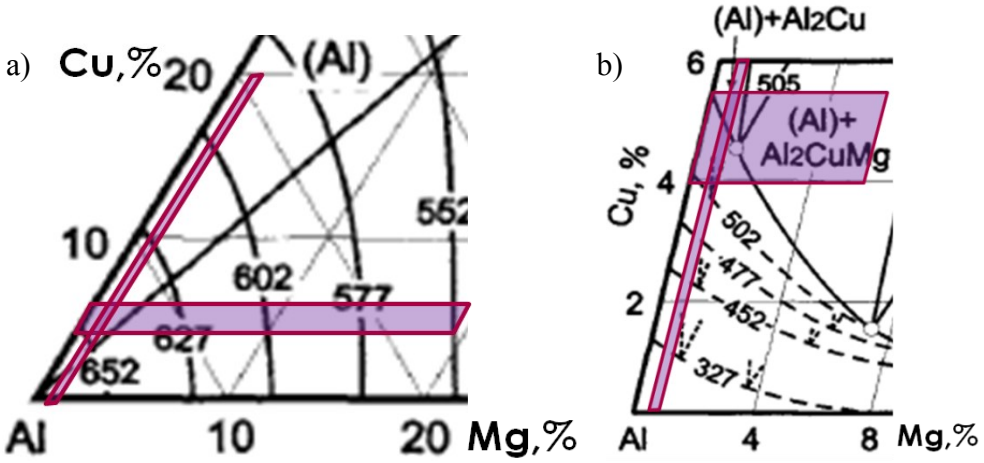

Figure 2.1. Al-Cu-Mg ternary system phase diagrams. The thin, vertically slanted shaded region represents the Mg concentrations in the AA2139 alloy. The horizontal shaded region represents the Cu concentrations in the AA2139 alloy. a) liquidus (estimated to be approximately 640-650°C, b) solidus (estimated to be approximately 527°C) [19].

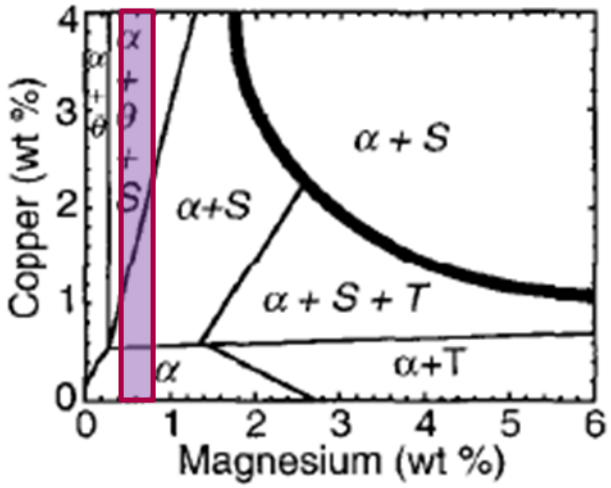

Figure 2.2. Al-Cu-Mg phase diagram at 190°C. The shaded region represents the Mg concentration in the AA2139 alloy. The thick solid line is the α/α+S phase boundary at 500°C [19]. The appropriate Cu concentration (4.5-5.5 wt%) for this alloy is just outside the range of this chart.

The blast resistance, its microstructure, and mechanical properties of AA2139 have been investigated [9,53–59]. AA2139-T8 is considered to be a high-strength Al alloy. However, Al alloys that contain a high Cu concentration are challenging to weld using fusion welding methods. Fusion welding Cu-based Al alloys leads to solidification cracking [60]. This is a problem since lightweight materials are economically and technologically advantageous. FSW is a relatively new welding technique that has been proven to successfully weld Cu-based Al alloys [54,61,62]. This technique is discussed next in section 2.4.

2.4 Friction Stir Welding

2.4.1 Introduction

High-strength Al alloys are usually heat treatable due to the fact that they are precipitation hardened [23]. Heat treatments can be used in addition to a number of other processing steps, which are explained in section 2.1.2. Heat treatable Al alloys, particularly the 2xxx series are difficult to join using fusion welding methods due to the resulting liquation and solidification

cracking [22]. In addition, the strength of the precipitation-hardened alloys is significantly reduced in the welded region [22]. Thus, new methods of joining Al alloys, such as FSW, which is the focus of this work, are utilized to improve joint strength.

FSW is a solid-state joining technique developed by The Welding Institute (TWI, UK) approximately 30 years ago [61,62]. This joining technique helps to circumvent issues that arise from fusion welding methods. FSW requires no additional material other than the initial plates or sheets of metal (i.e. the workpiece) to be welded and no additional heat/energy source other than that generated by the friction due to the rotational stirring of a non-consumable tool. Figure 2.3 illustrates the FSW process. As it's rotating, a downward force is applied to the tool while plunging into the joint of the workpieces. When it reaches the preprogramed depth, frictional heat is generated between the shoulder of the tool and the material [10]. In addition, adiabatic heat is generated due to the plastic deformation of the material flowing around tool. The heat input softens the material allowing it to flow around the tool. As the tool traverses, the now softened material flows around it from the advancing side (AS) to the retreating side (RS) and is compressed behind the tool and under the tool shoulder thereby completing the weld. There are two sides of the weld. The AS is defined as the side in which the translation and rotation directions are the same. The RS is defined as the side in which the translation and the rotation directions are opposite.

The heat and shear deformation induced by the stirring develop three unique microstructural regions: the stir zone (SZ), thermomechanically affected zone (TMAZ), and heat affected zone (HAZ) [10,11,63]. The mechanical properties, such as hardness and tensile strength, vary across these zones and are strongly dependent on the microstructural changes caused by the heat generation and the stirring [54,55,64,65]. Maximum temperatures range between 400-550°C, or 0.6-0.9T_m [11,66–68]. For AA2139, 550°C is near the solidus temperature range. The heat

generated and shape of the weld are affected by the welding parameters [63,65].

FSW of lightweight alloys has provided industrial advantages via the reduction of component weight by eliminating additional joining materials (rivets and fasteners), multiple material compatibility, and meeting dimension restrictions as demonstrated in the 2008 Ford GT application and the NASA's Space Shuttle Super-Light Weight Tank [69,70]. More benefits of FSW are shown in Table 2.3. In this dissertation, AA2139-T8 was friction stir welded to study its effects on the resulting microstructure and the mechanical properties (through the material thickness) as a function of welding temperature.

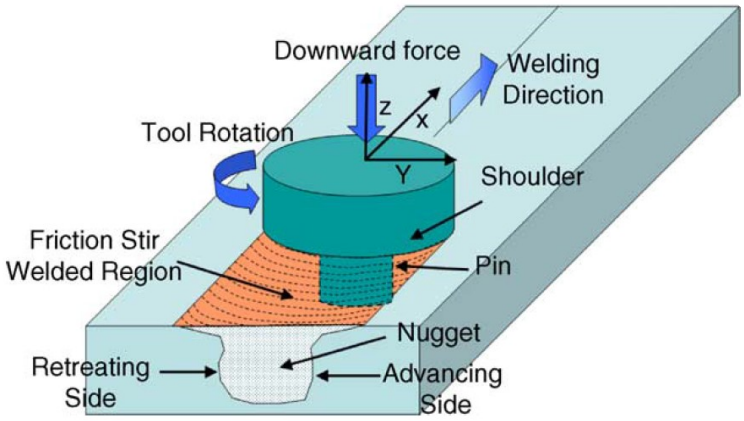

Figure 2.3. Illustration of the friction stir welding process and tool [11].

Table 2.3. Important benefits of friction stir welding [11].

Metallurgical benefits	Environmental benefits	Energy benefits
Solid phase process	No shielding gas required	Improved materials use (e.g. joining different thickness) allows for reduction in weight
Low distortion of workpiece	No surface cleaning required	Only 2.5% of the energy needed for a laser weld
Good dimensional stabilty and repeatability	Eliminate grinding wastes	Decreased fuel consumption in light weight aircraft, automotive, and ship applications
No loss of alloying elements	Eliminate solvents required for degreasing	
Excellent metallurgical properties in the joint area	Consumable materials saving, such as rugs wire or any other gases	
Fine microstructure		
Absence of cracking		
Replace multiple parts joined by fasteners		

2.4.2 Manufacturing Processes

2.4.2.1 Tool Material and Geometry

A non-consumable tool is necessary in FSW applications. The tooling material should be able to resist damage from both the high welding temperatures and the friction to allow for more than one use. The tooling material for Al alloys can be tool steel alloys, such as H13, or nickel (Ni)-cobalt (Co) based alloys, such as MP159 [10]. For academic and developmental investigations, tool steels are used because of their relatively low costs; though, these tools have lower tensile strengths and operating temperatures than the Ni-Co alloys. The Ni-Co based tools can withstand higher temperatures and welding forces, yet the alloying elements are costly. As a result, Ni-Co based tools are generally used for welding of high-strength and high-temperature Al alloys, such as the 2xxx and the 7xxx series. To reduce costs, a combination of materials can be used. For instance, the tool shoulder can be made of H13 tool steel, while the pin can be made of MP159 in order to withstand high cross forces during traversing. This was the case for the tool used in this dissertation for constant-speed FSW.

Tool geometry is another key factor for defect-free welds. The tool geometry includes the shape and size of the tool components (shoulder and pin) and other features, as seen in Figure 2.4. The two functions of the tool are to assist localized heating of the joint and material flow [11].

Therefore, the geometry should be designed according to the thickness of the plate. Generally, the thicker the plate, the greater the shoulder width and the tool pin diameter should be. Because the shoulder has a wider diameter than the pin, the shoulder generates the majority of the heat needed to soften the material [10,11]. In addition it facilitates a downward forging force that pushes material into the weld and consolidates it [10,11]. Scrolls features on the shoulder assist in the downward material flow. Features of the pin facilitate the 'stirring' of the softened material [11]. Threads, flutes, and flats on the pin can impact the welding forces, increase/decrease material flow, assist with the plunging, and impact the heat input due to the increased surface area of the pin [11]. Rabby et al. demonstrated that threads on the pin eliminated wormhole defects and adding flats improved material flow and reduce forces on the tool [71]. For such reasons, the tools used in this dissertation work incorporated scrolls and threaded pins with flats.

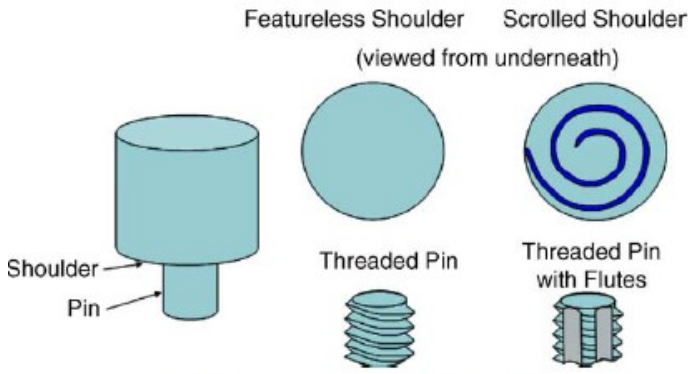

Figure 2.4. Illustration of the FSW tool features [11].

2.4.2.2 Welding Parameters

Both the tool geometry and the welding speed are the most critical parameters of FSW. There are two aspects to the FSW speed: the rotational speed (measured in revolutions per minute) and the traversing speed (measured in mm/min). Faster rotational speeds generate higher welding temperatures due to the larger diameter of the shoulder. This can be understood by the formula in Equation 2.1 for tangential radial velocity [m/s]

$$v = \omega r \tag{2.1}$$

where r is the radius [m] and ω is the angular velocity [rad/s]. As r increases, v increases, thus the tool shoulder would have a faster v compared to the smaller diameter of the pin. Increased rotational speeds results in more intense stirring and mixing of the material [11]. Translation of the tool moves the stirred material from the front to the back of the pin and completes the welding process [11]. Contrary to the rotational speed, faster traversing speeds result in cooler welding temperatures similar to how a faster travel speed reduces the heat input in fusion welds [10,63]. Faster FSW speeds lead to a narrower HAZ and increased hardness in the stir zone [72,73]. However, the SZ temperature is rarely monitored or controlled and, as evident in Table 2.4, there has been a limited amount of FSW research conducted on 25 mm thick plates [11].

It is expected that in thick plates, increased rotational speeds will yield a wider HAZ, however, it is uncertain if increases in the SZ hardness will result. The tool shoulder is primarily responsible for generating the heat and in thin plates, the rotating shoulder can force material flow through the thickness of the plate [10]. Thus, the heating and cooling of thick FSW plates may not be similar to that of thin plates due to the limited shoulder engagement. This hypothesis will be evaluated in this work through increasing the rotational speed while simultaneously controlling the traversing speed and the target welding temperatures. Controlling the FSW temperature is explained in the next section.

2.4.2.3 Thermal Management

Welding temperature is another parameter that needs to be carefully considered for targeted FSW applications. Controlling and monitoring the welding temperature may ensure that the same microstructure and mechanical properties near the start of the weld are equivalent to that near the end of the weld. Maintaining a near constant welding temperature can aid in the systematic optimization of other welding parameters to obtain a desirable microstructure. Ross et al. used

temperature control FSW in order to control the thickness of the intermetallic layer formed when welding an Al alloy to steel [74].

For a particular alloy or alloy system, thermal control can provide a basis for studying the microstructural evolution as a function of temperature. With enough experiments, a model can be used to simulate time-temperature-transformation (TTT) and continuous cooling transformation (CCT) curves and the microstructure can be directly correlated to the mechanical properties. Although there has been an increase in thermal monitoring, most methods use thermocouples inserted into the plate at various depths in the plate thickness and along the length of the joint [68,75]. There are limitations associated with this method. One such limitation is that the SZ temperature cannot be measured directly because the movement of the tool will disturb the position of the thermocouple. Thus, the temperatures measured are near the TMAZ and in the HAZ [68,75]. Another method of thermal monitoring is to use an infrared thermometer. However, the limitations become evident when used on the silver white reflective surface of Al.

Ross et al. demonstrated that thermocouples can be successfully spot welded to the tool surface to measure the temperature in the SZ [12,76]. The experiments provided evidence that when held at a constant speed without temperature control, the temperature changes along the length of the weld. In order to obtain and maintain the target welding temperature, the rotational speed must change. Constant temperature FSW has yet to be attempted on AA2139. In addition, there is limited work on FSW of thick plates. In general, studying the microstructure as a function of welding temperature for thick-plate Al alloys is lacking, and this dissertation was intended to fill that gap.

2.4.3 Microstructural Zones

As aforementioned, the microstructure of FSW Al alloys can be grouped into three categories: the SZ, TMAZ, and HAZ [10,11,63]. The base metal (BM), although not a formal

weld zone, is the easiest region to identify since it is the parent material and has been unaffected by the welding process. The BM maintains its original microstructure and mechanical properties throughout the welding process.

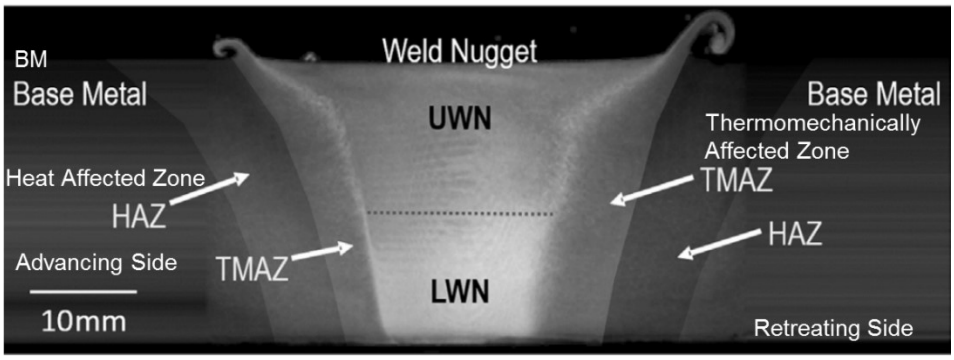

Figure 2.5. Scanning electron microscopy photomicrograph of the transverse cross section of a friction stir weld adapted from [77] with the labelled weld zones. The weld nugget is also referred to as the stir zone (SZ). UWN and LWN refer to the upper weld nugget and lower weld nugget, respectively.

The HAZ is located between the TMAZ and BM and has been exposed only to the thermal cycling [11,63,78]. The temperature in this zone can range from 250°C to 350°C and this results in coarsened strengthening precipitates, which is indicative of an overaged microstructure [11,68,75,78]. The HAZ has the same grain structure as the BM but reduced tensile strengths due to the coarsened precipitates.

The TMAZ is located between the HAZ and the SZ and has been exposed to both the thermal cycling and the plastic deformation from the tool [11,63]. It is a very narrow zone that typically exhibits rotated and elongated grains. Subgrain boundaries can be found within this zone due to the high dislocation density. Dissolution of strengthening precipitates occurs in the TMAZ.

The SZ is the region that comes in direct contact with the tool, thus it experiences thermal cycling, plastic deformation, and dynamic recrystallization, which results in refined, equiaxed grains [11,63]. The grain size in this region can range between 1-18 μm in various Al alloys and for various FSW thicknesses, as shown in

Table 2.4 [11]. This basin-shaped zone is the hottest of all the weld zones and experiences precipitate coarsening, dissolution and reprecipitation. As such, the hardness is significantly less than that of the BM, even when a localized hardness increase in the SZ is observed [63]. Thermocouples placed adjacent to the SZ in a 14 mm thick AA2219-O plate demonstrated that there is a thermal gradient of approximately 20°C through the thickness of the plate during FSW [75]. However, information on the temperature gradient in thick Al alloys is limited and not well explored for AA2139.

Post weld heat treatments (PWHTs) have been performed on FSWs in an effort to improve the hardness and tensile strength of the SZ. PWHTs performed by Elangovan and Balasubramanian explored the effects of solutionizing, solutionizing and artificial aging, and artificial aging on the tensile strength of FSW AA6061-T6 [79]. Artificial aging at 160°C for 18 hours was the only heat treatment that improved the tensile strength compared to the as-welded condition. It is unknown whether or not a PWHT would be as effective for thick Al-Cu-Mg-Ag alloys. This was evaluated in this dissertation.

Table 2.4. A summary of the stir zone grain size in FSW/FSP aluminum alloys. Notice that only one alloy has a thickness of 25 mm [11]. The referred references are found within the work of Mishra and Ma [11].

Material	Plate Thickness (mm)	Tool Geometry	Rotation Rate (RPM)	Traverse Speed (mm/min)	Grain Size (μm)	Reference
7075Al-T6	6.35	–	–	127	2–4	[4]
6061Al-T6	6.3	Cylindrical	300–1000	90–150	10	[5]
Al–Li–Cu	7.6	–	–	–	9	[6]
7075Al-T651	6.35	Threaded, cylindrical	350, 400	102,152	3.8, 7.5	[15]
6063Al-T4, T5	4	–	360	800–2450	5.9–17.8	[67]
6013Al-T4, T6	4	–	1400	400–450	10–15	[75]
1100Al	6	Cylindrical	400	60	4	[76]
5054Al	6	–	–	–	6	[77]
1080Al-O	4	–	–	–	20	[78]
5083Al-O	6	–	–	–	4	[78]
2017Al-T6	3	Threaded, cylindrical	1250	60	9–10	[79]
2095Al	1.6	–	1000	126–252	1.6	[80]
Al–Cu–Mg–Ag–T6	4	–	850	75	5	[81]
2024Al-T351	6	–	–	80	2–3	[82]
7010Al-T7651	6.35	–	180, 450	95	1.7, 6	[83]
7050Al-T651	6.35	–	350	15	1–4	[84]
Al–4Mg–1Zr	10	Threaded, cylindrical	350	102	1.5	[85]
2024Al	6.35	Threaded, cylindrical	200–300	25.4	2.0–3.9	[86]
7475Al	6.35	–	–	–	2.2	[87]
5083Al	6.35	Threaded, cylindrical	400	25.4	6	[88]
2519Al-T87	25.4	–	275	101.6	2–12	[89]

2.5 Summary

Information on the microstructure of Cu-based Al alloys and the FSW process and resulting microstructure of FSW Al alloys were explored in this chapter. A critical review of the literature reveals the following gaps in knowledge pertaining to FSW of Cu-based Al alloys:

(1) There is limited literature on the FSW of Al plates with a thickness of 25 mm or greater.

(2) *In situ* thermal control of FSW has been limited to the joining of plates less than 25 mm thick.

(3) Because AA2139-T8 is a recently developed alloy, there is limited information on the

FSW of this alloy and in particular the effects of FSW on the microstructural evolution and mechanical behavior. In particular, a detailed understanding of the phases (including their structures and volume fractions) that develop within the separate welded zones is lacking for FSW AA2139.

(4) Knowledge of the microstructural evolution in the weld zones as a function of controlled-temperature FSW is non-existent.

(5) The effect of controlled-temperature FSW on the processing, microstructure, and mechanical properties of thick Al alloy plates is unknown.

(6) The through-thickness temperature gradient that occurs during FSW, which incorporates the SZ temperature for constant-speed and constant-temperature conditions, is unknown.

(7) Identification of the different precipitate phases within the separate welded zones as a function of the FSW temperature is lacking.

Knowledge gaps (1) through (5) were addressed in this dissertation by conducting FSW on 25 mm thick AA2139-T8. FSW was performed using constant speed (50 mm/min/ 150 RPM) and constant temperature (490°C, 500°C, and 510°C). FSW temperature was measured via a thermocouple spot welded to the surface of tool shoulder. The evolution of the microstructure in the SZ was characterized using scanning electron microscopy (SEM) for both the constant-speed and constant-temperature welds, and transmission electron microscopy (TEM) was performed for the constant-speed welds. Mechanical testing (tensile test and Vickers hardness) was performed for both the constant-speed and constant-temperature welds. X-ray diffraction (XRD) was used to identify the different phases and characterize the microstructure evolution throughout all the weld zones in the constant-temperature FSWs, which specifically addresses gap (3) and contributes to

gap (7). The XRD results were paired with the Vickers hardness maps to correlate precipitate phases to mechanical performance. Knowledge gap (6), which requires multiple thermocouples to be placed in the tool pin, is outside of the scope of this dissertation research.

CHAPTER 3

EXPERIMENTAL METHODS

This section describes the experimental methods used for the material processing, friction stir welding (FSW), post-weld heat treatments (PWHT), metallurgical preparation, microstructural characterization, and mechanical testing. It also provides the dimensions of the plates and welds as well as the specimens extracted from the plates and welds used for the mechanical behavior characterization.

3.1 Materials and Processing

3.1.1 AA2139-T8

AA2139-T8 plates were provided to Michigan State University (MSU) by both Dr. Tomoko Sano, Combat Capabilities Command Army Research Laboratory (DEVCOM ARL, Aberdeen Proving Ground, MD), and Mr. P.J. McMullen, Concurrent Technologies Corporation (CTC, Johnstown, PA). The T8 temper specifies solution heat treatment (525-544°C), cold working (rolling), and artificial aging (163-256°C) [80]. The nominal composition of the plates (per the Aluminum Association) is listed in Table 3.1. The 762mm (RD) x 533mm (TD) x 25.4mm plates were FSW by EWI (Columbus, OH). The portion of the plates unaffected by the welding process served as the control. This material was designated as "BM" for base metal and was used for the baseline (or control) microstructure characterization and mechanical property analysis. Another set of AA2139-T8 plates were provided by CTC from a larger plate with dimensions of 2438 mm (RD) x 1575 mm (TD) x 25.4 mm. The measured composition of this plate is shown in Table 3.1. The compositions were measured using Spectro SPECTROMAXx arc/spark optical emission spectrometry. The average of three measurements is listed, indicating that the alloy is in the middle of the specified ranges. FSW was conducted on 101.6 mm (RD) x 304.8 mm (TD) x

25.4 mm plates machined from this bulk material.

Table 3.1. Composition limits for AA2139 (top) and the measured composition for the plate received from CTC (bottom). Plates given to DEVCOM ARL were from CTC.

Al	Cu	Mg	Ag	Mn	Si	Fe	Cr	Zn	Ti	V
Bal	4.5-5.5	0.2-0.8	0.15-0.6	0.2-0.6	0.10	0.15	0.05	0.25	0.15	0.05
Bal	4.92	0.41	0.39	0.33	0.047	0.11	0.002	0.024	0.12	0.009

3.1.2 Friction Stir Welding (FSW)

3.1.2.1 Constant-Speed FSW

Two plates, of dimension: 762 mm (RD) x 533 mm (TD) x 25.4 mm, of AA2139-T8 were joined via position-controlled (i.e. controlling the depth position of the tool into the material) FSW by EWI under the direction of the DEVCOM ARL. The welding parameters and tool dimensions are provided in Table 3.2 [55]. The final plunge position was fixed and the travel and rotational speeds were held constant at 50 mm/min (2 IPM) and 150 RPM, respectively. The advancing side (AS) and the retreating side (RS) are defined in section 2.4[4]. A schematic of FSW is shown in Figure 3.1. The welded plate (received from ARL) is shown in Figure 3.2 Welding was performed perpendicular to the plate rolling direction and over a length of 457 mm. Grinding was performed on the surface of the plates prior to welding to remove oxidation and other contaminants. The as-welded plate was received after some surface grinding had been performed, see Figure 3.2.

The tool used for constant-speed FSW was designed by EWI. The two-piece tool comprised of a 4340 steel shoulder and MP159 (Ni-Co alloy) pin, press-fit together. The shoulder

[4] All figures in this dissertation portray the AS on the left hand side and the retreating side on the right hand side unless otherwise stated.

has a diameter of 41.3 mm and no scroll features. The length of the pin is 24.7 mm and it contains counterclockwise threads and four flats.

Table 3.2. Constant-speed welding parameters with tool dimensions [55].

Parameter	Specification
Plunge rotation initial speed	250 RPM
Plunge initial depth	16.5 mm (0.65 in.)
Plunge rotation final speed	150 RPM
Plunge rotation final depth	25.3 mm (0.995 in.)
Plunge vertical speed	19 mm/min (0.75 IPM)
Travel speed	50 mm/min (2 IPM)
Rotation speed	150 RPM
Retraction speed	125 mm/min (5 IPM)
Retraction rotation speed	150 RPM
Tilt angle	3°
Total length	457 mm (18 in.)
Shoulder diameter	41.3 mm (1.625 in.)
Pin length	24.7 mm (0.972 in.)

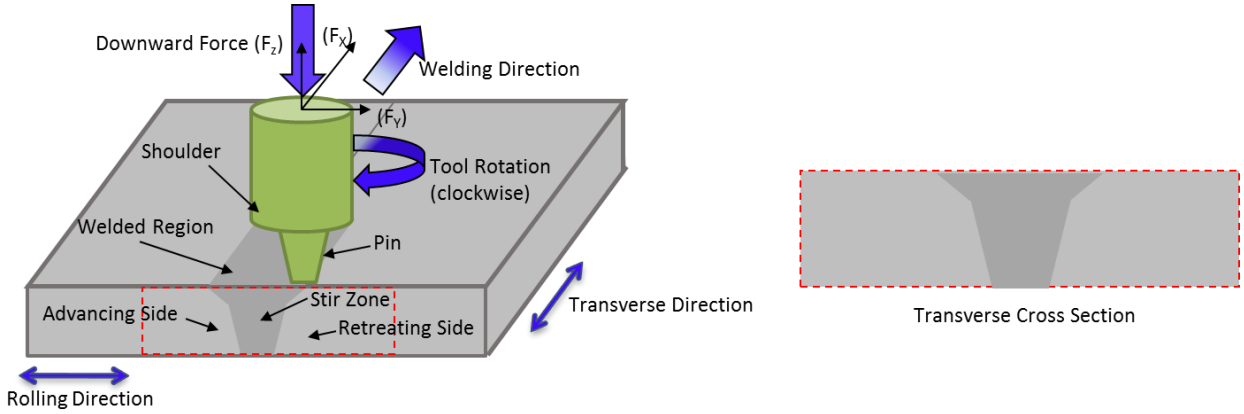

Figure 3.1. Schematic depicting the friction stir welding (FSW) process and the transverse cross sectional view. Adapted from Mishra and Ma [11].

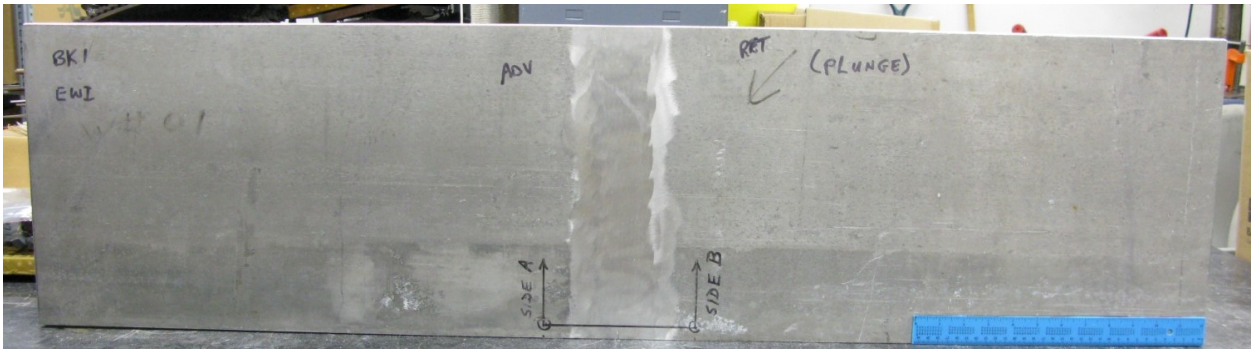

Figure 3.2. Digital image of the FSW plate received from the DEVCOM ARL. The blue ruler is 305 mm long.

3.1.2.2 Constant-Temperature FSW

Constant-temperature FSW was performed using a Transformation Technologies, Inc. (TTI, Elkhart, IN)[5] machine, see Figure 3.3, at the Pacific Northwest National Laboratory (PNNL, Richland, WA). Target temperatures were 490°C, 500°C, and 510°C. These temperatures were chosen below the solidus temperature, based on the Al-Cu-Mg and Al-Cu phase diagrams, see Figure 3.4, to avoid liquation. The constant-temperature FSW parameters and tool dimensions are depicted in Table 3.3. The plates used for the constant-temperature FSW were machined via water jet cutting into 102 mm (RD) x 305 mm (TD) x 25.4 mm sections. They were machined from one large AA2139-T8 rolled plate of dimensions: 2438 mm (RD) x 1575 mm (TD) x 25.4 mm. The plates were welded in the transverse direction for a length of 229 mm. FSW was conducted via position control while the rotational speed was adjusted to achieve and maintain the target temperature. Figure 3.5 through Figure 3.8 show plots of the FSW machine commands and tool responses used to achieve and maintain the targeted FSW temperatures. The commands that were

[5] The section of TTI that provided friction technologies has separated and is now Bond Technologies in Elkhart, IN.

held constant include the plunge depth (25 mm) and the travel speed (50 mm/min). The measured variables were tool forces, torque, spindle power, rotational speed, and temperature. The temperature was measured using a thermocouple embedded in the tool shoulder at approximately half the exposed radius, Figure 3.9. There was no evidence that the thermocouple interfered with the flow of the scrolls. Each machine response was recorded for the targeted welding temperatures of 490°C, 500°C, and 510°C. For all the constant-temperature FSW materials, the target temperature was not achieved until the process reached the midpoint length of the weld. As a result, samples were machined from the middle of the weld length to approximately 60 mm from the center of the tool exit hole. Comparison of the speeds for each temperature revealed that the rotational speed had to be increased in order to obtain higher temperatures, as shown in Figure 3.8. Comparison of the torques for each temperature revealed that higher torque was required to weld at lower temperatures, see Figure 3.8. At 500°C and 510°C, the torque measured was only half that required at 490°C. The machine spindle torque limit was approximately 680 N-m. Thus, welding temperatures below 490°C, coupled with a travel speed of 50 mm/min, would require a more robust motor.

The single piece H13 steel tool used for the constant-temperature welding was designed by PNNL. The tool rotation was in the counter clockwise direction. The shoulder has a diameter of 38 mm and consists of counter clockwise scrolls (viewed from the bottom of the pin). The pin length was 23.9 mm with counter clockwise threads and three flats placed at 120 degree angles. A pre-drilled countersink hole was made on the plates to reduce tool forces and extend tool life, Figure 3.10. The mechanical testing and microstructural characterization began approximately 2.5 months after FSW had been performed. The plates were stored at room temperature (RT) during this period.

Figure 3.3. Digital image of the Transformation Technologies, Inc (TTI) FSW machine used to perform FSW at constant temperature. It is located at PNNL.

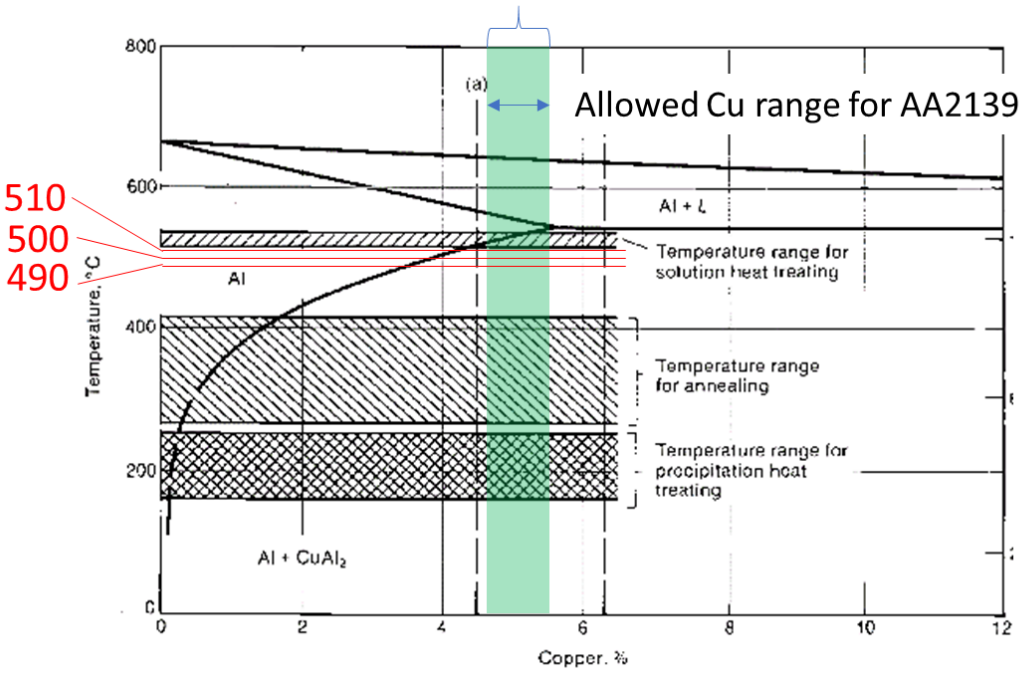

Figure 3.4. The Al-Cu binary phase diagram [80]. FSW temperatures were chosen below the eutectic temperature and the out of the Al+L phase region. For Al-Cu-Mg alloys, the liquidus and solidus temperatures range from 640-650°C and 510-527°C, respectively.

Table 3.3. Constant-temperature FSW parameters.

Parameter	Specification
Plunge rotation initial speed	250 RPM
Plunge initial depth	16.5 mm (0.65 in.)
Plunge rotation final speed	150 RPM
Plunge rotation final depth	24.9 mm (0.98 in.)
Plunge vertical speed	19 mm/min (0.75 IPM)
Travel speed	50 mm/min (2 IPM)
Rotation speed	Varied with temperature
Retraction speed	125 mm/min (5 IPM)
Retraction rotation speed	150 RPM
Total length	228.6 mm (9 in.)
Shoulder diameter	38 mm (1.5 in.)
Pin length	23.9 mm (0.94 in.)

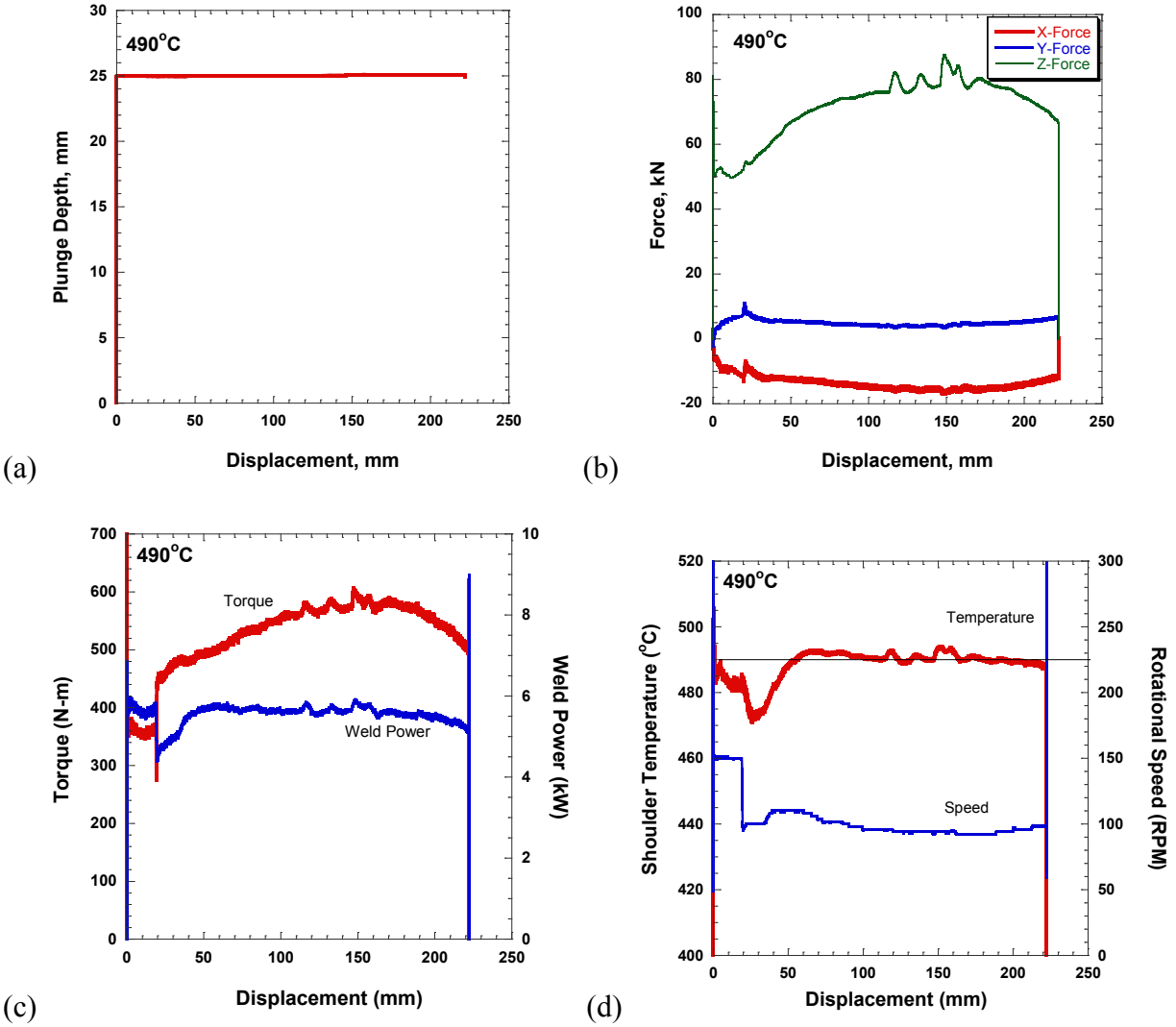

Figure 3.5. (a) Plunge depth versus displacement, (b) force versus displacement, (c) torque versus displacement, and (d) shoulder temperature and rotational speed versus displacement plots for the constant-temperature FSW at 490°C.

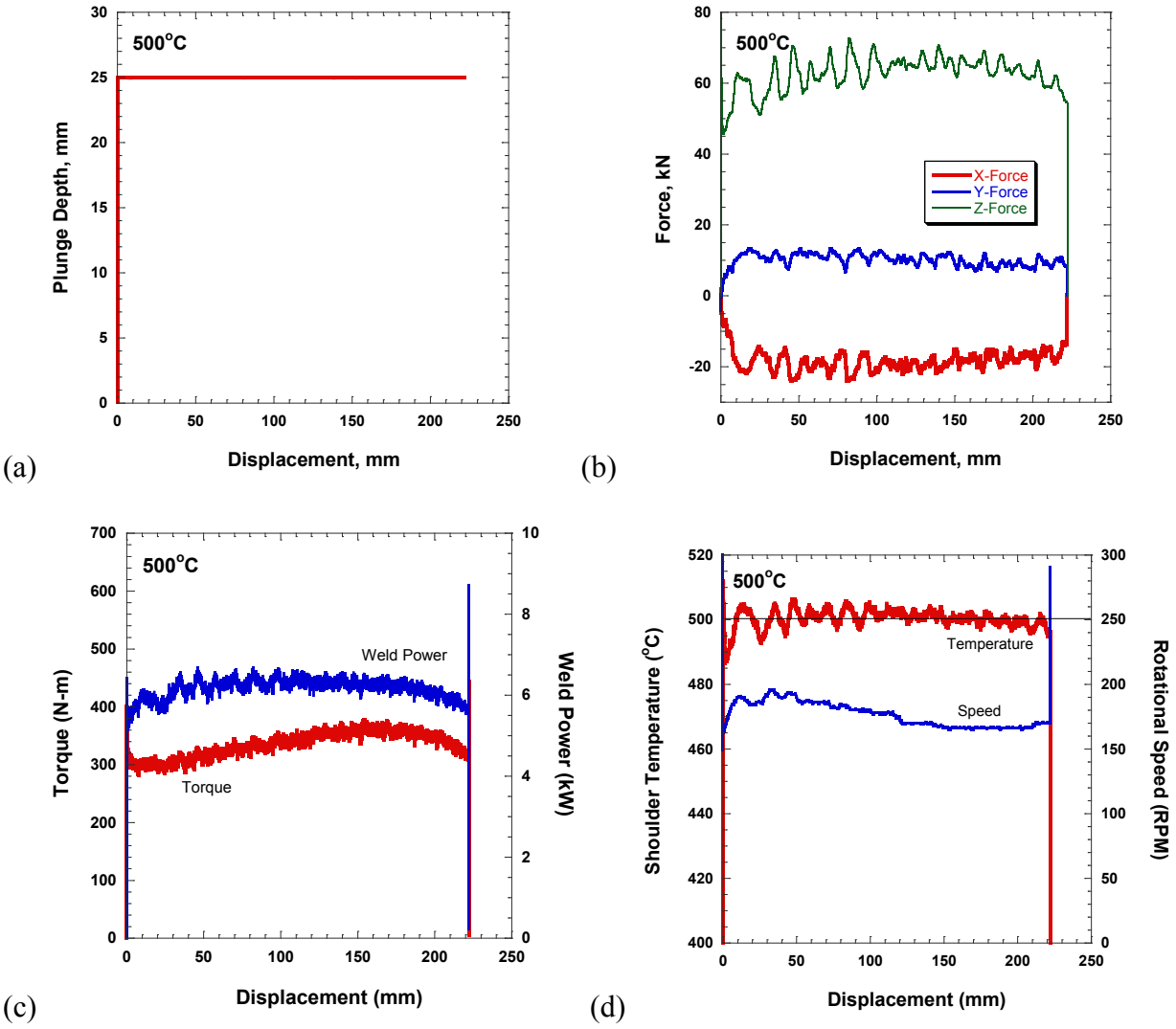

Figure 3.6. (a) Plunge depth versus displacement, (b) force versus displacement, (c) torque versus displacement, and (d) shoulder temperature versus displacement plots for the constant-temperature FSW at 500°C.

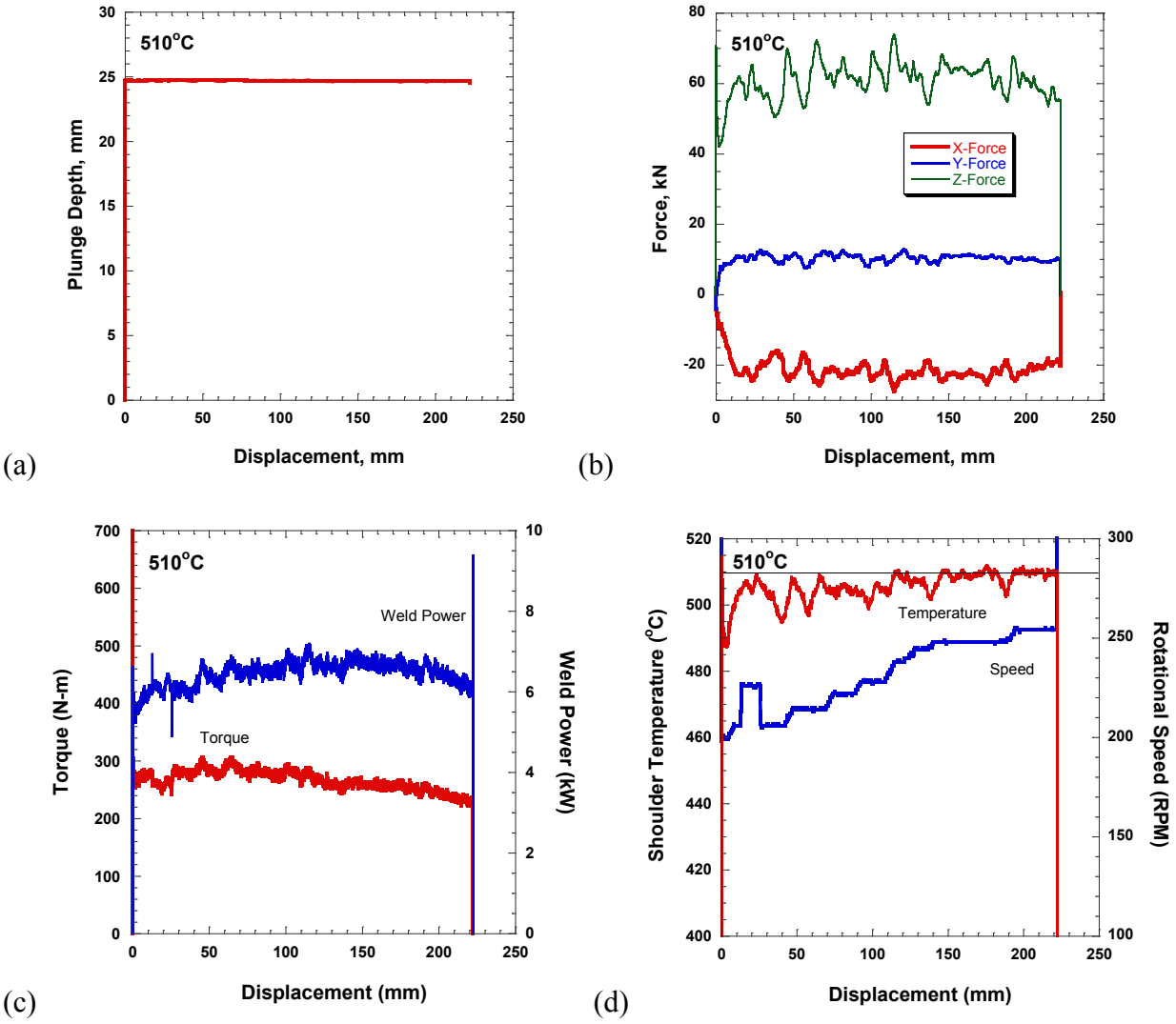

Figure 3.7. (a) Plunge depth versus displacement, (b) force versus displacement, (c) torque versus displacement, and (d) shoulder temperature versus displacement plots for the constant-temperature FSW at 510°C.

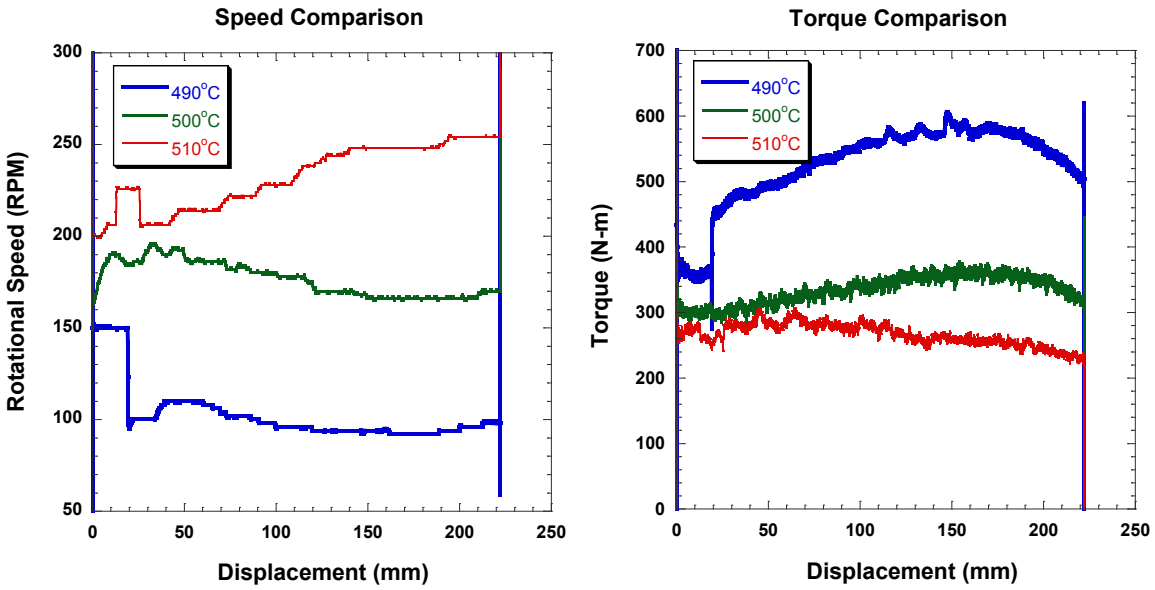

Figure 3.8. Comparison of the rotational speed (left) and torque (right) versus FSW tool displacement used to achieve and maintain the target temperatures at 490°C, 500°C, and 510°C.

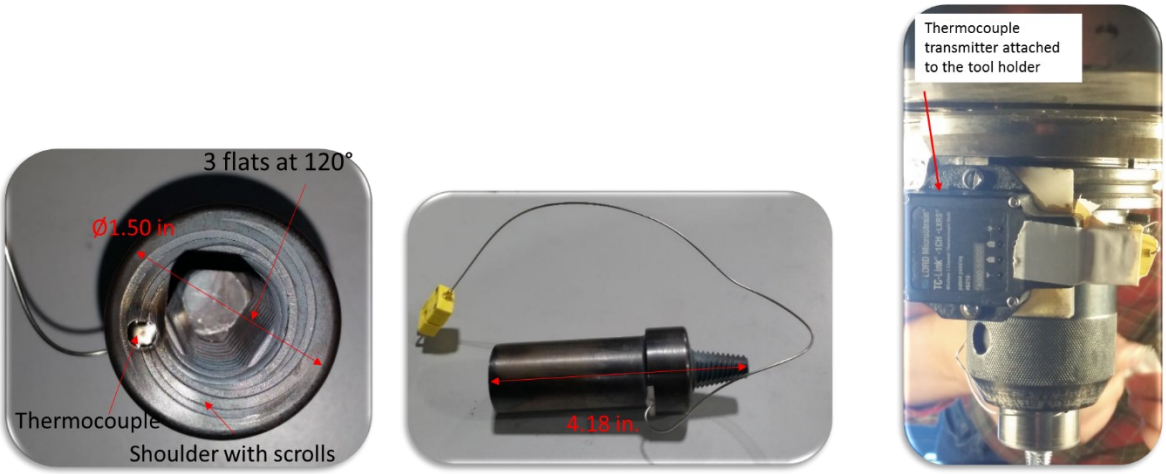

Figure 3.9. Digital images of the FSW tool routed with the thermocouple used for the constant-temperature FSW.

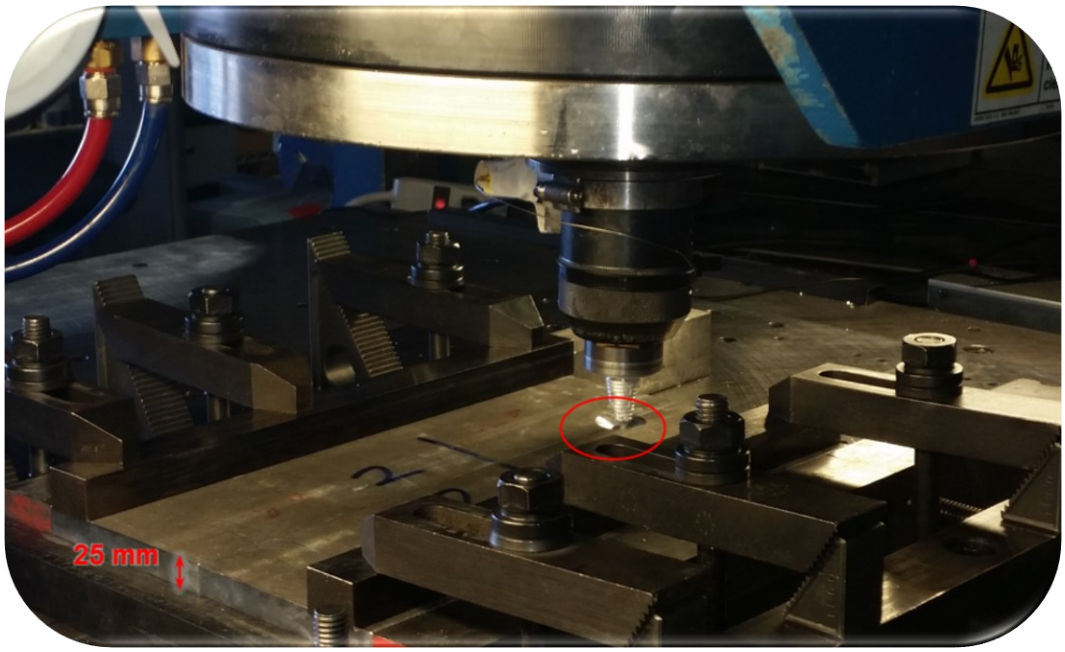

Figure 3.10. Digital image of the FSW tool and plate. Extensive clamping was used to minimize plate separation and shifting. A pre-drilled countersink hole makes the plunge process easier by reducing the forces on the tool and extending tool life.

3.1.3 Metallurgical Preparation

Samples used for experimentation were machined from the unwelded BM in both the RD and TD using wire electrodischarge machining (EDM). Standard metallurgical grinding and polishing procedures were applied to all samples prior to testing and characterization to remove contaminated surface layers. Silicon carbide (SiC) grinding paper (180 grit) was used for initial grinding to remove the EDM layer and prepare a planar surface. Once the EDM layer was removed, the sample was rinsed with water and ethanol or acetone and a finer grit was used. The next grit size was not used until the scratches from the previous grinding paper were removed. Between each grinding step, the sample was rinsed with water and ethanol. The final grinding step was with either 2400 or 4000 grit paper.

Samples were then sequentially polished using 6, 3, and 1 μm diamond pastes in conjunction with an alcohol-based lubricant. Samples were hand polished for approximately 15

minutes or until the sample had a uniform appearance upon visual inspection (i.e. minimal scratches). Between each step, the sample was washed with dish soap and water with a wet cotton swab or wet cotton ball and rinsed with ethanol. As a final step, the samples were then polished with colloidal silica (0.04μm). The samples were cleaned with water and soap, rinsed with ethanol, and dried with a stream of air[6].

3.1.4 Microscopy

Scanning electron microscopy (SEM) was conducted using either a field emission gun TESCAN Mira3 (Czech Republic) or a Hitachi S-3700N, containing a tungsten filament. The beam voltage used for secondary electron (SE) and backscattered electron (BSE) images was 25 keV. Electron dispersive spectroscopy (EDS) images were acquired at 20 kV. Fractography images were acquired using beam voltages ranging from 5 kV to 25 kV. Electron backscatter diffraction (EBSD) orientation maps were acquired using an EDAX (Mahwah, NJ) EBSD detector. EDAX TSL OIM™ software (v6.1) was used to acquire and process the data. EBSD orientation maps were acquired using a beam voltage of 25kV and a working distance of approximately 10 mm. EBSD orientation maps were also acquired for the transverse cross section of the FSW plates and a working distance of approximately 20 mm was used in such cases. An example of a transverse cross section is shown in Figure 3.1 and a schematic is show in Figure 3.13. The step sizes ranged from 0.011 to 10 μm depending on the region (i.e. finer steps sizes were used for the

[6] Through trial and error, one proven method to achieve a surface with minimal dried "ethanol drops" when viewed under the SEM was to have a thin layer of ethanol cover the sample surface before drying. Next, use the stream of air to simultaneously dry the sample and blow off the ethanol layer. The sample can be laid flat on a paper towel or angled to at least 45 degrees. If the sample is touching the table while lying flat or angled, it is best to line the table with a paper towel. This will wick any extra ethanol from the sample.

FSW zones compared with the BM regions). Grain sizes for the FSW region and the BM were determined using the EBSD data. A minimum 5° misorientation angle was used to differentiate between neighboring grains. The ASTM E112 standard for grain size measurement was used [46]. EBSD inverse pole figures (IPF) were also acquired to provide texture information. The precipitate volume percent was measured using the ImageJ software [81] on BSE and SE SEM images.

The samples used for TEM analysis were extracted from the transverse cross section (the welding direction is perpendicular to the page) for both the as-received and FSW analysis. The constant-speed FSW TEM samples were also extracted from the center of the SZ at the top, mid top, middle, mid bottom, and bottom and 10 mm into the RS at the mid top. The samples were mechanically polished to a thickness of approximately 150 μm and mechanically punched to a 3 mm diameter. These samples were then electrochemically polished using a Struer's Tenupol 5 jet polisher to perforation in an electrolyte containing 30% nitric acid and 70% methanol. The electropolishing conditions were -25°C and 12 V. When the time between preparation and analysis was prolonged, samples were ion milled at 4.5 keV at an angle of 3° for 30 minutes. All samples were stored in a vacuum or glove box until use.

Bright field (BF) and dark field (DF) TEM images and selected area diffraction patterns (SADPs) were acquired using either a TOPCON EM-002B, JEOL JEM-2000EXII, or JEOL JEM-2100F TEM. The voltage used was 200kV. SADPs and DF images were acquired to isolate the diffraction reflections and the resulting precipitates. High-resolution TEM photomicrographs (HRTEM) were acquired using a TOPCON EM-002B TEM.

3.1.5 X-ray Diffraction (XRD)

The samples prepared for X-ray diffraction were mechanically polished up to at least 2400 FEPA grit SiC paper. Secondary phases were identified using a Rigaku SmartLab X-Ray

Diffractometer (version 2.1, Tokyo, Japan). Data acquisition and analysis was accomplished using the PDXL2 software and the Inorganic Crystal Structure Database. Data was acquired at 40kV, 44mA, and λ=1.540549 Å under Bragg-Brentano conditions using Cu $K_{\alpha 1}$ radiation for 2θ values between 8-130° at step size of 0.05° at 6 secs/step at room temperature (RT). The incident length limiting slit size was 2mm. Scanning was performed at RT using parallel beam/parallel slit analyzer at 40kV, 44mA, and λ=1.540549 Å. Scanning was conducted at 2θ angles 18-90° with a step size of 0.015° and 12 seconds/step. Samples were stored in a vacuum desiccator until use.

In situ XRD aging experiments were conducted on the BM at temperatures of 409°C and 481°C (annealing) and 516°C (solutionizing). Experiments were conducted in the stage, shown in Figure 3.11, in a vacuum atmosphere to prevent oxidation. Samples were placed on a platinum sample holder. The furnace temperature was measured with a thermocouple inserted into the sample holder. Samples were heated from the as-received T8 temper at a rate of 30°C per minute until the target temperature was achieved. Samples were then heat soaked at various times and then XRD data acquisition was acquired after each soak. The sequence of cumulative heat soak times were 1) 100 minutes, 2) 100 minutes, 3) 100 minutes, 4) 160 minutes, 5) 550 minutes. The acquisition software was programmed to collect data immediately after each heat soak. Each XRD scan lasted 48 minutes and 18 seconds. The *in situ* aging experiment measurement parameters are as follows: no filter, 40kV, 44mA, parallel beam/parallel slit analyzer, using a 20 mm incident slit. Scanning was performed at 2θ angles 19-21°, 34-48°, and 76-84° at a step size of 0.05°, and a scan speed of 6 seconds/step. Data were also acquired after solutionizing using the same parameters and stage in air at RT.

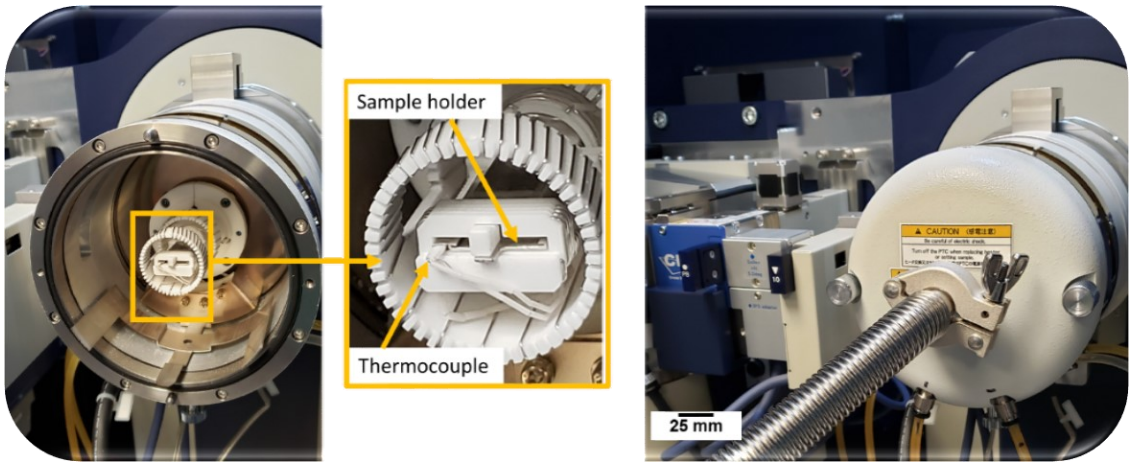

Figure 3.11. Digital images of the Rigaku XRD in situ heating stage. Left: uncovered with the platinum sample holder. Middle: higher magnification image of the heater assembly with the thermocouple inserted into the sample holder. Right: covered with the vacuum tube.

XRD was performed at RT on the constant-temperature friction stir welded samples. Data were acquired at 40kV, 44mA, and λ=1.540549 Å with Bragg-Brentano focusing, using Cu $K_{\alpha 1}$ radiation and a Cu K_{β} filter for 2θ values between 18-120° at a step size of 0.05° at 5 seconds/step. The incident length limiting slit size was 2mm. Data points were acquired from the vertical center of the weld at the top, middle, and bottom at a distance of 30 mm from the center of the weld, as shown in Figure 3.12. Spatial resolution increments were 10 mm. The sample surface was mechanically ground with up to 2400 FEPA grit SiC paper and then polished with diamond paste and colloidal silica. Samples were stored in a vacuum desiccator until use.

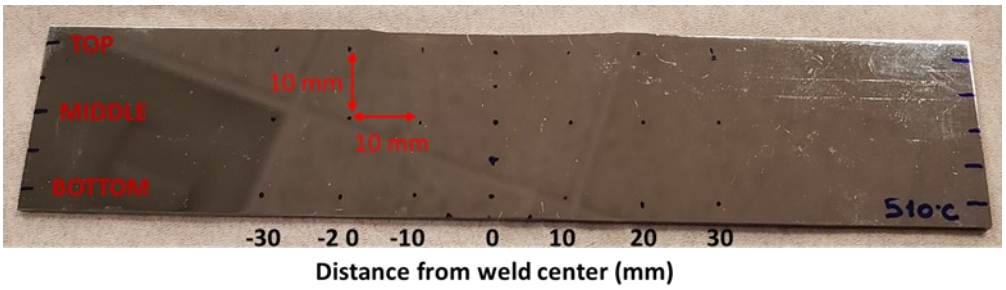

Figure 3.12. Digital image of the FSW sample with fiducial dots, separated by 10 mm, representing where the XRD scans were acquired at the top, middle, and bottom. As the sample was polished to a mirror finish but not etched, the weld cross section is not evident.

3.2 Mechanical Testing

3.2.1 Vickers hardness testing

Vickers hardness was conducted on a Sun-Tech Clark Instruments (Novi, MI) Vickers hardness machine. The indenter load was 0.1 kgf. Equation 3.1 provides the equation used to obtain the Vickers hardness number.

$$HV = \frac{1.8544 * kgf}{d_1 d_2}, \tag{3.1}$$

where kgf is the load in kilograms used and d_1 and d_2 are the indent diagonals, in mm. The indent diagonals ranged from 30 to 45 μm.

Hardness was performed on the transverse cross section, see Figure 3.1, of the FSW in five areas referred to as "top", "mid top", "middle", "mid bottom", and "bottom". The layer referred to as "mid top" was ~5 mm above the "middle" of the transverse cross section and the layer referred to as "top" was 10 mm above the "middle". The same description describes the "mid bottom" and "bottom" layers, located below the "middle" of the transverse cross section. Each indent was spaced 1 mm apart along the transverse cross section and extended from the base metal (BM) on the advancing side (AS) to the BM on the retreating side (RS). A schematic drawing is provided in Figure 3.13.

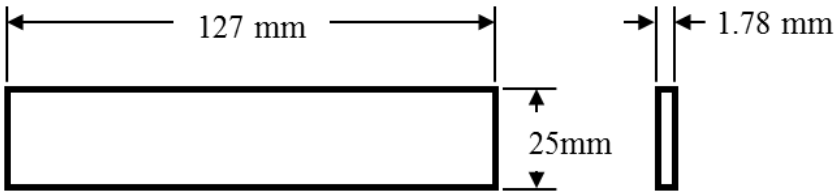

Figure 3.13. Schematic drawing of the transverse cross sectional area (shown in Figure 3.1 right) used for the Vickers hardness and XRD experiments.

Vickers hardness mapping was conducted using a Struers DuraScan 70 (Ballerup,

Denmark) automatic indenter with a force of 0.5 kg and a dwell time of 13 seconds. The data was acquired and processed using Ecos Workflow software. The array area was at least 95.5mm (3.76in) x 20mm (0.82in) with test points taken in 1mm increments, see Figure 3.14. At least 1,995 test points were acquired for each sample. Upon completion of the testing, the image of each indent was observed to ensure that the measurement was accurate. The indents were measured automatically via the software. A box surrounds the indent so that the diagonals touch the sides of the box. From this, d_1 and d_2 are determined. When the indent is not inside the box and the diagonals do not touch the sides of the box, they are considered inaccurate measurements. In these cases, the indent was manually remeasured by moving or resizing the box.

After testing, the sample was etched using Keller's reagent to reveal the transverse cross section of the weld, see Figure 3.15. The AS is on the left side of the weld and the RS is on the right side of the weld for all images depicting the transverse cross section (unless otherwise stated).

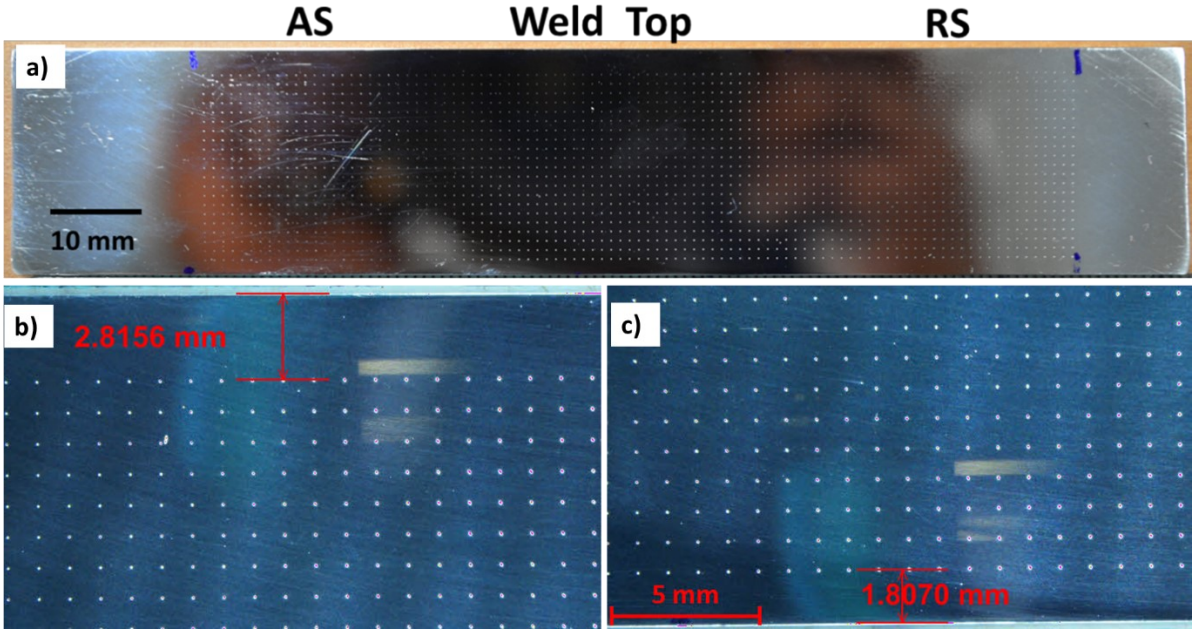

Figure 3.14. a) Digital photograph of the where the Vickers hardness indentation arrays were acquired with respect to the weld. b-c) The distance of the edge of the array to the b) top and c) bottom rows of indents is indicated in the red markings. Neighboring indents were spaced 1 mm apart from each other.

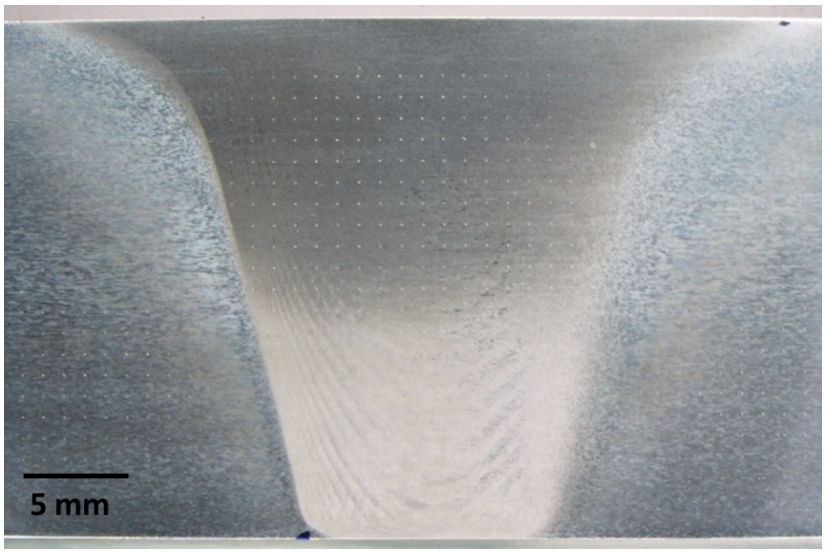

Figure 3.15. Optical micrograph of the etched cross-section of a constant-speed FSW specimen, where the array of hardness indents are evident.

3.2.2 Tensile Testing

For the tensile experiments, large rectangular dogbones were used in accordance with ASTM E8, see Figure 3.16. Samples were EDM sliced through the thickness of the plate. Schematic drawing of these samples is shown in Figure 3.17.

Tensile tests were conducted on the large dogbone samples using an MTS® servo-hydraulic, thermomechanical testing machine with an MTS® Flex Test SE controller (Eden Prairie, MN). An alumina rod extensometer was used to measure the strain. The thickness of the tensile specimens was reduced to 0.75 mm to ensure failure with the 10 kN load cell used with this MTS system. The tensile axis was parallel to the transverse direction (TD), see Figure 3.16. Tests were performed at RT and 300°C at a constant displacement rate of 0.025 mm-s^{-1}, which corresponded to a strain rate of approximately 10^{-3} s^{-1}. The temperature was controlled using a Barber Coleman temperature controller and thermocouples spot welded to the gage section of the samples. Room temperature tensile samples that were 3.2 mm thick were tested in the transverse

and rolling directions on the Instron 5984 tensile machine equipped with a 150 kN load cell and an Instron optical extensometer (Model # 2663-901). Room temperature tensile tests were conducted on the transverse cross section of the FSW joints on the same Instron machine. The dimensions of the dogbone shaped sample are illustrated in Figure 3.18 and Figure 3.19 depicts the sample with respect to the weld. The engineering stress (σ), 0.02% offset YS, elastic modulus (E), and the ultimate tensile strength (UTS) were measured.

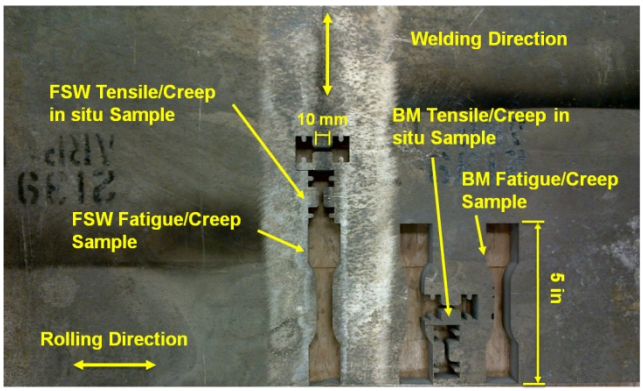

Figure 3.16. A digital image of one of the welded plates indicating where the samples were extracted for the mechanical behavior studies. Note that the central region (of light contrast) represents the welded region and to the right and left of that region represents the base metal regions.

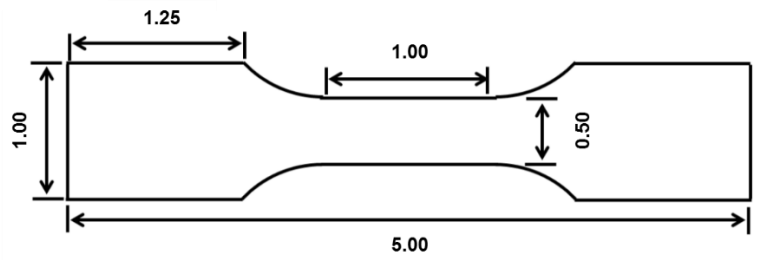

(a)

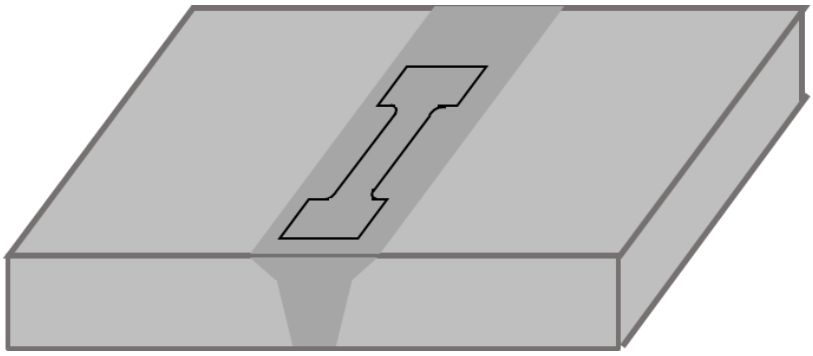

(b)

Figure 3.17. (a) Schematic drawing representing the dogbone-shaped sample geometry used for the constant-speed FSW tensile experiments. The dimensions are in inches. (b) Schematic showing the orientation of the dogbone shaped sample with respect to the weld used for the RT tensile testing of the constant-speed FSW material.

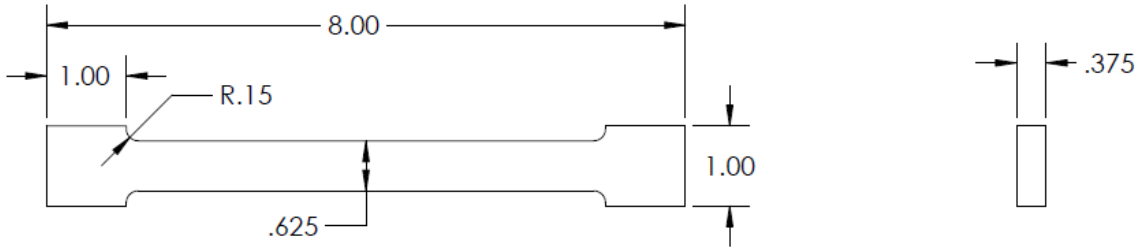

Figure 3.18. Schematic drawing of the dogbone-shaped sample geometry used measuring the RT tensile properties of the constant-temperature FSW materials. Samples were machined so that the transverse cross section was on the largest face of the gage section (see Figure 3.19). The dimensions are in inches.

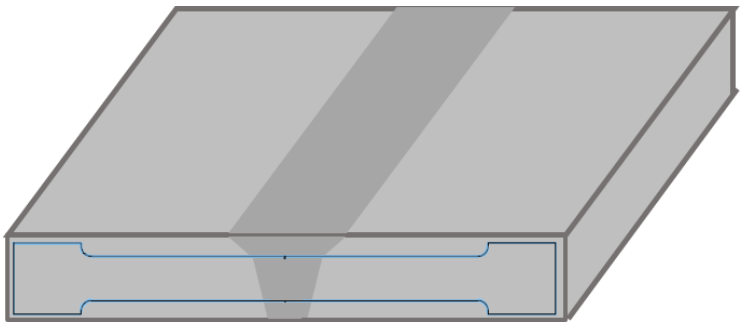

Figure 3.19 Schematic showing the orientation of the dogbone shaped sample with respect to the weld used for the RT tensile testing of the constant-temperature FSW materials.

3.3 Post-Weld Heat Treatment (PWHT)

Four transverse cross-section samples of the position-controlled, constant-speed FSW condition were machined using wire EDM to the dimensions shown in Figure 3.13. The samples were machined and polished to a mirror finish.

PWHTs were carried out at the Institute of Materials Research at Tohoku University in Sendai, Japan in order to determine the effects of post FSW heat treatment on the microstructural evolution and hardness. Aging temperatures and times were determined using the time-temperature-transformation (TTT) curve for an Al alloy with a composition of 4 wt.% Cu and 1.7 wt.% Mg, see Figure 3.20**,** that correlated to a graph of the expected mechanical strengths, see Figure 3.21 [19]. The chosen conditions were 200°C for 10 hrs and 247°C for 0.5, 0.9, and 2 hrs. The conditions chosen are explained according to the schematic plot of property changes during age hardening for an Al-4 wt% Cu-1.7 wt% Mg alloy as demonstrated in Figure 3.21. 200°C/10hrs falls in between curves D-E which sees an increase in the hardness, UTS, and the YS. 247°C/2hrs is approximately on the nose of curve E, which exhibits peak strengths and hardness. 247°C/0.9hr is shifted directly to the right of 247°C/0.5hr and falls between curves D-E, which should exhibit an increase in hardness. 247°C/0.5hr lies directly on the nose of curve D, which among all of the

four conditions chosen exhibits the lowest strengths and hardness. The expectation is that the order of strengths from the highest to the lowest would follow according to: 247°C/2hrs > 247°C/0.9hr ≥ 200°C/10hrs > 247°C/0.5hr. A vacuum tube furnace was utilized for the heat treatments. The furnace was first heated to the desired temperature, then the sample was quickly placed into the tube and evacuated. After the heat treatment, the samples were water quenched and rinsed with ethanol. The samples that were machined in the middle of the weld and parallel to the weld axis were tension tested. Vickers hardness was conducted on the heat treated samples using a Shimadzu HMV Microhardness Tester (Kyoto, Japan) as described in section 3.2.1.

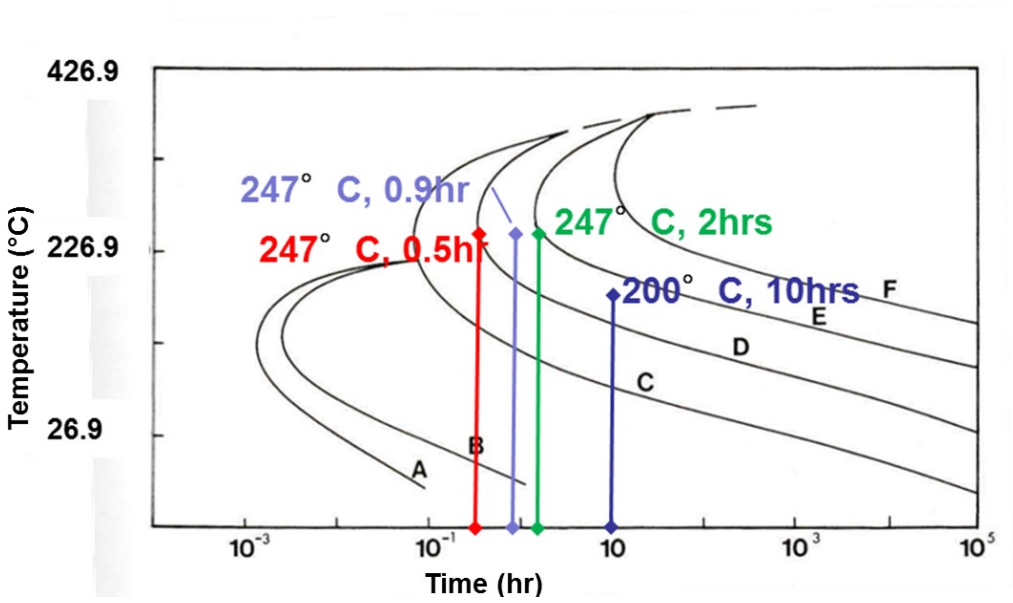

Figure 3.20. Time-Temperature-Transformation (TTT) curve for Al-4Cu-1.7Mg wt.%. The letters A-F correspond to the properties provided in Figure 3.21 [19].

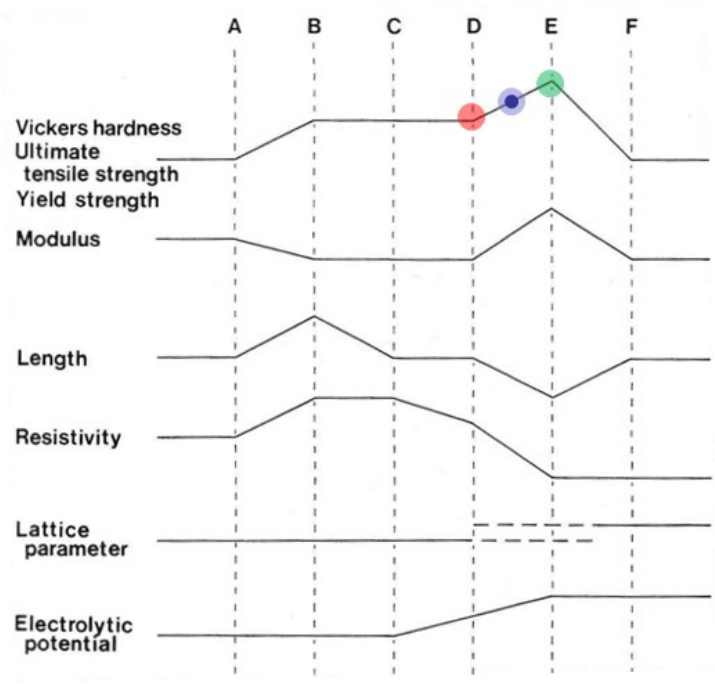

Figure 3.21. The effects of aging on some of the properties of Al-4Cu-1.7Mg wt.%. The letters A-F correspond to the TTT curve provided in Figure 3.20 [19].

CHAPTER 4

RESULTS AND DISCUSSION

The results, analysis, and discussion of the results are provided in this chapter. This chapter compares the effect of FSW on 25 mm thick AA2139-T8 as function of the welding parameters and welding temperature. First, the microstructure and mechanical behavior of the as-received material, which served as the experimental control, are presented, evaluated, and compared to literature, including U.S. Department of Defense technical reports. Next, the microstructure and mechanical behavior for the constant-speed FSW are analyzed and discussed. An evaluation of the results of the PWHT on the constant-speed FSW is included. Then, the effects of constant-temperature FSW on the evolution of the microstructure and the mechanical behavior are evaluated and discussed. Emphasis is placed on the precipitation and grain growth dynamics. Finally, the evolution of the precipitate phases, which were analyzed using the XRD data, is discussed.

4.1 AA2139-T8

The unwelded AA2139-T8 served as the control. Quantitative and qualitative results are presented for the characterization of the microstructure, which involved optical microscopy (OM), SEM, TEM, and XRD, and the mechanical behavior, which involved Vickers hardness and tensile testing. Discussion of the results is also presented in this section as well as a comparison of the data with literature and technical reports.

4.1.1 Microstructure

The as-received AA2139-T8 exhibited large, elongated grains in the transverse plane, see Figure 4.1. The grain morphology and size, which resulted from the solutionizing and cold rolling procedures of the T8 temper process, are consistent with observations in literature [82]. Specifically, the elongated grains were a result of the cold rolling. EDS results demonstrated that

these phases were Cu-rich, see Figure 4.2, Table 4.1, and Table 4.2.

XRD was performed on the as-received base metal to identify the precipitate phases, see Figure 4.3. Thermally metastable precipitates, θ' and Ω, were detected. The equilibrium θ phase was also detected. The equilibrium θ and metastable Ω phases have overlapping peaks which makes it difficult to discern which phase (or phases) is responsible for such peaks. A 2θ peak at 34.64° appears in the Bragg-Brentano focusing but not in the parallel beam/parallel slit analyzer result. Calculations indicate that this peak is the Cu K_β of the face-centered cubic (FCC) Al matrix.

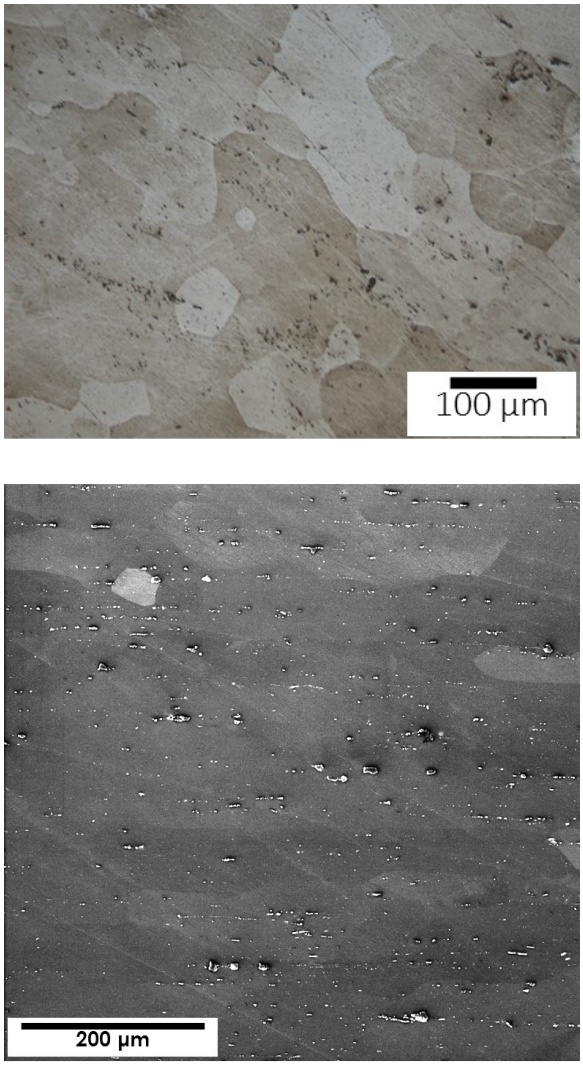

Figure 4.1. (a) OM photomicrograph of the plan view and (b) SE SEM photomicrograph of the transverse section of the as-received AA2139-T8 microstructure.

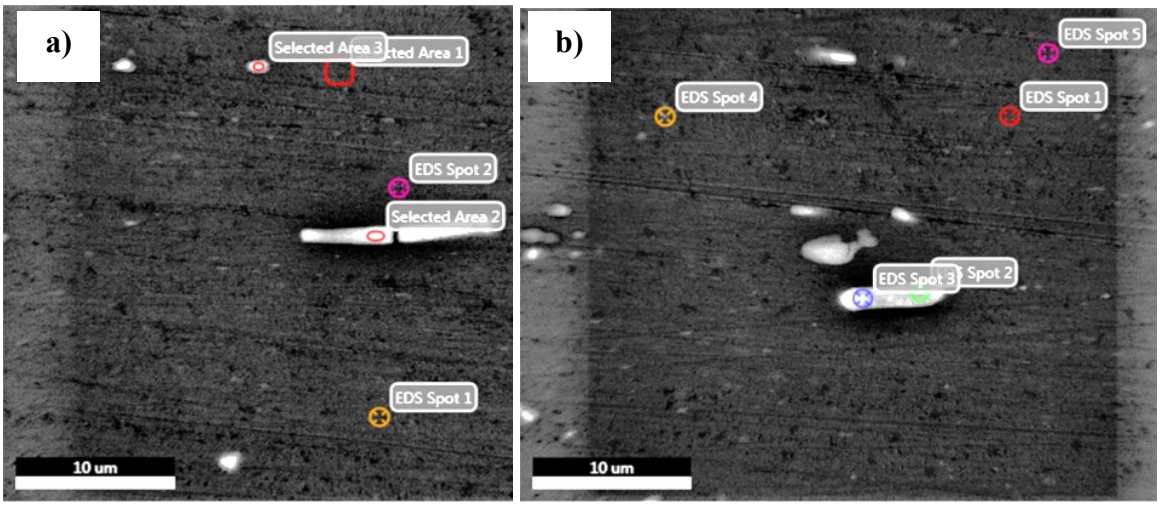

Figure 4.2. SE SEM photomicrographs of the as-received AA2139-T8 microstructure. The marked spots represent where EDS measurements were taken. a) Such EDS measurements are listed in Table 4.1, b) Such EDS measurements are listed in Table 4.2.

Table 4.1. Elemental wt.% based on the EDS measurements of selected areas in Figure 4.2a.

Element	Selected Area 1	Selected Area 2	Selected Area 3	EDS Spot 1	EDS Spot 2
O K	0.3	0.3	0.2	0	0
MgK	0.8	0.9	1	1	0.9
AlK	91.5	77.4	85.7	93.1	93.2
SiK	0	0.4	0.4	0.3	0.2
AgL	0.7	0.2	0.4	0.6	0.5
MnK	0.5	1.5	1.1	0.3	0.3
FeK	0.2	3.0	1.7	0.1	0.2
CuK	2.9	16	9.3	4.5	4.7

Table 4.2. Elemental wt.% based on the EDS measurements of selected areas in Figure 4.2b.

Element	EDS Spot 1	EDS Spot 2	EDS Spot 3	EDS Spot 4	EDS Spot 5
O K	0.1	0.4	0.5	0.2	0
MgK	1	0.9	0.8	0.9	1
AlK	93.1	63.3	65.7	91.9	93
SiK	0.4	0.2	0.2	0.4	0.4
AgL	0.7	0.2	0.1	0.7	0.7
MnK	0.2	2.4	2.2	1.1	0.3
FeK	0.1	4.7	4.6	0.1	0.1
CuK	4.4	27.4	25.6	4.8	4.4

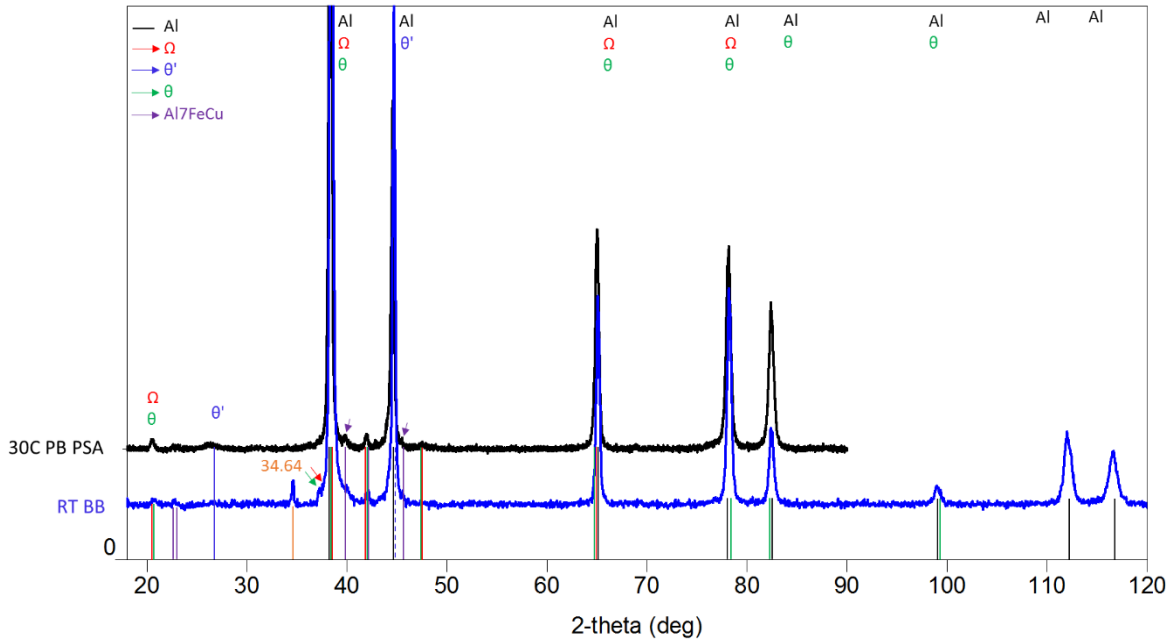

Figure 4.3. X-ray diffraction intensity versus 2-theta plot for the as-received AA2139-T8. The orange peakbar with a 2θ angle of 34.64 degrees indicates a Cu K_β peak.

TEM bright field (BF) photomicrographs and indexed selected area diffraction patterns (SADPs) of AA2139-T8 are provided in Figure 4.4. Additional TEM dark field (DF) photomicrographs highlighting the θ' and Ω phases are in APPENDIX A. The superlattice reflections in the SADPs confirm the presence of the precipitates captured in the BF photomicrographs. Studies on the Al-Cu-Mg and Al-Cu-Mg-Ag alloy systems have determined that the primary precipitates are the θ' (Al_2Cu, tetragonal, a=4.0495Å, c=5.80Å, space group: I-4m2), θ (Al_2Cu, body-centered tetragonal, a=4.0495 Å, c=5.80Å, space group: I4/mcm), Ω (Al_2Cu, orthorhombic, a=4.96, b=8.59 Å, c=8.48Å, space group: Fmmm) [36], and S-type phases (Al_2CuMg, orthorhombic, a=4.96Å, b=8.59Å, c=8.48Å, space group: Fmmm) [27,28,31,36–39]. To confirm the presence of these precipitates, CrystalMaker® software was used to simulate the θ' and Ω precipitate phases. The simulated SADPs in the three zone axes are referenced in APPENDIX B. The S-type phases were not simulated due to the low Cu:Mg ratio; a Cu:Mg weight ratio of 2:2 (or an atomic ratio of approximately 1) is necessary to nucleate the precursors for the

S-type precipitation [32]. Three variants of the $<100>_{\theta'}$ diffraction patterns were then overlaid on the simulated [001] α-matrix (FCC Al) zone axis. The simulated θ' diffraction spots between the (020) and (220), (220) and (200), (200) and (000), and (000) and (020) match with those observed experimentally in Figure 4.4a and the combined experimental and simulated diffraction spots in the $[001]_{\alpha}$ zone axis are shown in Figure 4.5a. Three variants of the $<110>_{\theta'}$ diffraction pattern were overlaid on the simulated $[110]_{\alpha}$ zone axis, shown in Figure 4.5b. The simulated θ' diffraction spots are consistent with those observed in the experimental diffraction pattern in Figure 4.4d and are combined in Figure 4.5b. Three variants of the $<111>_{\theta'}$ diffraction pattern were overlaid on the $<111>_{\alpha}$ zone axis simulation. The combined simulated $<111>_{\theta'}$ and $<111>_{\alpha}$ diffraction patterns are consistent with those observed experimentally, see Figure 4.4e, and are combined in Figure 4.5c. Diffraction pattern simulations were also performed for the Ω phase and are referenced in APPENDIX B. All the experimentally-observed spots were confirmed through simulation and the literature [32,36,37]. Precipitate diffraction spots are labeled and indexed accordingly in the experimental SADPs, Figure 4.5. A good method to differentiate between the θ' and Ω diffraction spots in the $<001>_{\alpha}$ zone axis is to remember the θ' diffraction spots are located in a lower case "t" shape or cross ("t" for θ) and the Ω spots are located in the outer corners like the letter "O" ("O" for Ω). Dark field TEM photomicrographs in APPENDIX A (with the corresponding SADPs) reveal the morphology of the θ' and Ω precipitates. The precipitate volume percent in the <100> zone axis (Figure 4.4a) is 11.9%. Experimental and simulated SADPs confirmed that no S-type precipitates were present in the as-received BM.

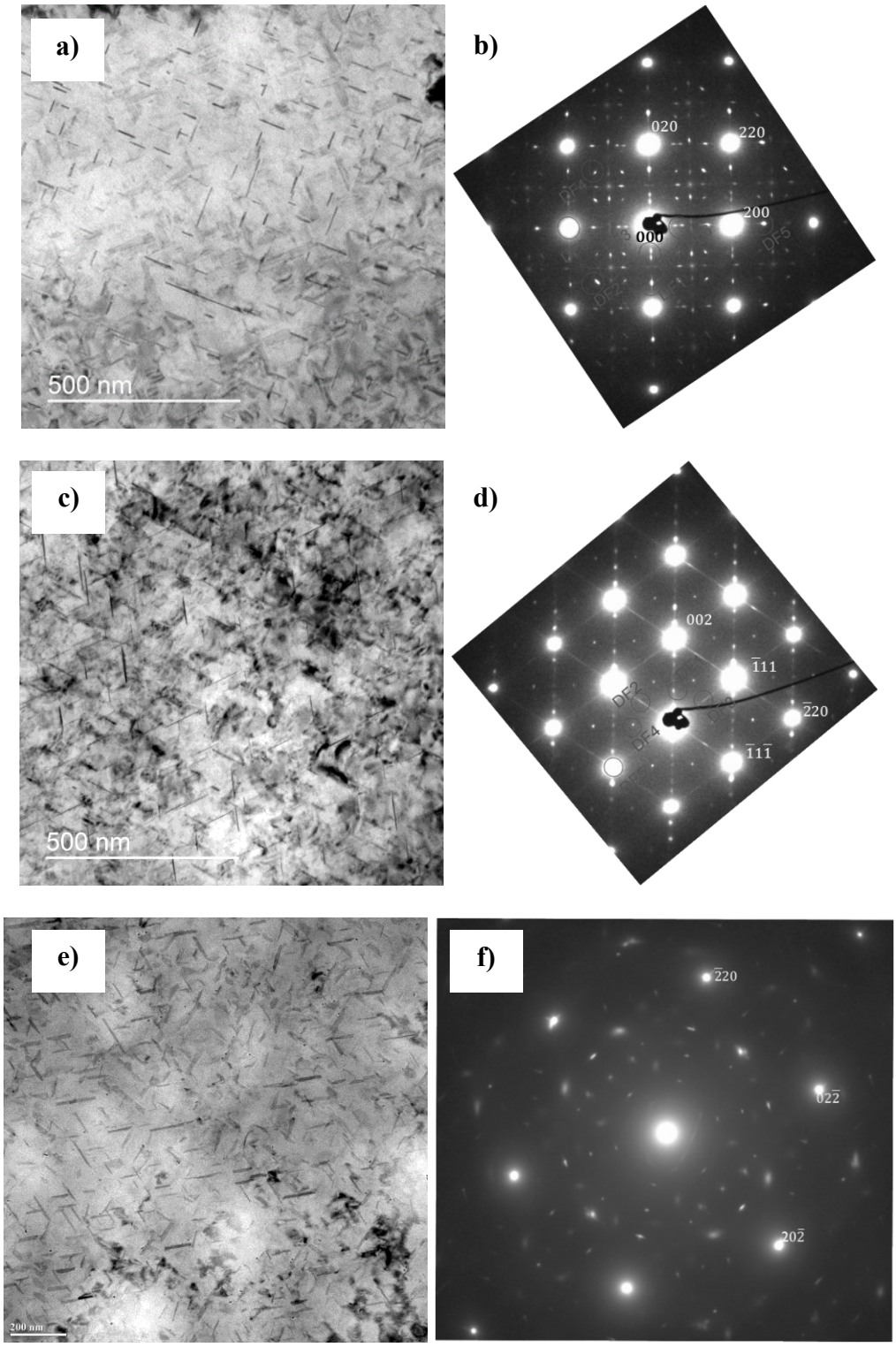

Figure 4.4. Bright field TEM photomicrographs along with the corresponding SADPs for the as received AA2139-T8 alloy; a) and b) <100>, c) and d) <110>, and e) and f) <111> zone axes. Aluminum matrix diffraction spots are indexed. Precipitate phases are indicated by streaks (d) and smaller diffraction spots (b, d, e). The scale bar in e) is 200 nm.

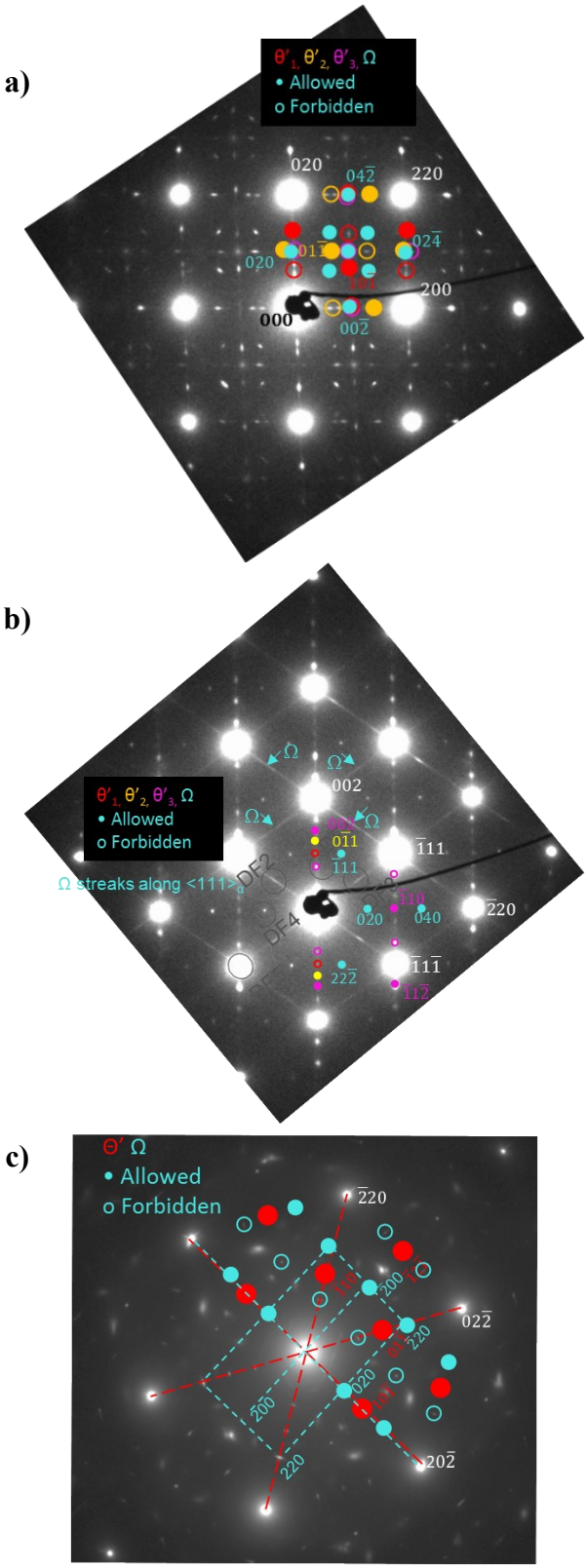

Figure 4.5. Indexed precipitate diffraction spots on the FCC Al-matrix SADPs in the a) <100>, b) <110>, and c) <111> zone axes.

XRD *in situ* heat treatments were performed at 409°C, 481°C, and 516°C, see Figure 4.6b-d. These temperatures are similar to typical annealing and solutionizing temperatures used for this alloy. The peaks for the different heat treatment times are portrayed in Figure 4.6b-d and are shown next to the as-received base metal, see Figure 4.6a, for comparison. A summary of the precipitate phases present during the *in situ* heat treatments is provided in Table 4.3. No precipitates were detected during the solutionizing heat treatment at 516°C and θ' was not detected at any of the temperatures and treatment times. This indicates that all the precipitates were dissolved during the 516°C heat treatment. Heat treatments at 409°C and 481°C show increased θ and Ω peak intensities with increased heat-treatment times. Although θ and Ω have overlapping peaks, the increase in θ/Ω peak intensities is likely due to the coarsening and increased volume percent of the θ phase. Equilibrium θ coarsening would occur via Ostwald ripening at the expense of the θ' and Ω phases. The Al matrix phase and the θ precipitate phase have overlapping peaks at high angles; however, it is uncertain from the diffraction plots if the absence of the shared peaks or varied intensities is primarily due to precipitate phase transformations, or a transition in the Al matrix texture. XRD was performed on these same heat treated samples after natural aging at RT and the observed precipitate phases are listed in Table 4.4.

The Ω phase is unique to the Al-Cu-Mg-Ag alloy system and is not always present in the precursor alloy system Al-Cu-Mg. In the Al-Cu-Mg alloys, θ' is usually accompanied with the S-type precipitates. The S-type precipitates appear in Al-Cu-Mg alloys when the Cu:Mg weight ratio is approximately 2.2 [32] (approximately 1.5-4) [31–34] with precipitation temperatures of 180°C aged for 2.5 hours [28], 250°C aged for 300 hours, and 300°C [31]. Precipitation of the S-type was found at lower temperatures with aging times ranging from 6 hours to 72 hours [31,83]. The studied alloy had a Cu:Mg weight ratio of approximately 12, which was too enriched with Cu to

support the S-type formation. This also supports the simulated and experimental TEM observation and analysis of the precipitate phase, Ω. In addition, it was detected in the room temperature (RT) XRD experiments which is consistent with the widely accepted Ω precipitation kinetics:

SSS → Guinier-Preston Zone I → Guinier-Preston Zone II (θ") → θ' + Ω → θ

The Ω→θ transformation kinetics is slower than the θ'→θ transformation [27,37]. The Ω precipitate was present during *in situ* heat treatments at all aging times. This demonstrates the stability of Ω at elevated temperatures. As expected, no precipitates were identified at 516°C, which is considered a solutionizing temperature. The θ' and Ω precipitates returned after cooling from the 516°C *in situ* heat treatment.

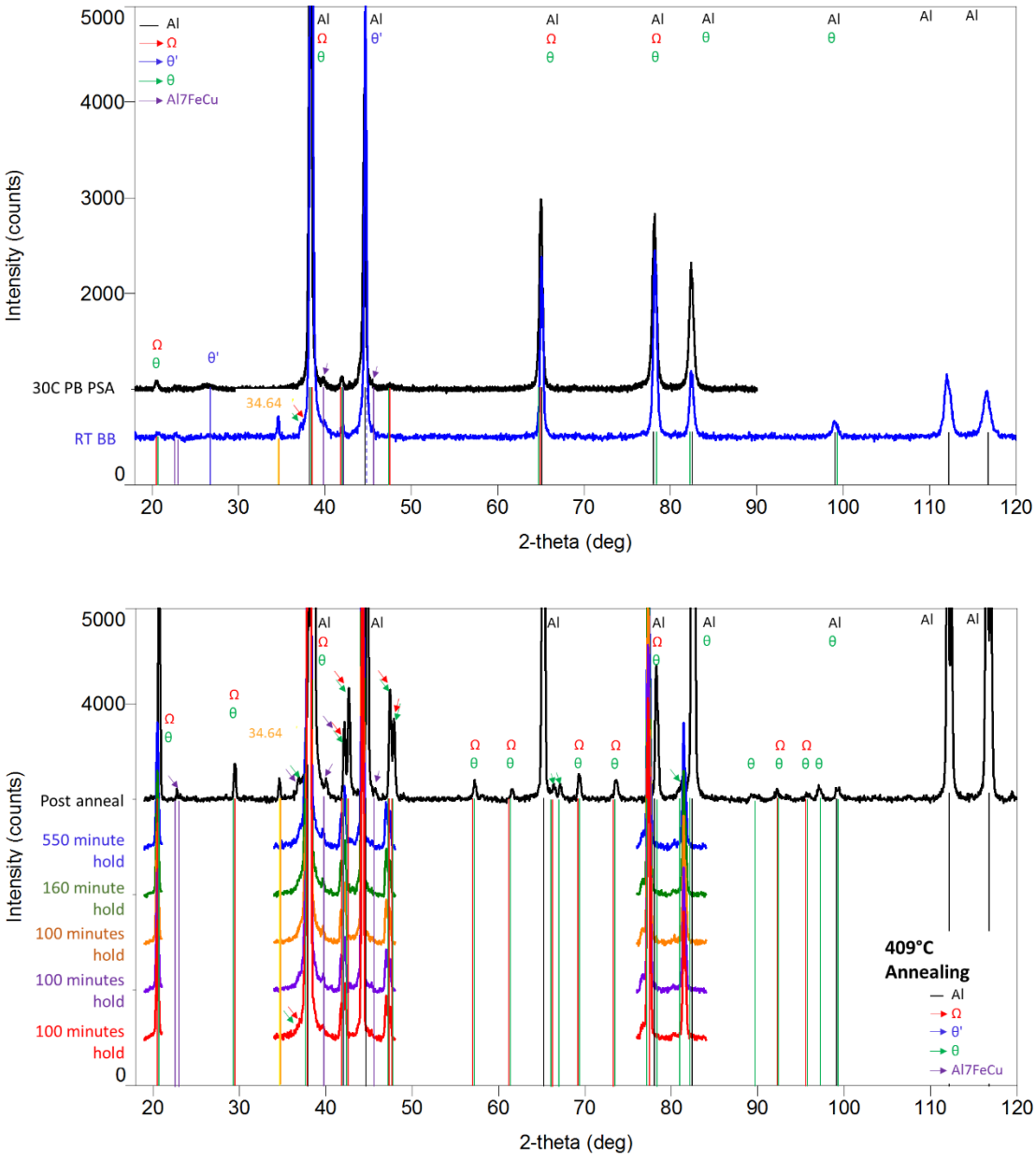

Figure 4.6. XRD intensity versus 2-theta data of 2139-T8 a) as-received, b) *in situ* and post annealed at 409°C, c) *in situ* and post annealed at 481°C, and d) *in situ* and post solutionized at 516°C. Cu Ka radiation. Parallel beam/parallel slit analyzer (PB/PSA) was used for all of the annealed and solutionized experiments. The orange peakbar indicates Cu Kβ radiation. The XRD scan times took approximately 48 minutes.

Figure 4.6 (continued)

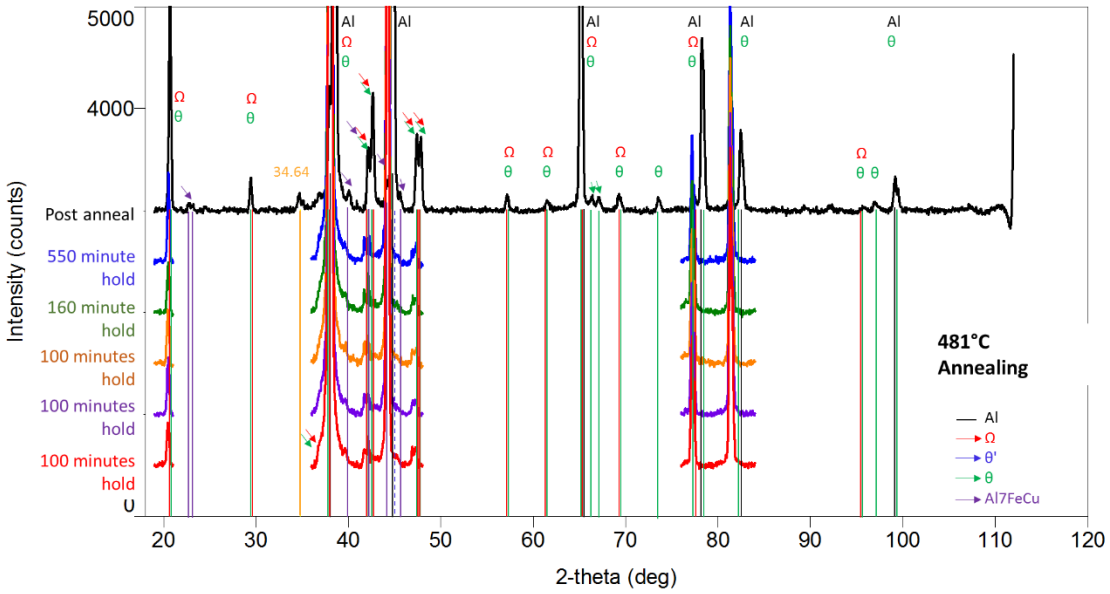

c)

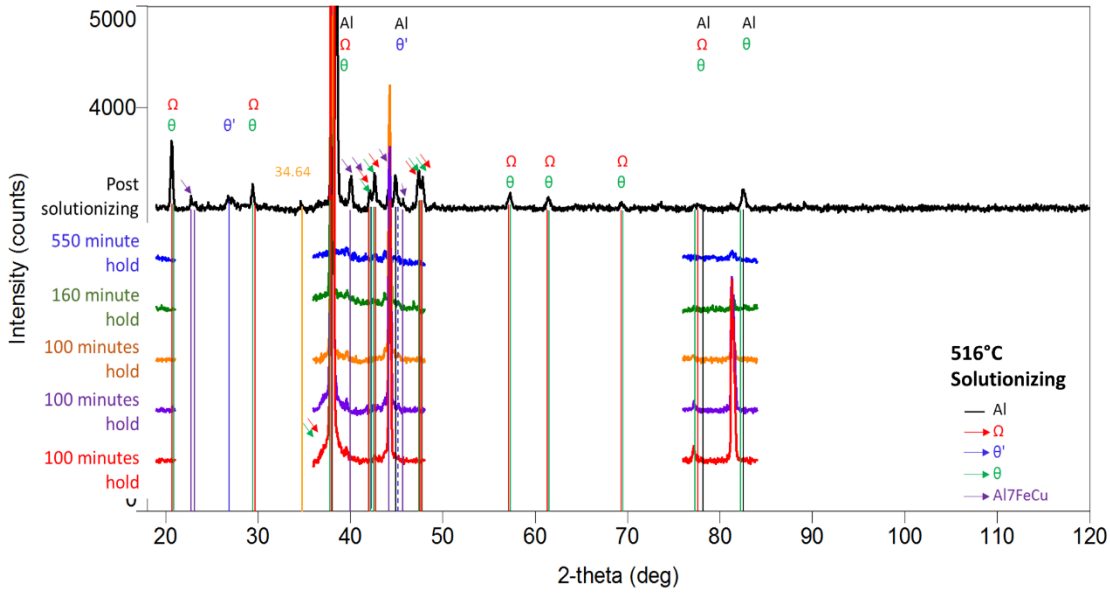

d)

Table 4.3. Summary of precipitate phases present during the XRD *in situ* heat treatments shown in Figure 4.6.

	Hold Time (mins)	409°C	481°C	516°C
1.	100	θ/Ω	θ/Ω	θ/Ω
2.	100	θ/Ω	θ/Ω	θ/Ω
3.	100	θ/Ω	θ/Ω	None
4.	160	θ/Ω	θ/Ω	None
5.	550	θ/Ω	θ/Ω	None

Table 4.4. List of precipitates identified through XRD analysis of AA2139-T8, which was naturally aged after heat treating at 409°C, 481°C, and 516°C.

Heat Treatment (°C)	Natural Aging Time (min)	Phases Present
409	8640	θ, Ω
481	300	θ, Ω
516	1509	θ', θ, Ω

4.1.2 Hardness Behavior

Vickers hardness testing was performed on the transverse plane at the middle of the as-received AA2139-T8 plate and at 5 mm above (mid top) and below (mid bottom) the middle of the plate. The Vickers hardness values of AA2139-T8 ranged between 182 to 200 at the mid top, 172 to 192 at the middle, and 177 to 199 at the mid bottom.

4.1.3 Tensile Behavior

Tensile tests were conducted in both the rolling and transverse directions for the AA2139-T8 and the YS, UTS, and ε_f are provided in Table 4.5. The RD exhibited a slightly higher YS and ε_f, although, the TD exhibited a higher UTS values. The tensile properties also varied through the thickness of the plate. In the TD and the RD, the YS decreased towards the middle of the plate.

Table 4.5. Measured average tensile properties of the base metal through the plate thickness. The standard deviation is provided in parentheses[7].

	YS (MPa)	UTS (MPa)	ε_f	E (GPa)
Rolling Direction	452.0 (19.5)	490.5 (6.4)	8.6% (3.4)	62.2 (10.2)
Transverse Direction	441.3 (20.5)	501.2 (15.5)	7.4% (1.2)	64.3 (3.4)

The hardness values and tensile YS of the as-received AA2139-T8 varied throughout the thickness of the plate. This is due to the nonuniform deformation of the cold rolling process [84]. The difference in tensile properties in the RD and TD demonstrates some mechanical anisotropy, which is expected in a cold rolled alloy [85]. Tensile testing on 25 mm thick AA2139-T8 was performed on smooth, cylindrical samples in the transverse direction at the Southwest Research Institute (SwRI) [82]. The average YS was 472 MPa and the elastic modulus was 74 GPa.

4.2 Effects of Constant-Speed Friction Stir Welding

Quantitative and qualitative results are presented with respect to the characterization of the microstructure and mechanical behavior for the constant-speed FSW process. Optical microscopy, SEM, and TEM were used to characterize the microstructure. Vickers hardness and tensile experiments were employed to characterize the mechanical behavior. Qualitative and quantitative data concerning the weld zones, the through thickness variation in the microstructure, and the precipitate phases are presented. The through-depth thickness regions of the weld are referred to as top (also termed the "weld crown"), mid top, middle, mid bottom, and bottom (also termed the

[7] Six samples were tested in the rolling direction and five samples were tested in the transverse direction.

"weld root").

The evolution of the microstructure and the mechanical behavior, which includes the tension testing and Vickers microhardness results, through the thickness of the weld are discussed. The results of the PWHTs and its effect on the microstructure and mechanical behavior are also discussed.

4.2.1 Microstructure

The microstructure of the weld, see Figures 4.7 and 4.8, differed from that of the as-received AA2139-T8 (also referred to as the unwelded BM). The FSW process created a basin-shaped weld profile, which is shown in the macroetched, transverse cross section of the weld, see Figures 4.7 and 4.8a. This shape is dependent on the tool shape and other features (e.g. threads, scrolls, flats, flutes, etc.) [11,63]. The SZ is the basin-shaped region of the weld. The AS of the weld is distinguishable by a sharp border that outlines the SZ. On the RS, this border is more diffuse and the contrast between the SZ and the adjacent TMAZ is obscure. These descriptions hold true for all of the welding conditions presented in this work. For all the transverse cross-sectional images, the AS is on the left side of the figure and the tool rotation and traversing was into the page. For the constant-speed FSW, the SZ has a marked distinction between the upper and lower halves. These regions are defined as the UWN and LWN and each have different microstructures and mechanical properties, which will be shown in section 4.2.3. In addition, there are striations within the SZ; these patterns are onion rings and are due to the tool rotation and traversing [11,63].

Figure 4.7. Optical macrograph of the etched constant-speed FSW in the transverse cross section. The advancing side (AS) is on the left side and the retreating side (RS) is on the right side.

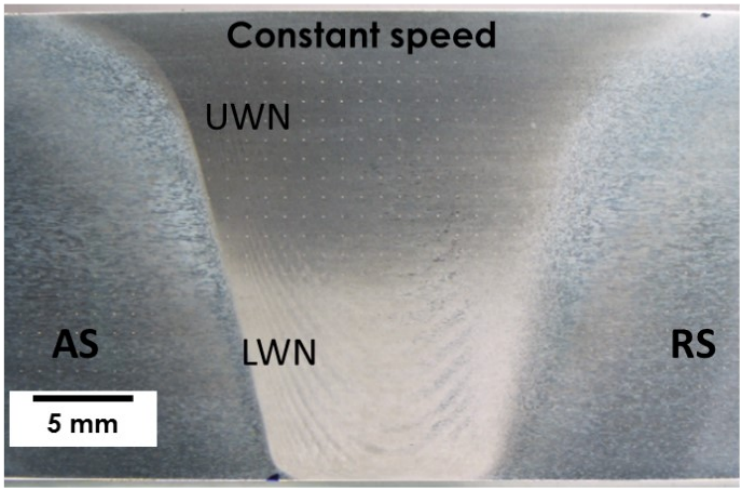

Figure 4.8. Optical macrograph of the etched constant-speed FSW in the transverse cross section. Small dots are indents from the Vickers hardness test which are 1 mm apart. The advancing side (AS) is on the left side and the retreating side (RS) is on the right side.

The microstructure of the HAZ, TMAZ, and SZ was further characterized using EBSD, see Figure 4.9. Only affected thermally, the HAZ is defined as an overaged parent material, bearing physical resemblance to the parent material but exhibiting lower mechanical strength [11,63,86]. The TMAZ region encases the rotated elongated recrystallized grains, which is the second hottest weld zone and has the lowest mechanical strength [11,63,86]. Grain rotation is due to the tool rotation and travel. The magnitude of the grain refinement in the equiaxed SZ is evident in Figure 4.9. The equiaxed microstructure is more clearly seen in the higher-magnification photomicrographs presented in Figure 4.11. The SZ comes into direct contact with the tool and

thus, is the hottest weld zone and yields a dynamically recrystallized microstructure.

In addition to the varying microstructures delineating the weld zones, the microstructure in the SZ varied throughout the depth of the weld. Five areas were characterized through the depth of the SZ as indicated in Figure 4.10. SE SEM photomicrographs of the SZ indicate a gradient in both the grain size and the precipitate size and distribution through the thickness of the SZ at the top, mid top, middle, mid bottom, and bottom, see Figure 4.11. The grain size gradient is evident in the EBSD images in Figure 4.12. The average grain sizes and precipitate volume percents are listed Table 4.6 and Table 4.7. The average grain size decreased and the precipitate volume percent increased from the top of the weld to the bottom for the constant-speed FSW, with the exception of the middle, where there was a slight decrease (~0.4%) in the precipitate volume percent. The spatial distribution and morphology of the precipitates also differed between the top of the weld and the bottom due to thermal defects, which will be discussed in more detail later. At the top, the precipitates at the grain boundaries were either thin and continuous or spherical. Towards the bottom of the weld, the precipitates were discrete, had more distinct shapes, and were distributed at the grain boundaries and as well as within the interior of the grains.

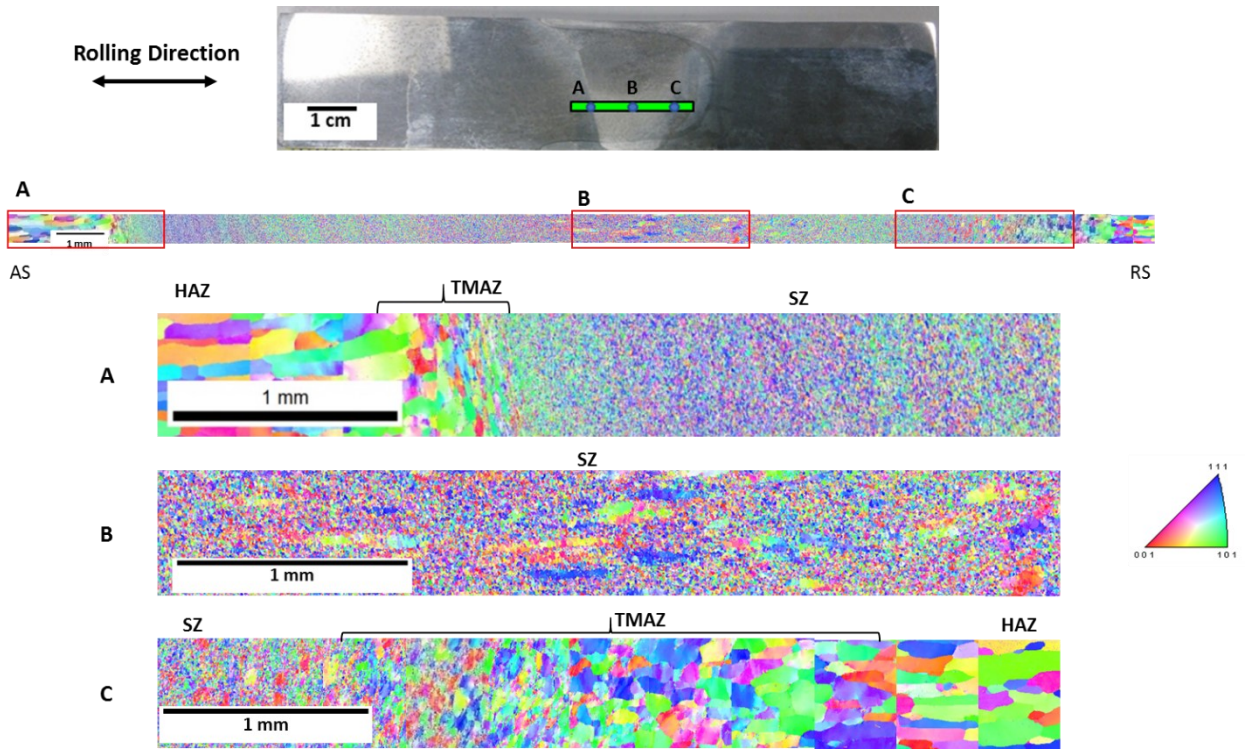

Figure 4.9. EBSD orientation maps of the cross section of the constant-speed FSW 9 mm from the bottom edge of the sample. The green box indicates where the EBSD was acquired. The top row is a continuous montage of many individual scans, some of which are provided in higher magnification below in A) to C). A) The AS of the weld is shown. High magnification maps are shown of the HAZ, TMAZ, and SZ. B) The center of the SZ is shown. C) The RS of the weld is shown with high magnification maps of the SZ, TMAZ, and HAZ. The IPF color coded FCC unit triangle is based upon the sample normal direction. The advancing side (AS) is on the left side while the retreating side (RS) is on the right side.

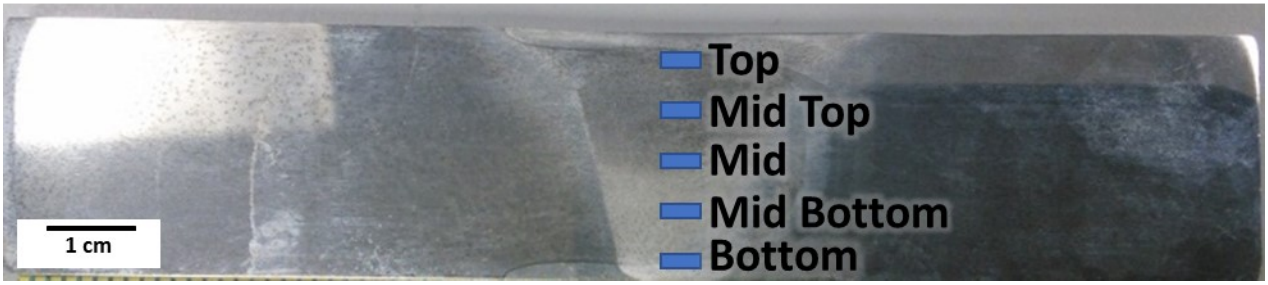

Figure 4.10. Transverse cross section of the FSW with blue boxes indicating the positions of the top, middle top, middle, middle bottom, and bottom. The advancing side (AS) is on the left side while the retreating side (RS) is on the right side.

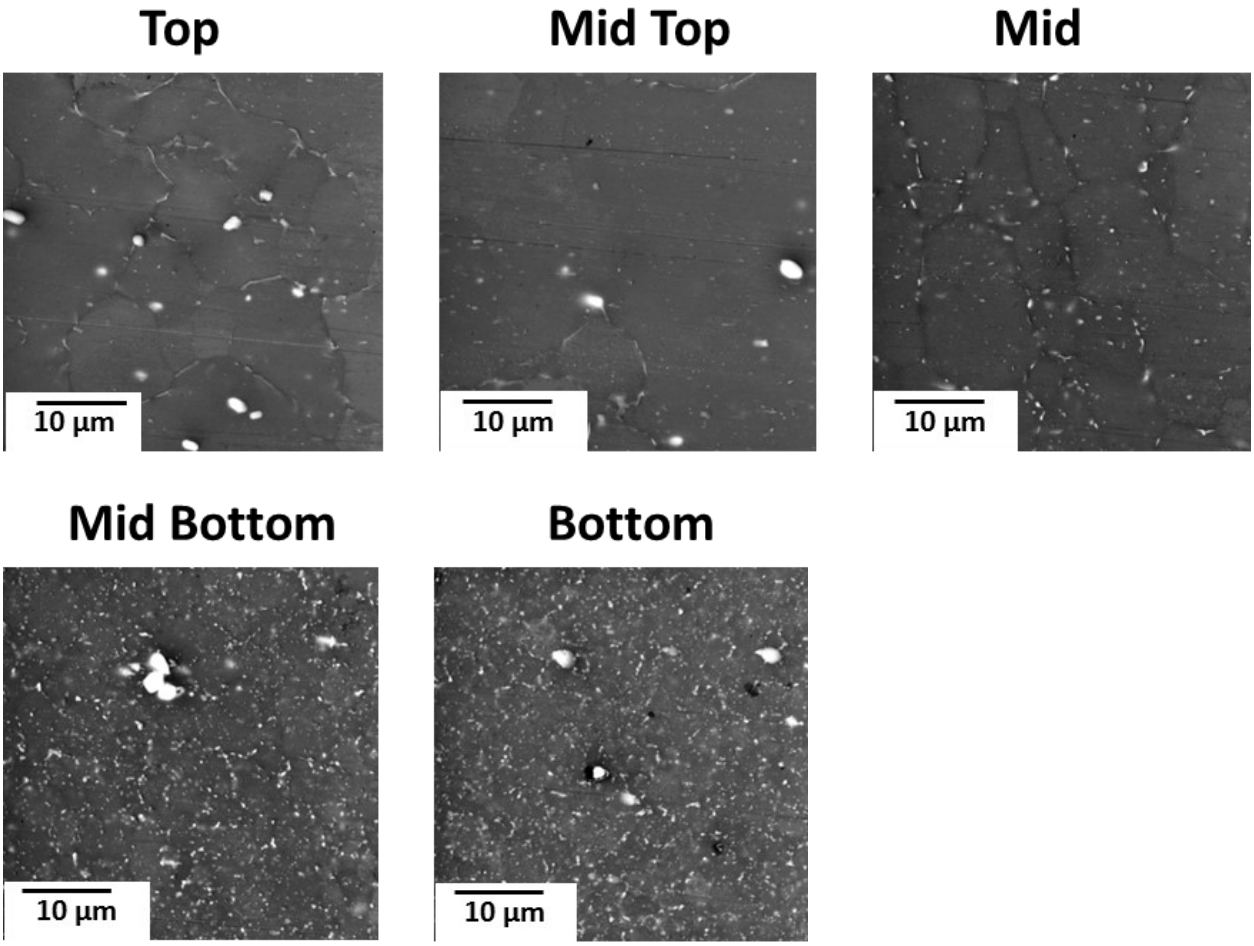

Figure 4.11. SE SEM photomicrographs of the microstructure through the depth of the stir zone for the constant-speed FSW. The welding direction is perpendicular to the page.

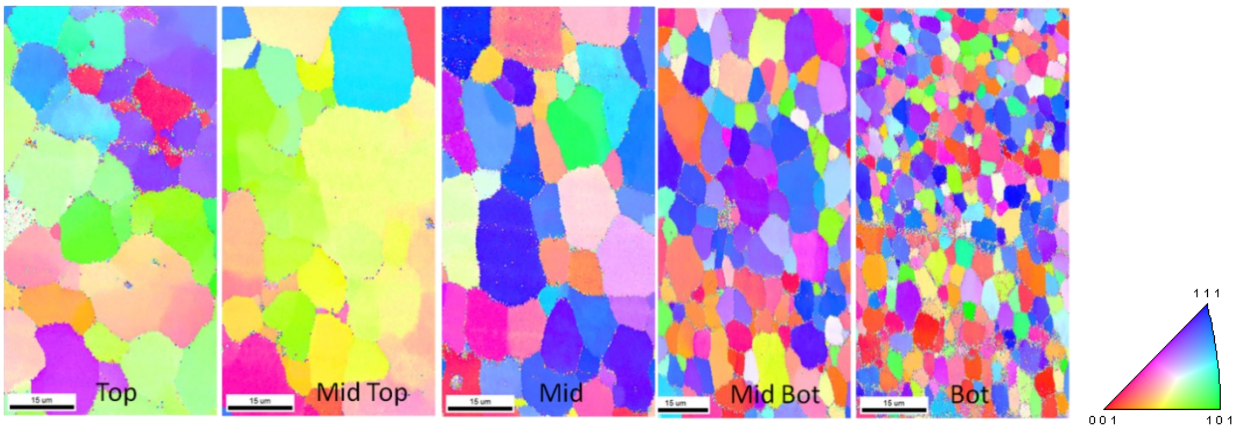

Figure 4.12. EBSD orientation maps showing the variation in grain size through the depth of the constant-speed FSW stir zone at the top, mid top, middle, mid bottom, and bottom. The scale bar is 15μm. The welding direction is parallel to the page.

Table 4.6. Average grain size through the depth of the constant-speed FSW.

Stir zone average grain size, μm				
Top	**Mid Top**	**Middle**	**Mid Bottom**	**Bottom**
30.0	24.0	15.0	11.0	6.0

Table 4.7. Precipitate volume percent through the depth of the constant-speed FSW.

Stir zone area precipitate volume percent, %				
Top	**Mid Top**	**Middle**	**Mid Bottom**	**Bottom**
2.70	2.60	2.20	9.10	11.00

The constant-speed FSW microstructure was analyzed with TEM to identify the θ' and Ω precipitates along with other secondary phases within the SZ, see Figures 4.13 to 4.22, coupled with EDS, see Figures 4.23 to 4.25. The precipitate reflections observed in the BM in the <100>, <110>, and <111> zone axes, observed in Figure 4.4 and Figure 4.5, were not observed through

the center of the thickness of the SZ[8]. This demonstrates that the θ' and Ω phases dissolved during the FSW process. Dark field TEM photomicrographs for the top, see Figure 4.19 and Figure 4.23, middle, see Figure 4.21c, mid bottom, see Figure 4.22c and Figure 4.24, and bottom, see Figure 4.25, also provide evidence of the lack of these precipitate phases. A closer look at the coarse precipitates in Figure 4.21 and Figure 4.22 show that they are located within the matrix grains and at the grain boundaries. In the LWN, these precipitates appear to be interacting with dislocations. Although dislocation analysis was outside of the scope of this dissertation work, the dislocations in the SZ are believed to have contributed to the coarsening of the precipitates. At +10 mm from the weld center in the weld mid top, BF TEM photomicrographs and SADPs reveal coarsened Ω precipitates, see Figures 4.16 to 4.18, and 4.20. The smaller diffraction spots indicate the presence of incoherent precipitates. EDS analysis on these precipitates indicate they are rich in Cu, C, O, Fe, and Co. Mg was not detected in these precipitates.

[8] The constant speed SZ mid top at 0 mm from the center of the weld could not be analyzed by TEM due to errors in sample preparation. The sample was damaged during electropolishing and a perforation could not be established for viewing. Thus, +10 mm was analyzed to provide information for the mid top layer.

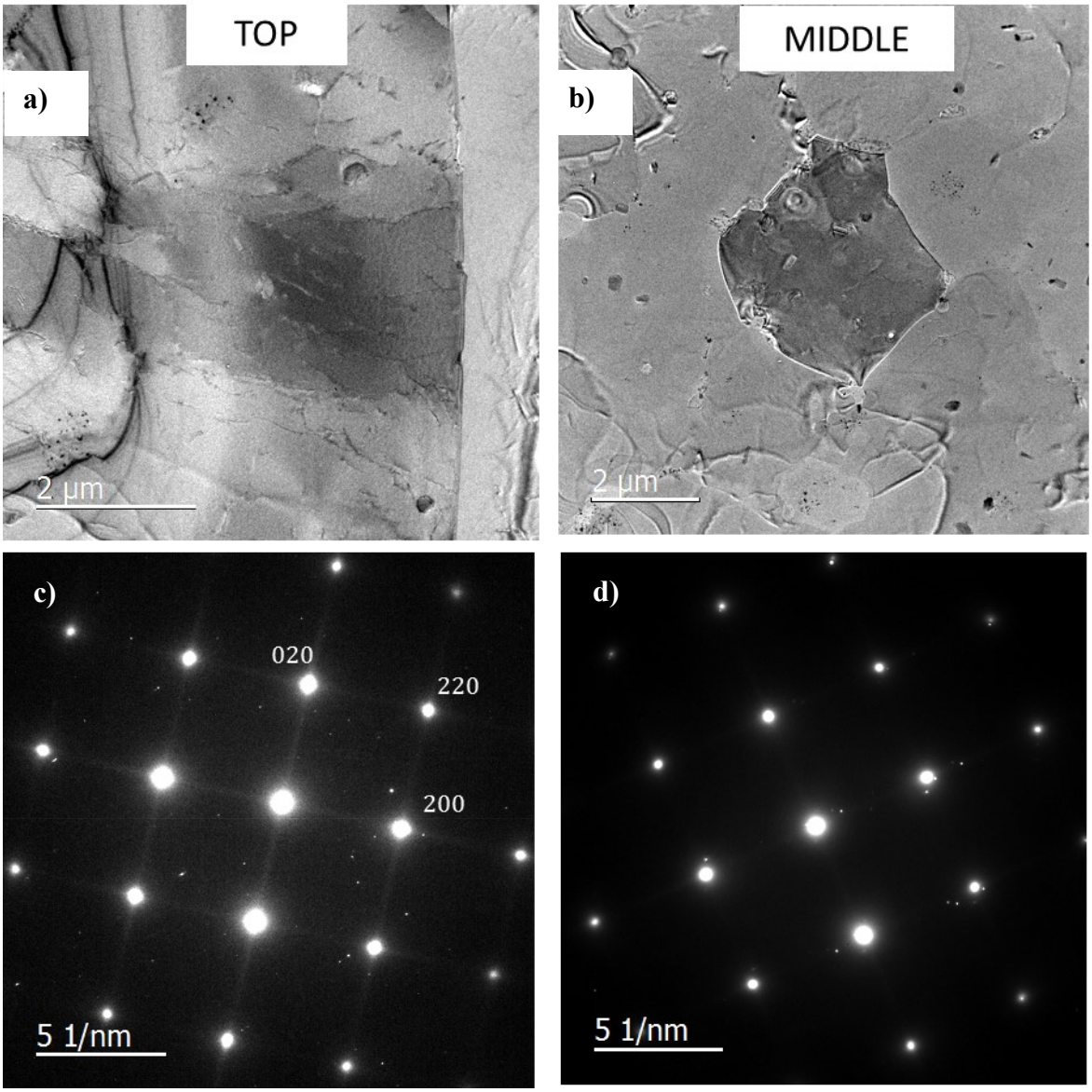

Figure 4.13. Bright field (BF) TEM photomicrographs and the corresponding SADP in the SZ (<100> zone axis) of the top layer a) and c) and middle layer b) and d), mid bottom layer e) and g), and bottom layer f) and h) The welding direction is perpendicular to the page. Dark grains are the refracting grains and where the SADP was acquired.

Figure 4.13 (continued)

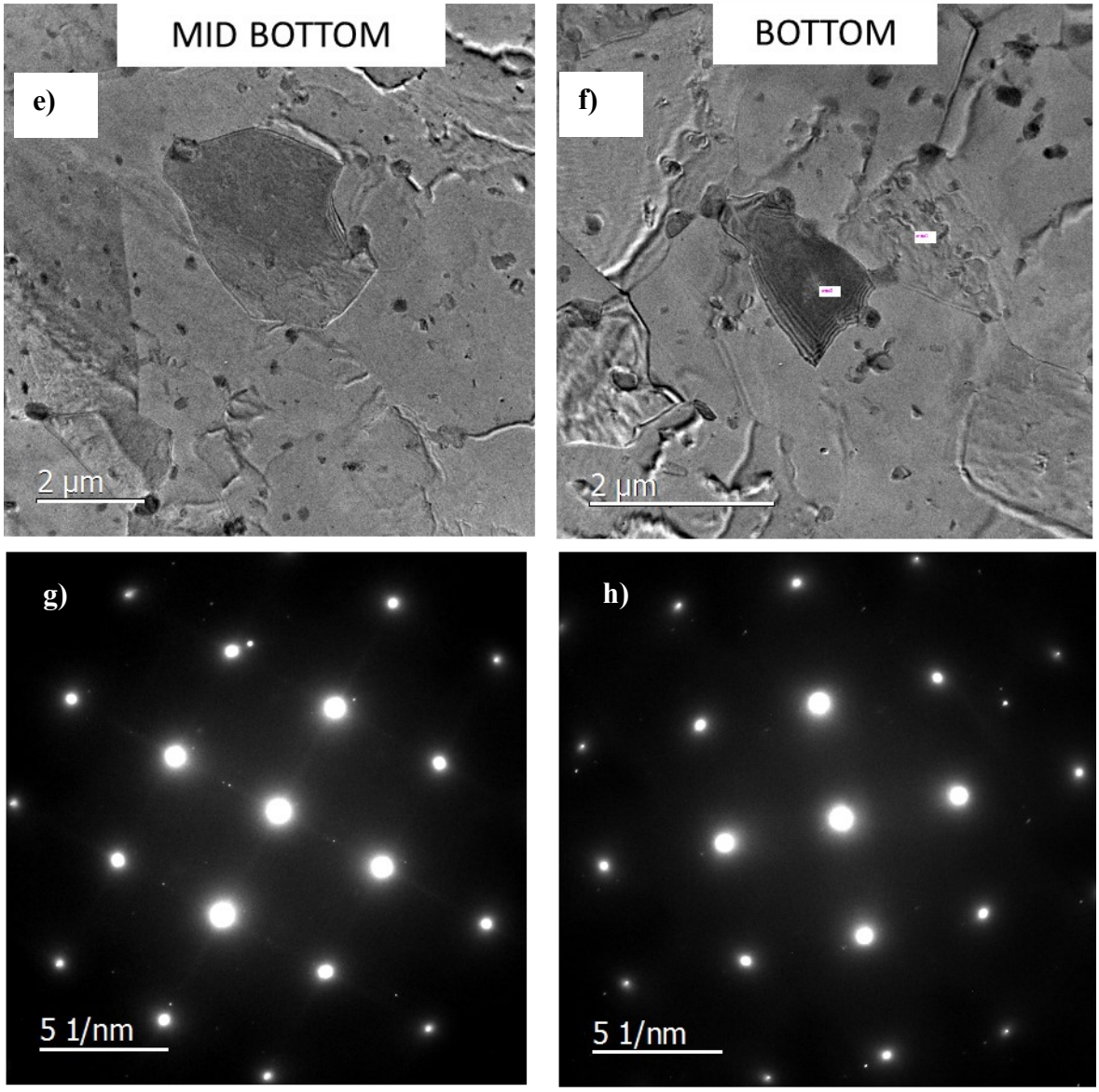

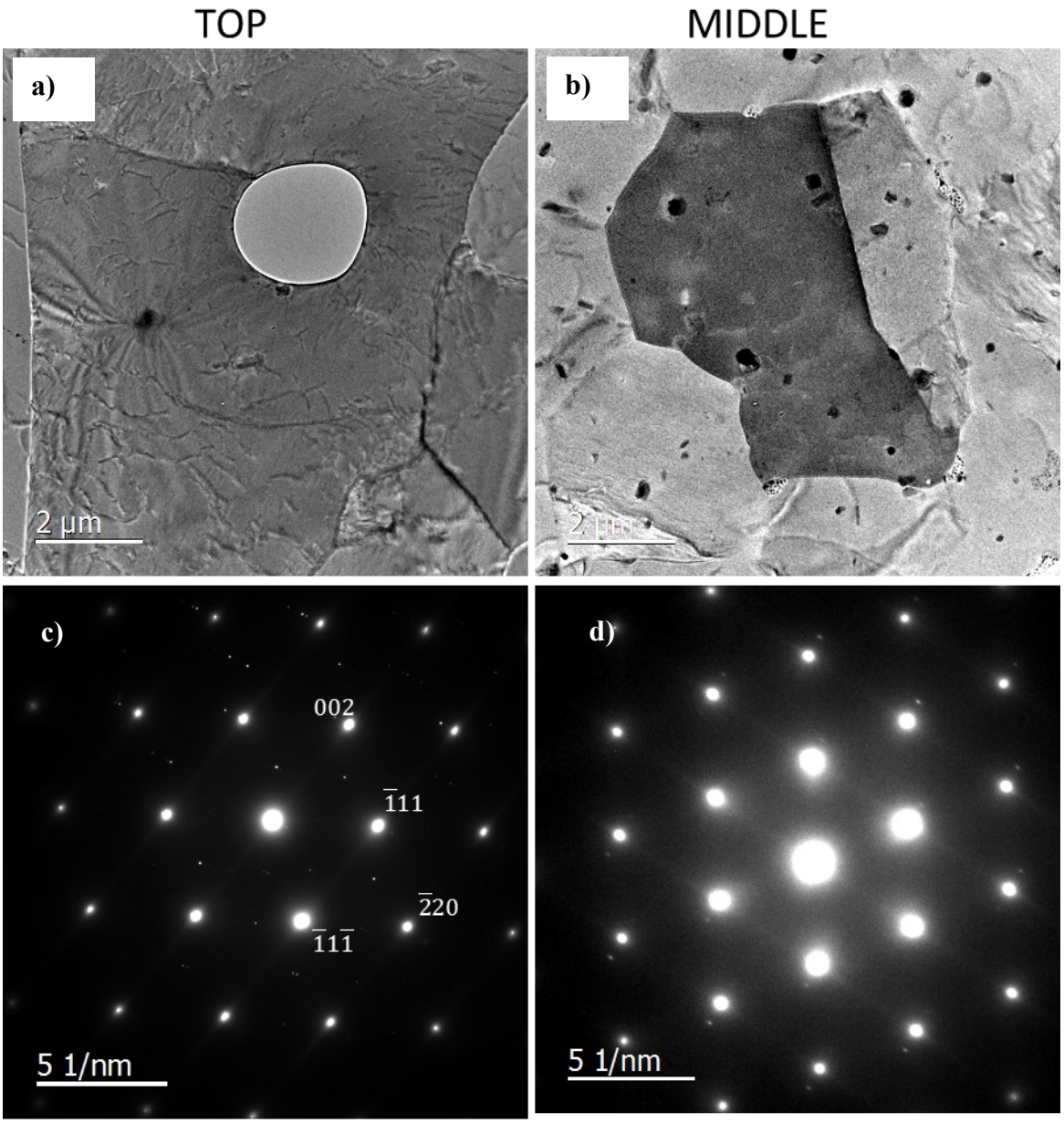

Figure 4.14. Bright field TEM photomicrographs and diffraction patterns in the SZ (<110> zone axis). The welding direction is perpendicular to the page. Dark grains are the refracting grains and where the SADP was acquired.

Figure 4.14 (continued)

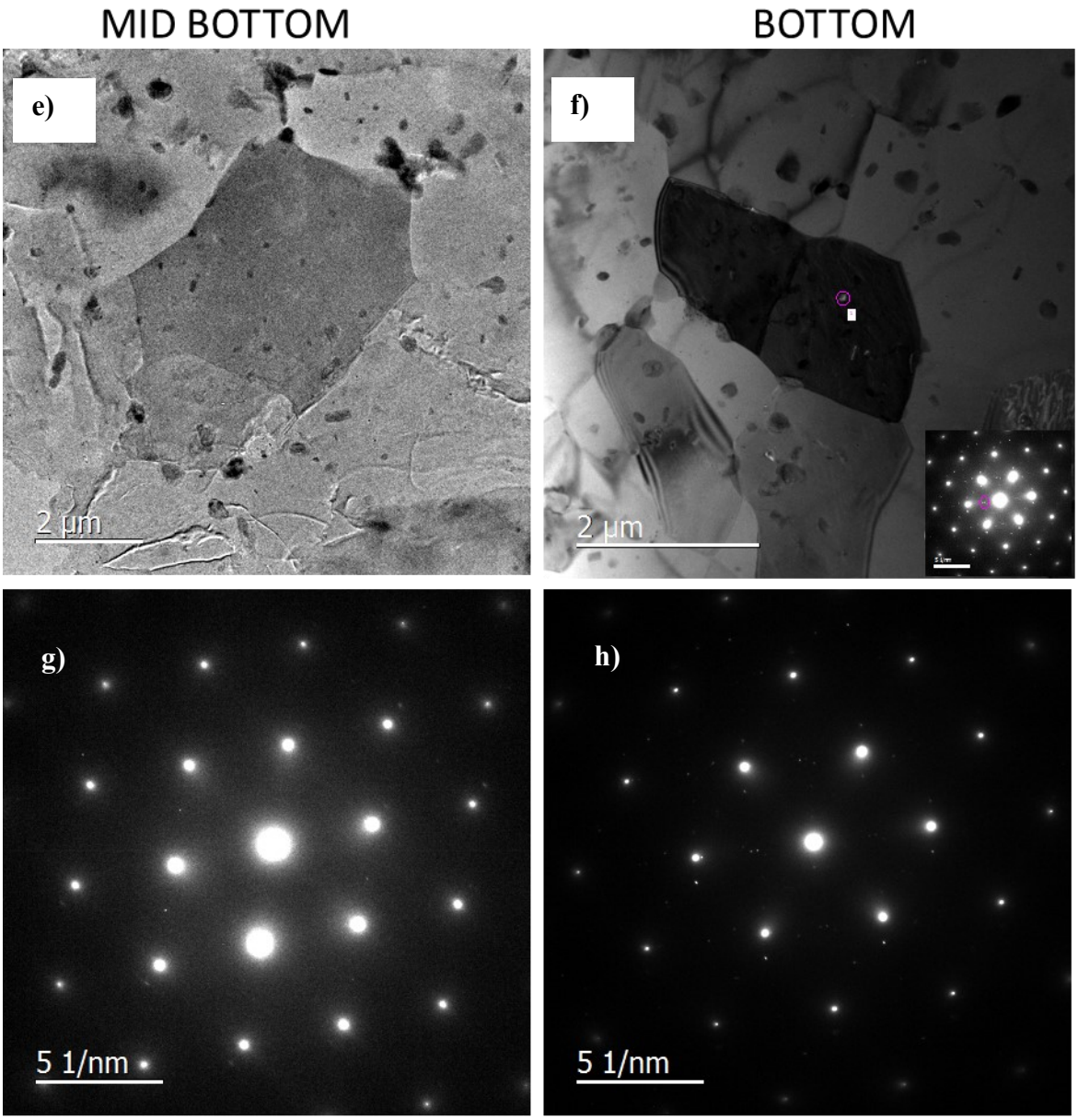

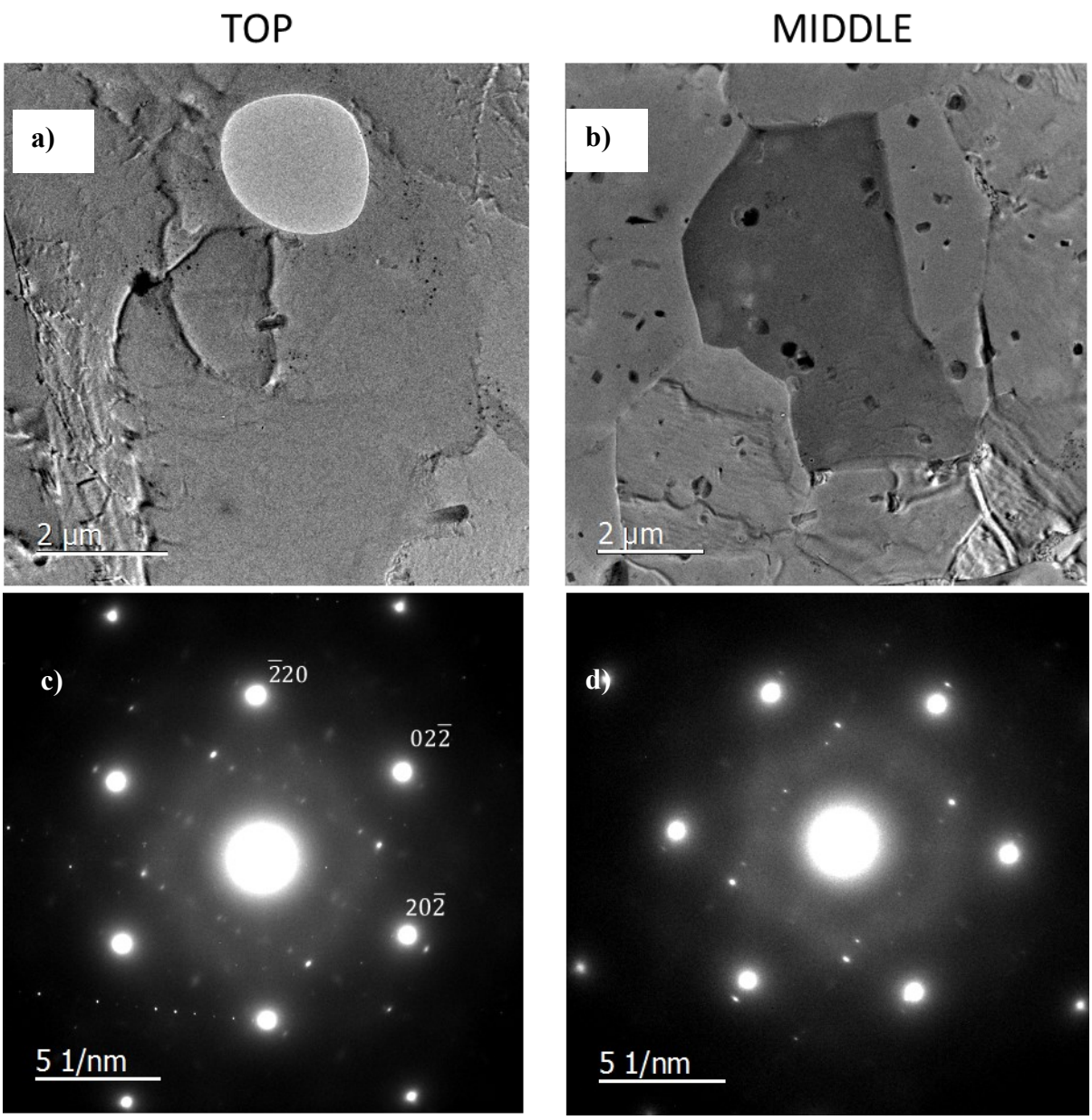

Figure 4.15. Bright field (BF) TEM photomicrographs and diffraction patterns in the SZ (<111> zone axis). The welding direction is perpendicular to the page. Dark grains are the refracting grains and where the SADP was acquired.

Figure 4.15 (continued)

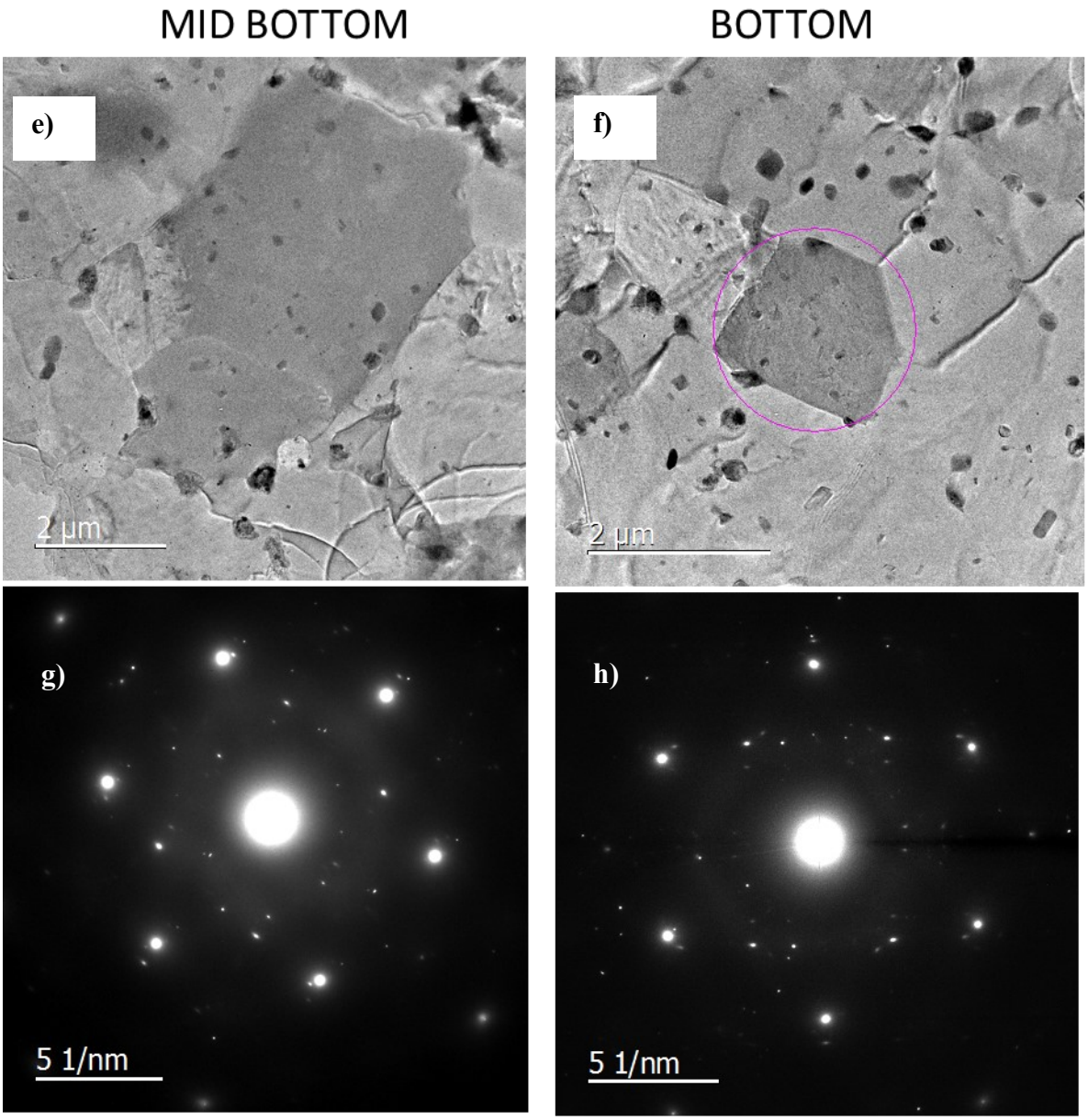

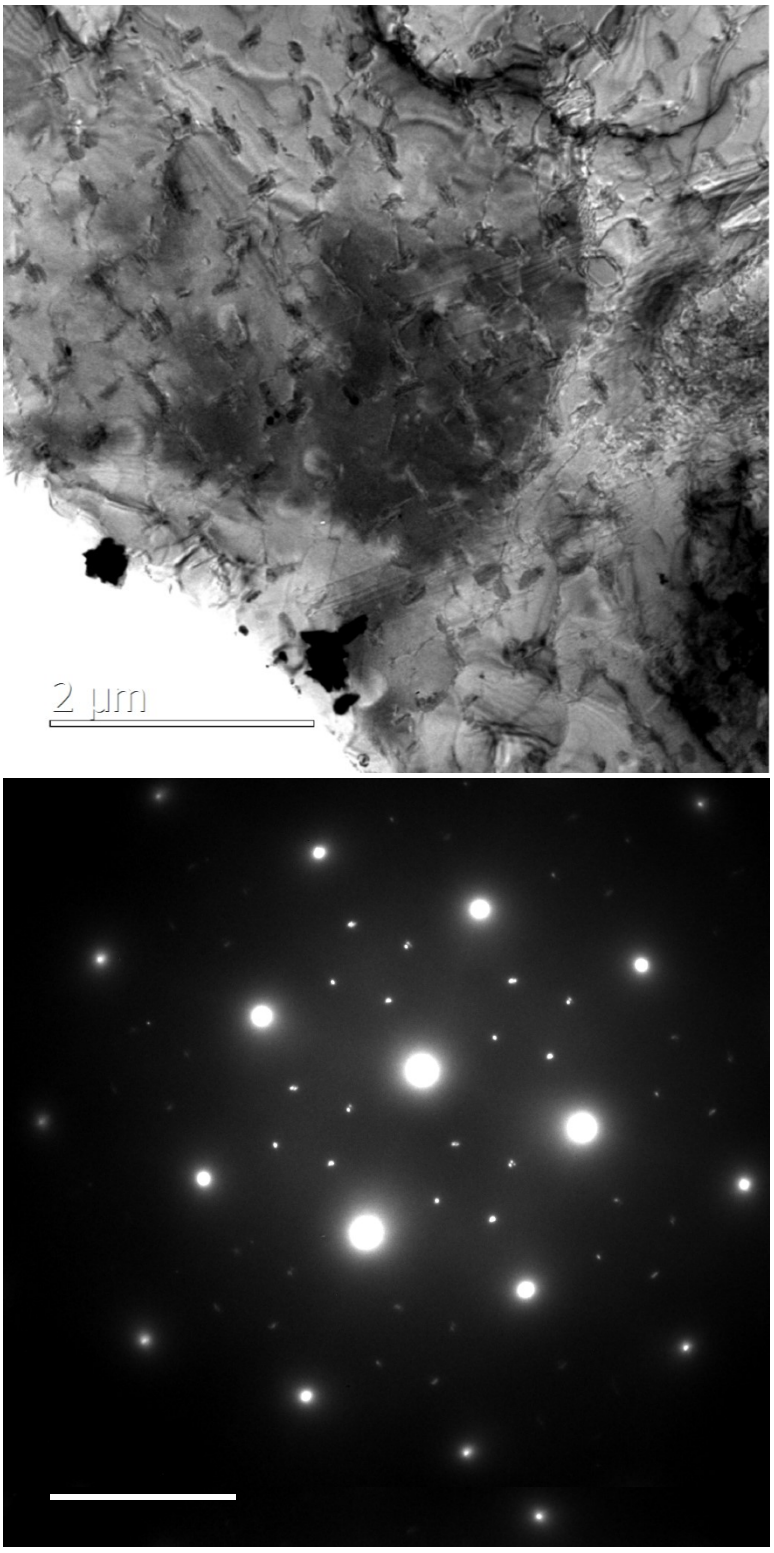

Figure 4.16. Bright field TEM photomicrographs and SADP from the mid top, +10 mm (RS) from the center of the weld (<100> zone axis). The SADPs indicate that only the Ω precipitate phase remains. The welding direction is perpendicular to the page.

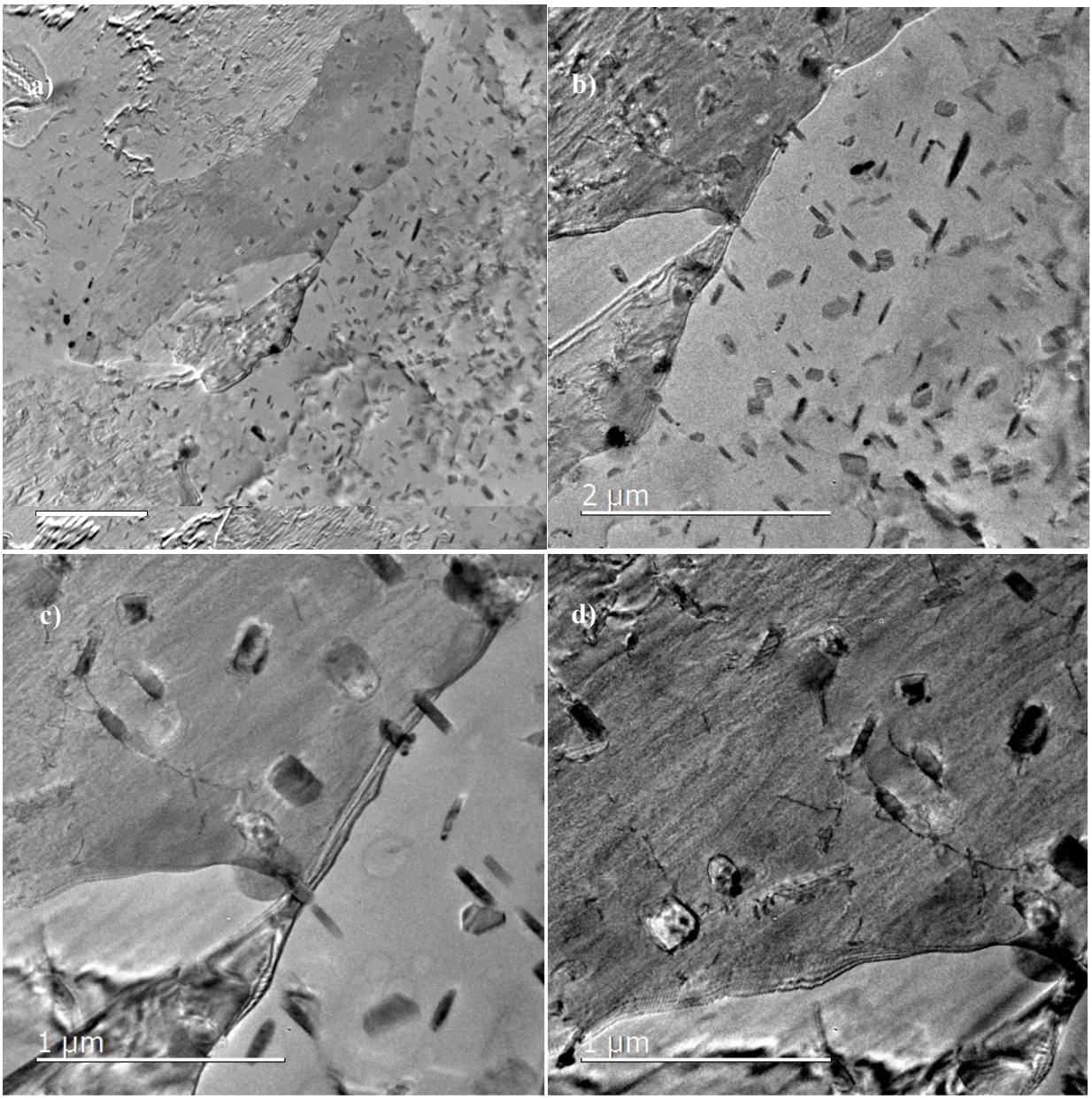

Figure 4.17. (a)-(d) Bright field and diffraction pattern from the mid top +10 mm (RS) from the center of the weld (<110> zone axis), (e) the respective SADP in the <110> zone axis. The welding direction is perpendicular to the page. Dislocations pinned down by precipitates can be seen in c) and d). e) SADP shows that the Ω precipitate remains and θ' is absent.

Figure 4.17 (continued)

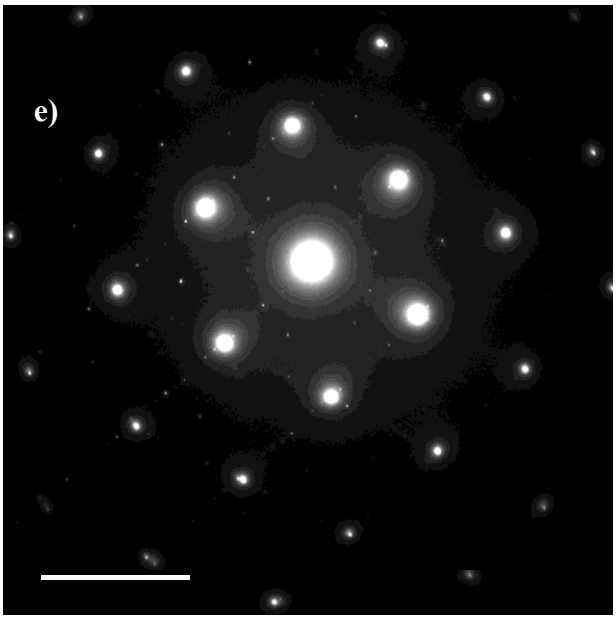

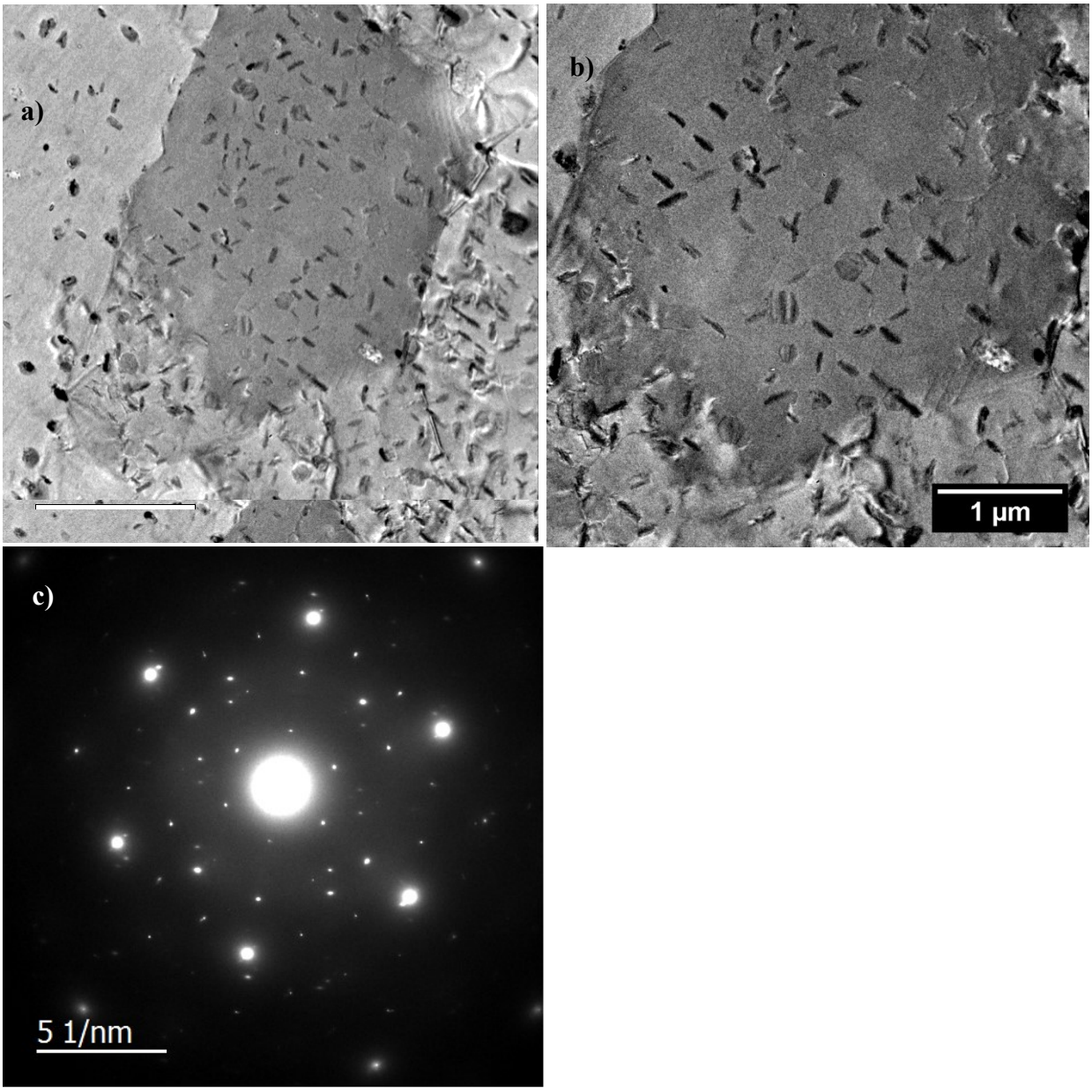

Figure 4.18. (a)-(b) Bright field TEM photomicrographs and diffraction pattern from the mid top, +10 mm (RS) from the center of the weld (<111> zone axis), (c) the respective SADP in the <111> zone axis. The welding direction is perpendicular to the page.

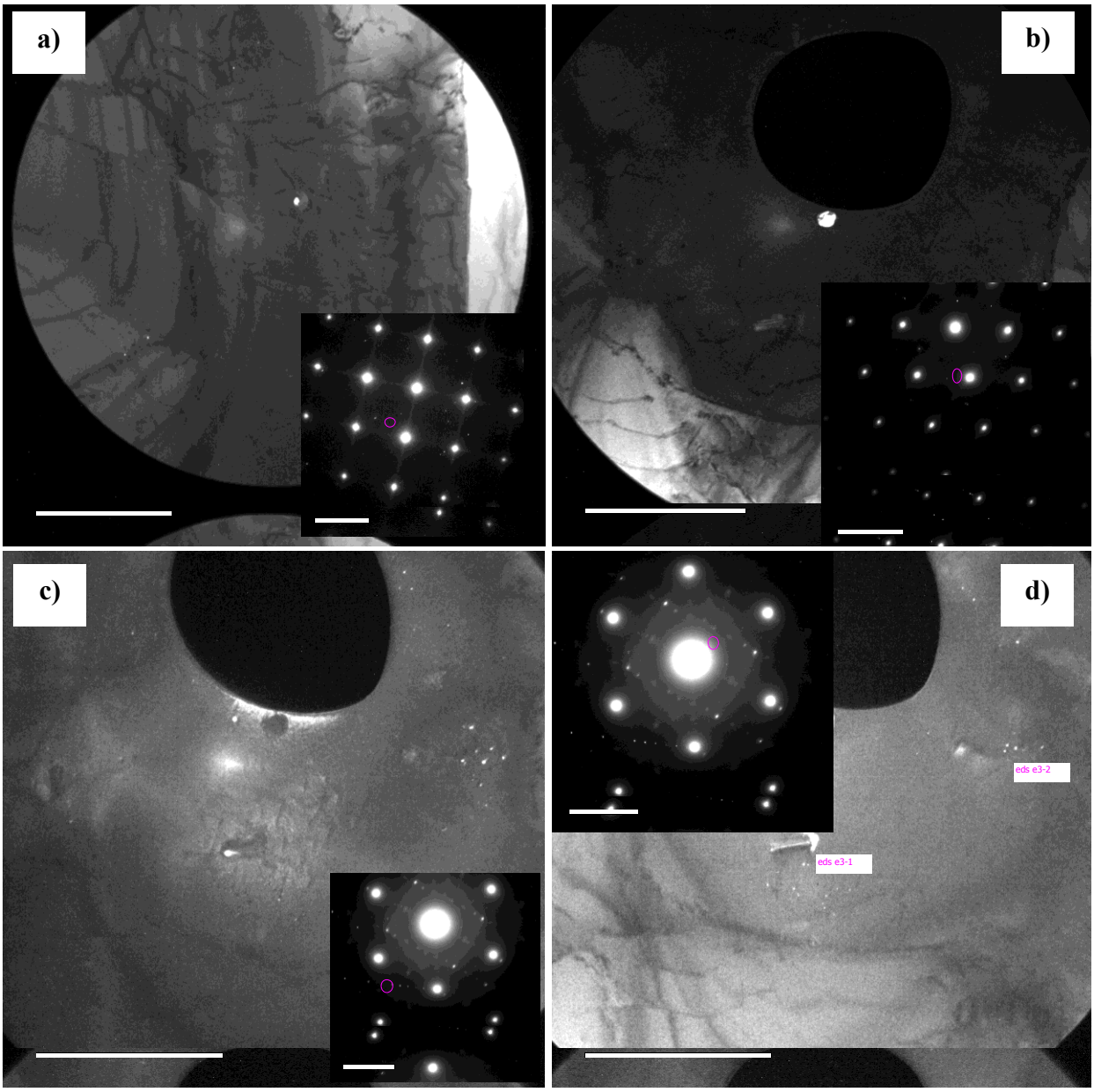

Figure 4.19. Dark field TEM photomicrographs with inset diffraction patterns in the SZ top (a) <100> zone axis, (b) <110> zone axis, and (c)-(d) <111> zone axis. The spot associated with the DF images is circled in purple. The welding direction is perpendicular to the page.

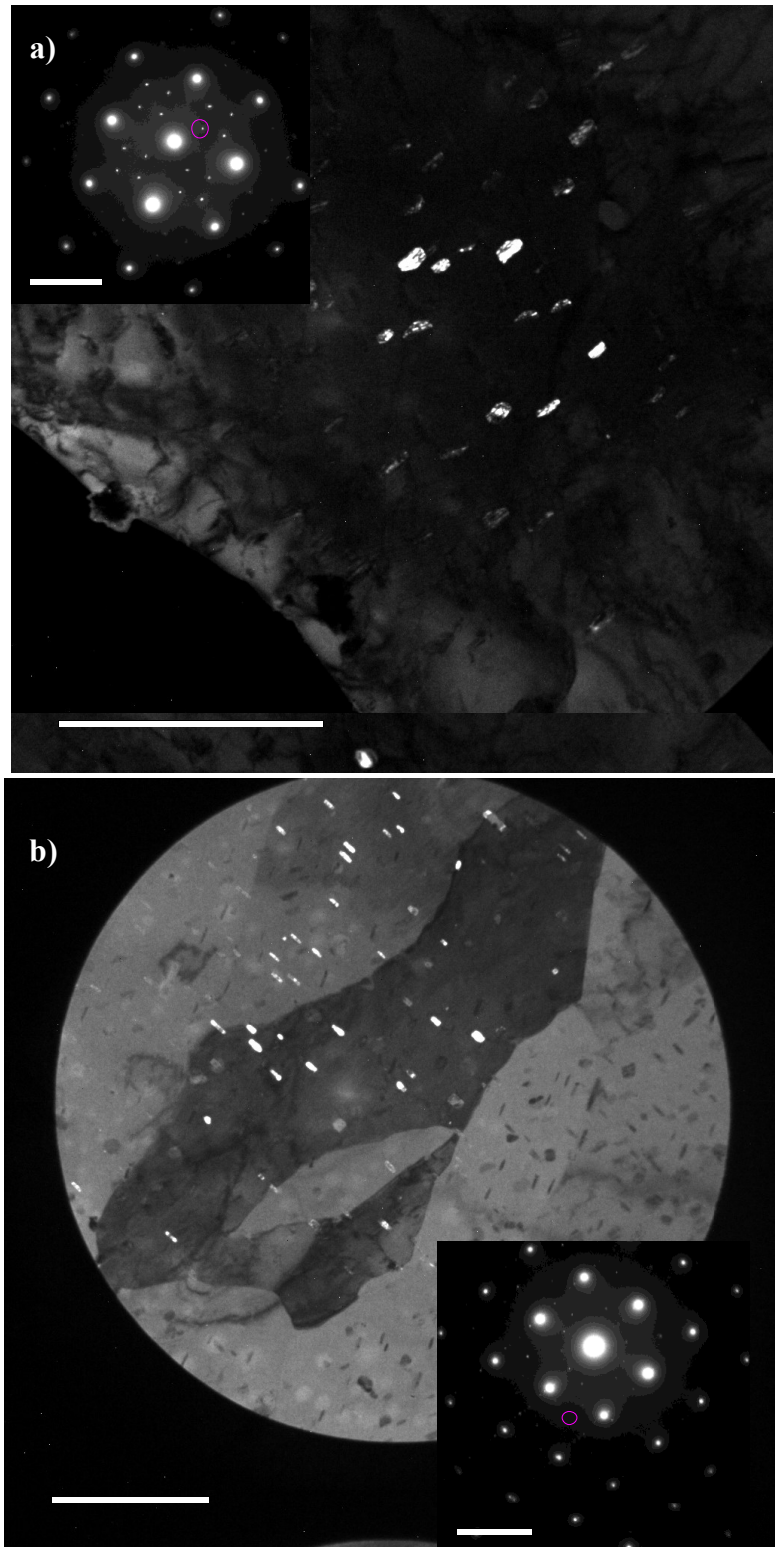

Figure 4.20. Dark field TEM photomicrographs with inset diffraction patterns from the mid top, +10 mm (RS) from the center of the weld. (a) <100> zone axis, (b)-(c) <110> zone axis, and (d) <111> zone axis. The spot associated with the DF images is circled in purple. The welding direction is perpendicular to the page.

Figure 4.20 (continued)

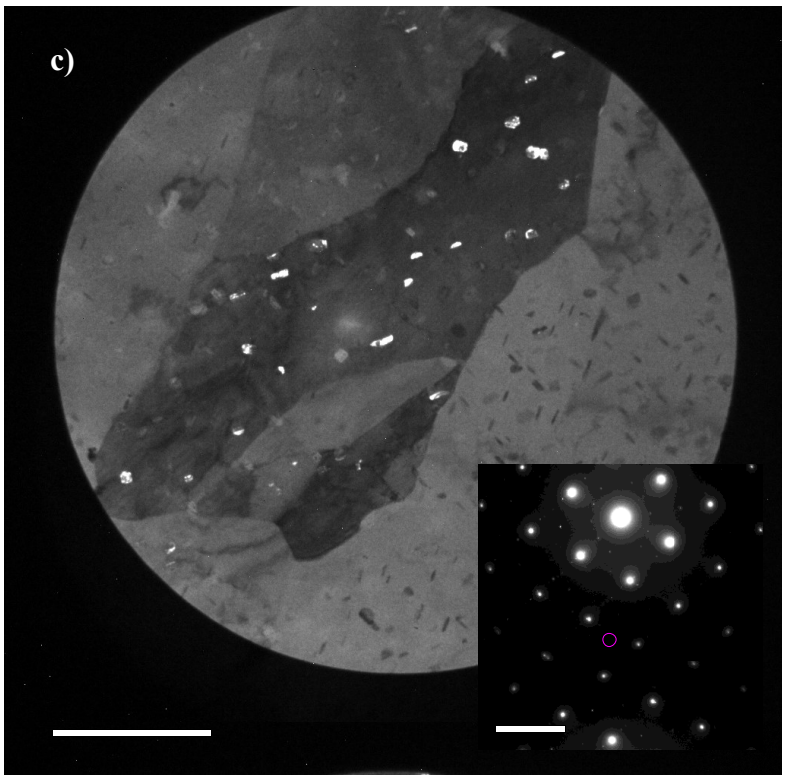

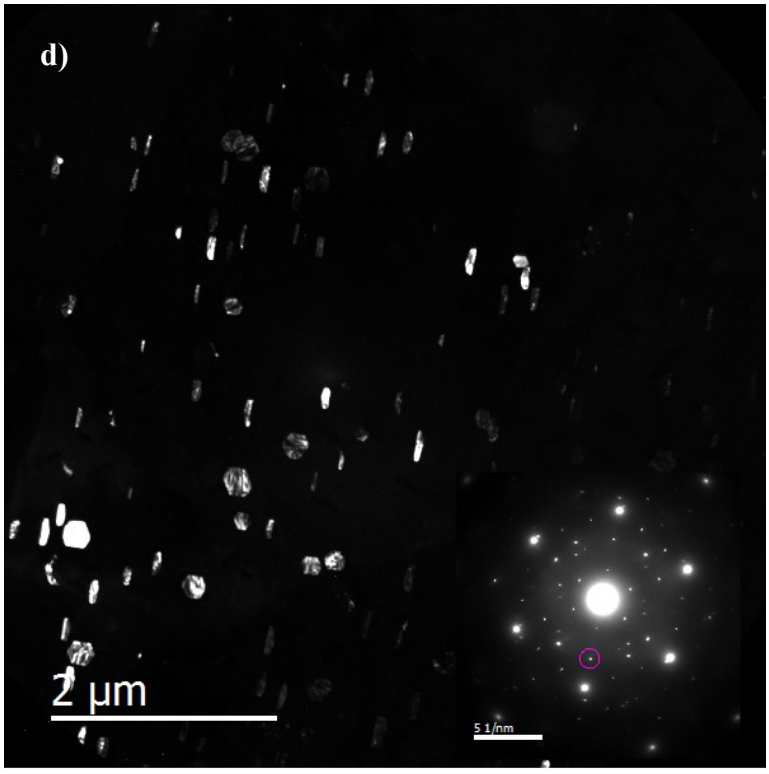

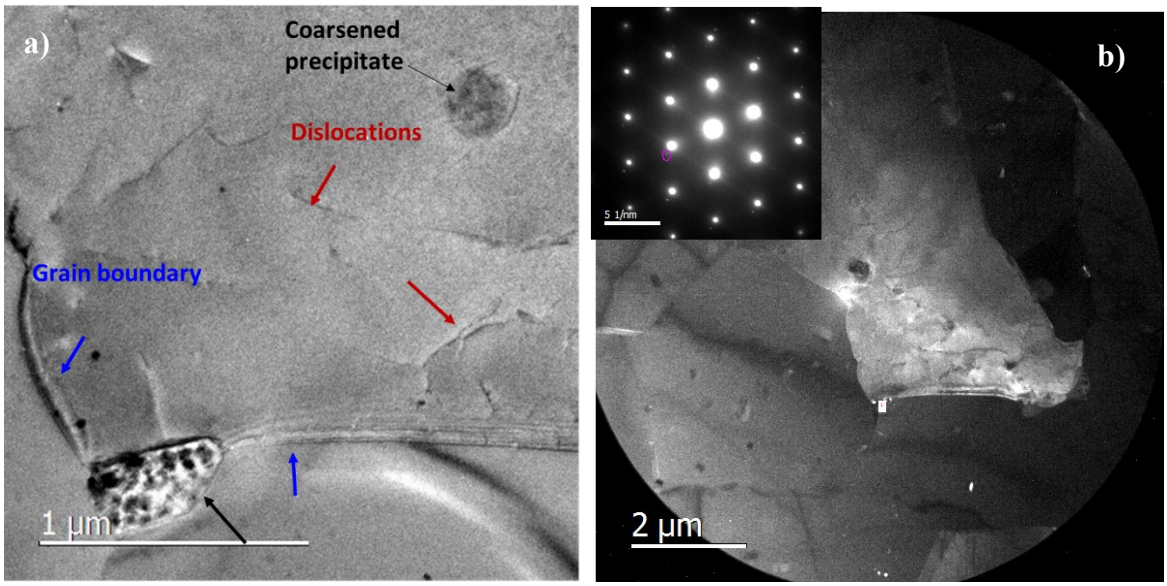

Figure 4.21. (a) Bright field photomicrographs in the <110> zone axis and (b) dark field photomicrograph at the <110> zone axis with inset diffraction pattern taken from the middle at the center of the SZ. The welding direction is perpendicular to the page.

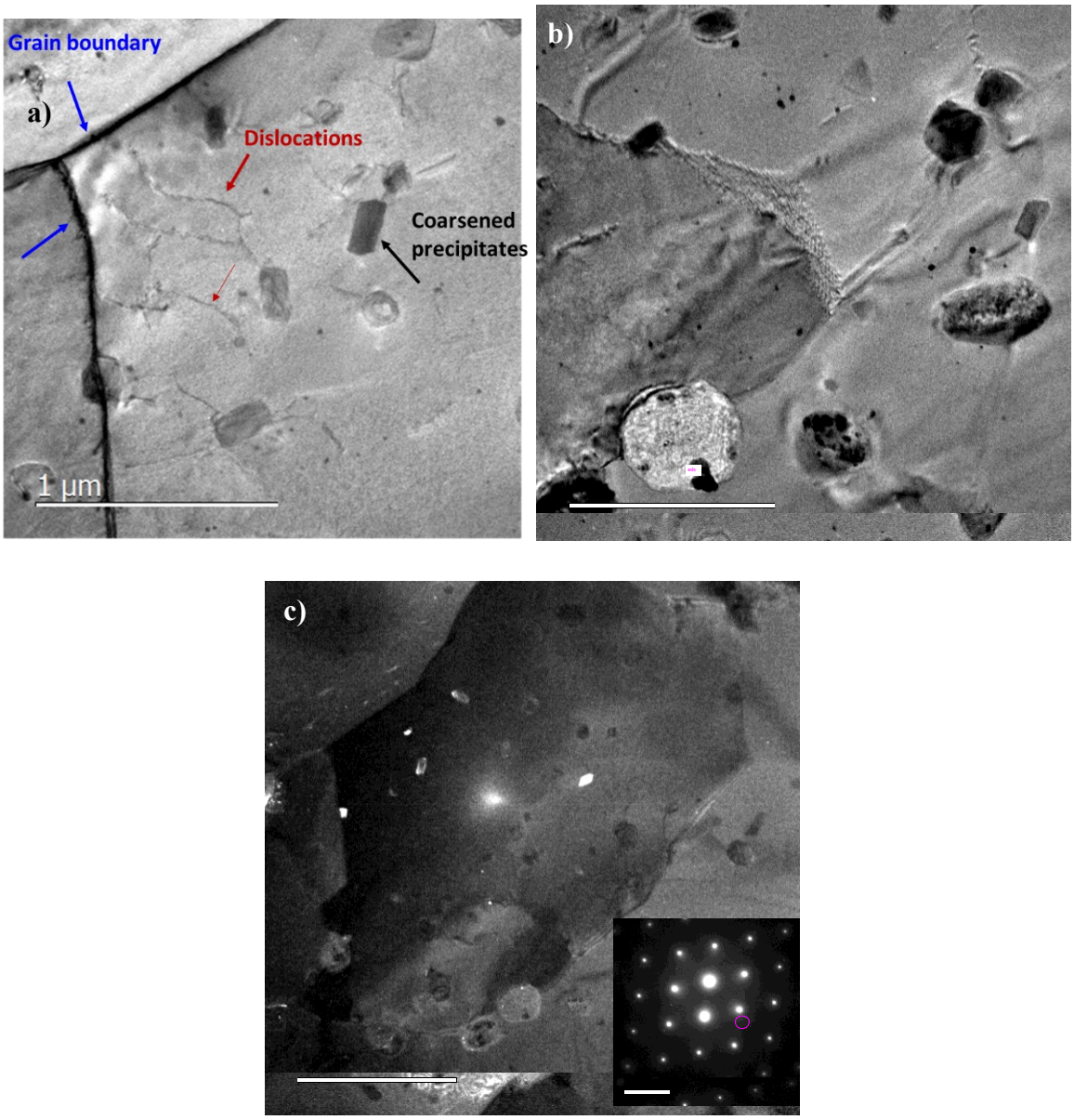

Figure 4.22. (a)-(b) Bright field TEM photomicrographs in the <110> zone axis and (c) dark field photomicrograph at the <110> zone axis with inset diffraction pattern taken from the mid bottom at the center of the SZ. The welding direction is perpendicular to the page. Dislocations can be seen in a). Precipitates pinning down grain boundaries can be seen in a) and b). The dark field TEM photomicrograph demonstrates that θ' and Ω are not present.

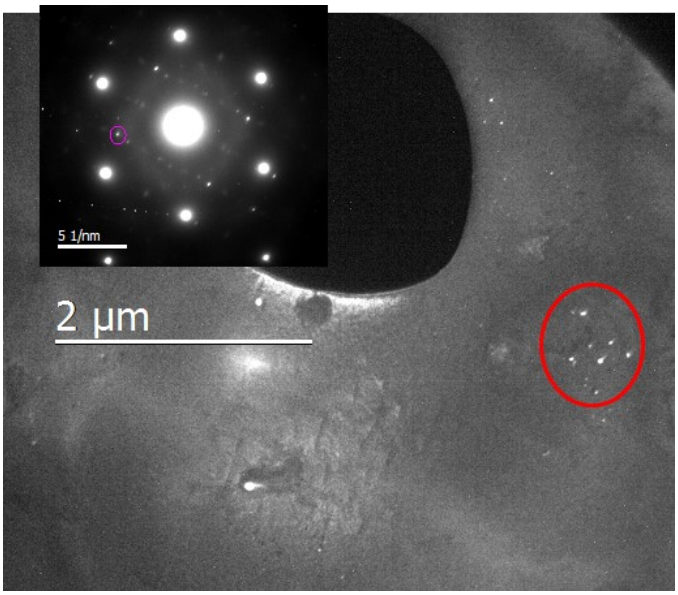

Element	Weight%
C K	33.17
O K	2.28
Al K	61.46
Cu K	3.09
Totals	100.00

Figure 4.23. Dark field TEM photomicrograph with inset SADP of the constant-speed FSW top. The purple circle correlates to the diffraction spot to the illuminated secondary phases in the DF image. Elemental EDS measurements on the right correspond to the region circled in red. The welding direction is perpendicular to the page.

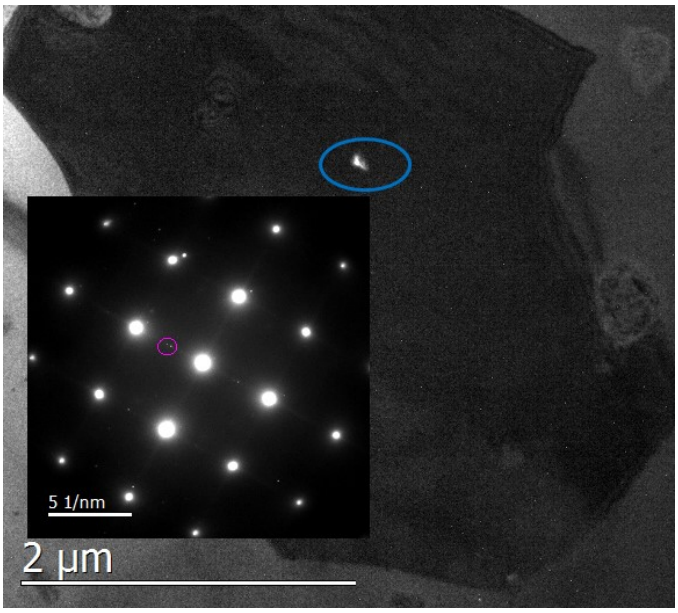

Element	Weight %
C K	7.65
O K	25.23
Al K	25.96
Fe K	4.40
Co K	4.76
Cu K	32.01
Total	100.00

Figure 4.24. Dark field TEM photomicrograph with inset SADP of the constant-speed FSW mid bottom. The purple circle correlates to the diffraction spot to the illuminated secondary phases in the DF image. Elemental EDS measurements on the right correspond to the region circled in blue. The welding direction is perpendicular to the page.

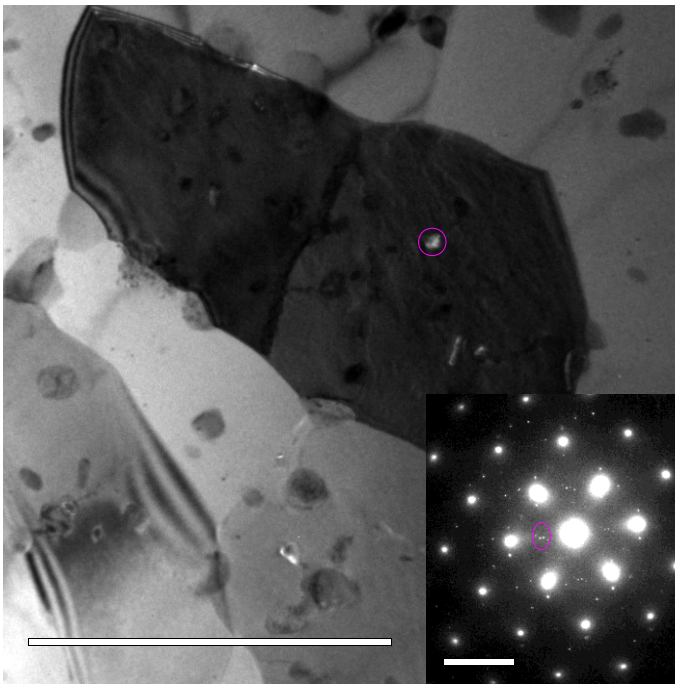

Element	Weight%
Mg K	0.00
Al K	85.76
Si K	0.00
Fe K	2.38
Co K	3.49
Cu K	8.37
Totals	100.00

Figure 4.25. Dark field TEM photomicrograph with inset SADP of the constant-speed FSW bottom. The purple circle correlates to the diffraction spot to the illuminated secondary phases in the DF images. EDS measurements on the right correspond to region in the DF image circled in purple. The welding direction is perpendicular to the page.

4.2.2 Effects of FSW on the Microstructure

The SZ was divided by two regions known as the UWN and the LWN, distinguished by the differences in the average grain sizes. As demonstrated in Table 4.6 and Table 4.7, a microstructural gradient was observed through the depth of the SZ. The average grain size was larger at the top and decreased towards the bottom of the weld. The average precipitate volume percent through the depth of the SZ increased from the top of the weld towards the bottom of the weld. TEM analysis in the center of the SZ demonstrated that the thermally-metastable precipitates, θ' and Ω, dissolved throughout the depth of the SZ. Only the Ω precipitate was observed 10 mm away from the center of the SZ and towards the RS at the mid top, which is near the TMAZ. The θ' precipitate was not observed indicating either the dissolution of the θ' or its transformation to the equilibrium θ precipitate.

The change in microstructure throughout the depth of the SZ suggests a thermal gradient throughout the depth of the weld. The thermal gradient is reflective of the heating and cooling of the weld. This relationship is summarized in Figure 4.26. Higher temperatures are experienced at the top of the weld due to the rotating tool shoulder, as explained in Equation 2.1. The wide diameter of the tool shoulder generates more frictional heat than the pin, which has a smaller diameter [10]. The high temperatures in the SZ led to the dissolution of the θ' and Ω precipitates. The hotter temperature in the UWN led to the dissolution of most of the θ precipitates. This is evident by the lower precipitate volume percent, consistent with TEM analysis, in the UWN. As a result, there was an increase in the Cu-solute concentration. The higher temperatures in the UWN also led to coarser grains by increasing GB mobility as expressed in Equation (4.1) [25]

$$M\left\{\frac{A_2 n_1 v_1 V_m^2}{N_a RT} exp\left(\frac{\Delta S^a}{R}\right)\right\} exp\left(\frac{-\Delta H^a}{RT}\right) \quad (4.1)$$

where M is the mobility of grain boundary, A_2 is the probability of the atoms from grain 1 being accommodated in grain 2, n is the number of atoms, v is the temperature-independent frequency of atoms jumping, V_m is the molar volume, R is the ideal gas constant, T is the temperature in Kelvin, N_a is Avogadro's constant, and S^a and H^a are the activation entropy and enthalpy in molar quantities. Mishra and Sidhar note that the temperature gradient through thin sheets of 2xxx Al alloys are minimal since the tool shoulder engages the entire SZ [10]. This implies that a thick plate would experience a distinct gradient in temperature, and consequently, in microstructure. This would not be observed in thin plates because the material flow by the tool shoulder rotation penetrates the entire SZ and produces a near homogenous structure.

The microstructure of the SZ also reflects differences in the heat rejection rates, otherwise known as cooling rates. Conductive heat transfer occurs at the bottom of the weld through contact with the weld backing plate and through the thickness of the Al plate. Conductive heat transfer is

expressed in Equation (4.2)

$$Q = -kA\frac{dT}{dx} \tag{4.2}$$

where Q is the heat transfer [Wm^{-2}], k is the thermal conductivity of the material [$Wm^{-1}K^{-1}$], dx is the material thickness, A is the area in which heat transfer occurs, and dT is the difference in temperature. Convection heat transfer occurs at the weld crown by the cooler ambient air and is expressed by Equation (4.3)

$$Q = hAdT \tag{4.3}$$

where h is the convective heat transfer coefficient, A is the cross sectional area of the surface. The quantity dT can be represented as $(T_f - T_s)$, where T_s is the surface temperature of the surface and T_f is the temperature of the fluid, which in this study is air. The h for free air ranges from 2.5-25 $Wm^{-2}K^{-1}$ [87]. The k for AA2024, an Al-Cu-Mg alloy, and AA2219, an Al-Cu alloy, is 121 $Wm^{-1}K^{-1}$ [88,89]. The k for general steel is 52 $Wm^{-1}K^{-1}$ [87]. Thus, as expected, conductive heat transfer is higher and would occur at a faster rate than convective heat transfer.

It has been observed that coarse GB precipitates in FSWs are a result of very slow cooling rates, however, the distribution and identification of these precipitates were not clarified [10]. In contrast to this observation, a higher volume percent of coarse grain boundary precipitates were observed in the LWN of the SZ. The difference in the observation can be explained through a higher weld temperature at the crown coupled with slow heat transfer. This permits grain growth, dissolution of thermally metastable precipitates, and the growth of equilibrium phases. This is confirmed by the TEM photomicrographs acquired at the top of the weld demonstrating the absence of Ω and θ' precipitate phases. Mahoney et al. used K-type thermocouples embedded through the thickness of 6.35 mm thick AA7075-T651 to measure the temperature up to 11 mm

from the edge of the SZ [68]. The measured difference in temperature between the top and bottom of the weld ranged from 2-60°C. Xu et al. observed a 20°C temperature gradient through the thickness of a 14 mm thick, AA2219-O plate [75]. The lower welding temperature at the weld bottom coupled with a faster heat transfer would inhibit grain growth. This temperature, however, is still high enough to appreciably facilitate diffusion of solutes to the GBs. The solutes aggregate in the GBs and initiate precipitate nucleation of the θ precipitate and growth of the already present θ. The increase in available Cu solute was due to the dissolution of θ' and Ω, which enriched the Al-matrix with Cu solutes. As demonstrated in the XRD *in situ* as-received AA2139-T8 heat treatment, θ' dissolves while the θ/Ω precipitates coarsen and θ' was not detected again until natural aging at RT after the solutionizing. The XRD *in situ* heat treatments were conducted at known temperatures and times, which is in contrast to the unknown welding temperature for the constant-speed FSW. The reported peak FSW temperatures ranged between 0.6 - 0.9T_m and were hot enough to dissolve the precipitates [10]. To confirm the effects of FSW temperatures on the microstructure, the welding temperature was monitored and controlled. These thermally-controlled experiments are presented and discussed in sections 4.3.2 and 4.3.5. In addition to an increase in Cu-solute, other elements were found in the SZ.

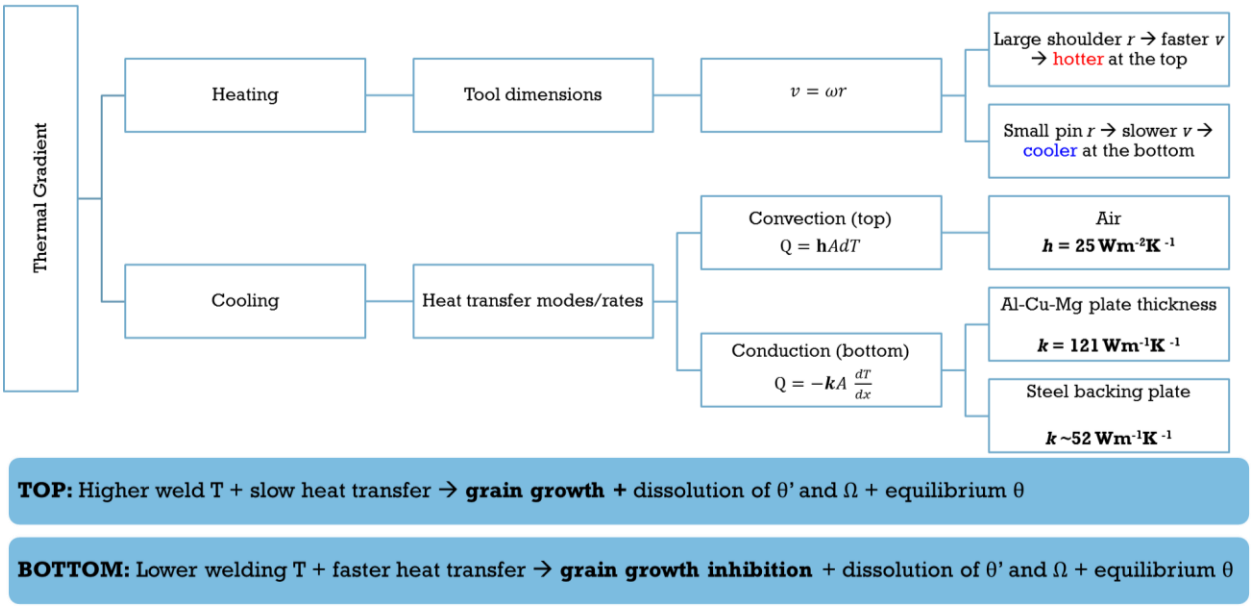

Figure 4.26. Schematic depiction of the cause of the thermal gradient throughout the thickness of the weld.

The TEM EDS and XRD detection of C and Co indicate tool erosion during the constant-speed FSW process. Iron and O were also detected via TEM EDS. The detection of Fe can be explained by the presence of the Fe-rich constituent phase, Al_7FeCu, which was also identified in the XRD results for the as-received AA2139-T8. Thus, this is an insoluble phase that is inherent to the alloy. Tool erosion may also have contributed to the Fe content in the FSW. Oxidation of the alloy before welding may explain the presence of O.

4.2.3 Mechanical Behavior

4.2.3.1 Hardness Behavior

Vickers hardness testing was performed across the transverse cross section of the constant-speed FSW. Hardness was plotted and evaluated in five areas through the thickness at the top (also termed the 'weld crown'), mid top, middle, mid bottom, and bottom (also termed the 'weld root'). Hardness maps were superimposed on the hardness tested and etched samples, as shown in Figure 4.27. Each pixel represents a 1 mm x 1 mm area. The center of the pixel is where the

indent was placed. The color scale of the map follows the red-orange-yellow-green-blue-indigo-violet (ROYGBIV) scale in that dark red indents represent the highest hardness value and dark blue/indigo/violet indents represent the lowest hardness value. The hardness arrays captured all of the FSW zones. The BM was not tested due to equipment complications.

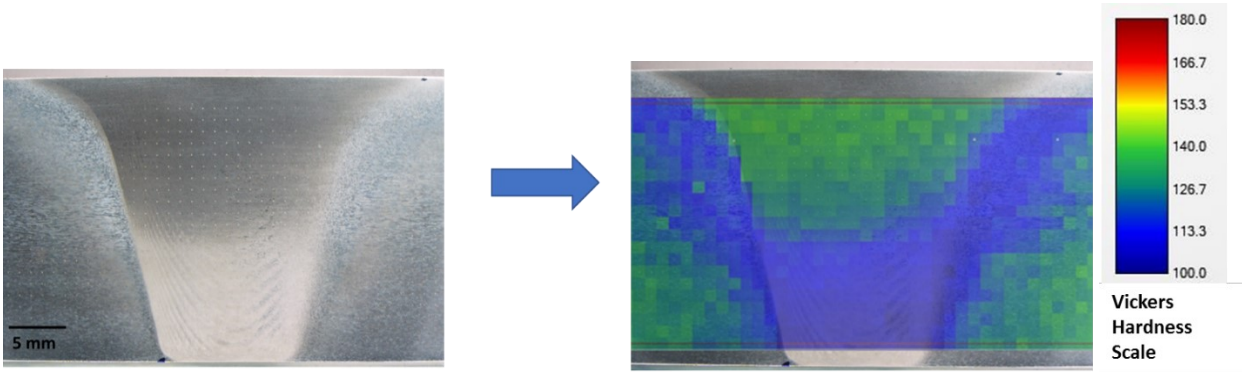

Figure 4.27. Demonstration of how the HV map overlays on the etched welds. The sample was welded via constant-speed FSW.

The hardness map in Figure 4.28 revealed differences in the average hardness between the weld zones. Higher-magnification images of the SZ are shown Figure 4.29. The UWN and LWN are clearly revealed and the average hardness between the two was markedly different. The UWN is shown in green, which correlates to an average hardness is 140 HV and the LWN is highlighted in blue, which correlates to an average hardness of 113 HV.

The HAZ was also qualitatively compared using Figure 4.28. The HAZ is bordered by the red and blue regions on the hardness map.

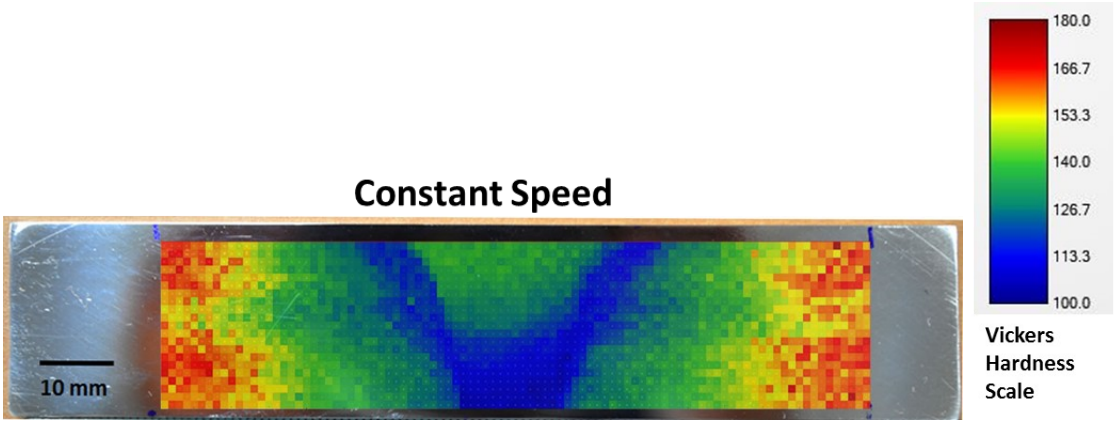

Figure 4.28. Vickers microhardness map across the transverse cross section of the constant-speed FSW. Each pixel represents an 1 mm x 1 mm area.

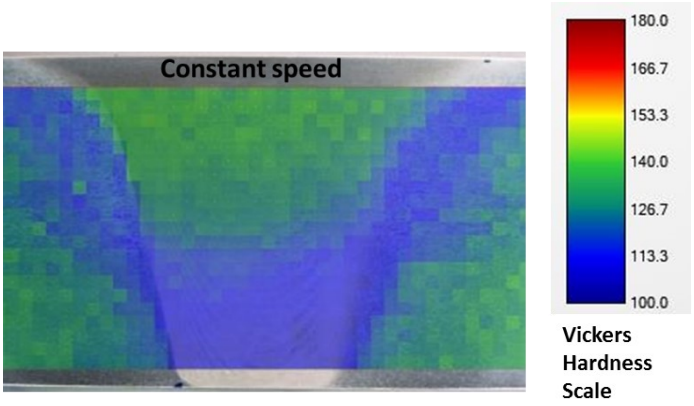

Figure 4.29. Vickers microhardness map overlaid on only the welded region.

Values from the Vickers hardness map are plotted for the weld top, mid top, middle, mid bottom, and bottom, as seen in Figure 4.30. The negative x-axis values represent the AS of the weld, while the positive values represent the RS. The constant-speed plot did not include the BM, where the 160-180HV plateau would be expected at each end of the curves. The maximum hardness values in the SZ in Table 4.8 further demonstrate the gradient in hardness observed in the weld.

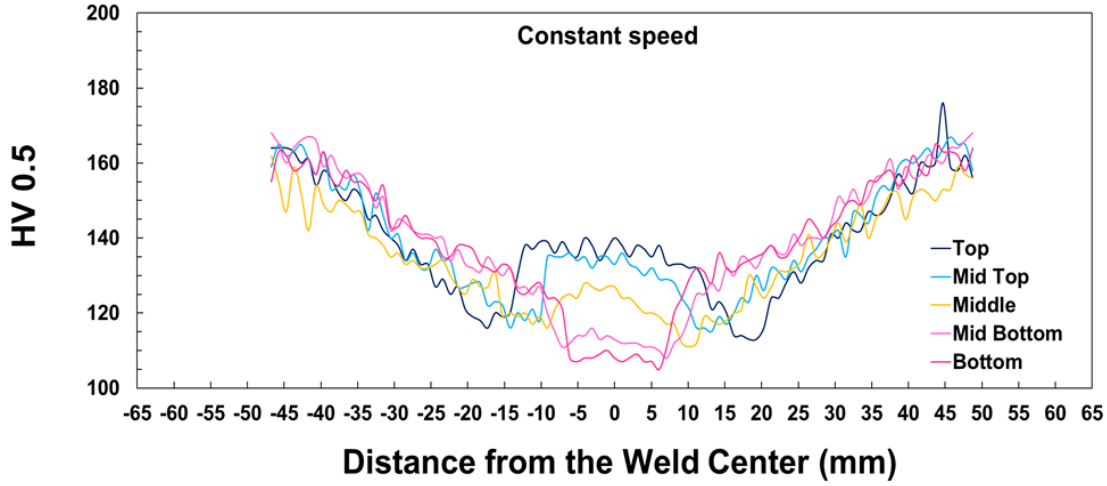

Figure 4.30. Vickers hardness plot of the constant-speed FSW through the thickness of the weld. HV0.5 represents a 0.5 kg load used for indentation.

Table 4.8. Maximum Vickers hardness values through the depth of the SZ for the constant-speed FSW.

Top	Mid Top	Middle	Mid Bottom	Bottom
140	136	128	116	110

4.2.3.2 Tensile Behavior

Tensile tests were performed on the constant-speed weld at RT and 300°C. The tensile axis was parallel to the welding direction, which is also the TD of the plate. The engineering stress-strain plots are shown in Figure 4.31 and the tensile YS, UTS, E, and ε_f are provided Table 4.9. RT tensile tests were conducted for the top, middle, and bottom of the weld. The top of the weld had the highest YS and UTS. The middle and bottom had similar YS, with the bottom being 2 MPa higher. The bottom also had a higher UTS and almost double the ε_f compared to that for the middle. The middle and bottom exhibited yield point elongation, which occurs when there is an increase in strain without an increase in stress. The weld bottom had a longer yield point elongation than the middle of the weld. 300°C tensile testing was conducted for the middle of the

weld. As expected, at 300°C the YS and UTS values were less than those measured at RT.

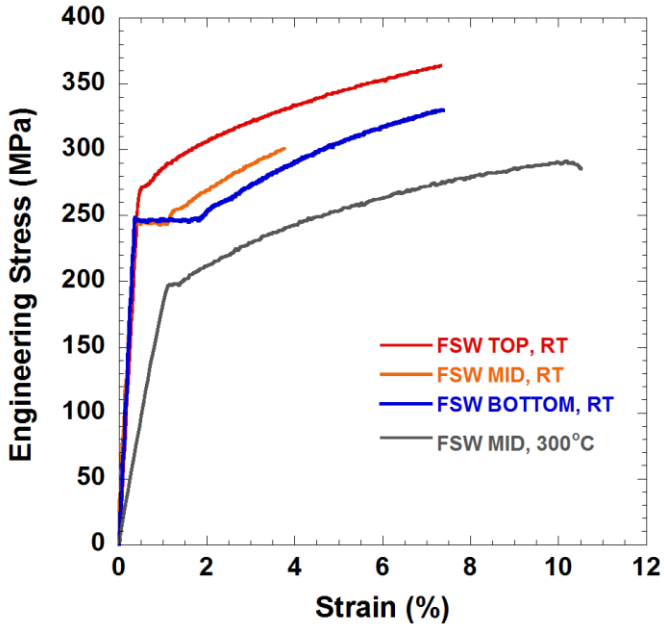

Figure 4.31. Stress-strain plot of the constant-speed FSW at the top, middle, and bottom of the stir zone. The sample tested at 300°C was machined near the middle region of the weld. The tensile axis of the samples were parallel to the weld direction.

Table 4.9. Tensile properties of constant-speed FSW through the depth of the weld. It is noted that an extensometer was not used at 300°C and for this case the elongation to failure was estimated from the sample dimensions before and after the test and the E value was not measured.

	FSW top, RT	FSW middle, RT	FSW bottom, RT	FSW middle, 300°C
UTS (MPa)	360	301	330	290
YS (MPa)	272	243	245	197.5
E (GPa)	61.1	61	70	n/a
ε_f (%)	7.38	3.77	7.42	10.51

n/a: not available

4.2.4 Effects of FSW on the Mechanical Behavior

The hardness and tensile strengths of the SZ were lower than the base metal. In addition,

the variation in the RT longitudinal tensile results and the hardness results through the depth of the SZ for the constant-speed FSW can be attributed to the microstructural variations in the SZ. The YS at the weld top was higher than the middle and bottom of the weld. This is consistent with the Vickers hardness results, which also decreased from the top of the weld to the bottom. That is, the UWN has a higher hardness and tensile strengths than the LWN. An explanation for this result is provided below.

Grain boundary strengthening is modeled by the Hall-Petch relationship in Equation 4.4

$$\sigma_y = \sigma_0 + k_y d^{-1/2} \tag{4.4}$$

where σ_y is the YS, σ_0 and k_y are material constants, and d is the diameter of the grain [1]. According to the Hall-Petch relationship [1], the YS, which is proportional to the Vickers hardness, increases with decreasing average grain size. As previously discussed, the average matrix grain size decreased from the top of the weld towards the bottom of the weld. In addition, the grains in the SZ were significantly finer than those in the base metal. Thus, GB strengthening is not considered to be the dominant strengthening mechanism for the constant-speed FSW, which is consistent with literature [90].

In precipitate strengthening, the volume percent, size, and distribution of the precipitates affect how well they inhibit dislocation motion and thereby strengthen the alloy. The likely reason why the SZ exhibited a lower strength and hardness than the BM was because the θ' and Ω precipitates dissolved in the SZ. Only the θ phase precipitate was present in the SZ, and it exhibited a higher volume percent at the LWN compared with the UWN. Thus, it is expected that solid-solution strengthening, as a result of the increase in the concentration of Cu-solutes in the UWN [77], was responsible for the higher strengths and hardness values exhibited by the UWN compared to the LWN. To summarize, the UWN exhibited a larger grain size and smaller precipitate volume

percent and therefore the solutes originally concentrated in the precipitates were present in higher concentration in the matrix grains in the UWN compared to their LWN counterparts. This resulted in greater solid-solution strengthening. As presented previously, the θ phase precipitates were coarser toward the bottom (LWN) and finer toward the top (UWN) and this led to a greater precipitate volume percent in the LWN compared to the UWN. Thus, even though the precipitate phase volume percent increased slightly (from ~2% to ~11%) from the UWN to the LWN, the small increase in precipitation strengthening expected from this relatively small increased precipitation volume percent is not expected to have overtaken the solid-solution strengthening effect, which is expected to have decreased slightly from the UWN to the LWN. Overall, the non-equilibrium SZ microstructure, which resulted from the constant-speed FSW, was graded throughout depth of the SZ and this dictated the mechanical properties.

The deformation behavior also varied through the depth of the SZ for the constant-speed FSW. As demonstrated in the engineering stress-strain plot in Figure 4.31, the middle and the bottom of the FSW exhibited yield point elongation, with the weld bottom having approximately twice the yield elongation as the middle. The weld top also exhibited this phenomenon to a smaller degree. This phenomenon is usually observed in solution-strengthened alloys and is therefore consistent with the above discussion regarding the mechanical properties [77].

4.2.5 Post Weld Heat Treatment

PWHTs were performed on the constant-speed FSW with the objective of increasing the strength of the weld. The as-welded state has lower strength than the BM, thus PWHTs are considered to be a means to recover the lost strength and hardness due to the non-equilibrium microstructure that evolved during the FSW process. Four heat treatments were conducted in a vacuum tube furnace for 200°C for 10 hrs (200°C/10h), 247°C for 0.5, 0.9, and 2 hr (247°C/0.5h, 247°C/0.9h, and 247°C/2h). The microstructures which yielded the lowest and highest hardness

values were characterized using SEM. Vickers hardness was performed across the transverse cross section in five areas: top (also termed the 'weld crown'), mid top, middle, mid bottom, and bottom (also termed the 'weld root'). The tensile properties near the middle of the weld were evaluated.

The results of the PWHT on the microstructure and mechanical properties for constant-speed FSW are discussed in the next section. Discussion of the PWHT that yielded the highest hardness, 200°C/10h, and the least hardness, 247°C/2h, are provided below. Overall no significant benefits were observed with PWHT.

4.2.5.1 Microstructure

The microstructures following PWHTs were characterized using SEM. Figure 4.32 and Figure 4.33 reveal the microstructure gradient in both grain size and precipitate size and distribution through the thickness of the SZ at the top, mid top, middle, mid bottom, and bottom for the samples heat treated at 200°C/10h and 247°C/2h. The average grain sizes were obtained via EBSD (see Figure 4.34 and Figure 4.35) and are plotted for comparison in Figure 4.36. Figure 4.37 shows the comparison plot for the precipitate volume. In both heat treatments, the grains were larger at the weld top and smaller at the weld bottom, which is consistent with the as-welded samples. The precipitate volume percent for PWHTs at 247°C/10h and 200°C/10h increased through the depth of the weld. The precipitate volume percent had an inverse relationship with the grain size, in that the top, which had larger grains, had a lower precipitate volume percent than the weld root, which exhibited smaller grains. This is consistent with the as-welded constant-speed FSW.

EBSD orientation maps across the transverse cross section of the PWHTs were acquired approximately 9 mm from the bottom of the weld following heat treatments at 200°C/10h and 247°C/10h. Only two PWHTs were analyzed with EBSD due to the large amount of time required for sample preparation and the associated EBSD data acquisition. Approximately 34 scans were

stitched together to yield Figure 4.38 and Figure 4.39, which include the HAZ and TMAZ in both the RS and AS and the SZ. The HAZ for both PWHTs showed no detectable change in the microstructure. The AS TMAZ/SZ interface in PWHT heat treated at 200°C/10h appeared more refined and had a different texture than the as-welded condition seen in Figure 4.9. In the SZ near the AS TMAZ, the onion rings appear more diffuse in the 200°C/10h PWHT in that the purple/blue and green texture banding was not as sharp as those observed in the as-welded condition in Figure 4.9. In the center of the SZ, the grains are more refined and the heterogenous growth observed in the as-welded condition was not observed. In the SZ leading into the TMAZ on the RS, the microstructure was more refined than observed in the as-welded condition. Similar observations were made for the 247°C/2h heat treated PWHT for the advancing side TMAZ and the SZ center. The retreating side TMAZ was wider with more visible grains than that for the 200°C/2h heat treated PWHT.

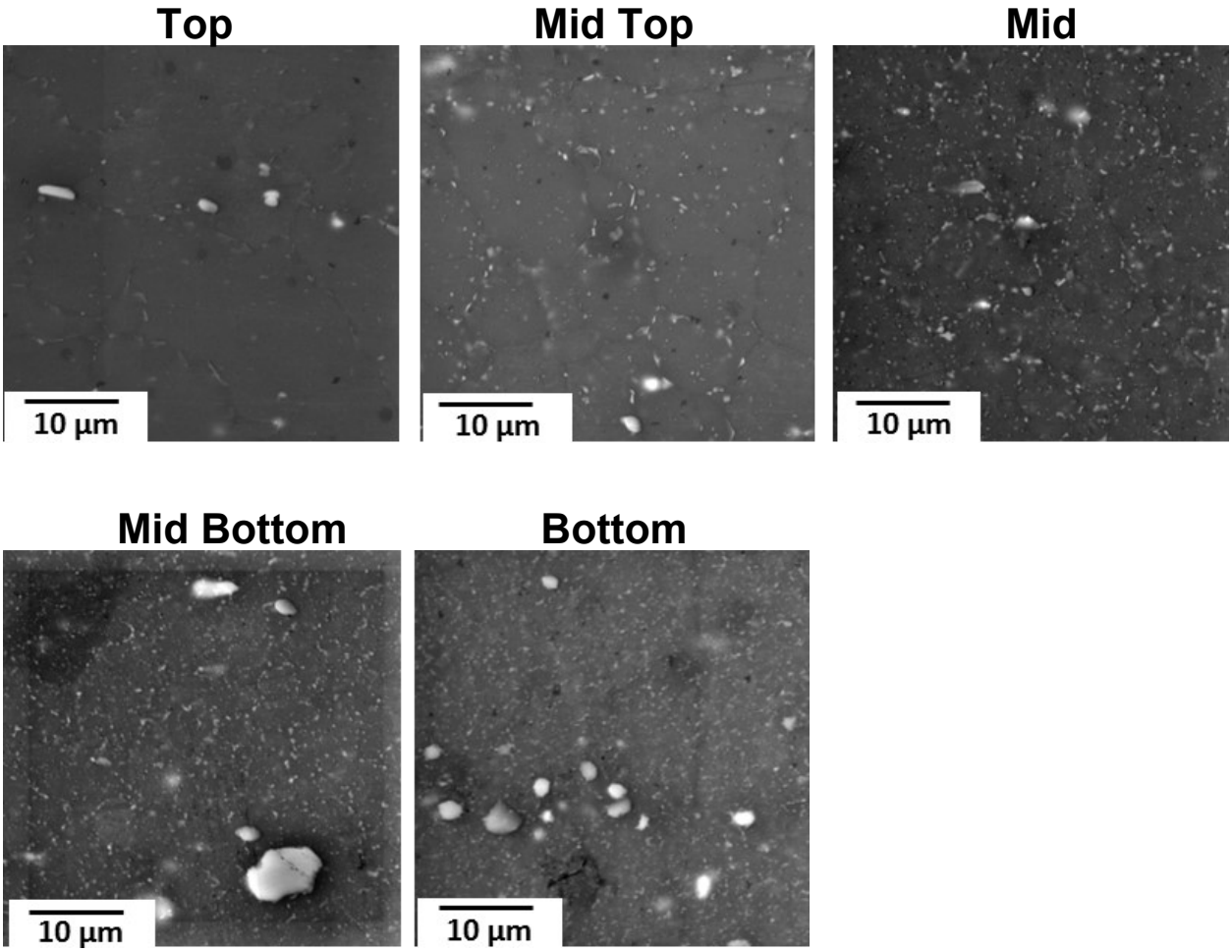

Figure 4.32. SE SEM photomicrographs of the microstructure through the depth of the SZ of the constant-speed FSW PWHT heat treated at 200°C for 10 hrs.

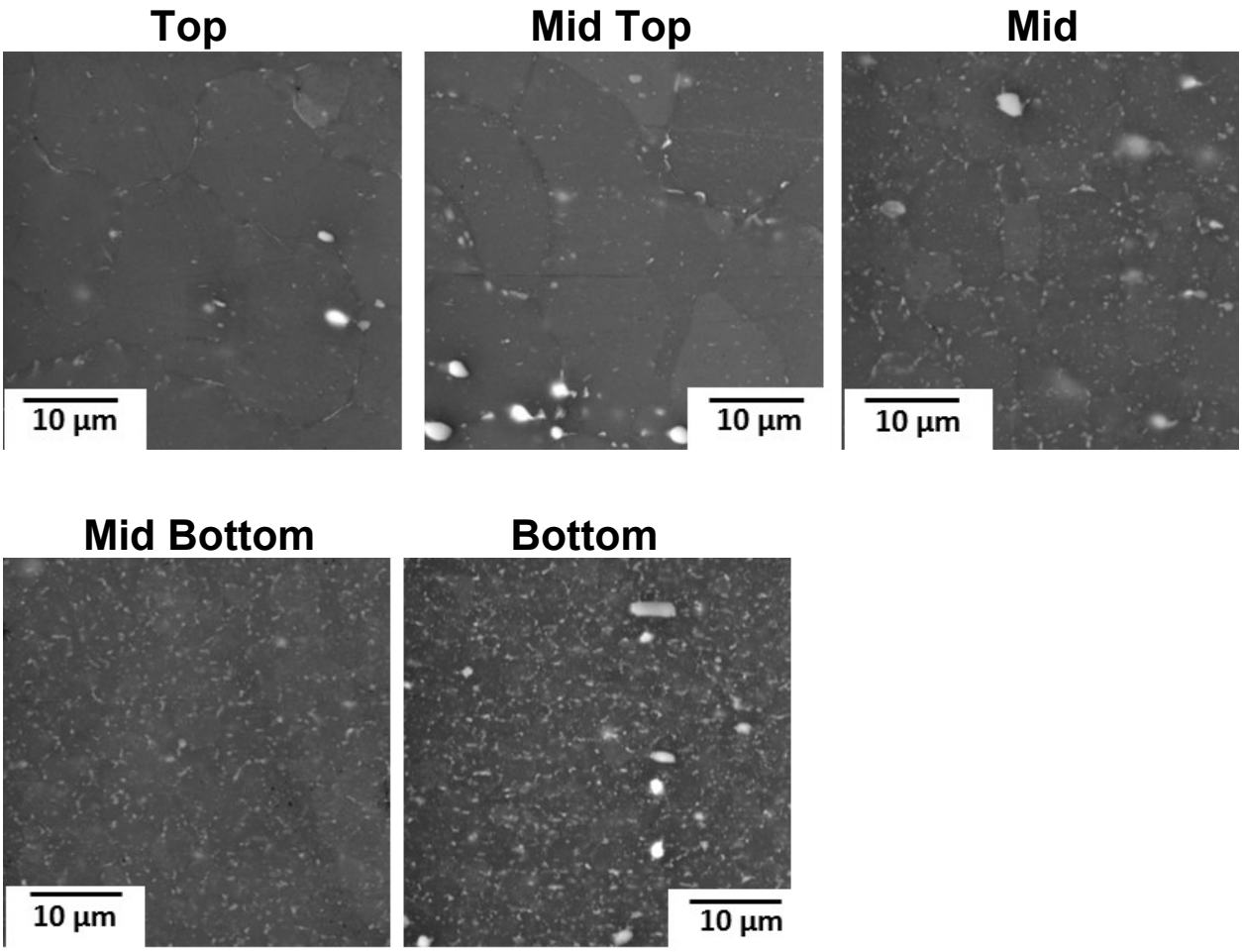

Figure 4.33. SE SEM photomicrographs of the microstructure through the depth of the SZ of the constant-speed FSW PWHT heat treated at 247°C for 2 hrs.

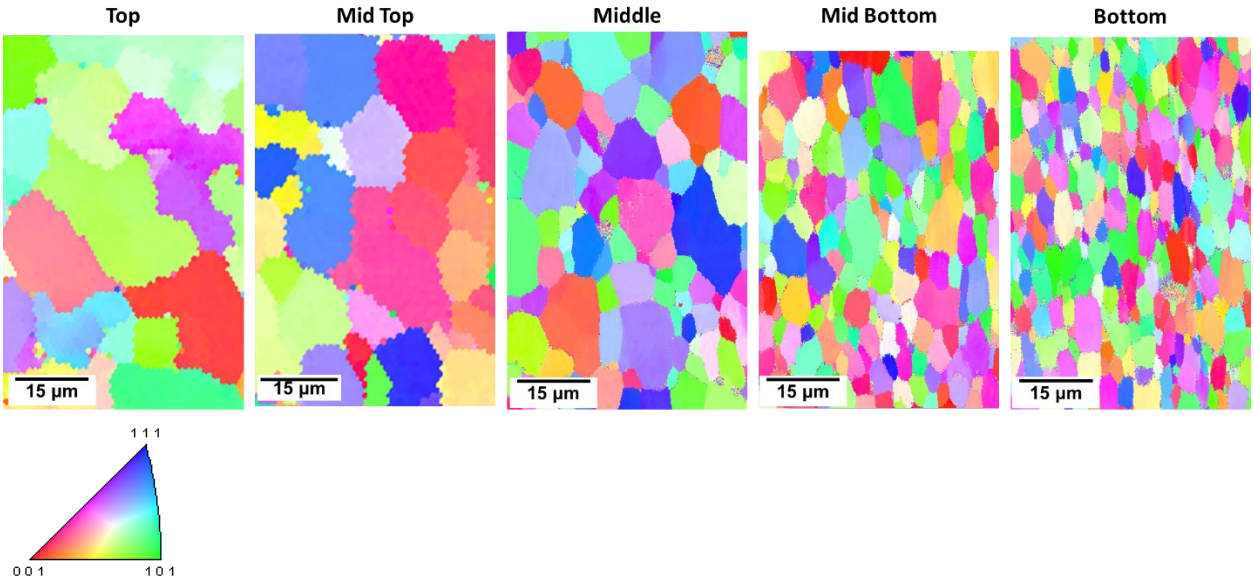

Figure 4.34. EBSD orientation maps showing the variation in grain size through the depth of the 247°C/2h PWHT at the top, mid top, middle, mid bottom, and bottom.

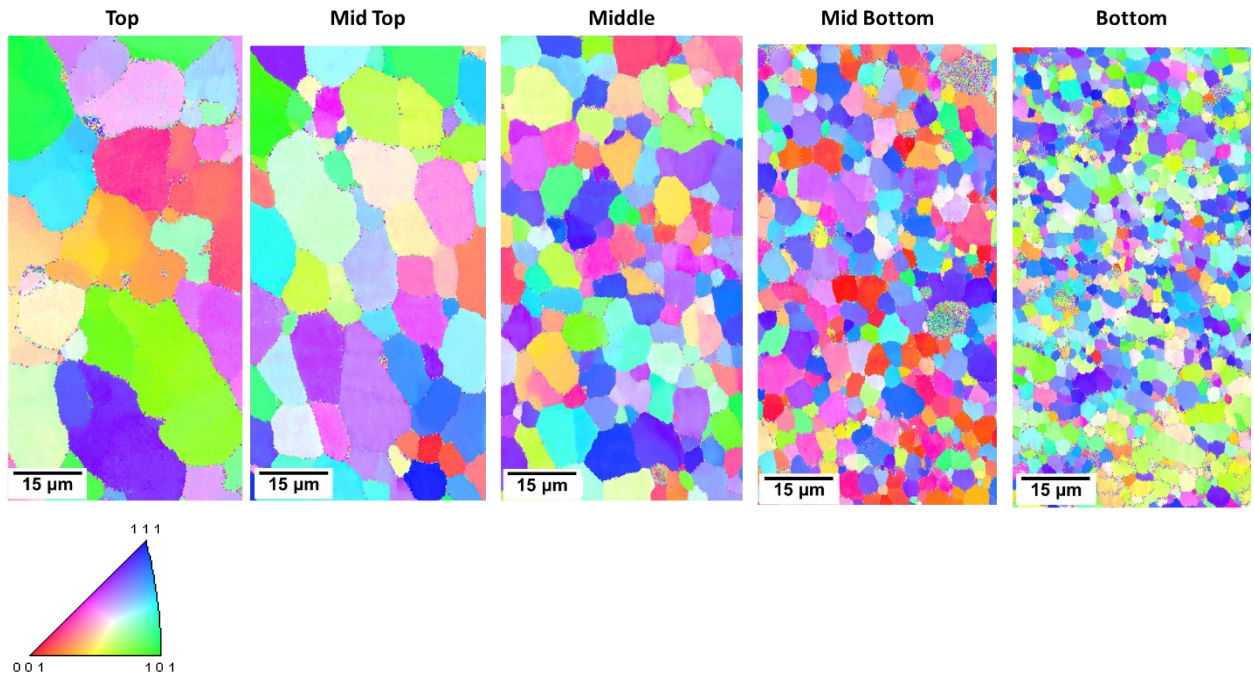

Figure 4.35. EBSD orientation maps showing the variation in grain size through the depth of the 200°C/10h PWHT at the top, mid top, middle, mid bottom, and bottom.

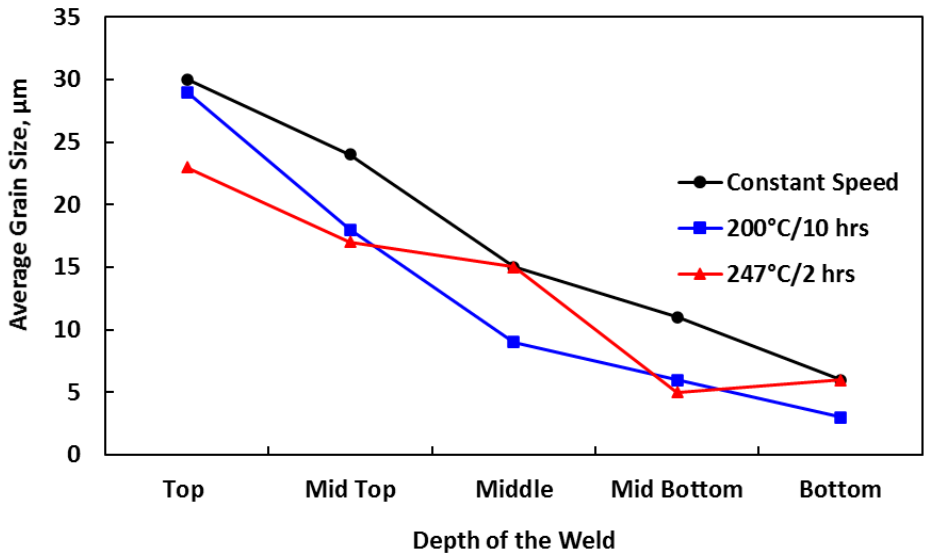

Figure 4.36. Average grain size versus the depth of the as-welded and post weld heat treated FSWs.

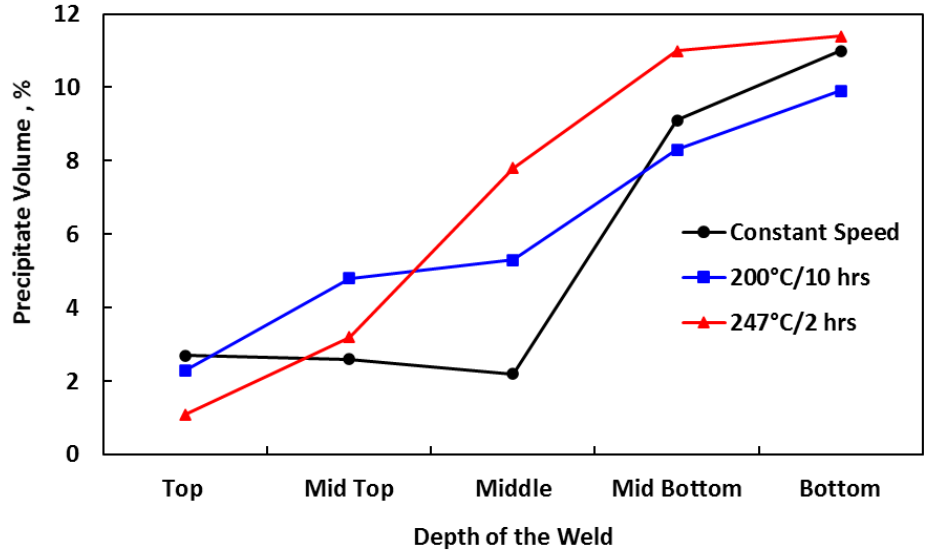

Figure 4.37. Precipitate volume versus the depth of the as-welded and post weld heat treated FSWs.

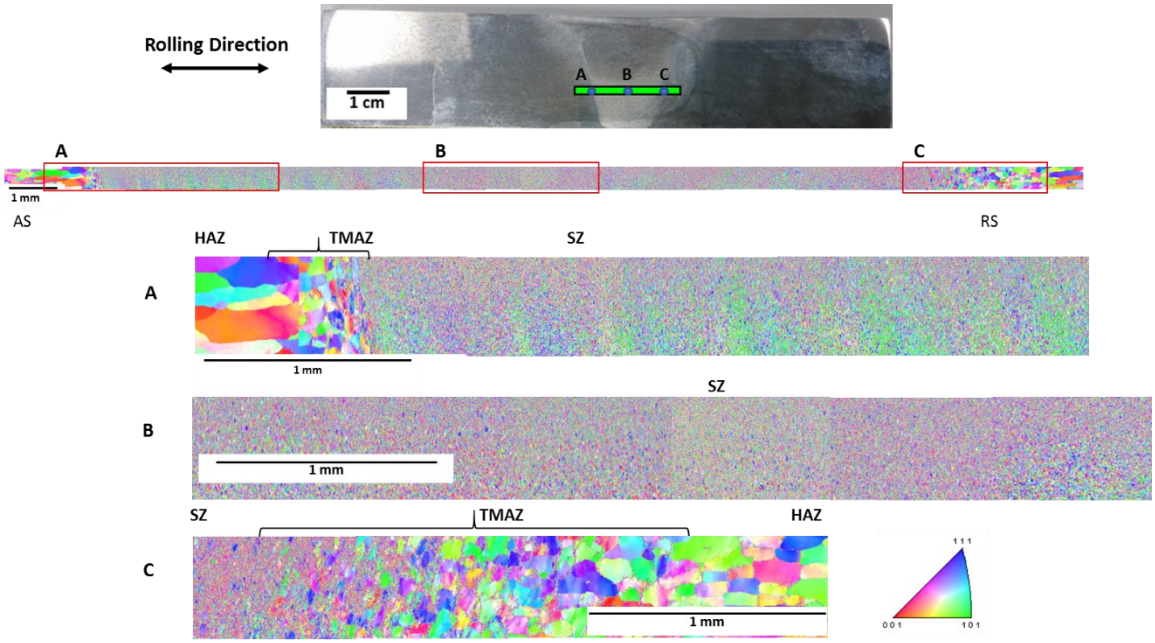

Figure 4.38. EBSD orientation maps of the PWHT (200°C/10h) FSW cross section 10 mm from the bottom edge of the sample, as shown in the green box macroetched image. The top row is a continuous montage of many individual scans, some of which are provided in higher magnification below in A) to C). A) The AS of the weld is shown. High magnification maps are shown of the HAZ, TMAZ, and SZ. B) The center of the SZ is shown. C) The RS of the weld is shown with high magnification maps of the SZ, TMAZ, and HAZ. The IPF color coded FCC unit triangle is based upon the sample normal direction.

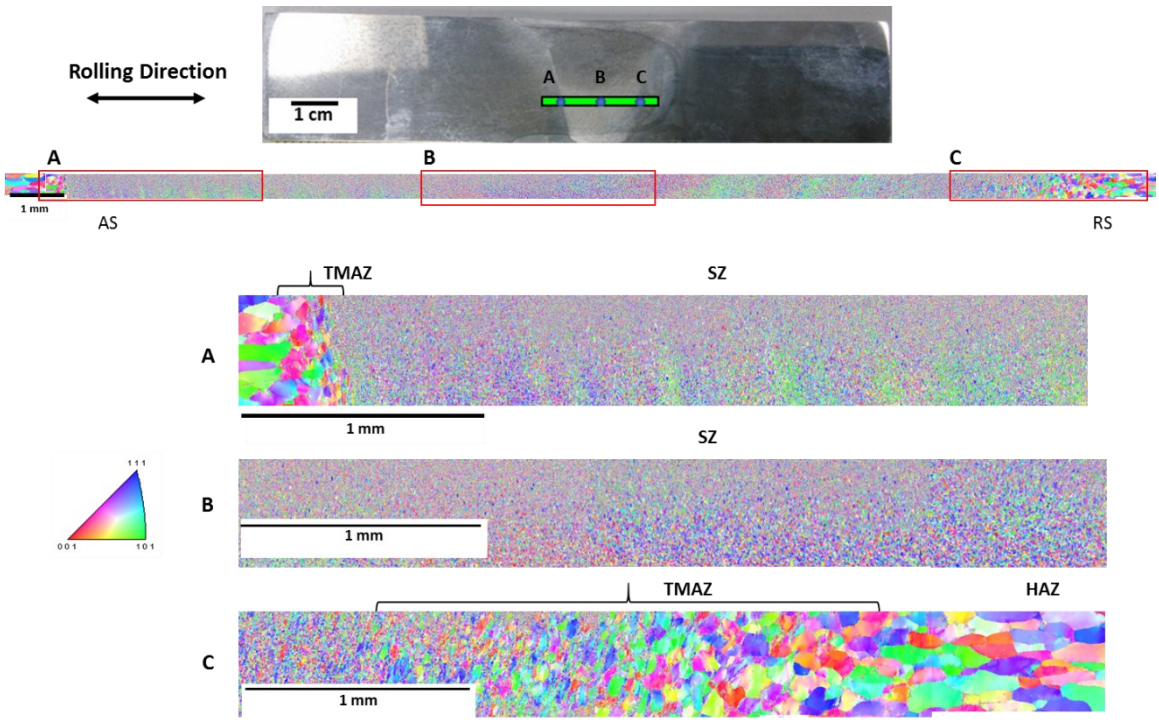

Figure 4.39. EBSD of the PWHT (247°C/2h) FSW cross section 9 mm from the bottom edge of the sample, as depicted in the macroetched image. The top row is a continuous montage of many individual scans, some of which are provided in higher magnification below in A) to C). A) The AS of the weld is shown. High magnification maps are shown of the TMAZ, and SZ. B) The center of the SZ is shown. C) The RS of the weld is shown with high magnification maps of the TMAZ, and HAZ. The IPF color coded FCC unit triangle is based upon the sample normal direction.

Consistent with the as-welded condition, the average grain size of the PWHTs decreased through the depth of the SZ for both the PWHTs at 200°C/10h and 247°C/2h. Unstable grain growth was not expected due to the lower heat treatment temperatures which were below the solutionizing temperatures. Heat treatment at elevated temperatures closer to the solutionizing temperature or at $T>0.5T_m$ facilitates unstable grain growth by means of secondary recrystallization, otherwise known as abnormal grain growth [91]. Secondary recrystallization has been observed to start at the onion rings, which are comprised of repetitive alternating dislocation densities, grain sizes, and textures which may be different than the remainder of the SZ [91]. The EBSD orientation maps of the SZ cross section depicted in Figure 4.9, Figure 4.38, and Figure

4.39 demonstrate the alternating textures of the onion rings for FSWs in the as-welded, 200°C/10h and 247°C/2h conditions. Although secondary recrystallization was not observed as a result of the PWHT, differences in the average grain sizes were observed when compared to the as-welded FSW.

The average grain size of the 200°C/10h PWHT was smaller than the as-welded condition at all depths of the thickness except the top of the SZ. The average grain size of the 247°C/2h PWHT was smaller than the as-welded condition at the top, mid-top, and middle of the SZ. Although the heat treatment temperatures were not hot enough to facilitate grain boundary movement or grain growth, it is also impossible for a reduction in average grain size to occur without the nucleation of or transition to a new matrix phase. Thus, it is assumed that the differences in grain size to the as-welded sample are due to differences in the welding temperature, which was unknown. This presents a strong case for constant-temperature FSW, which, if cooling rates are the same, provides an objective method to study the effects of specific FSW temperatures on the microstructure and post welding processes of precipitation-strengthened Al-Cu-Mg-Ag alloy.

The precipitate volume percent increased through the depth of the SZ, which was also consistent with the as-welded condition. When each layer through the depth of the weld is compared to the as-welded condition and to the other PWHT, it becomes evident that the issue of inconsistent welding temperature has also affected the precipitate volume. For instance, if we assume that a treatment at 247°C for 2 hrs is sufficient to coarsen the equilibrium θ phase, then the increase in the precipitate volume percent at the mid top, middle, and mid bottom layers is explained. The slight increase in precipitates at the bottom of the weld suggests that the concentration of solute alone is insufficient for precipitate coarsening. The precipitate volume at

the weld top, however, is less than the as-welded condition, which does not follow the precipitation kinetics of this alloy that states that the equilibrium θ phase is the final transformation. Thus, an increase in precipitate volume percent should have been observed instead of a decrease.

4.2.5.2 Hardness

Vickers hardness testing was performed across the transverse cross section of the PWHT samples heat treated at 200°C/10h, 247°C/0.5h, 247°C/0.9h, and 247°C/2h in five areas through the thickness of the weld, as seen in Figures 4.41 to 4.44. The as-welded condition is provided as reference for Vickers hardness acquired using a 0.1 kgf load (HV0.1) in Figure 4.40. The maximum hardness values in the SZ are recorded in Table 4.10. The negative values on the x-axis represent the advancing side of the weld and the positive values represent the retreating. For all four PWHTs, the BM hardness decreased. In the 200°C/10h PWHT, the localized hardness in the mid top of the SZ increased. The top remained the same but had a similar hardness to the heat treated BM. The middle exhibited a slight reduction in hardness by 2HV and the mid bottom and bottom decreased more significantly by 8HV. The difference in peak hardness between the mid top and middle was 24HV. This is higher than the 10HV difference observed in the as-welded material.

The 247°C heat treated samples all exhibited general reductions in peak hardness through the depth of the SZ compared to the 200°C/10h PWHT and the as-welded condition. The one exception to this observation was the SZ mid top for 247°C/0.5h, which increased in hardness by 8HV from the as-welded, although it was lower than the equivalent region of the 200°C/10h sample by 6HV. The 247°C/2h heat treated samples exhibited the lowest hardness values. The difference in peak hardness between the mid top and middle was 27HV, 23HV, and 23HV for the heat treated 247°C/0.5h, 247°C/0.9h, and 247°C/2h samples, respectively. This demonstrated that the distinction in mechanical properties between the upper and lower weld nuggets increased from

the as-welded state. The BM hardness for the 247°C/0.5h heat treated samples was similar to that of the 200°C/10h heat treated samples while prolonged treatment at 247°C exhibited a drop by approximately 20HV compared with the 200°C/10h and 247°C/0.5h heat treatments.

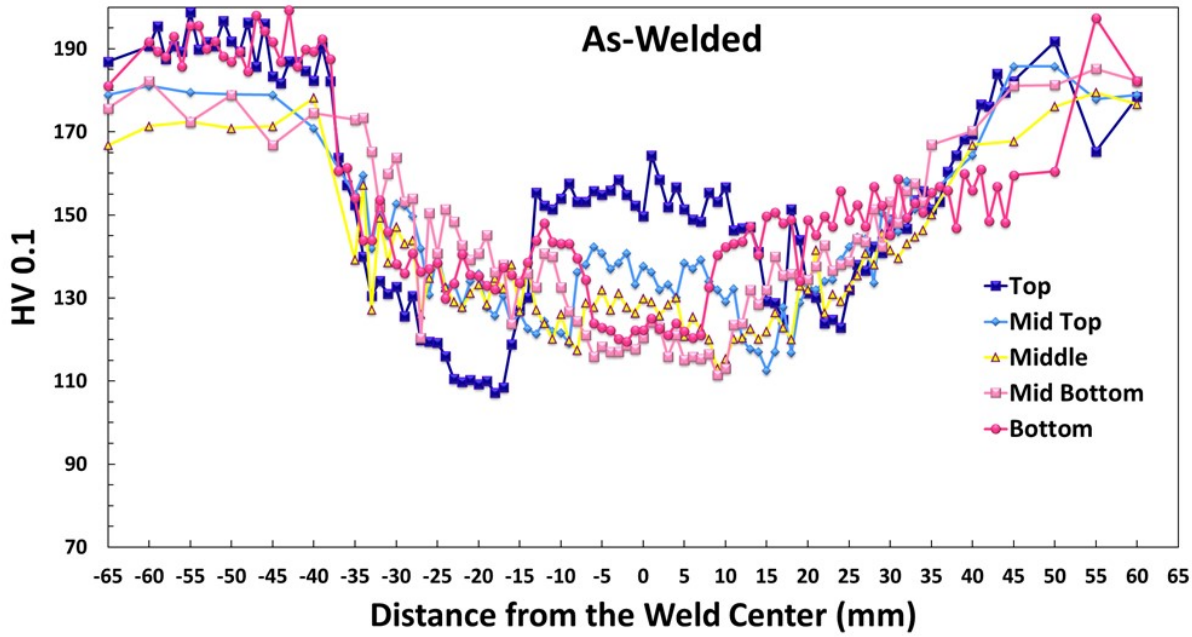

Figure 4.40. Vickers hardness plot through the thickness for the constant-speed, as-welded FSW. Hardness data was acquired using a 0.1 kgf load (HV0.1).

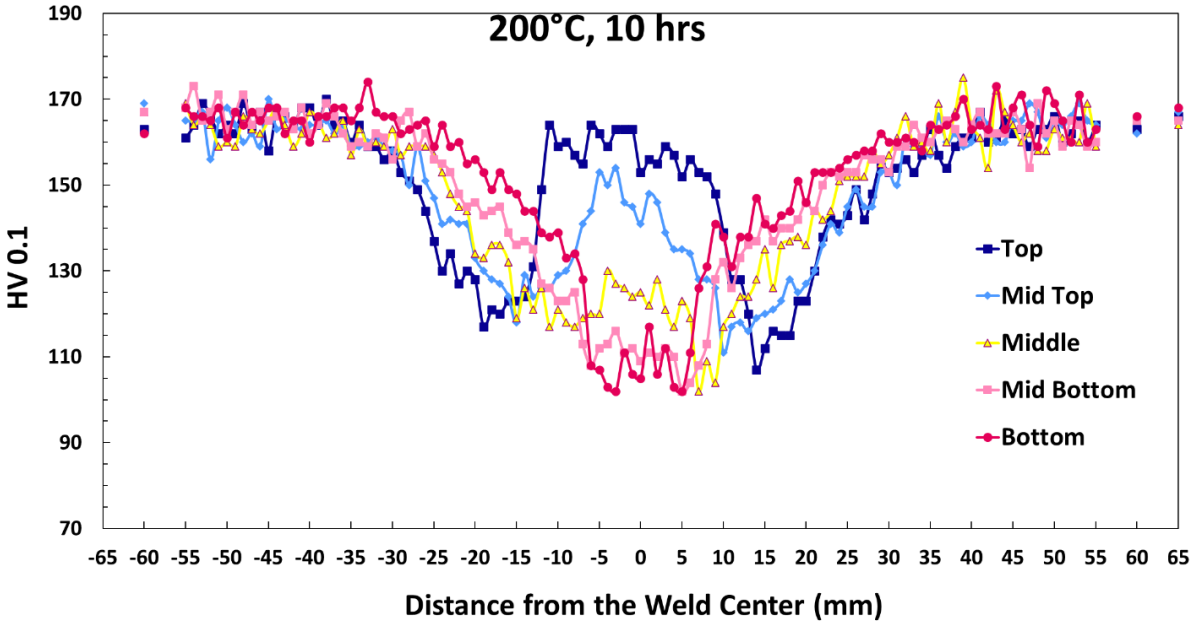

Figure 4.41. Vickers hardness plot through the thickness of the weld for the constant-speed FSW PHWT at heat treated at 200°C for 10 hrs.

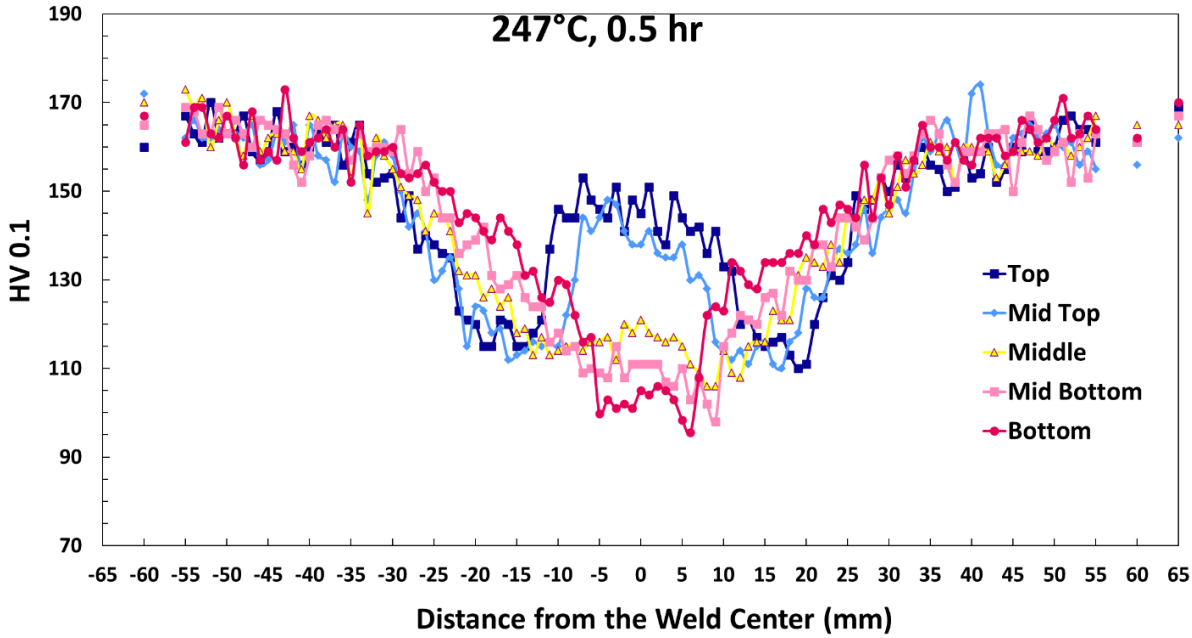

Figure 4.42. Vickers hardness plot through the thickness of the weld for the constant-speed FSW PHWT heat treated at 247°C for 0.5 hr.

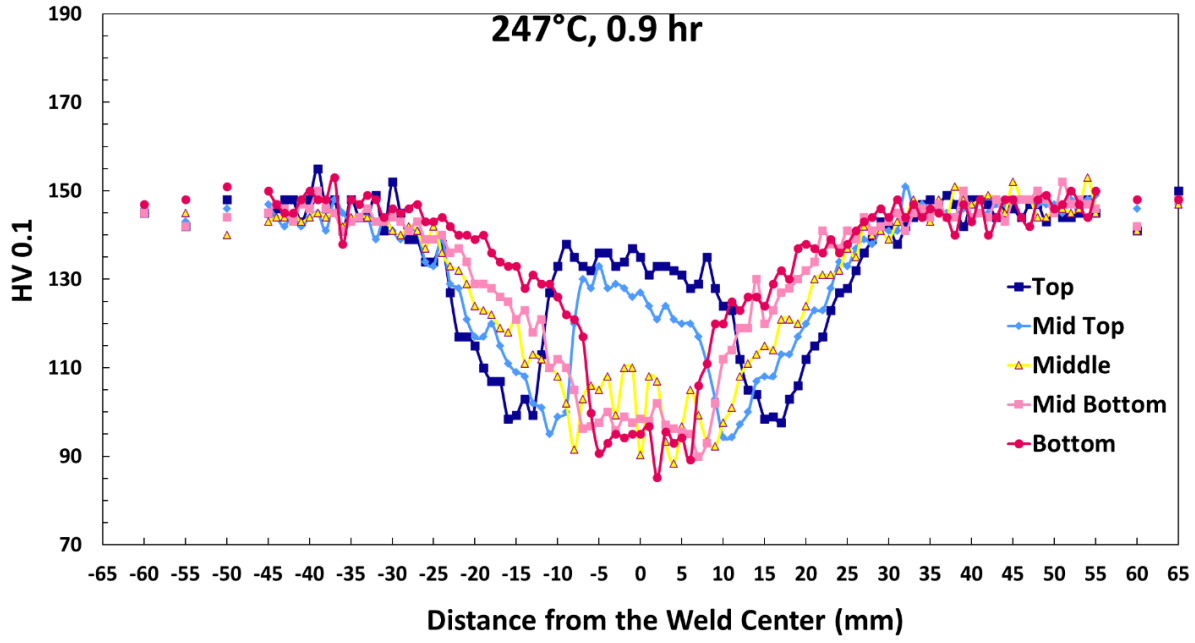

Figure 4.43. Vickers hardness plot through the thickness of the weld for the constant-speed FSW PHWT heat treated at 247°C for 0.9 hr.

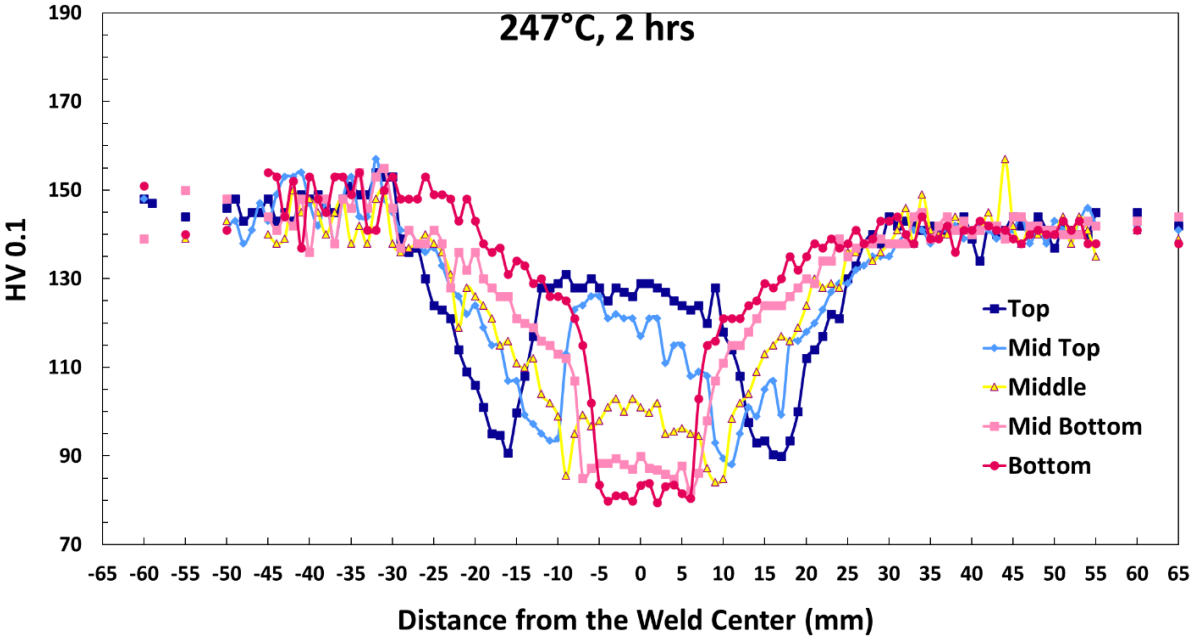

Figure 4.44. Vickers hardness plot through the thickness of the weld for the constant-speed FSW PHWT heat treated at 247°C for 2 hrs.

Table 4.10. Maximum Vickers hardness values through the depth of the stir zone for the constant-speed as-welded and PWHT FSWs.

	Top	Mid Top	Middle	Mid Bottom	Bottom
As-welded	164	142	132	124	125
200°C/10h	164	154	130	116	117
247°C/0.5h	153	148	121	115	106
247°C/0.9h	138	133	110	112	97
247°C/2h	131	126	103	90	84

4.2.5.3 Tensile

Tensile tests performed in the TD on all four PWHT samples indicated that the properties varied. The engineering stress versus engineering strain curves are shown in Figure 4.45 and the YS, UTS, ε_f, and elastic modulus (E) are tabulated in

Table 4.11. The sample heat treated at 200°C/10h exhibited a higher YS than the as-welded state (Δ63 MPa) and the heat treatments at 247°C. The 200°C heat treatment marginally reduced the UTS by 6 MPa but significantly reduced the ε_f from 7.38% to 1.7%. Samples heat treated at 247°C exhibited both YS and UTS inferior to the as-welded state and the 200°C heat treatment. Heat treatment at 247°C for 0.5h resulted in the lowest YS and UTS, however, it exhibited the highest ε_f at 4.7%. Heat treatment for 0.9h resulted in a slighter better YS, UTS, and ε_f. PWHT at 247°C for 2h resulted in better YS and UTS, however, it exhibited the lowest ε_f at 3.3%. PWHT at 200°C/10h yielded the highest strengths, with the YS surpassing that of the as-welded, and also resulted in the lowest observed ε_f. The observed tensile strengths for the 247°C heat treatments were inconsistent with the measured Vickers hardness results, in that prolonged times generated reduction in hardness, but improvements to the tensile strength. All heat treatments exhibited a reduction in ε_f by at least 50% with the 200°C heat treatment providing the lowest ε_f.

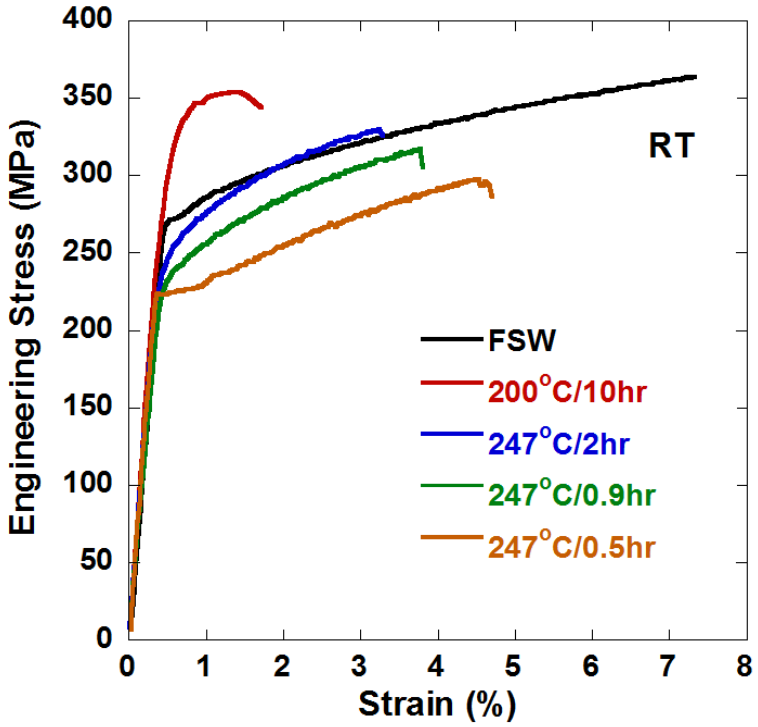

Figure 4.45. Room temperature engineering stress versus engineering strain curves of constant-speed FSW for as-welded and PWHT conditions. Samples were extracted from the middle of the weld.

Table 4.11. Tensile properties of the as-welded and PWHT FSW samples. Samples were extracted from the middle of the weld.

	FSW, RT	PWHT 200°C 10hrs	PWHT 247°C 0.5hr	PWHT 247°C 0.9hr	PWHT 247°C 2hrs
UTS (MPa)	360	354	298	317	330
YS (MPa)	272	335	223	233	256
ε_f (%)	7.38	1.7	4.7	3.8	3.3
E (GPa)	61.1	69.8	66.4	55	64.5

4.2.5.4 Discussion of the Mechanical Behavior of PWHT

The three PWHTs at 247°C did not yield an overall increase of the hardness and tensile

strength when compared to the as-welded, constant-speed FSW. However, the 200°C/10h heat treatment exhibited higher hardness than the other heat treatments as demonstrated in the Vickers hardness plot and maximum peak hardness table in Figure 4.41 and Table 4.10 The maximum hardness at the top and mid top of the PWHT 200°C/10h remained the same or increased, which may indicate that the nucleation of the strengthening precipitates, θ' and Ω, occurred. Another localized improvement in hardness was observed in the mid top of 247°C/0.5h, but a decrease was observed at the weld top. Both hardness values are less than that of 200°C, which indicates that 247°C is too high of a temperature. Prolonged times at 247°C also led to further decreases in hardness with 247°C/2h exhibiting the lowest hardness values.

The difference in hardness between the UWN and the LWN became more pronounced with each heat treatment. Based on these results, a clear advantage for PWHT was not obtained.

The tensile strengths of the samples subjected to the PWHTs followed a similar trend as the hardness tests, in that with increasing heat treatment temperature and time, the strengths decreased. The one exception to this is tensile sample heat treated at 200°C/10h where the YS increased and the UTS was similar to the as-welded sample. It was originally hypothesized that heat treatments at 247°C would favor precipitate growth/coarsening, whereas PWHT at 200°C would favor less precipitate growth. Based on the tensile and hardness results, little precipitation growth was observed in the UWN at temperatures $T_{PWHT} \leq 200°C$. This is due to the higher welding temperatures and slower cooling rate at the UWN, which resulted in increased solute concentration in that region. Lower welding temperatures coupled with faster cooling rates at the LWN would promote precipitate growth of the equilibrium θ precipitate as discussed in section 4.2.1.

The mechanical behavior demonstrated that none of the PWHT improved the overall

hardness and tensile strength of the weld. The hypothesis that subjecting the constant-speed FSW materials to the prescribed PWHTs to increase their strengths was disproved for a 25 mm thick Al-Cu-Mg-Ag alloy. No significant benefits to the mechanical behavior were observed. Thus, it is believed that non-equilibrium microstructures were maintained after the prescribed PWHTs and this resulted in only slight changes in the mechanical properties. Utilizing a TTT curve to inform PWHT temperatures requires knowledge of the heating and cooling of the welding process in order to understand the as-welded microstructure. This is necessary in order to apply a heat treatment temperature and time for a predicted transition in microstructure to for expected improvements in specific mechanical properties such as tensile strength and hardness. This is especially true for thick plates, which have steep temperature gradients, competing heat transfer modes, and yield various microstructures through the thickness of the weld.

4.3 Effects of Constant-Temperature FSW

Constant-temperature FSW was performed on 25 mm thick AA2139-T8 to assess the effects of welding temperature on the microstructure and the mechanical properties. Quantitative and qualitative results are presented with respect to the characterization of the microstructure and mechanical behavior for the constant-temperature FSW process. Optical microscopy and SEM were used to characterize the microstructure. Vickers hardness and tensile experiments were employed to assess the mechanical behavior. Qualitative and quantitative data concerning the weld zones, the through thickness variation in microstructure, and precipitate phases are presented and discussed. Through depth thickness of the weld (top, mid top, middle, mid bottom, and bottom) are consistent with the constant-speed FSW layers, as shown in Figure 4.10. The microstructure and the mechanical behavior are discussed.

4.3.1 Microstructure

The macroetched transverse cross section of the constant-temperature welds are shown in

Figure 4.46b-d. In Figure 4.46a, the dark and light contrast in the SZ represents the UWN and the LWN, respectively. Based on this observation, the UWN and LWN were not observed in the SZ of the 490°C constant-temperature FSW, unlike that for the constant-speed FSW. This is consistent with the variations observed in the hardness and tensile properties to be described later. In the SZ of FSW/500°C, the contrast difference between the upper and lower regions, as shown in Figure 4.46c, indicates the formation of the UWN and LWN. This is supported by the increased precipitate volume percent observed in the lower half of the constant-speed FSW. Transverse bands-like protrusions emanating from the AS of the SZ can also be observed in Figure 4.46c. The transverse bands seem to be similar to that of the onion rings seen in the constant-speed weld (Figure 4.46a) in that they are reflective of the tool rotation. The TMAZ is also more recognizable in this sample, as the width of the zone is wider than that of the constant-speed and FSW/490°C. The SZ of FSW/510°C, as seen in Figure 4.46d, does not appear to have the UWN and LWN, but similar to FSW/500°C, the traverse bands at the bottom half of the SZ emanates from the AS. The upper half of the SZ near the crown of the weld is pinched which indicates increased material flow around the tool where the tool pin and shoulder interface is located.

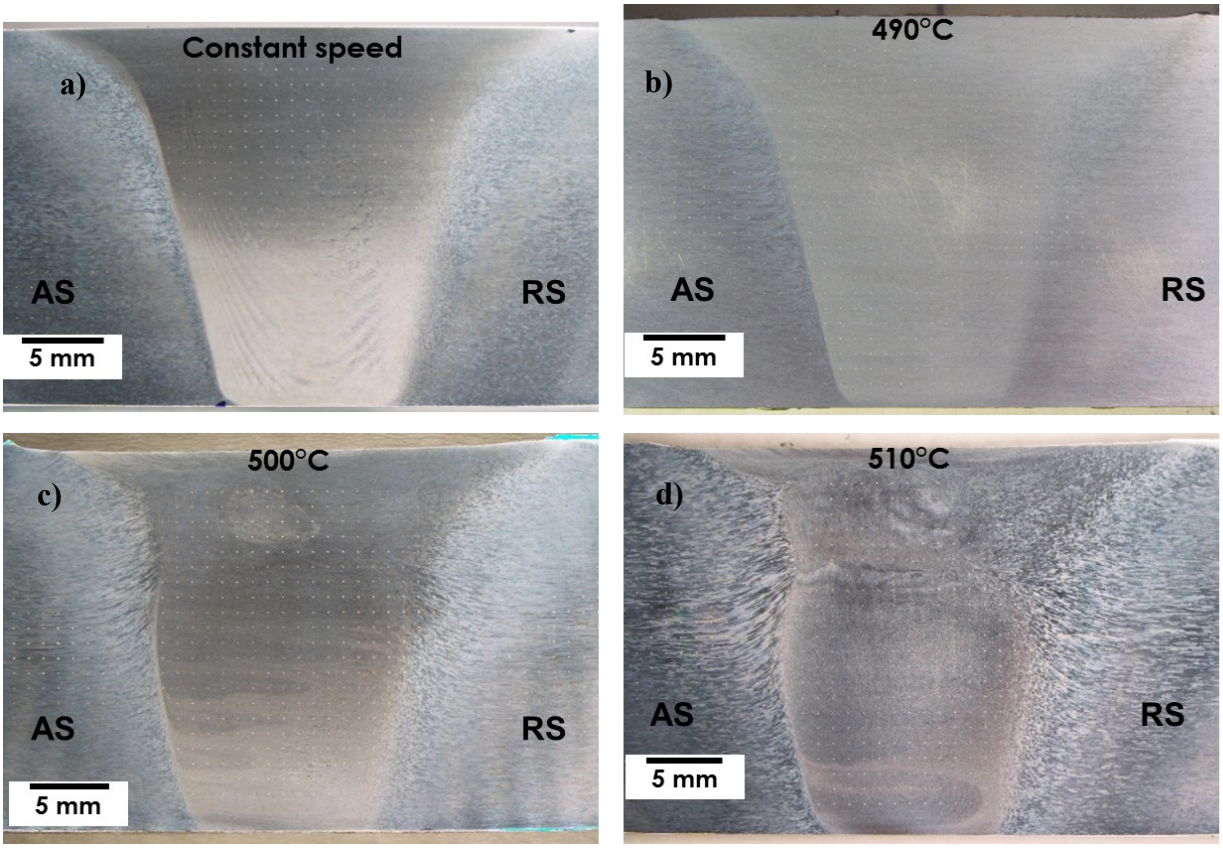

Figure 4.46. Optical macrograph of the etched a) constant-speed FSW and constant-temperature FSWs at b) 490°C, c) 500°C, and d) 510°C in the transverse cross section. Small dots are indents from the Vickers hardness test. The advancing side is on the left.

Table 4.12. Average grain size through the depth of the FSWs. Constant-speed FSW is provided for comparison.

	Stir zone average grain size, μm				
FSW Process	**Top**	**Mid Top**	**Middle**	**Mid Bottom**	**Bottom**
Constant Speed	30.0	24.0	15.0	11.0	6.0
FSW/490C	3.7	3.4	3.1	2.6	2.4
FSW/500C	12.7	11.4	9.2	6.4	3.3
FSW/510C	12.6	8.1	9.9	9.9	6.8

Table 4.13. Measured precipitate volume percent through the depth of the constant-temperature FSW materials. The constant-speed FSW measurements are provided for comparison.

	Stir zone area precipitate volume percent, %				
FSW Process	**Top**	**Mid Top**	**Middle**	**Mid Bottom**	**Bottom**
Constant Speed	2.70	2.60	2.20	9.10	11.00
FSW/490C	7.16	8.89	10.50	9.22	10.40
FSW/500C	1.8	3.21	3.9	5.15	6.75
FSW/510C	3.43	3.03	3.19	3.71	4.03

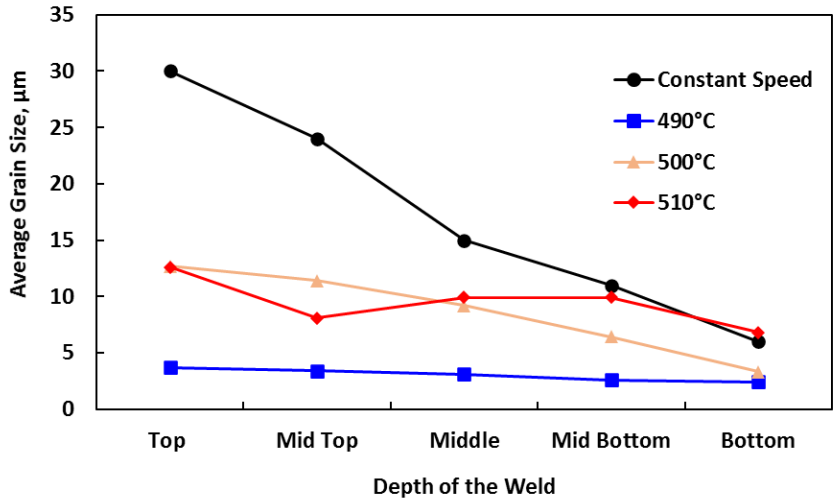

Figure 4.47. Average grain size throughout the depth of the weld for the constant-temperature and constant-speed FSWs.

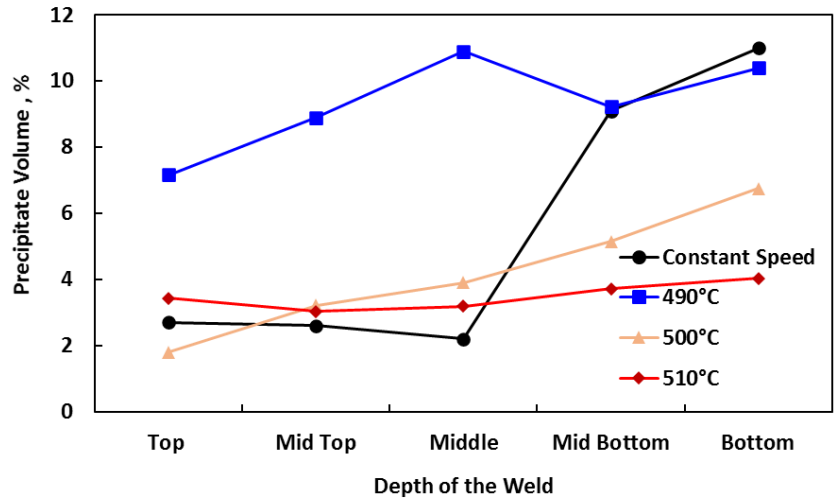

Figure 4.48. Average precipitate volume percent throughout the depth of the weld for the constant-temperature and constant-speed FSWs.

The microstructure in the SZ varied through the depth of the weld. SE SEM photomicrographs of the SZ show a gradient in both the grain size, and the precipitate size and distribution through the thickness of the SZ at the top, mid top, middle, mid bottom, and bottom for all constant-temperature FSWs, shown in Figure 4.49 to Figure 4.51. The average grain sizes and precipitate volume percents are listed in Table 4.12 and Table 4.13 and the comparative plots are shown in Figure 4.47 and Figure 4.48 for the constant-temperature FSWs, with the constant-speed FSW provided for comparison. The average grain size decreased from the top of the weld to the bottom of the weld for FSW/490°C and FSW/500°C. The average grain size in FSW/510°C decreased from the top of the weld through the mid top. The average grain size increased at the middle and mid bottom, then decreased at bottom. The precipitate volume percent increased from the top of the weld towards the bottom of the weld in FSW/490°C, with the exception of a local decrease in precipitate volume measured at the mid bottom. The precipitate volume consistently increased from the top of the weld to the bottom at FSW/500°C. FSW/510°C exhibited local decreases in the precipitate volume at the mid top and middle of the weld. For all conditions, the grains were larger at the top and smaller at the weld root and the precipitate volume was lower at the top and greater at the bottom. The distribution and morphology of the precipitates also differed between the top of the weld and the bottom. At the top, the precipitates at the GBs were either thin and continuous or spherical. Towards the bottom of the weld, the precipitates varied in shapes and were distributed both at the GBs and within the grain interiors. The exception to this is FSW/490°C, where the precipitate distribution and morphology was consistent through the depth of the weld.

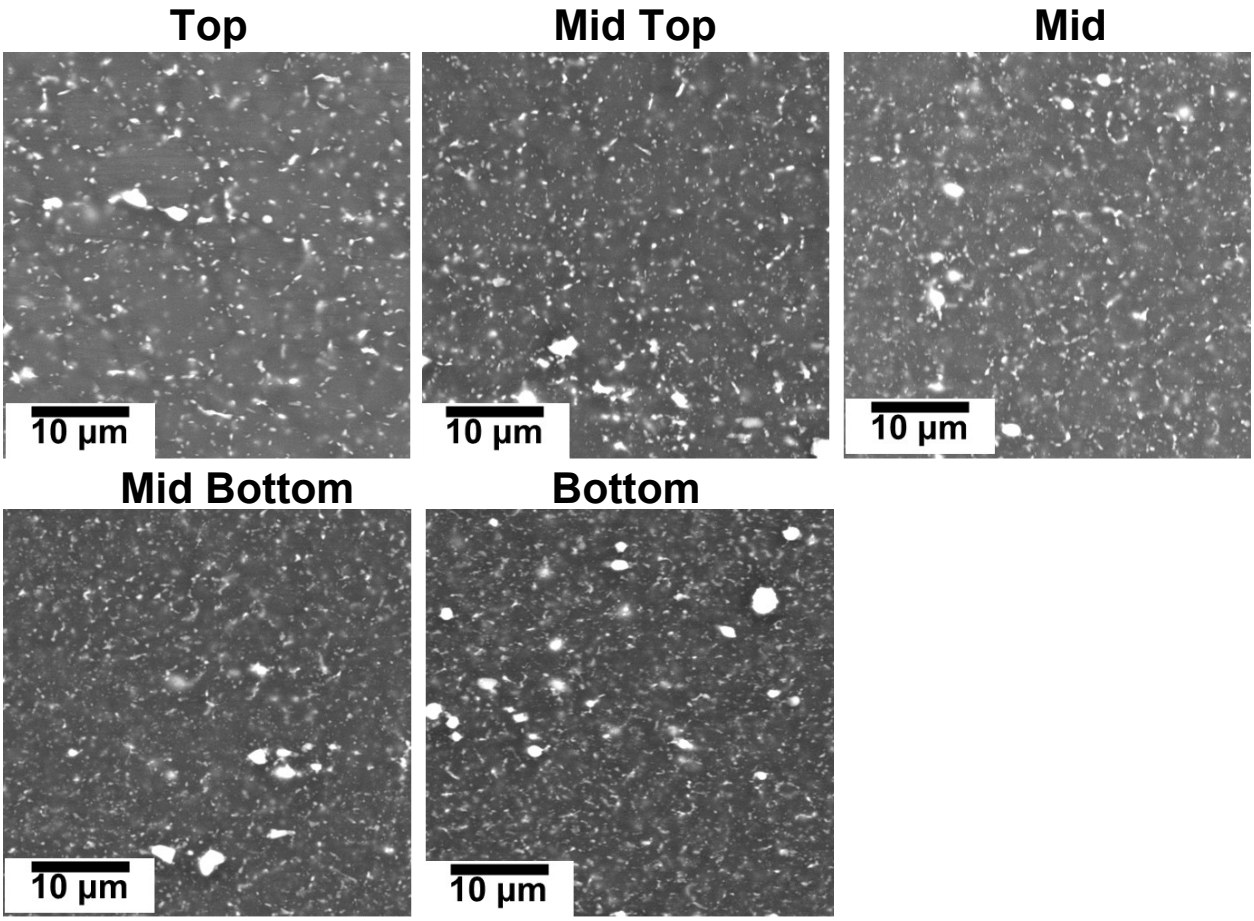

Figure 4.49. SE SEM photomicrographs of the microstructure through the depth of the SZ of the constant-temperature FSW at 490°C.

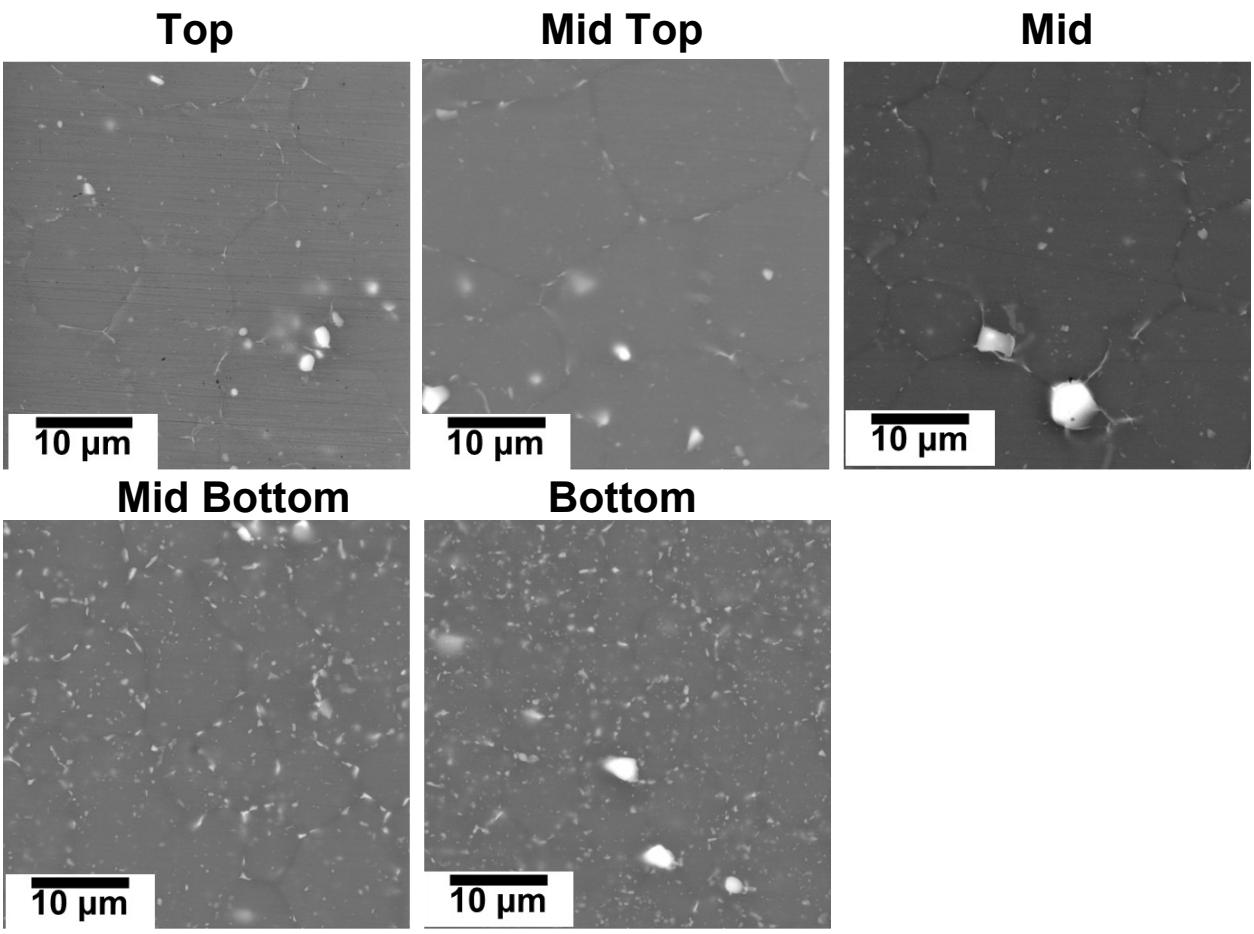

Figure 4.50. SE SEM photomicrographs of the microstructure through the depth of the SZ of the constant-temperature FSW at 500°C.

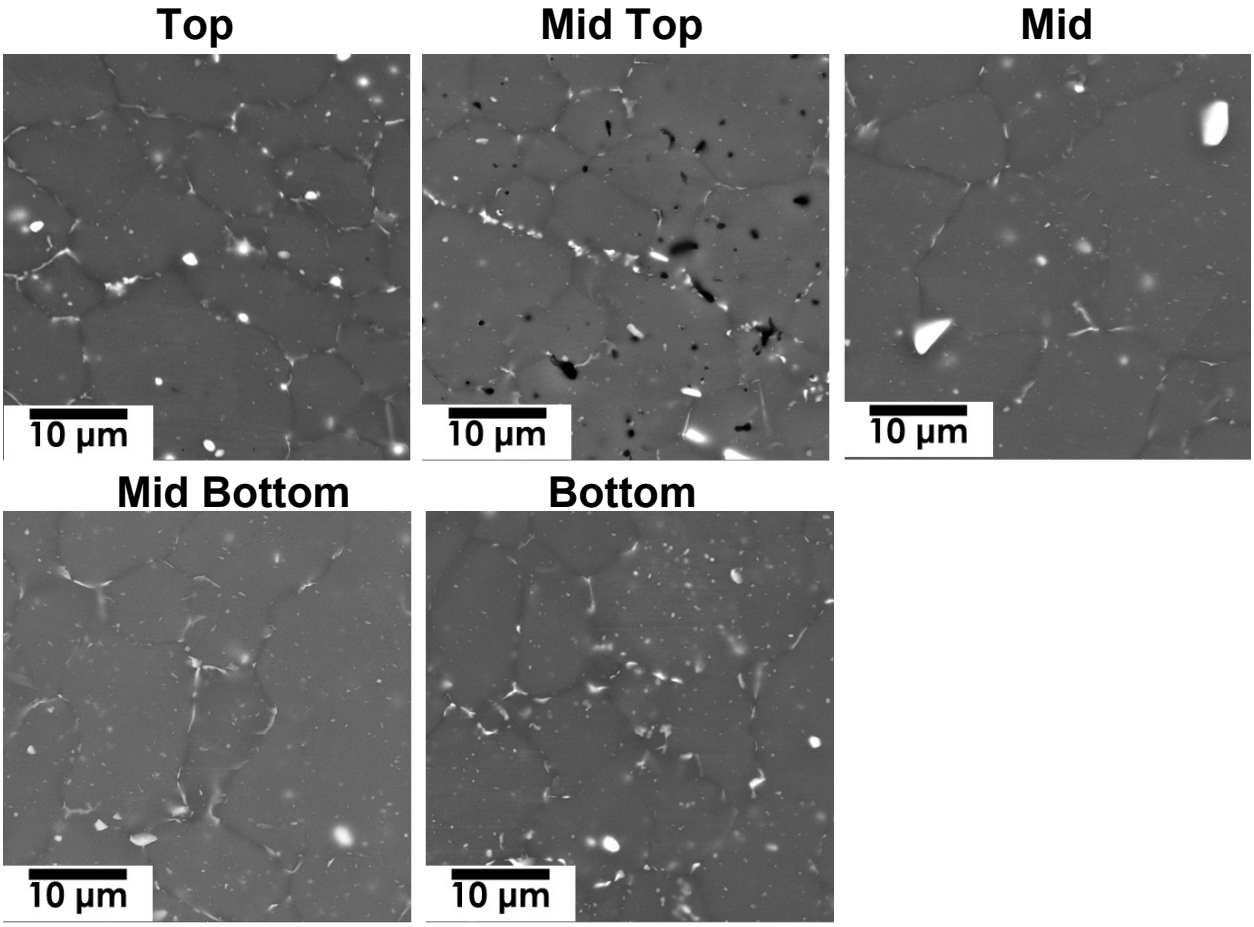

Figure 4.51. SE SEM photomicrographs of the microstructure through the depth of the SZ of the constant-temperature FSW at 510°C.

4.3.2 Effect of FSW Temperature on Microstructure Discussion

The effects of FSW temperature on the microstructure of 25 mm thick AA2139-T8 are discussed in this section. FSW was conducted at 490°C, 500°C, and 510°C. In all of the welds, there was a gradient in the microstructure; the average grain size decreased from the top of the weld to the bottom. In addition, the precipitate volume percent exhibited an inverse relationship, in that the precipitate volume increased from the top of the weld to the bottom. The results are consistent with the constant-speed FSW results discussed in section 4.2.1. This correlates to a gradient in welding temperature, with the top of the weld experiencing the highest temperature due

to a higher rotational speed of the tool shoulder. This is also correlated to the gradient in the cooling rate as explained in section 4.2.1. However, this does not fully address why the grain size increased for the constant-temperature 500°C FSW.

There are a couple of explanations for why the grain growth occurred for the constant-temperature 500°C FSW and not for the constant-temperature 490°C FSW. The first is that 490°C is insufficient for grain growth. The microstructure at 490°C exhibited refined grains and with a relatively high precipitate volume percent (7.16% at the top and 10.4% at the bottom). In the TEM images of the constant-speed FSW, coarse precipitates were found at the GBs. This could result in pinning GBs and therefore inhibit grain growth. On the other hand, 500°C may be sufficient for measurable grain growth in the times associated with FSW processing. At 500°C, the equilibrium θ was expected to be dissolving, based on the constant-speed FSW results, which would result in a reduced volume of precipitates that could potentially pin GBs, thereby allowing grain growth. This would also mean that the concentration of Cu-solutes in the solid solution increased, which results in solid-solution strengthening. The summary of the discussion of the grain growth is shown in Figure 4.52. In the next section, solid-solution strengthening in the UWN of the 500°C constant-temperature FSW is discussed.

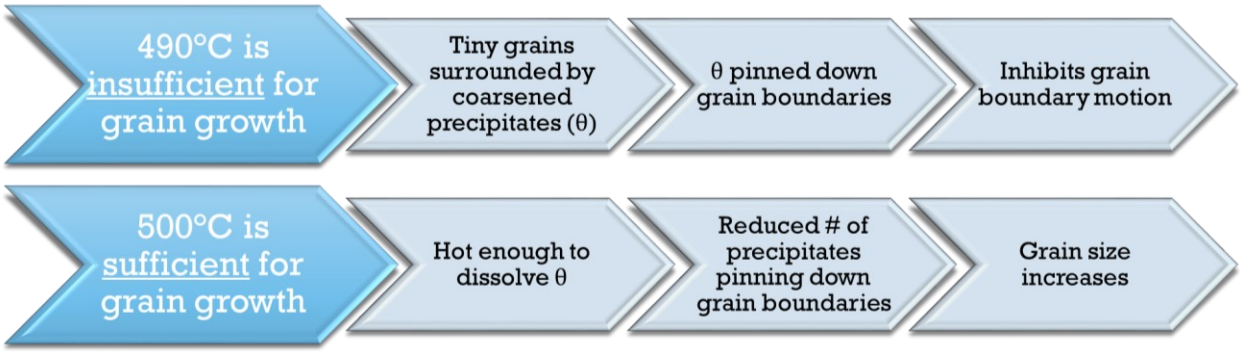

Figure 4.52. Summary of the cause of the grain growth observed in the 500°C constant-temperature FSW.

4.3.3 Hardness Behavior Results

Vickers hardness testing was performed across the transverse cross section of the constant-temperature welds—FSW/490°C, FSW/500°C, and FSW/510°C, similar to the constant-speed FSW. The superimposed hardness maps on the etched samples are shown in Figure 4.53 and a higher magnification images of the SZ is shown in Figure 4.54. The constant-speed FSW hardness map is provided in both figures for comparison to the constant-temperature FSWs.

Comparison of the hardness maps of each of the weld revealed differences in the average hardness. This is in contrast with the FSW/490°C weld, which exhibited a solid blue SZ indicating no UWN or LWN. The dark blue correlates to an average hardness of 100 throughout the thickness of the SZ. The FSW/500°C weld exhibited areas of higher hardness towards the upper half of the SZ and lower hardness towards the lower half. This implies the formation of an UWN and LWN for constant-temperature FSW when T>490°C. The SZ of the FSW/510°C was almost uniformly colored, and although there are bands of blue, there is no distinguishable presence of an UWN and LWN. In the upper half of FSW/500°C and FSW/510°C, there are some low hardness values indicated by blue pixels. These blue pixels are associated with voids in the top and mid top of the SZ are a result of the FSW process.

The HAZ of each weld was also qualitatively compared using Figure 4.53. The HAZ is bordered by the red and blue regions on the hardness maps. The width of the HAZ increased with increased temperature.

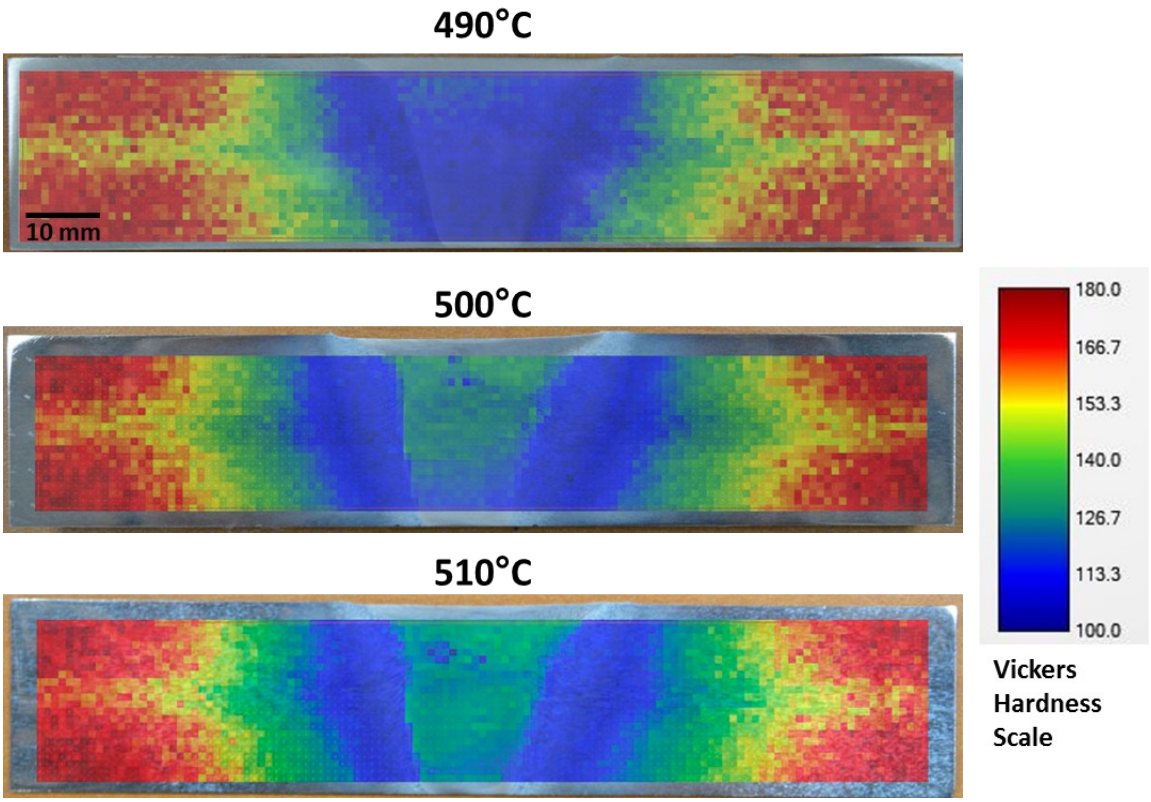

Figure 4.53. Vickers microhardness map across the transverse cross section of the constant-temperature FSWs. The scale bar is constant for all of the welds. Each pixel represents an 1 mm x 1 mm area. The advancing side is on the left.

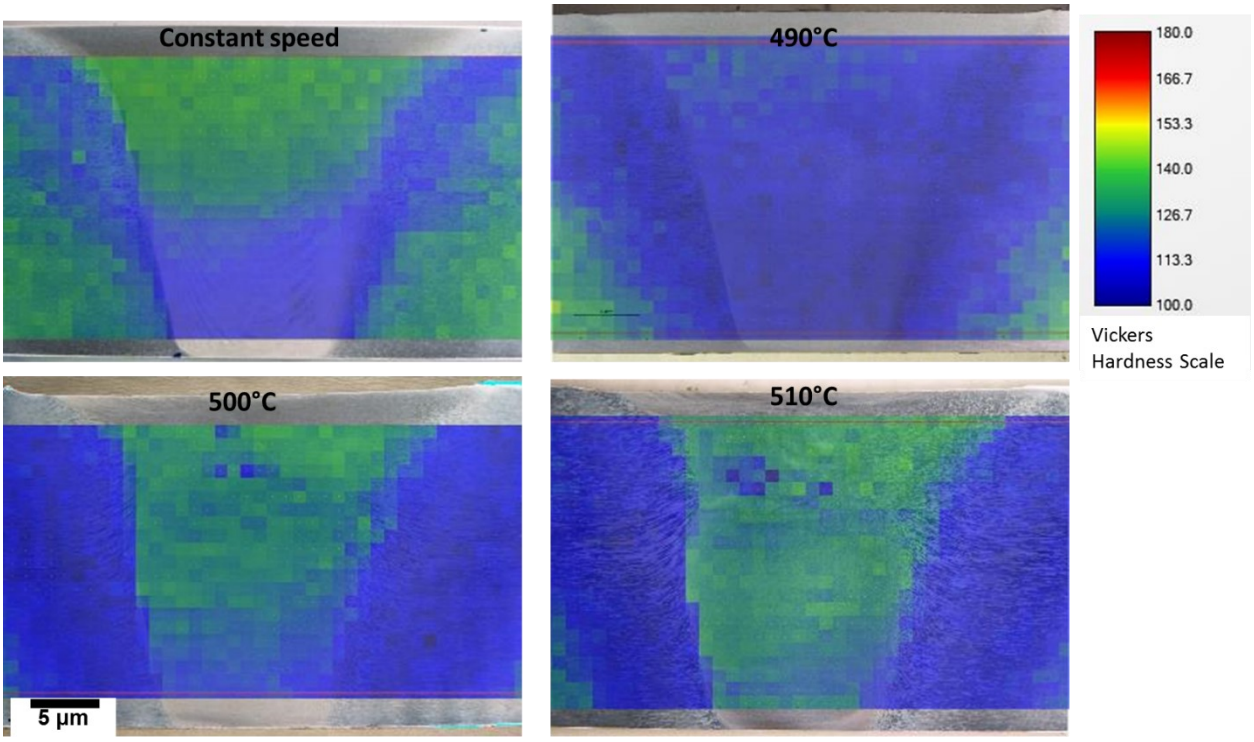

Figure 4.54. Vickers microhardness map overlaid on only the welded region for the constant-temperature and constant-speed FSWs. The constant-speed weld is provided for comparison. Each pixel represents an 1 mm x 1 mm area. The advancing side is on the left.

High-magnification OM photomicrographs and hardness maps are provided in order to characterize the hardness of TMAZ, see Figure 4.55 and Figure 4.56 (490°C), Figure 4.57 and Figure 4.58 (500°C), and Figure 4.59 and Figure 4.60 (510°C). At 490°C, the TMAZ and SZ have similar hardness values. This changed at 500°C and 510°C in which the SZ exhibited higher hardness than the TMAZ. The TMAZ is a narrow weld zone with rotated grains exhibiting widths at approximately 3 mm at the weld top. Thus, the 1mm x 1mm spatial resolution of the Vickers hardness testing could not accurately measure the hardness within this weld zone. Indents that did land within this zone resulted in a dark blue pixel. For future hardness testing on the TMAZ, it is recommended to use a smaller mapping resolution that is no larger than 0.5 mm x 0.5 mm at specific locations to provide enough data and increase the probability of capturing the TMAZ and the SZ/TMAZ and TMAZ/HAZ interfaces.

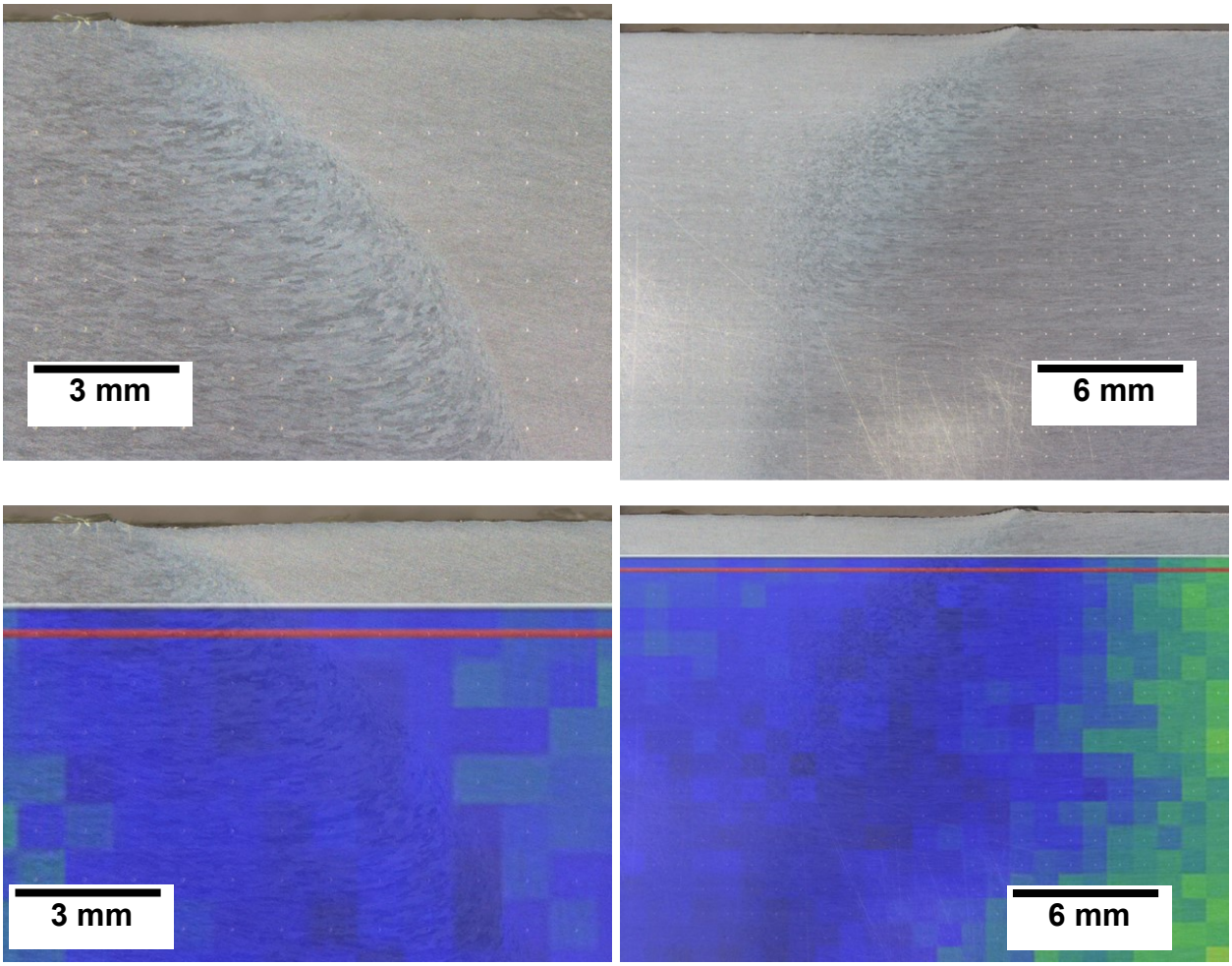

Figure 4.55. OM photomicrograph of the top of the 490°C FSW with the overlaid HV map below it for the AS (left) and the RS (right). The Vickers hardness map is overlaid on the photomicrographs. The color map follows the ROYGBIV scale with red being the highest hardness. The rotated grains indicate the TMAZ. The shown SZ and the TMAZ have similar hardness values. The green pixels indicate the HAZ. Each pixel is 1 mm in width and height.

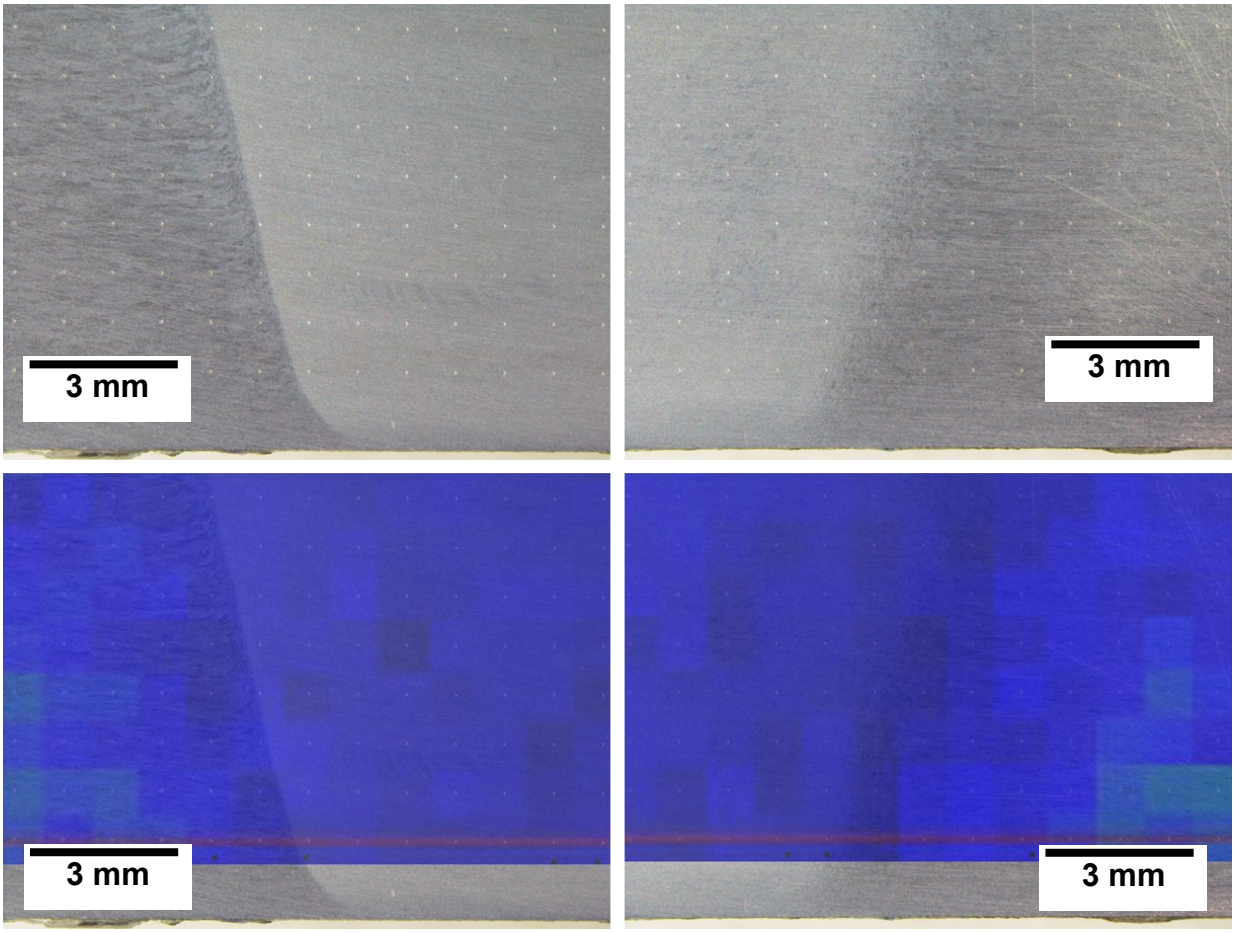

Figure 4.56. OM photomicrograph of the bottom of the 490°C FSW with the overlaid HV map below it for the AS (left) and the RS (right). The Vickers hardness map is overlaid on the photomicrographs. The color map follows the ROYGBIV scale with red being the highest hardness. The rotated grains indicate the TMAZ. The shown SZ and the TMAZ have similar hardness values. Each pixel is 1 mm in width and height.

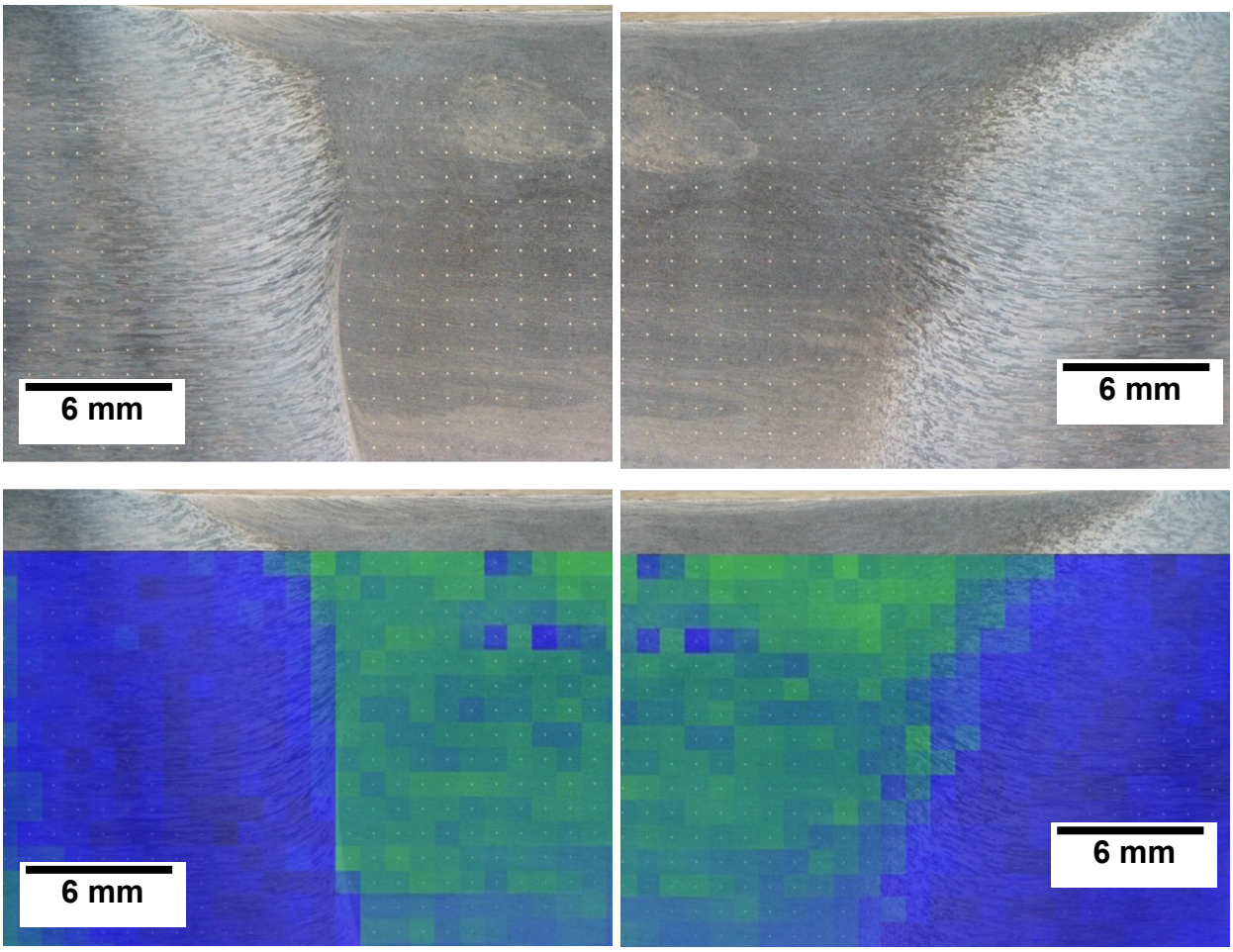

Figure 4.57. OM photomicrograph of the top of the 500°C FSW with the overlaid HV map below it for the AS (left) and the RS (right). The Vickers hardness map is overlaid on the photomicrographs. The color map follows the ROYGBIV scale with red being the highest hardness. The rotated grains indicate the TMAZ. The shown SZ has a higher hardness than the TMAZ. Each pixel is 1 mm in width and height.

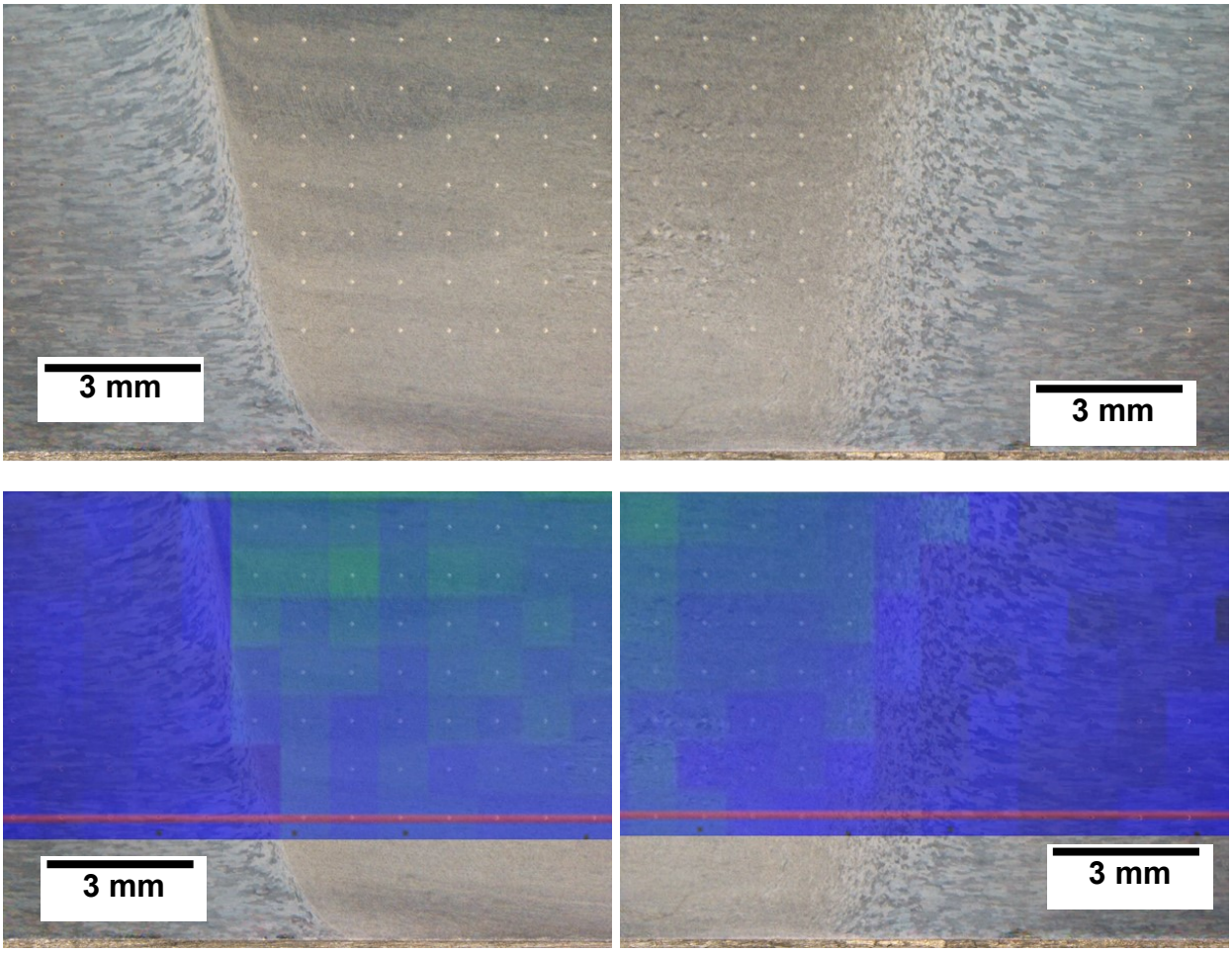

Figure 4.58. OM photomicrograph of the bottom of the 500°C FSW with the overlaid HV map below it for the AS (left) and the RS (right). The Vickers hardness map is overlaid on the photomicrographs. The color map follows the ROYGBIV scale with red being the highest hardness. The rotated grains indicate the TMAZ. The shown SZ has a higher hardness than the TMAZ. Each pixel is 1 mm in width and height.

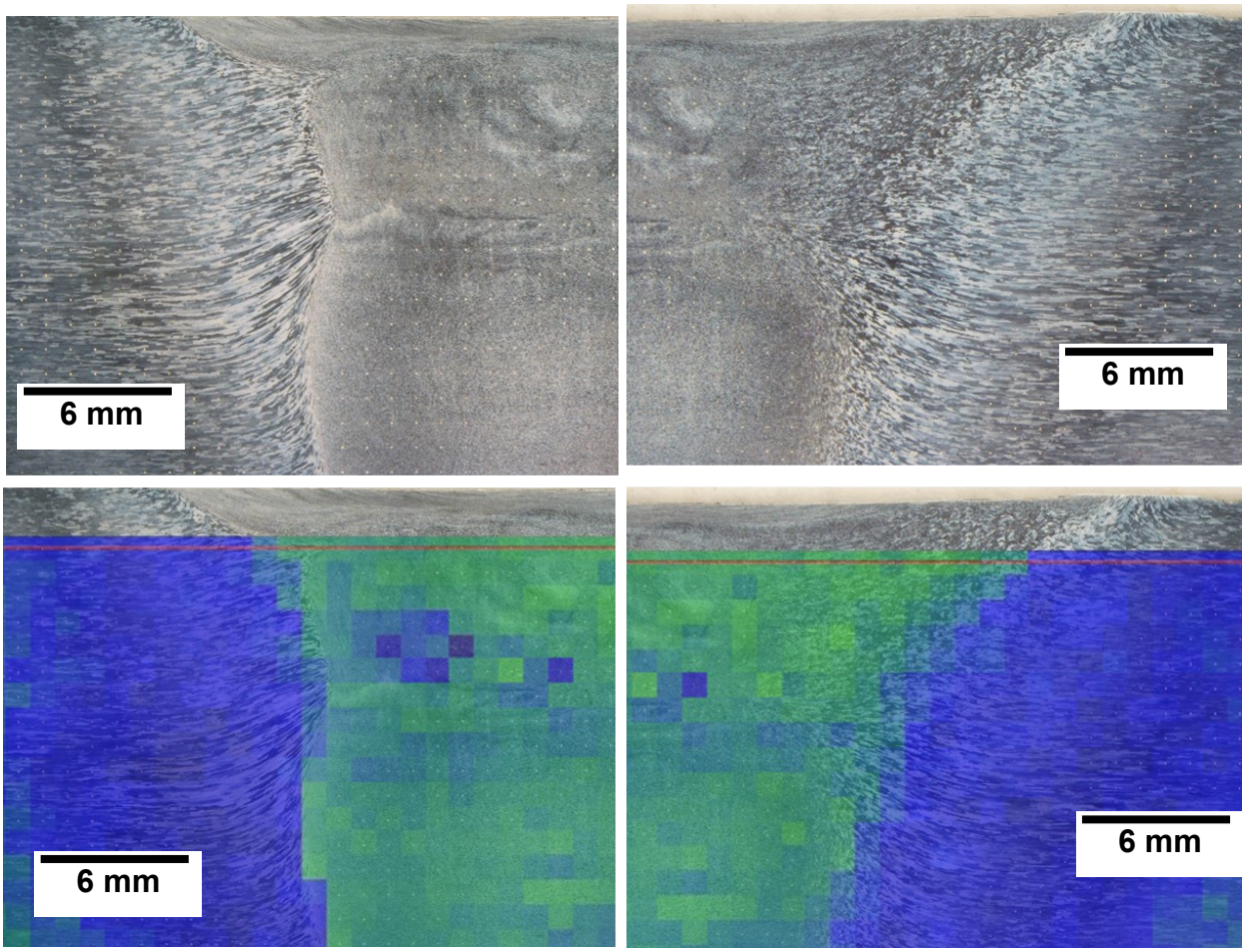

Figure 4.59. OM photomicrograph of the top of the 510°C FSW with the overlaid HV map below it for the AS (left) and the RS (right). The Vickers hardness map is overlaid on the photomicrographs. The color map follows the ROYGBIV scale with red being the highest hardness. The rotated grains indicate the TMAZ. The shown SZ has a higher hardness than the TMAZ. Each pixel is 1 mm in width and height.

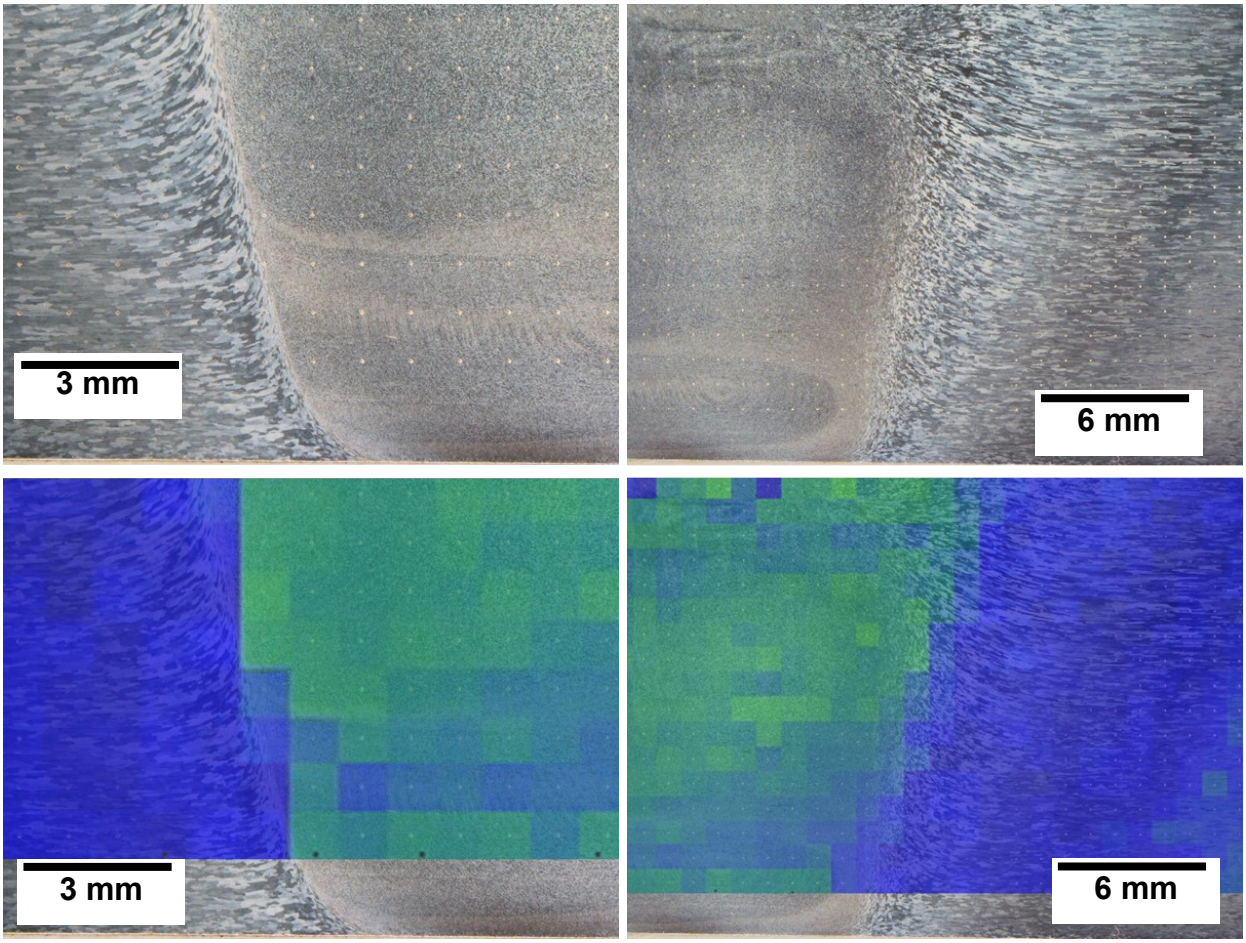

Figure 4.60. OM photomicrograph of the bottom of the 510°C friction stir weld with the overlaid HV map below it for the AS (left) and the RS (right). The Vickers hardness map is overlaid on the photomicrographs. The color map follows the ROYGBIV scale with red being the highest hardness. The rotated grains indicate the TMAZ. The shown SZ has a higher hardness than the TMAZ. Each pixel is 1 mm in width and height.

Values from the Vickers hardness maps are plotted for the weld top, mid top, middle, mid bottom, and bottom, as seen in Figure 4.61. Localized hardness was observed at 490°C at the top and mid top, but the magnitude was not as significant when compared to that of the constant-speed weld. At 500°C, the hardness plot demonstrates localized hardness was recovered in the SZ and throughout the thickness of the weld. The sharp decrease in hardness in the SZ was due to voids. A similar observation was made at 510°C. The maximum hardness values in the SZ in Table 4.14 further demonstrate the gradient in hardness observed in the welds. In addition, with increasing

temperature the weld top gets closer in hardness to that of the constant-speed.

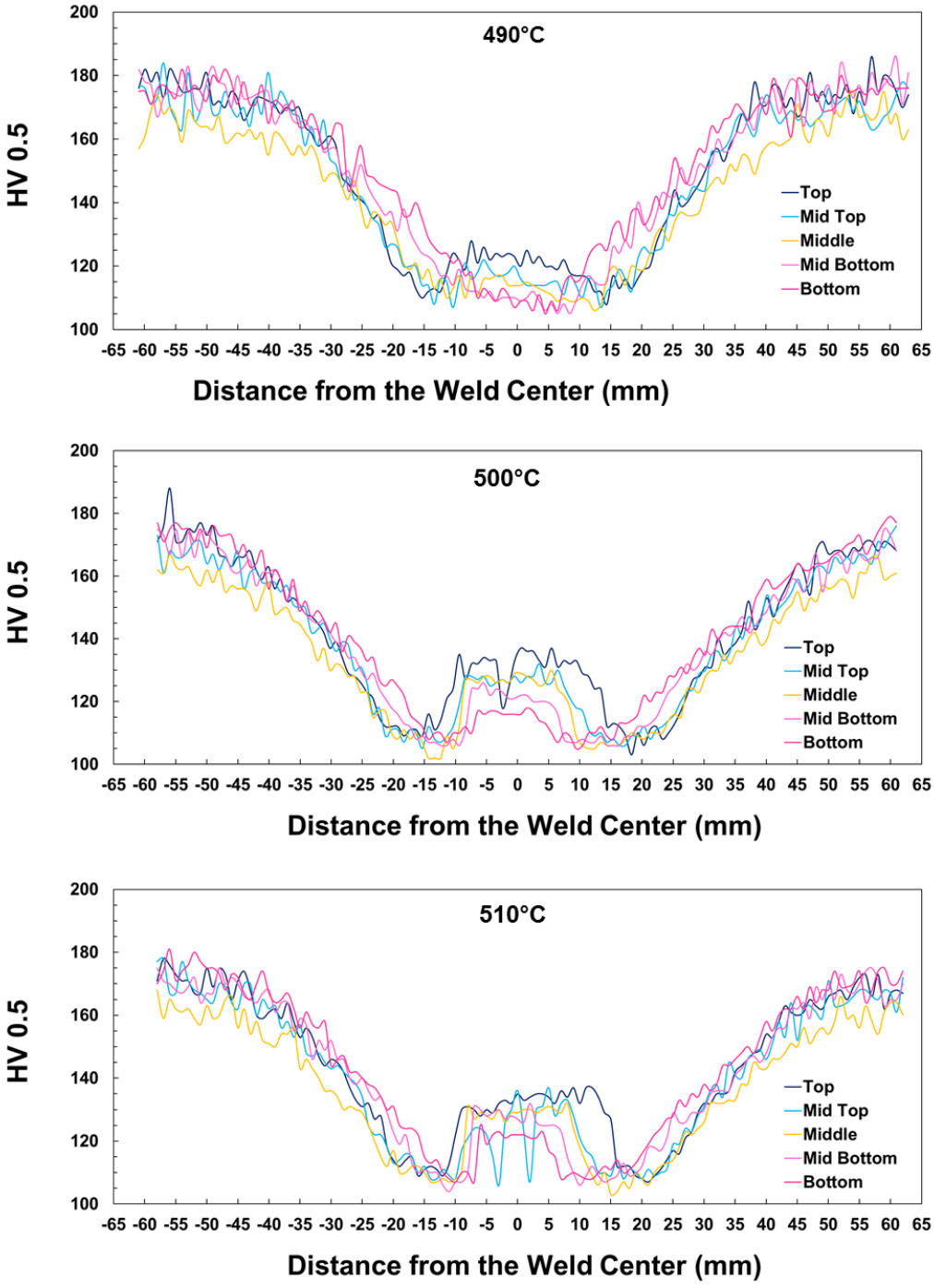

Figure 4.61. Vickers hardness (using a 0.5 kgf load) plot of the constant-temperature FSWs through the thickness of the weld. This data was acquired from the hardness maps in Figure 4.53. Localized hardness in the SZ increases with temperature. Voids in the 510°C sample led to sudden decreases in hardness. The negative values on the x-axis represent the advancing side of the weld, while the positive values represent the retreating side. Some images of the actual indents are provided in the plots for comparison.

Table 4.14. Maximum Vickers hardness values through the depth of the SZ for the constant-temperature and constant-speed FSWs.

	Top	Mid Top	Middle	Mid Bottom	Bottom
Constant Speed	140	136	128	116	110
FSW/490C	128	123	126	113	113
FSW/500C	137	132	130	126	118
FSW/510C	138	137	136	126	125

4.3.4 Tensile Behavior Results

The results of the tensile tests performed on the constant-temperature FSW materials at RT are presented in this section. The tensile axis was perpendicular to the welding direction, which is also the RD of the plate. The gage section contained mostly the mid top, middle, and mid bottom of the weld and also contained the BM. The engineering stress-strain plot is shown in Figure 4.62, the tensile properties are provided in Table 4.15, and the average of these values are provided in Table 4.16. FSW/490°C and FSW/500°C had similar tensile properties and joint efficiencies. FSW/510°C exhibited the lowest tensile properties due to the voids present in the welds. Even with the gage section reduced to exclude portions of the weld top and bottom, the voids still remained. These voids acted as crack initiation points and resulted in premature failure.

Digital images of the fractured tensile tested samples are shown in Figure 4.63, Figure 4.64, and Figure 4.65 for FSW/490°C, FSW/500°C, and FSW/510°C, respectively. All FSW/490°C exhibited fracture on the RS along the SZ/TMAZ interface. The FSW/500°C fracture occurred well into the HAZ on the RS and double necking was observed on the AS near the TMAZ. As a result of the voids, the FSW/510°C samples fractured in the SZ. In the first sample, the crack initiated at the voids in the SZ and propagated towards the RS and can be seen in the bottom view in Figure 4.65.

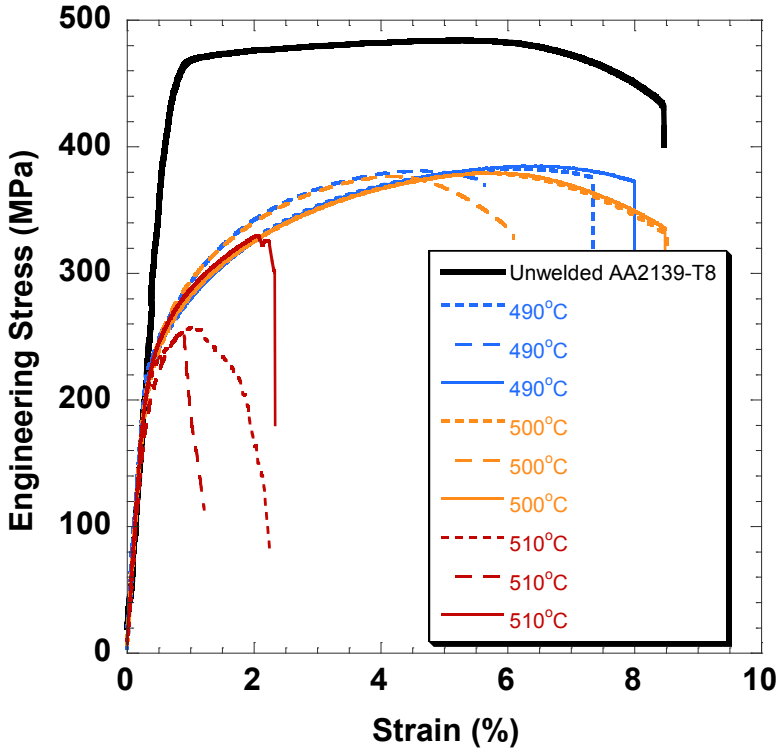

Figure 4.62. Weld joint comparison of the constant-temperature FSW. The as-received, base metal AA2139-T8 stress-strain curve is also provided for comparison. Constant-temperature FSW tensile samples are shown in Figures 4.63 through 4.65.

Table 4.15. Tensile properties of constant-temperature FSW joints shown in Figures 4.63 through 4.65. Joint efficiency is defined as the ratio of the UTS of the FSW joint to the unwelded base metal. *Samples are listed in the same order as the legend in the stress-strain plot of Figure 4.62.

	YS (MPa)	UTS (MPa)	E (GPa)	ε_f (%)	Joint Eff. (%)	Fracture Location
AA2139-T8	459.6	483.2	69.6	6.7	--	--
490°C	246.8	382.6	72.5	7.3	79.2	Retreating Side
490°C	253.0	380.8	66.9	5.6	78.8	Retreating Side
490°C	243.4	384.7	68.7	8.0	79.6	Retreating Side
500°C	244.9	379.0	65.7	8.5	78.4	Retreating Side
500°C	255.7	376.5	63.6	5.9	77.9	Retreating Side
500°C	244.5	379.4	71.4	8.5	78.5	Retreating Side
510°C	233.0	257.4	70.2	2.2	53.3	Stir Zone
510°C	231.3	255.0	58.8	1.6	52.8	Stir Zone
510°C	250.3	329.8	68.5	2.3	68.2	Advancing Side

Table 4.16. Average of the constant-temperature FSW tensile property values listed Table 4.15. The standard deviation is in parentheses. Constant-temperature FSW at 510°C exhibited the lowest values due to voids in the SZ, which served crack initiation sites.

	YS (MPa)	UTS (MPa)	E (GPa)	εf (%)	Joint Eff. (%)
AA2139-T8	459.6	483.2	69.6	6.7	--
490°C	247.7 (4.9)	382.7 (2)	69.4 (2.9)	7.0 (1.2)	79.2 (0.4)
500°C	248.4 (6.4)	378.3 (1.6)	66.9 (4)	7.6 (1.5)	78.3 (0.3)
510°C	238.2 (10.5)	280.7 (42.5)	65.8 (6.2)	2.0 (0.4)	58.1 (8.8)

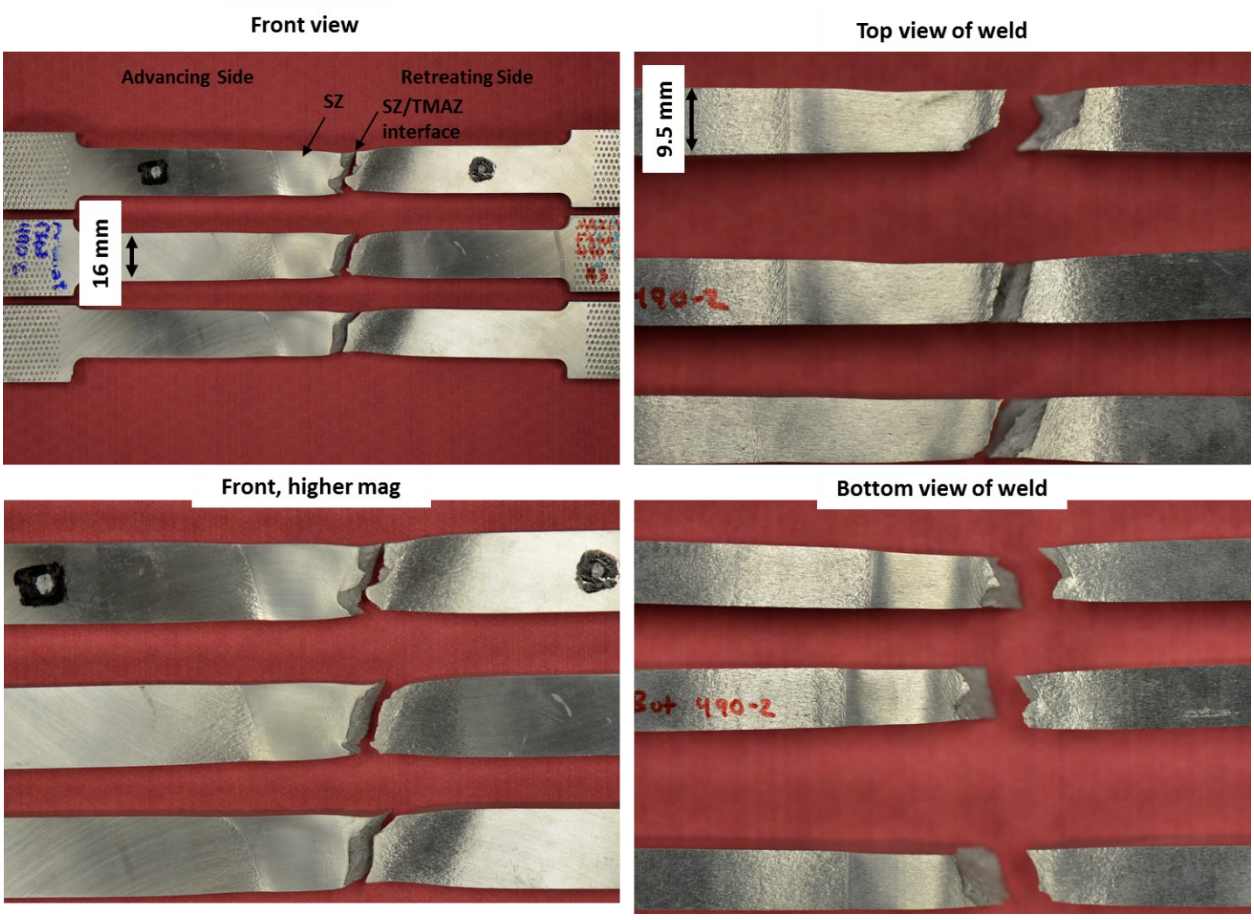

Figure 4.63. Digital images of the RT tensile tested 490°C constant-temperature FSW samples. The advancing side is on the left for all samples and images.

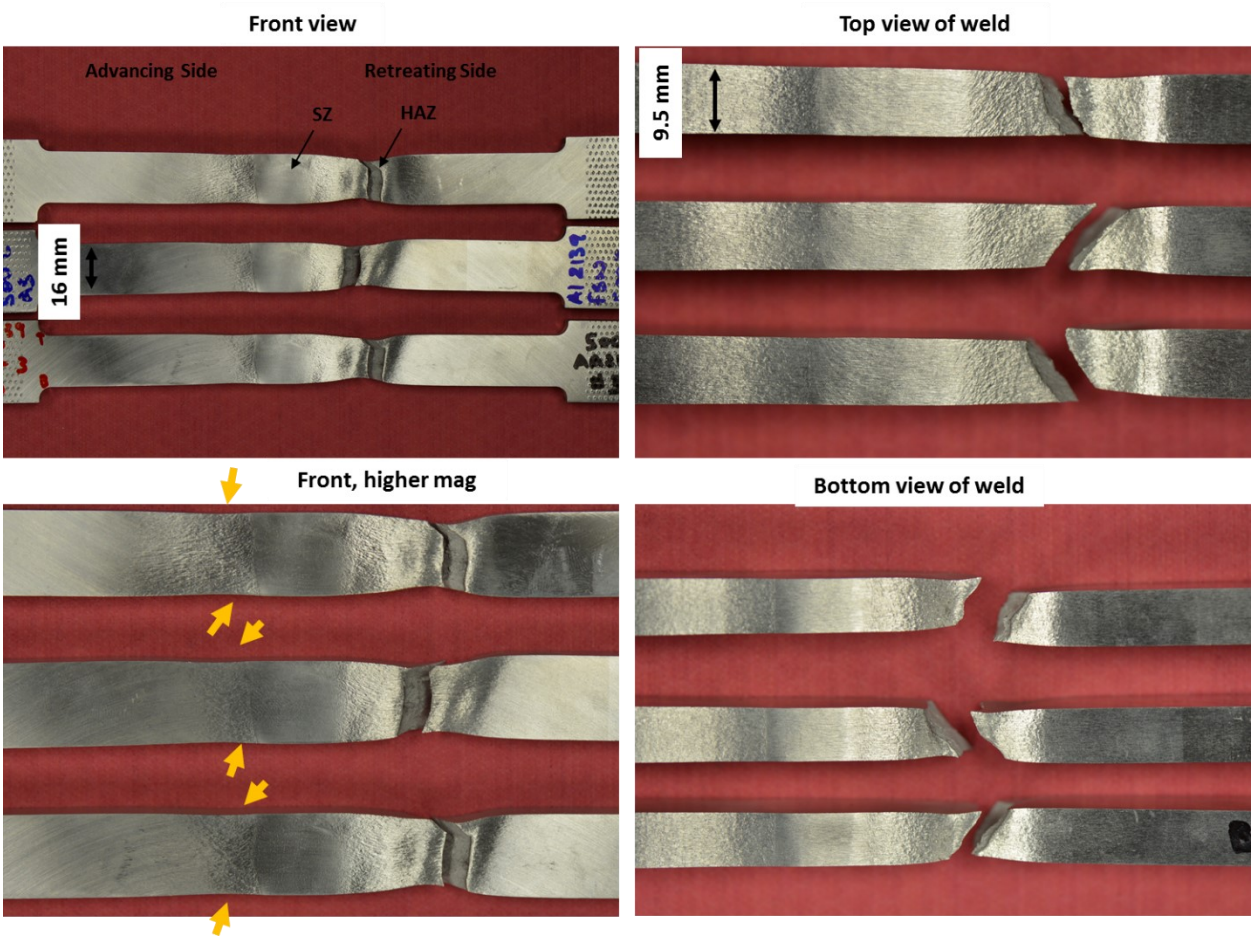

Figure 4.64. Digital images of the RT tensile tested 500°C constant-temperature FSW samples. Yellow arrows indicate areas of additional necking. The advancing side is on the left for all samples and images.

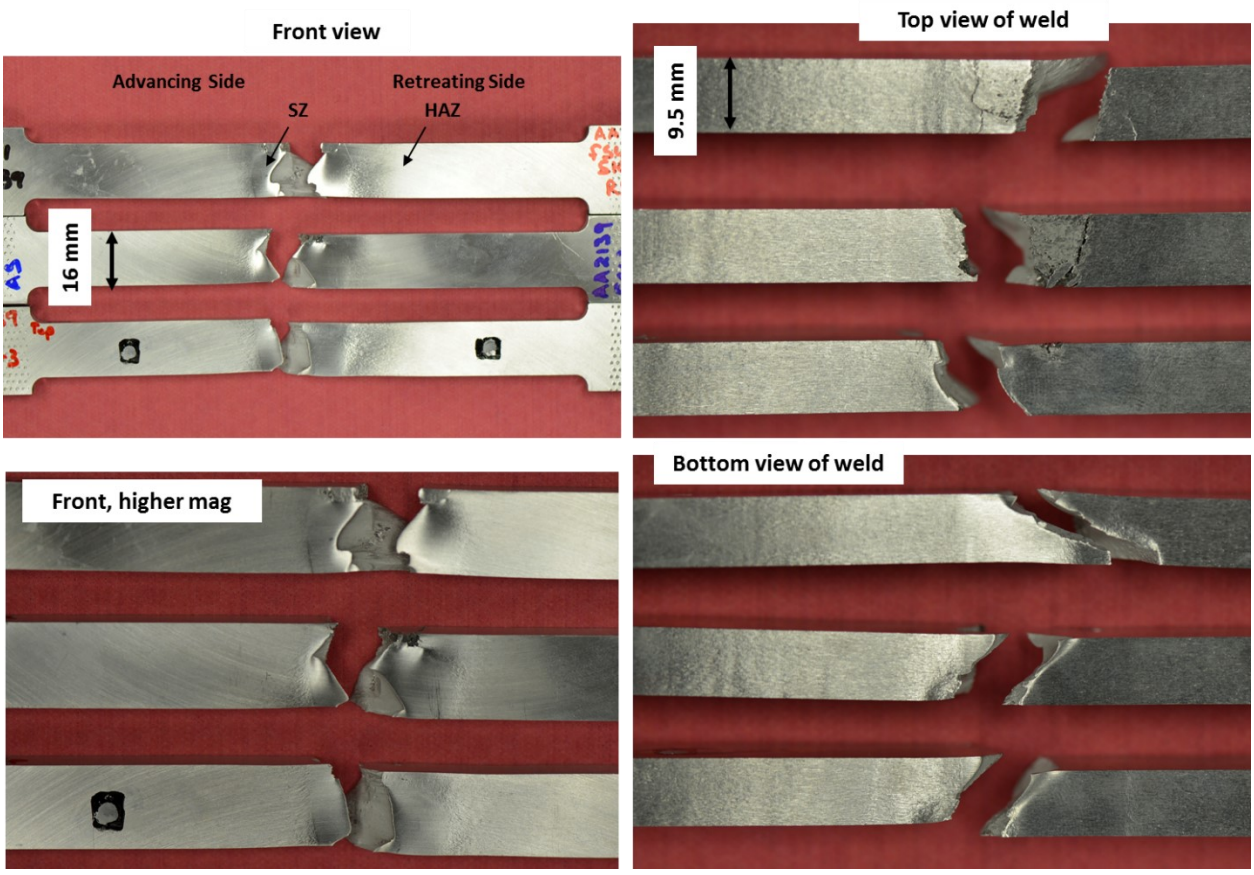

Figure 4.65. Digital images of the RT tensile tested 510°C constant-temperature FSW samples. The advancing side is on the left for all samples and images.

4.3.5 Effect of FSW Temperature on Mechanical Behavior

The effects of FSW temperature on the mechanical behavior of 25mm thick AA2139-T8 are discussed in this section. FSW was conducted at 490°C, 500°C, and 510°C. The results of the Vickers hardness and tensile properties are discussed.

The hardness maps and plots showed that the hardness increased in the SZ with increasing FSW temperature. At T ≥ 500°C, the magnitude of the localized hardness increase was greater than that observed at T=490°C. The emergence of what is interpreted as a distinction between the UWN and LWN in the SZ at 500°C was all but diminished at 510°C, see Figure 4.53 and Figure 4.54.

The UWN/LWN distinction seen in the constant-speed FSW hardness map, Figure 4.28, was not observed in the same form as the constant-temperature FSWs. The differences between the tools used may not have contributed to the change in the UWN/LWN shape. Rabby demonstrated that for a 25.4 mm thick, AA6061 Al alloy, increasing the number of flats improved material flow around the tool, which also reduced the size of wormhole defects [71]. It was also demonstrated that a threaded pin assisted in downward material flow. Lastly, Rabby proved that the shape of the weld did not differ between a threaded pin with three flats and four flats until higher rotational speeds. At 400 RPM and 203 mm/min, a threaded pin with three flats resulted in a wider weld nugget than the pin with four flats. As a reminder, the constant-speed FSW used a threaded pin with four flats and the constant-temperature FSWs used a threaded pin with three flats. Figure 4.46 shows that the shape of the weld nugget changes at T=500°C indicating that rotational speeds used to obtain and maintain the temperature may have been too high for that tool design. Thus, higher temperatures using faster rotational speeds may require more flats. Nonetheless, this does not explain the difference in the appearance of the UWN/LWN in the SZ. The shape of the constant-speed SZ is similar to that of the 490°C FSW, but the hardness map demonstrates that there is some similarity of the constant-speed UWN/LWN to that of 500°C FSW. It is possible that there may have been more downward flow at higher temperatures (500°C and 510°C) due to the softened material. The difference between the widths of the plates joined may have contributed to this. The width of each plate joined in the constant-speed FSW was 762 mm while the width of each plate was 101.6 mm for the constant-temperature FSWs. A wider plate would impact the lateral cooling of the weld and, consequently, the size of the HAZ and TMAZ. The impact of BM size on the weld nugget shape, weld zone size, resulting mechanical properties is outside the scope of this dissertation. This study would entail comparing different base metal

widths and possibly investigating active cooling methods of the weld (forced air, cryogenic cooling, water spray, etc.) while controlling the temperature. This is recommended for future work to inform welding parameter and tooling development for applications that use both large and small plates.

Although FSW/490°C had the lowest hardness values in the SZ, it exhibited similar tensile properties to FSW/500°C. The fracture locations shifted from the SZ/TMAZ interface in the FSW/490°C welds to the HAZ in the FSW/500°C welds. Although further investigation on the underlying mechanisms for the observations is ongoing, it is evident that the hardness of the SZ does not significantly affect the joint efficiency or tensile strengths at FSW temperatures 490°C ≤ T ≤ 500°C. It does, however, affect the fracture location and indicates the influence of the precipitates (or lack thereof) on dislocation motion. It is believed in the welding community that a narrower TMAZ and HAZ increases tensile properties but this was not observed when FSW/490°C and FSW/500°C were compared. This may be explained by analyzing the effect on FSW temperature on the precipitate phases in section 4.4.3. Narrowing the HAZ is a best practice employed in fusion welding as it is often the cause of the degradation of the weld joint properties [92,93]. The size and microstructure of the HAZ can be controlled by limiting certain variables such as the welding process, heat input, (this is a function of travel speed, voltage, current, and preheating and interpass temperatures) and cooling [93]. This best practice is applied to both steels and aluminum alloys, especially precipitation strengthened alloys. In the case of the 490°C and 500°C FSWs, higher welding temperatures led to a higher SZ hardness and a wider HAZ but did not significantly impact the tensile strengths.

FSW/510°C had the highest hardness values in the SZ. However, the voids in the SZ, which locally reduced the hardness, also served as crack initiation points and led to premature

failure of the test specimen.

A summary of the mechanical behavior of the constant-temperature FSWs is provided in Figure 4.66. The increase in SZ hardness with temperature is a result of the solid-solution strengthening due to the increased Cu-solute concentration in the matrix grains as a result of the dissolved θ', Ω, and θ precipitates. The weakest regions of the FSW/490°C and FSW/500°C were the SZ/TMAZ interface and the HAZ, where tensile fracture occurred. Thus the SZ for these materials was stronger than the SZ/TMAZ interface and the HAZ, and therefore the evolving microstructure within the SZ did not directly dictate the tensile strength of the weld.

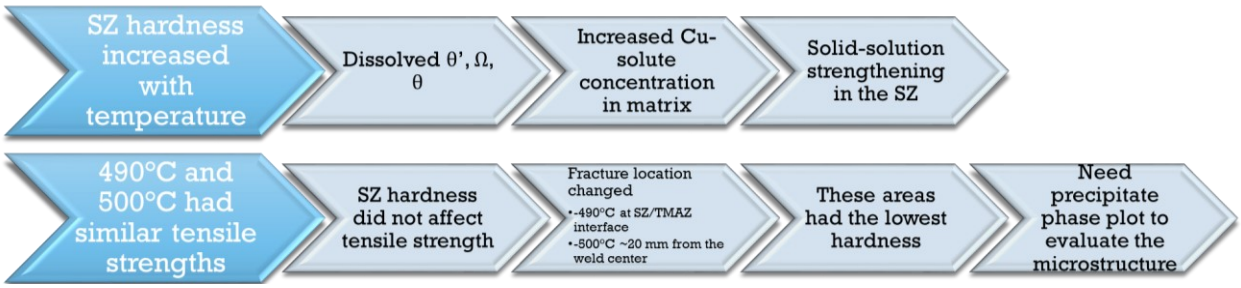

Figure 4.66. Schematic depiction explaining the mechanical behavior exhibited by the constant-temperature FSWs.

4.4 Precipitate Phase Plot of Constant-Temperature FSW

The results of the XRD data of the constant-temperature FSWs—FSW/490°C, FSW/500°C, and FSW/510°C, are presented in this section. The diffraction data was used to construct a phase plot to depict the precipitates as a function of FSW temperature and position in the welded area, which is also discussed in this section. First, the identified phases are analyzed and discussed. Next, the microstructure of the constant-temperature FSWs are correlated to the Vickers hardness. Then, the implications of the phase plot on the mechanical properties are discussed.

4.4.1 Construction of the Precipitate Phase Plot

X-ray diffraction was conducted on the constant-temperature friction stir welds and the

peaks are presented as a function of temperature, distance from the weld center, and depth of the weld in Figures 4.67 through 4.73. Plots of intensity versus 2-theta comparing the FSW microstructure to the as-received AA2139-T8 base metal can be found in APPENDIX F. Diffraction plots shown in Figures 4.67 through 4.73 are also grouped by temperature in APPENDIX G. The Al-matrix phase peaks and precipitate phase peaks were identified and labelled.

All three metastable precipitate phases, θ', Ω, and equilibrium θ, were identified at all FSW temperatures; however, these phases were not uniformly distributed through the welded area. The constituent phase, Al_7CuFe, was identified at every temperature and position. As mentioned in the XRD analysis of the as-received AA2139-T8, the θ and Ω precipitate phases have overlapping peaks which makes it difficult to discern between the two. Thus, these XRD peaks are labelled as both phases. The precipitate phase plot includes both phases where the overlapping θ and Ω peaks are identified. These overlapping peaks are referred to as θ/Ω.

A plot of the precipitate phases throughout the weld zones and the depth of the weld were plotted as a function of welding temperature in Figure 4.74. The constituent phase was not included in the plot. The data markers were offset by 2°C and 2 mm for better visualization.

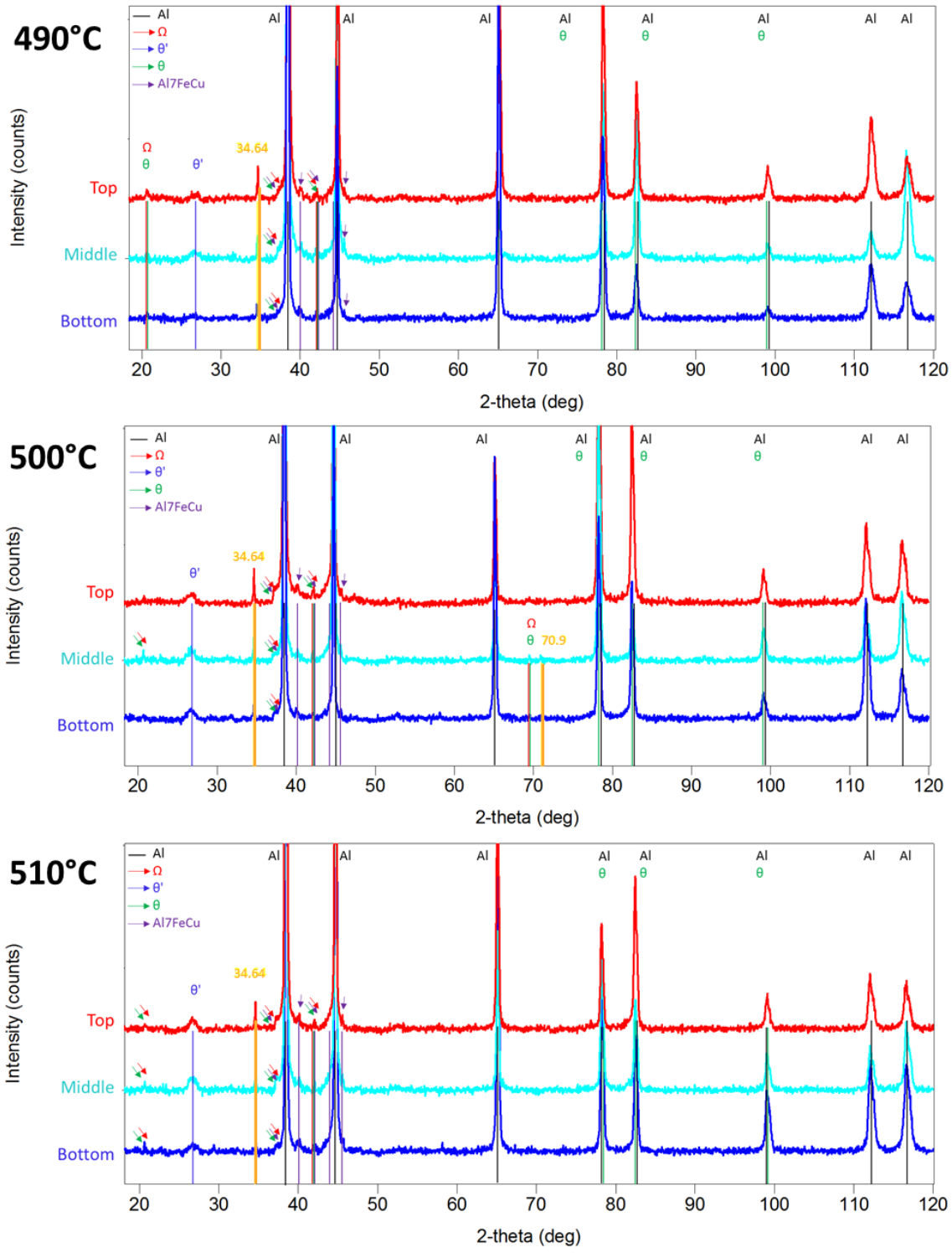

Figure 4.67. XRD comparison of the constant-temperature FSWs -30 mm (advancing side) from the center of the weld.

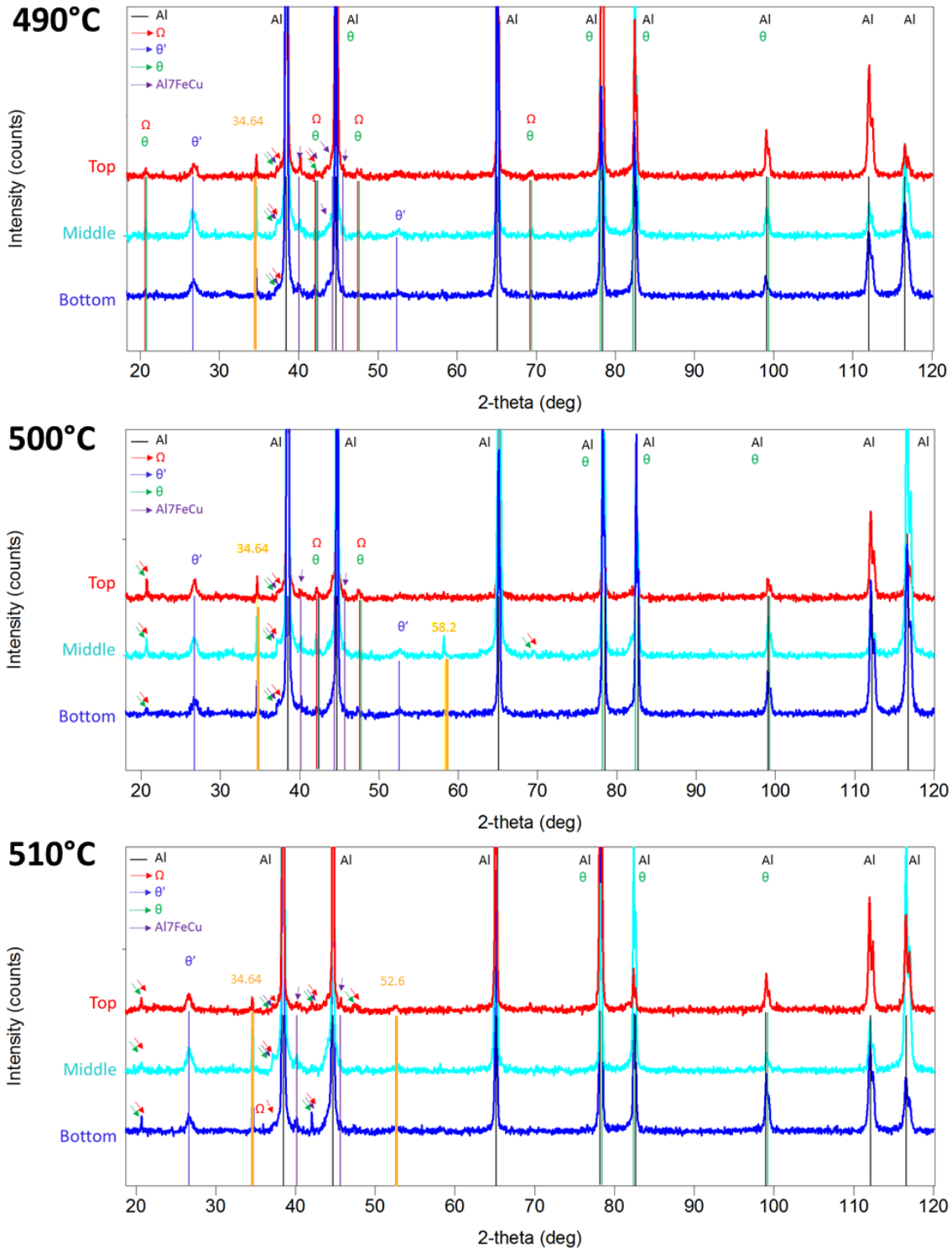

Figure 4.68. XRD comparison of the constant-temperature FSWs -20 mm (advancing side) from the center of the weld.

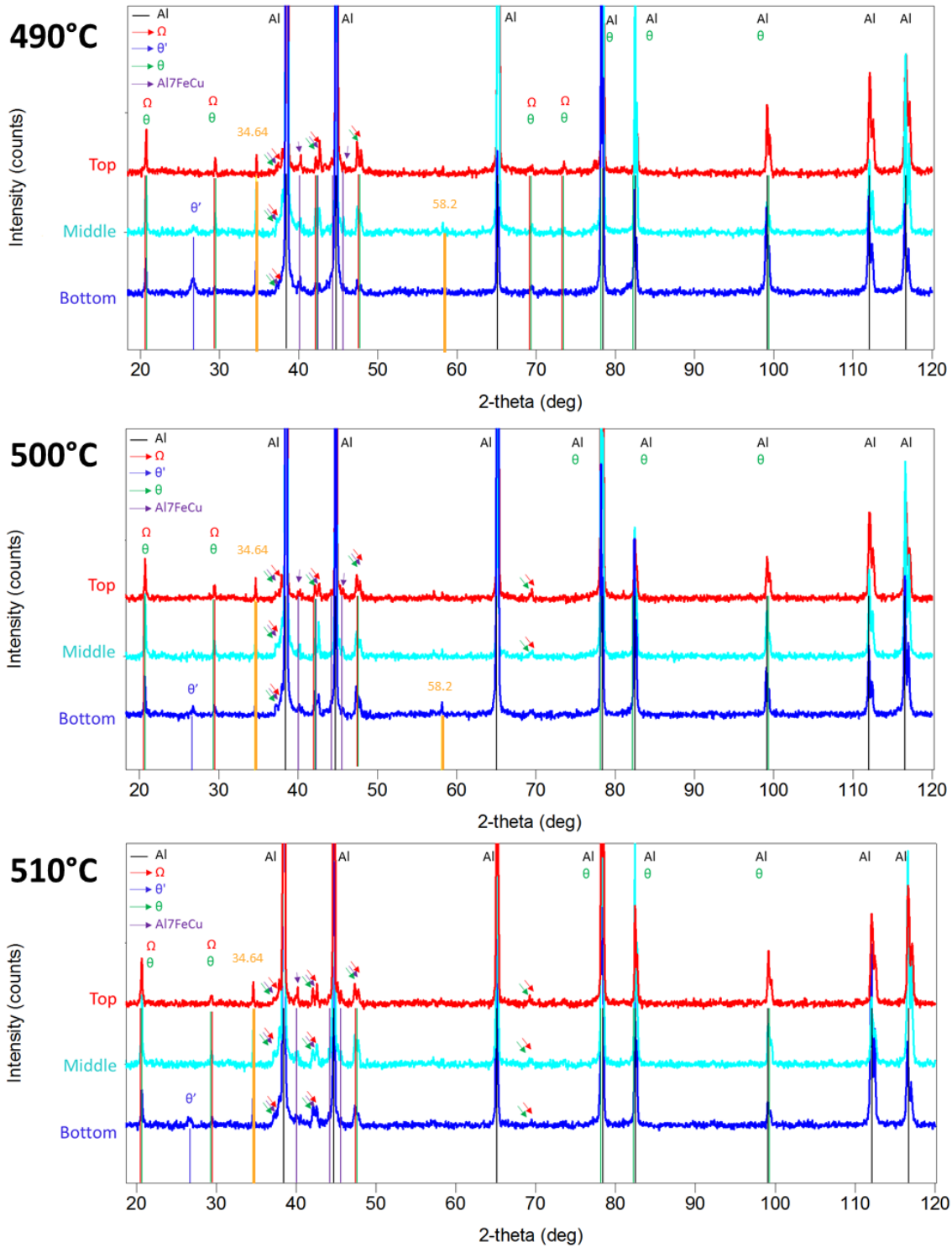

Figure 4.69. XRD comparison of the constant-temperature FSWs -10 mm (advancing side) from the center of the weld.

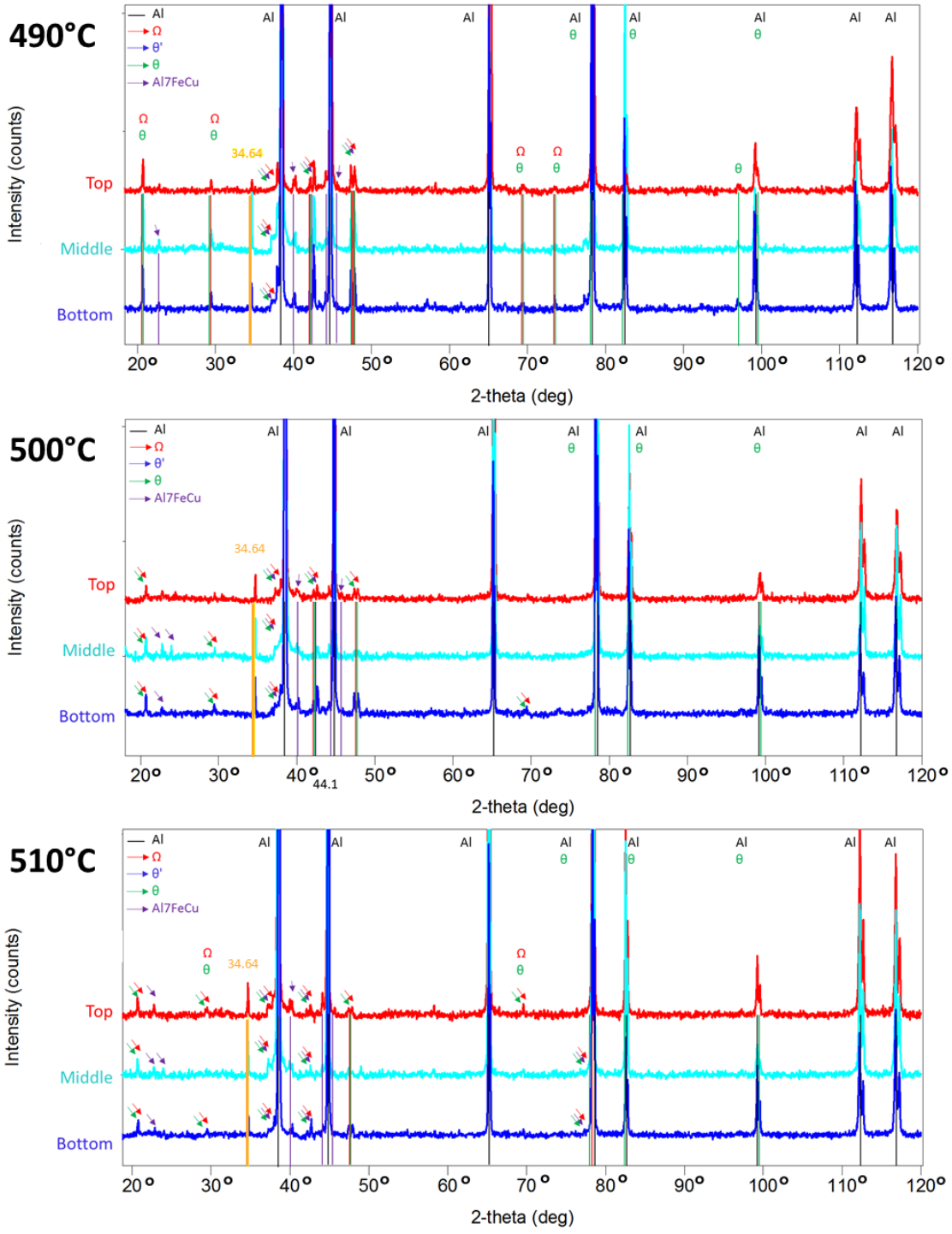

Figure 4.70. XRD comparison of the constant-temperature FSWs at the center of the weld.

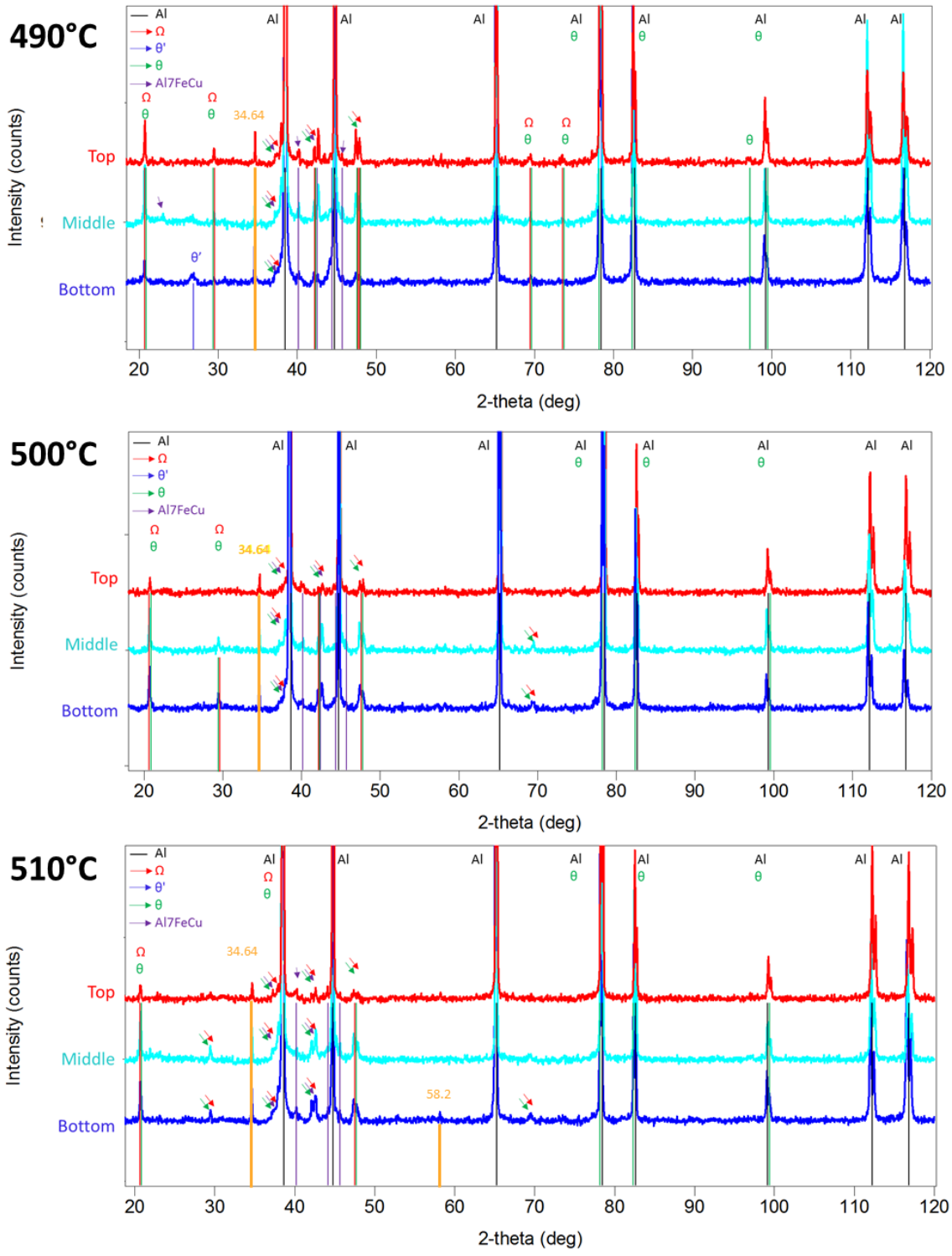

Figure 4.71. XRD comparison of the constant-temperature FSWs +10 mm (retreating side) from the center of the weld.

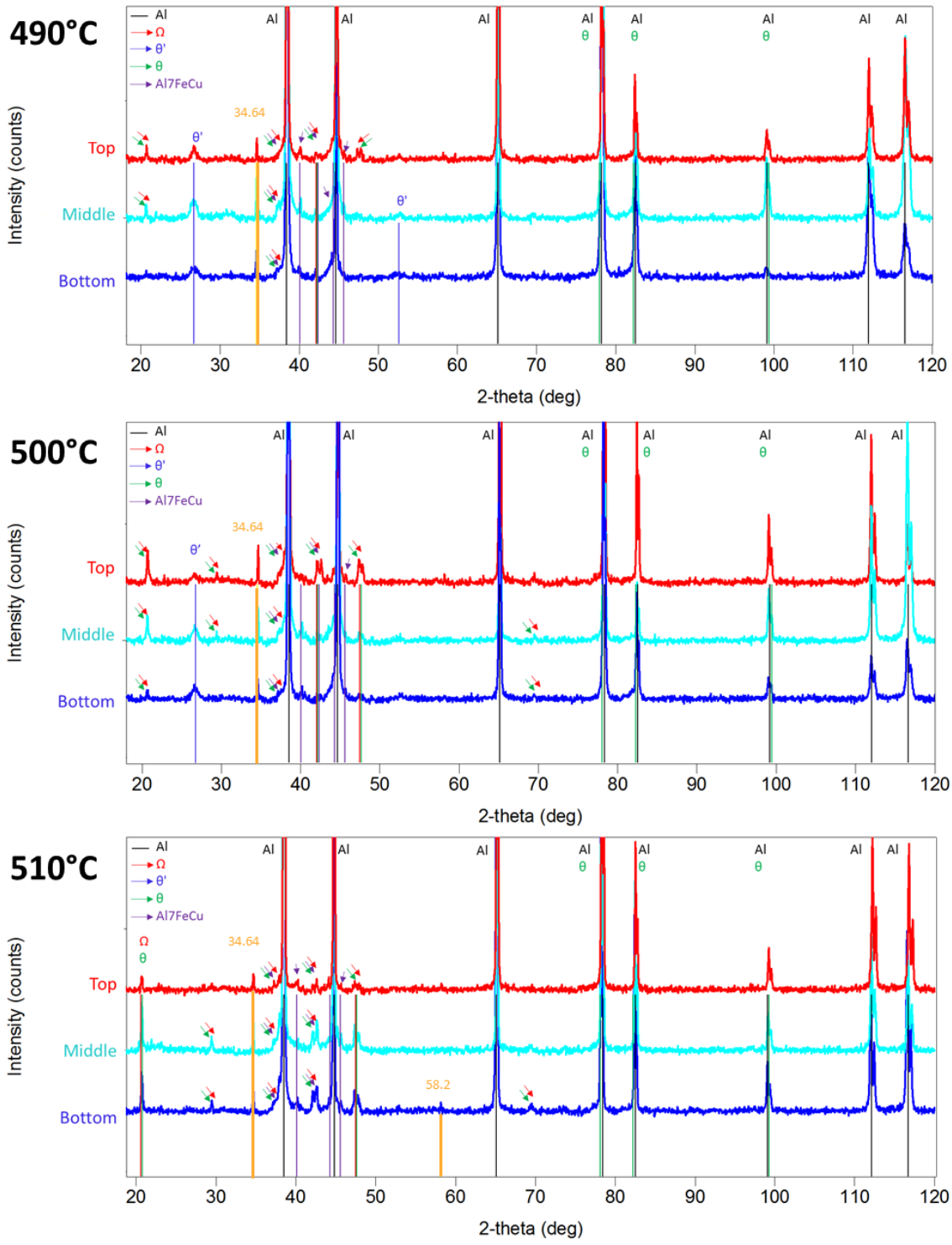

Figure 4.72. XRD comparison of the constant-temperature FSWs +20 mm (retreating side) from the center of the weld.

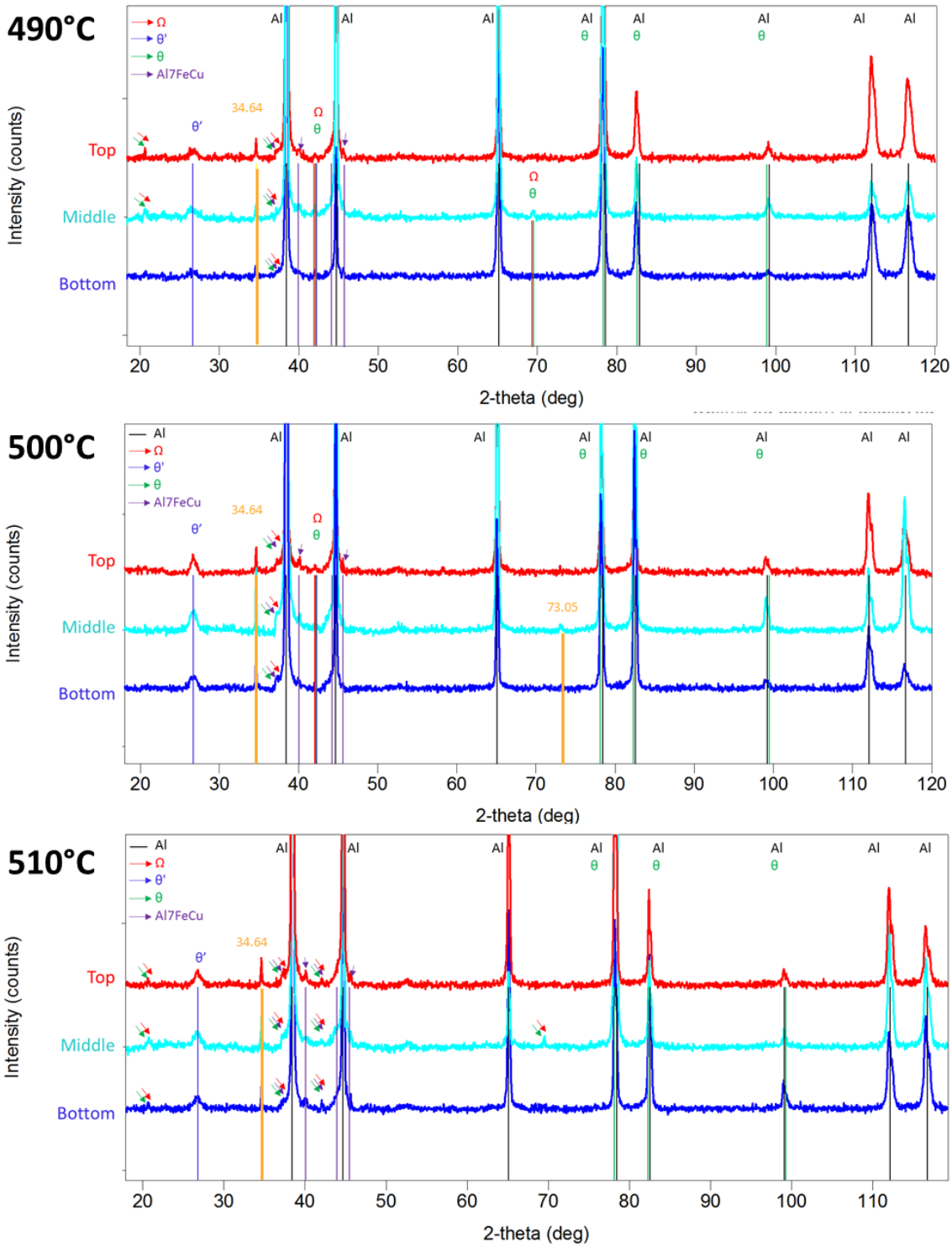

Figure 4.73. XRD comparison of the constant-temperature FSWs +30 mm (retreating side) from the center of the weld.

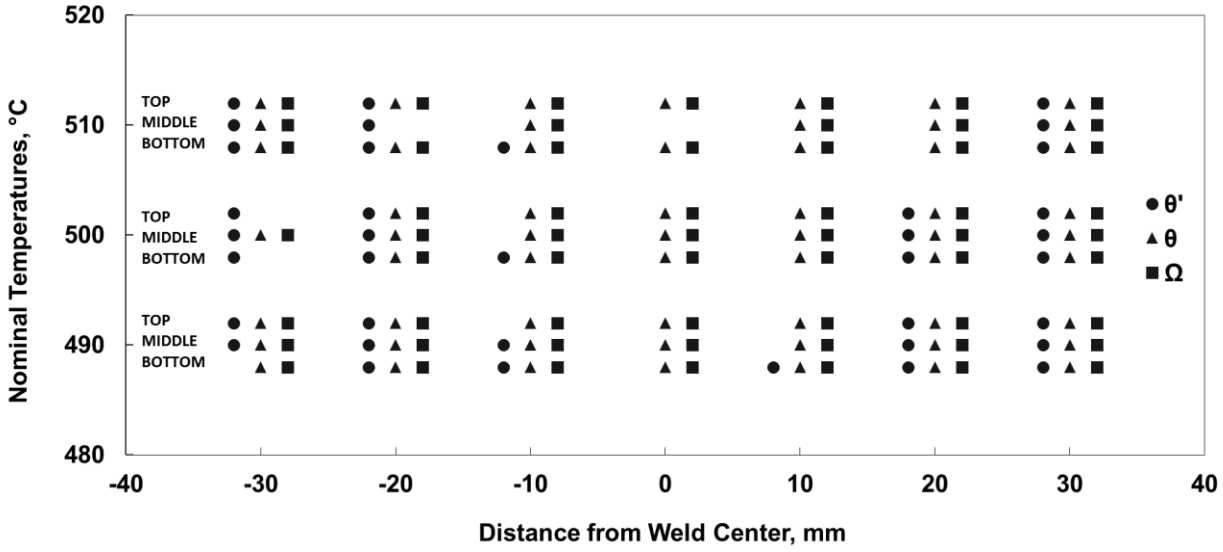

Figure 4.74. Phases present in the FSWs at the target weld temperatures: 490°C, 500°C, and 510°C according to their position in the weld. Negative distance is for the AS, while positive distance is for the RS.

4.4.2 Precipitate Phase Plot Analysis

The phase plot identified the strengthening precipitates, θ' and Ω, and the equilibrium θ precipitate. As mentioned in section 4.1.1, the Ω and equilibrium θ precipitates have overlapping XRD peaks; therefore, where it is unclear that the precipitates are either Ω or θ, the nomenclature used is θ/Ω. Not including the constituent phase Al_7FeCu, as expected, the θ/Ω precipitates were the only phases identified in the center of the weld, 0 mm, for all FSW temperatures. This is due to the elevated temperatures in the center of the weld that facilitate the phase transformation [10,11]. The phase transformation for the θ-type precipitates is θ"→θ'→θ. Thus, the presence of equilibrium θ is due to a combination of overaging and an increase of matrix saturation of Cu solutes due to θ' dissolution. Although θ and Ω share XRD peaks, it is not expected for Ω to be present based on the TEM results for the constant-speed FSW, as seen in Figures 4.13 through 4.15. Unexpectedly, none of the precipitates were detected at center of the weld at 510°C in the middle layer. Such an observation suggests that the temperature was high enough to dissolve all of the precipitate phases. Further investigation on what is driving this effect is ongoing.

At -10 mm and +10 mm from the center of the weld, the precipitates present were equivalent between 500°C and 510°C through the thickness of the weld. At 490°C, the θ' phase was detected at the bottom layer and, at -10 mm, the middle layer. At this distance, the asymmetry of the microstructure of the weld becomes evident. The thermocycling differences between the AS and RS become noticeable in that the precipitate phases present or absent at -10 mm from the center of the weld were not identical to +10 mm. Xu et al. placed thermocouples in a 14 mm thick plate adjacent to the weld (10 mm and 18 mm from the weld centerline—their FSW tool had a shoulder diameter of 28 mm) in order to measure the temperature as a function of distance away from the weld centerline [75]. The results revealed that the temperatures on the AS were higher than the RS. At 10 mm and 18 mm from the weld centerline, the difference in temperatures between the AS and RS reached up to 25°C. This may explain why at +10 mm and -10 mm the precipitation of θ' is not equivalent between the AS and RS. However, there is still issue explaining why θ' was observed on the AS and not on the RS at 500°C and 510°C. The solvus temperature for Al alloys with 4.5-5.5 wt.% Cu is approximately 470-485°C [25]. This could explain why the top and middle layers at 500°C and 510°C and the top layer at 490°C do not have θ'. It is also possible that both Ω and equilibrium θ coexist since θ' to θ transformations occur faster than Ω to θ transformations. This would be consistent with the TEM images acquired at +10 mm (RS) at the mid top layer in the constant-speed FSW, Figure 4.17, Figure 4.18, and Figure 4.20, where only the Ω precipitate was identified in the SADPs. However, this still does not explain why θ' was present on the AS at all temperatures at the bottom layer and dissolved completely on the RS at 500°C and 510°C. This suggests that the RS may be hotter than the AS, but literature has demonstrated otherwise on thinner Al alloys [75]. It also suggests that the RS cools slower than the AS. TEM analysis at this distance from the weld is needed for further

confirmation due to the fact that the plastic flow involves multiple severe plastic deformation techniques (hot working, forging, extrusion), and the presence of the θ' phase at -10 mm and +10 mm should not be thought of as reprecipitation. If reprecipitation of θ' was possible, then the top of the weld, which experiences the peak welding temperature—near or above the θ solvus—and the slowest cooling, would have precipitated the θ' phase and the θ/Ω precipitates would be absent, or the θ' and Ω phases would both be present in a fine distribution and high volume fraction. The differential scanning calorimetry analysis performed by Li and Shenoy [29] used a heating rate of 20°C/min which is significantly slower than that of the FSW process, which can reach heating rates of 282°C/min at 10 mm from the weld centerline in a 14 mm thick plate [75]. At ±10 mm from the weld centerline, the data points are very near or at the interface of the SZ and TMAZ. Thus, the reason why the precipitation sequence is seemingly complex at this location is due to a number of reasons: (1) the thermomechanical process; (2) the time at peak temperature; and (3) the post weld cooling.

At -20 mm and +20 mm from the center of the weld, all precipitate phases were present at all depths of the weld except at 510°C. At 510°C and +20 mm, the θ' precipitate was absent at all depths of the weld. Li and Shenoy [29] performed differential scanning calorimetry on a T8 tempered, Al-Cu-Mg-Ag alloy (Al-5.1Cu-0.8Mg-0.5Ag-0.7Mn-0.13Zr, wt.%) from RT to 550°C at a ramp rate of 20°C/min. They demonstrated that the Ω phase dissolves between 150-400°C. Additionally, θ' precipitation occurred at temperatures between ~250-325°C, while θ' coarsening occurred at temperatures above ~325°C; dissolution of the θ' phase or precipitation of equilibrium θ was not discussed [29]. However, Ringer et al. [27] proved that artificial aging an Al-Cu-Mg-Ag alloy at prolonged times between 250-370°C led to the precipitation of equilibrium θ. Thus, it is possible that the missing θ' phase at 510°C and +20 mm from the center of the weld indicates

transformation to the equilibrium θ phase. Also note that in Li and Shenoy's study, the Ω phase was present at all temperatures, but dissolving [29]. Only the middle layer at 510°C and -20 mm was missing the θ/Ω precipitates. In addition, 20 mm from the weld center is considered the HAZ. The absent precipitates at +20 mm and 510°C indicate that a progression in precipitation kinetics occurred between 500°C and 510°C when welding. This also confirms that the temperature at this distance was higher than at the lower FSW temperatures. The middle layer at -20 mm, however, was unusual as this indicated that precipitation kinetics were as follows: Ω dissolution, then θ' coarsening + Ω dissolution, then θ' and θ/Ω dissolution, and finally the reprecipitation of θ'. This suggests that the middle layer is both hotter than the top and bottom of the weld and cools slower than them. This observation seems inconsistent with the other welding temperatures and positions. However, the work of Mahoney et al. demonstrated that in a 6.35 mm plate of AA7075-T651, the temperature of the plate near the edge of the SZ can increase from the surface of the weld towards the middle of the plate [68]. The observation in the phase plot seems to confirm this. Additionally, in a few instances, the bottom of the plate exhibited higher temperatures than the top surface of the plate [68]. Ongoing research is needed to further investigate *in situ* welding temperatures through the depth of the plate to understand this observation.

At -30 mm and +30 mm from the center of the weld, it was expected that all of the strengthening precipitates would be present as this distance is well into the HAZ and closest to the BM. At this distance from the center of the weld, at all thicknesses, it was believed that the strengthening precipitates, θ' and Ω, would be present but coarsened. However, not all of these precipitates were present at all thicknesses and FSW temperatures. At the highest temperature, all phases were present, but at the lower temperatures, the θ/Ω phase was absent at the top and bottom of the weld at 500°C and the θ' phase was absent at the bottom at 490°C at -30 mm. At +30 mm,

θ’ and θ/Ω are present at all depths and at all temperatures. At -30 mm and 500°C, the θ/Ω absence suggests re-precipitation of the θ’ phase after θ/Ω dissolution. However, in order for that to occur in the HAZ, a heat soak similar to solutionizing temperatures and time would have to occur; the HAZ is the coolest region out of the three weld zones. The presence of all precipitates in the middle at -30 mm and 500°C indicates a complex relationship with the FSW temperature and cooling methods that is not yet understood. The presence of all three precipitates at 510°C indicates that precipitation kinetics due to FSW generally consisted of growth of all three precipitates. One could say that in the case of equilibrium θ, transformation from θ’ to θ was in process. TEM analysis is needed to further confirm the phases present at all temperatures at -30 mm.

The phase plot clearly demonstrates the asymmetry in the weld microstructure. With increasing distance from the center of the weld, 0 mm, the precipitate phases present were not identical on either side of the weld. In addition, the phase plot also reveals complex heating and cooling when $T \geq 500°C$. The lack of θ’ near the SZ and through the thickness of the plate indicates that any increases in Cu concentration in the matrix generally did not yield reprecipitation of the θ’ regardless of welding temperature and cooling rate.

More *in situ* investigations are also needed to further understand the temperature gradient through the plate thickness in thick Al alloys. TEM analysis is also needed to further confirm the identified precipitate phases, especially where thermomechanical processing occurs. Lastly, modeling and simulation of the FSW process should be investigated for thick Al-Cu-Mg-Ag alloys with high Cu:Mg ratios. Such a study should employ a multiphysics model and include peak welding temperatures and time at temperature. Thermal conductivity, emissivity, heat capacity, and flow stress of the alloy are variables that will be needed for the model. When creating the

model, care should be taken to incorporate the effects of Cu and Ag towards the thermal conductivity of the alloy. Thus, how sensitive thermal conductivity is to Cu and Ag should be evaluated. In addition, the modeling should elucidate if θ' or its nucleates (i.e. the predecessors θ" and GP zones) are affected by the tool rotation, flow with the material, and preferentially reside on either the RS or AS. Banding of the dispersions in the onion rings suggests that the precipitates flow with the material. This investigation would provide much needed information on the dissolution and precipitation kinetics in the thermomechanical zones (i.e. SZ and TMAZ) of thick, FSW Al-Cu-Mg-Ag alloys.

4.4.3 Effect of FSW Processing on Microstructure to Mechanical Behavior

The precipitate phase plot, Figure 4.74, is utilized to correlate the FSW processing (i.e. the temperatures) to the weld microstructure and mechanical properties. The precipitates in the precipitate phase plot are compared to the Vickers hardness maps which are spatially representative, see Figure 4.75. The precipitate phase plot is also used to discuss the tensile test results in section 0.

4.4.3.1 FSW at 490°C

To obtain 490°C, the spindle speed was 150 RPM when plunging and then reduced to speeds ranging between 98-110 RPM to maintain the temperature as shown in Figure 3.5. The blue area on the Vickers hardness map in Figure 4.75 correlate to -10 to 10 mm (bottom), -20 to +20 mm (middle and top) and has the lowest hardness. The FSW processing led to relatively no θ' and Ω precipitates within the SZ. However, near the TMAZ/SZ interface at -10 and +10 mm from the weld center at the bottom layer, it is possible that the detected θ' and Ω precipitates are coarsened. This change in microstructure from the center of the weld towards the base metal may explain why the tensile samples fractured in this area on the retreating side. Tensile tests paired with digital imaging correlation confirmed that fracture initiates in this area before propagating

towards the top of the weld [94]. Thus, it is believed that the evolving microstructure (equiaxed SZ grains to the rotated TMAZ grains along with coarsened θ precipitates to coarsened Ω and θ') affect the deformation. The fracture appears to be characteristic of welds conducted at 490°C as this fracture location differs from the 500°C FSW.

4.4.3.2 FSW at 500°C

To maintain the 500°C welding temperature, rotational speeds ranged between 170 to 180 RPM, see Figure 3.6. Grain growth in the SZ was observed at this temperature. In contrasts to the 490°C friction stir weld, the lowest hardness areas (blue in color) were outside of the SZ with the exception bottom layer. Although the hardness is relatively the same in this area bounded between 10 to 20 mm from the weld center (it extends to 30 mm on the retreating side in the middle layer), θ' is detected further away from the SZ where the hardness increases (green in color) in the HAZ. In comparison to the 490°C weld where the fracture was located at the interface of SZ/TMAZ, the 500°C weld fracture location was in the HAZ on the retreating side. This raises questions as to why the fracture would move to the HAZ instead of remaining in the SZ/TMAZ interface due to the juxtaposition of the hardened SZ and softer TMAZ. TEM and chemical analysis in the SZ would provide clarity to this observation and on the possible strengthening mechanisms in the SZ. Studies have demonstrated that the dynamically recrystallized SZ has a low dislocation density but it is not clear as to whether there is a gradient through the weld thickness [10,11]. Solid solution strengthening and reprecipitation and coarsening via dislocation may be observed in the SZ when there are two hardness regimes, the upper and lower weld nugget. In the upper weld nugget where the hardness is higher and cooling is slower, solid solution strengthening due to the re-solutioned precipitates θ' and Ω/θ may be observed [63,77]. The lower precipitate volume percent and the absence of the strengthening precipitates in the precipitate phase plot (and the constant-speed TEM images) supports this, however, TEM analysis on the

500°C weld is necessary to confirm this. In the lower weld nugget where the cooling rate was faster and the welding temperature was cooler, heterogeneous nucleation and growth of precipitates facilitated by dislocations may be observed [63,77]. The coarsened precipitates and dislocations seen in Figure 4.21 and Figure 4.22 supports this hypothesis. Digital image correlation for the 500°C FSW tensile tests can further provide information on where stress is concentrated and why the HAZ was preferred over the SZ/TMAZ interface. Regardless of differences in the microstructure and the Vickers hardness, the tensile performance was similar to that of the 490°C FSWs. Thus, FSW at 500°C is an acceptable welding temperature.

4.4.3.3 FSW at 510°C

To maintain the target FSW temperature of 510°C, the rotational speeds ranged between 237 to 253 RPM, see Figure 3.7. At 510°C, grain growth in the upper and lower half of the SZ was observed. In addition, the entire SZ increased in hardness in comparison to the 490°C and 500°C friction stir welds. The missing precipitates in the middle layer of the SZ suggests that the middle of the weld may be hotter than the top and bottom of the weld. Regardless of the increase in hardness and grain size in the SZ, FSW at 510°C led to voids in the mid top and top layers of the SZ, which served as crack initiation sites during the tensile tests. As a result, premature failure occurred for every sample and any advantage the improved SZ would have provided was not observed. FSW temperatures ≥510°C is not recommended to produce quality welds.

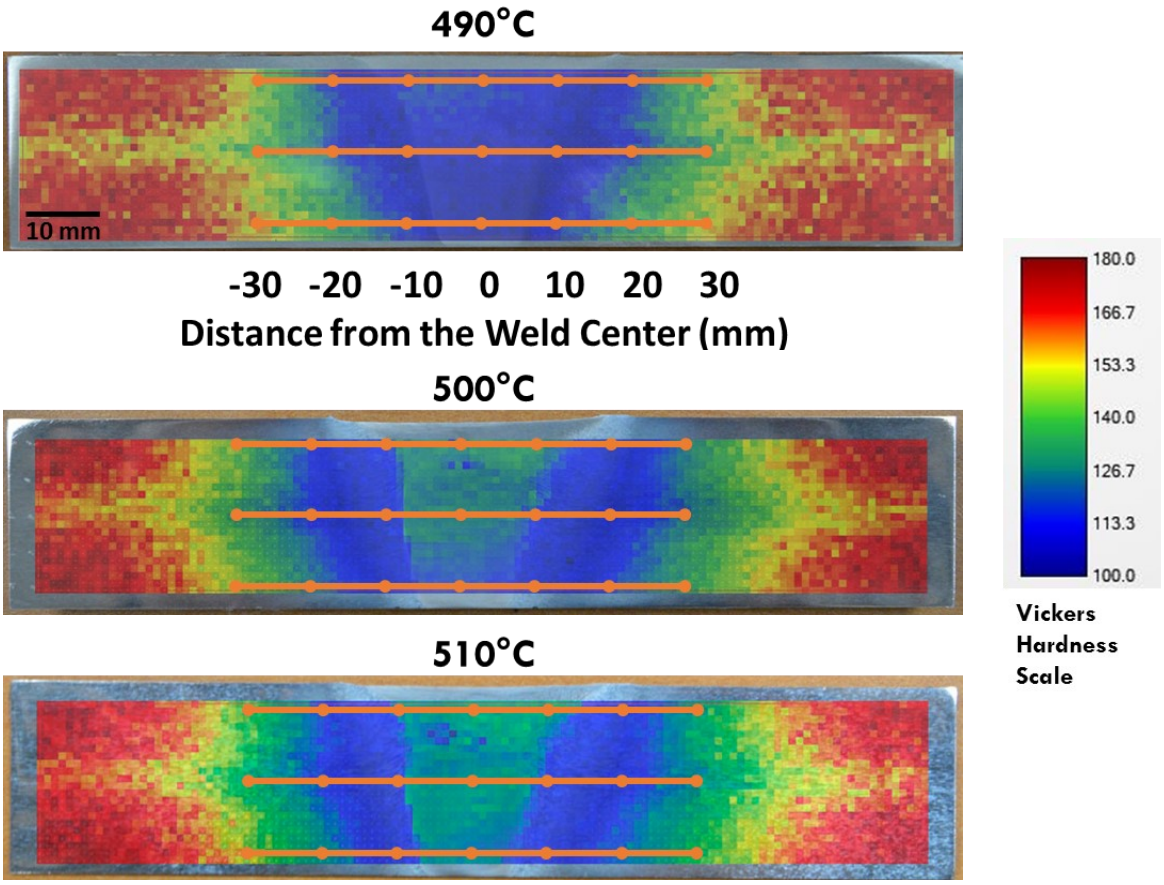

Figure 4.75. Constant-temperature FSWs Vickers hardness maps with orange markers showing where the XRD data was acquired (i.e. at the top, middle, and bottom layers). Negative distances represent the AS, while positive distances represent the RS.

CHAPTER 5

SUMMARY, CONCLUSIONS, AND FUTURE WORK

5.1 Summary

This dissertation described a systemic study of FSW processing of a 25 mm thick Al-Cu-Mg-Ag alloy, AA2139-T8. Processing-microstructure-property relationships were studied using both constant-speed (150 RPM and 50 mm/min) and constant-temperature FSW (performed at 490°C, 500°C, and 510°C). Thermocouples were spot welded to the surface of the tool shoulder for *in situ* temperature measurements during the constant-temperature FSW. The microstructural evolution throughout the thickness of the weld was analyzed via optical microscopy, SEM, TEM, and XRD. The mechanical behavior was analyzed using RT and 300°C tensile experiments and RT Vickers hardness experiments. The distribution of the different precipitates was plotted throughout the welded area for the constant-temperature FSW materials. The work in this dissertation provides new insights into the effects of constant temperature FSW on the microstructural evolution and the mechanical properties through the weld thickness. The knowledge gained from this work will not only assist in determining optimal welding parameters for this alloy for targeted applications, but will also serve as a framework for future research targeted at understanding processing-microstructure-property relationships of a variety of metallic systems undergoing not only FSW under controlled conditions but also undergoing different controlled thermomechanical processing treatments.

5.2 Conclusions

5.2.1 Microstructure of Constant-Speed FSW

(1) The average grains size throughout the depth of the SZ exhibited an inverse relationship with the precipitate volume percent (i.e. the grain size decreased from the weld top to bottom,

while the precipitate volume percent increased from the weld top to bottom). This is due to the differences in peak welding temperatures at the top (hotter) and bottom (cooler). Differences in temperature are due to the tool dimensions; the relatively large shoulder diameter generates more heat than the relatively small pin diameter. Thus, the temperature at the weld top was high enough for both grain growth and precipitate dissolution to occur. In addition, the heat transfer methods differed between the top (ambient air convection) and the bottom (conduction); conduction heat transfer rates are faster than convection heat transfer rates. As a result, the bottom of the weld experienced faster cooling rates, which inhibited grain growth.

(2) Due to the complicated thermomechanical processing occurring within the welded region, the SZ exhibited a lower precipitate volume percent than the BM.

(3) Metastable precipitates, θ' and Ω, were not observed in the center of the SZ due to their dissolution during the FSW process.

(4) The Ω phase precipitates were detected away from the center of the SZ in the UWN. The *in situ* XRD heat treatments demonstrated that θ' dissolves before Ω.

(5) PWHT resulted in a slightly increased precipitate volume percent throughout the depth of the weld, but did not significantly affect the average grain size.

5.2.2 Mechanical Behavior of Constant-Speed FSW

(1) The SZ exhibited lower strengths and hardness than the BM.

(2) The SZ exhibited an UWN and LWN, and the UWN exhibited higher Vickers hardness and tensile strengths than the LWN. TEM did not reveal the θ' and Ω precipitates in the SZ, while the θ phase precipitate volume percent increased slightly from the UWN to the LWN Solid-solution strengthening was explained to be the dominant strengthening mechanism within the SZ.

(3) PWHT above 247°C did not increase the tensile strength or Vickers hardness of the weld. PWHT at 200°C locally increased the hardness and tensile YS of the UWN. This suggests

that reprecipitation of the dissolved strengthening phases, θ' and Ω, may have occurred at 200°C.

5.2.3 Microstructure of Constant-Temperature FSW

(1) Similar to the constant-speed FSW, there was a gradient in the grain size and precipitate volume percent. In general, the grain size decreased from the top of the weld towards the bottom and the precipitate volume percent increased from the top to the bottom. The explanation for this observation is the same as depicted in (1) in section 5.2.1.

(2) Compared with the other constant-temperature FSWs, the 490°C constant-temperature FSW yielded the smallest average grain size and the highest precipitate volume percent throughout the SZ.

(3) No distinct UWN and LWN were observed in the 490°C constant-temperature FSW.

(4) Voids were detected in the upper half of the weld in the SZ for the 510°C and 500°C constant-temperature FSWs.

(5) Grain growth was observed for the 510°C and 500°C constant-temperature FSWs.

(6) The average grain size increased with increased welding temperature.

(7) The shape of the SZ and the width of the TMAZ was influenced by the pin-shoulder interface with increasing temperature. There was more plastic flow due to the fact that the rotational speed had to increase to maintain the higher target welding temperature. In addition, voids were present within the pin-shoulder interface for the 510°C and 500°C constant-temperature FSWs. At higher temperatures, the voids were more deleterious to the tensile strength of the weld. Void formation was likely due to the competing material flow from the shoulder and the pin.

5.2.4 Mechanical Behavior of Constant-Temperature FSW

(1) The hardness values were similar throughout the SZ for the 490°C constant-temperature FSW.

(2) A gradient in the hardness values was observed with the top exhibiting the highest

hardness values and the bottom exhibiting the lowest hardness values for the 510°C and 500°C constant-temperature FSWs.

(3) The 490°C and 500°C FSWs exhibited similar tensile properties while 510°C FSWs exhibited the lowest tensile YS, UTS, ε_f, and joint efficiency. This reduction in the mechanical properties was due to the voids, which served as crack initiation sites.

(4) RT tensile fractures in the 490°C and 500°C constant-temperature FSW samples occurred near the TMAZ/SZ interface and in the HAZ on the RS. The precipitate analysis indicated that the RS was hotter than the AS, which helps explain why the fracture occurred on the RS.

(5) The highest average joint efficiency was observed in the 490°C constant-temperature FSW due to a reduced HAZ. However, the highest average ε_f was exhibited by the 500°C constant-temperature FSW due to failure in the HAZ rather than at the SZ/TMAZ interface, which occurred for the 490°C constant-temperature FSW samples.

5.2.5 Impact of Constant-Temperature FSW on Optimizing FSW Processing

(1) In order to achieve higher target FSW temperatures in a 25 mm thick Al-Cu-Mg-Ag alloy, the rotational speed must be increased. Rotational speeds of 98-110 RPM, 170-180 RPM, and 237-253 RPM yielded welding temperatures of 490°C, 500°C, and 510°C, respectively.

(2) At temperatures $\leq$490°C, the torque was double that of the samples welded at temperatures $\geq$500°C.

(3) Welding at T=490°C yielded fractures along the SZ/TMAZ interface on the RS, whereas welding at T=500°C yielded fractures in the HAZ. Thus, increasing the hardness of the SZ, which occurs at T=500°C, moves the fracture site away from the SZ without impacting the tensile strengths and ε_f.

(4) Welding at T=510°C introduced large voids and grooves in the weld that reduced the tensile YS, UTS, ε_f, and joint efficiency. Therefore, it is not recommended to weld at 510°C. However, more work is needed to determine if the voids are a function of tooling (features and material) and/or welding travel speeds.

(5) The PWHTs did not improve the overall mechanical behavior in the constant-speed FSWs. This is due to the two different weld nuggets, UWN and LWN, which exhibited distinct microstructures. It was observed that in the UWN, where the precipitate volume percent was lower and the hardness was higher, PWHT did improve the hardness when compared to the as-welded sample. It is possible that in the 500°C and 510°C constant-temperature FSWs, PWHT may improve the hardness in the SZ since the microstructure and hardness throughout the SZ is similar to that in the UWN of the as-welded constant-speed FSW. This improvement in hardness due to the PWHT could be due to reprecipitation of the θ' and Ω phases. However, it is not expected that the adjacent weld zones, TMAZ and HAZ, will see improvement as they contain coarsened precipitates and equilibrium phases. As a result, localized PWHT on the SZ should be employed.

5.3 Recommendations for Future Work

(1) To gain a more thorough understanding of the TMAZ, ASTM sub-standard size tensile samples, or a modified version of them, along with Vickers hardness tests, with a spatial resolution no larger than 0.5 mm x 0.5 mm, should be employed. Tensile failure of the 490°C and 500°C constant-temperature FSWs occurred at the SZ/TMAZ and HAZ/TMAZ interfaces. Using TEM and XRD to characterize the precipitate phases present at these interfaces would permit a more thorough correlation of the microstructure to the mechanical properties.

(2) Incorporating more thermocouples in the middle and root of the tool pin would allow more direct monitoring of the FSW temperatures in the middle and bottom of the weld. This

information would help elucidate the observed mid-plate softening upon FSW and the driving forces behind dissolved precipitates at the middle of the weld as indicated by the XRD data.

(3) TEM and EDS analysis in the center of the weld, at incremented distances from the center, and throughout the depth of the weld will provide more information on how the microstructure changes with temperature. Such analysis should focus on dislocation networks and phase transformations.

(4) Previous work was performed on the heat transfer throughout the plate, but this was performed without temperature-controlled FSW. In addition, this has not been performed on plates of thicknesses greater than or equal to 25 mm nor AA2139. The temperature-controlled FSW of 25 mm thick AA2139-T8 plates had a number of challenges, most of which centered around the thermal conductivity of this alloy. For other Al alloys, namely 25 mm thick AA5083, the rotational speed was reduced during welding in order to maintain the target weld temperature. In the case of AA2139, the rotational speed had to be continually increased to reach and maintain the target temperature. Investigations on the hot deformation behavior and the strain rate sensitivity of the flow stress would provide useful insight on FSW temperatures, tool forces, and tool design.

(5) Modelling and simulation of the precipitation events in FSW, thick Al-Cu-Mg-Ag alloys is still needed to understand the impact of the FSW on the precipitation sequence. However, the influence of the Mg and Ag alloying elements must be incorporated as they are critical to the precipitation of the Ω phase.

(6) This work was limited to a welding speed of 50 mm/min due to the machine capabilities and tooling design. For industrial applications that require a high throughput, this speed may not be sufficient and the tooling design may not be capable of handling the forces. An investigation on constant-temperature FSW as a function of speed and the influence of the microstructure and

mechanical properties is recommended.

(7) The influence of various tooling designs (features, dimensions, material) on welding speeds, temperature, microstructure, and tool forces should be studied.

(8) The investigation in (6) could then be used to study high strain-rate activity as a function of welding temperature.

(9) Another limitation of this dissertation was the thickness of the plate, 25 mm, on which a one-pass welding was performed. That is, only one pass of the tool was made to create the weld. For sectors that require much thicker plates, multiple passes may be needed in order to weld the full thickness of the plate. For instance, a 76.2 mm (3 inch) thick plate may require one pass on the top side and the bottom side of the plate with a 38 mm long tool. Understanding how welding temperature influences the microstructure and properties of a double-pass weld is necessary. This could inform the welding parameters and sequence. For instance, should both sides be welded at the same temperature or should one side be hotter than the other? In addition, for dissimilar temperatures, is it recommended that the hottest temperature be the first weld pass? Is it beneficial that the RS for the second pass is on the same side of the plate as the first pass to improve the fracture (ε_f, fracture location) and does this change with dissimilar welding temperatures?

APPENDICES

APPENDIX A

DARK FIELD TRANSMISSION ELECTRON MICROSCOPY

This section contains the dark field (DF) TEM photomicrographs of the unwelded AA2139-T8 in the <100> and <110> zone axes. Selected area diffraction patterns are provided with the highlighted diffraction spots correlated to the DF photomicrographs. Bright field (BF) photomicrographs are provided for reference.

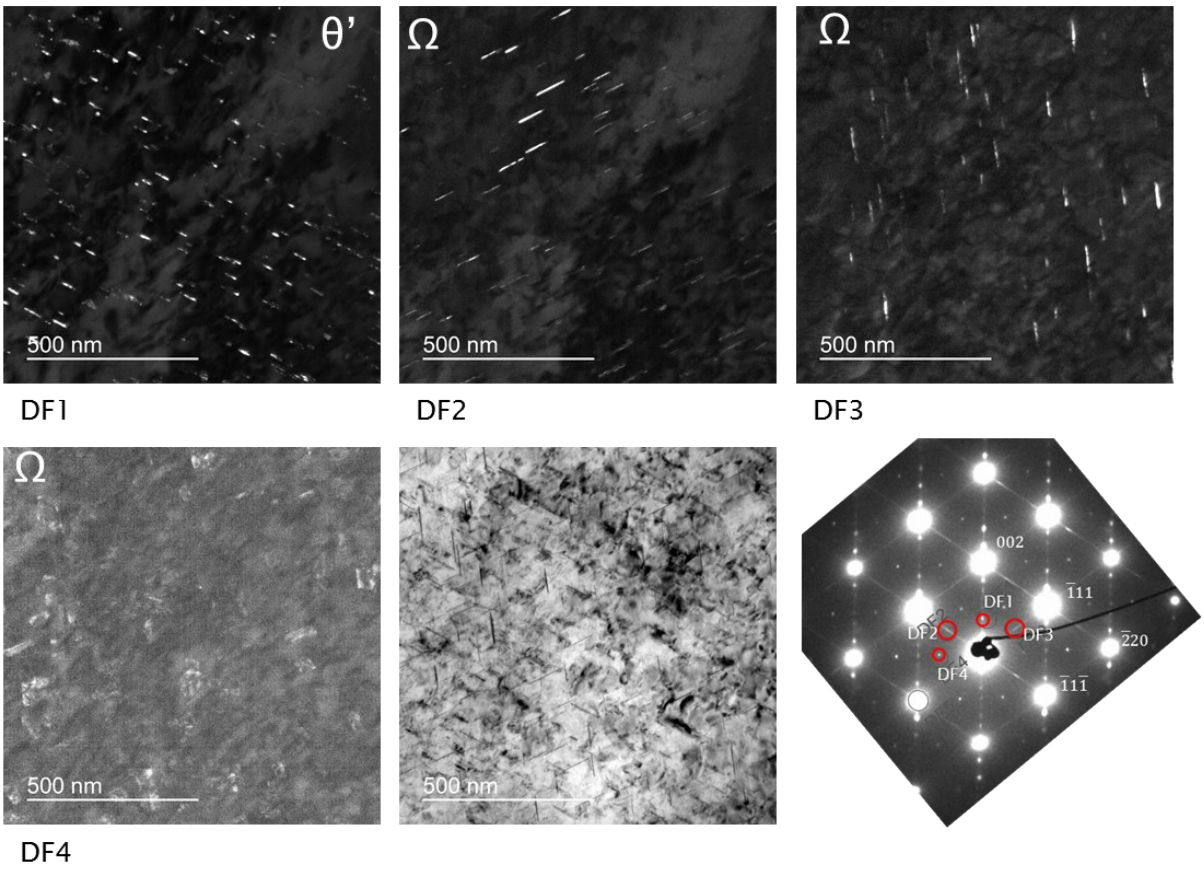

Figure A.1. TEM photomicrographs of the unwelded AA2139-T8 depicting the θ' and the Ω phases in the <110> zone axis. Dark field (DF) photomicrographs are indicated in the first four images, while the last photomicrograph indicates the BF photomicrograph.

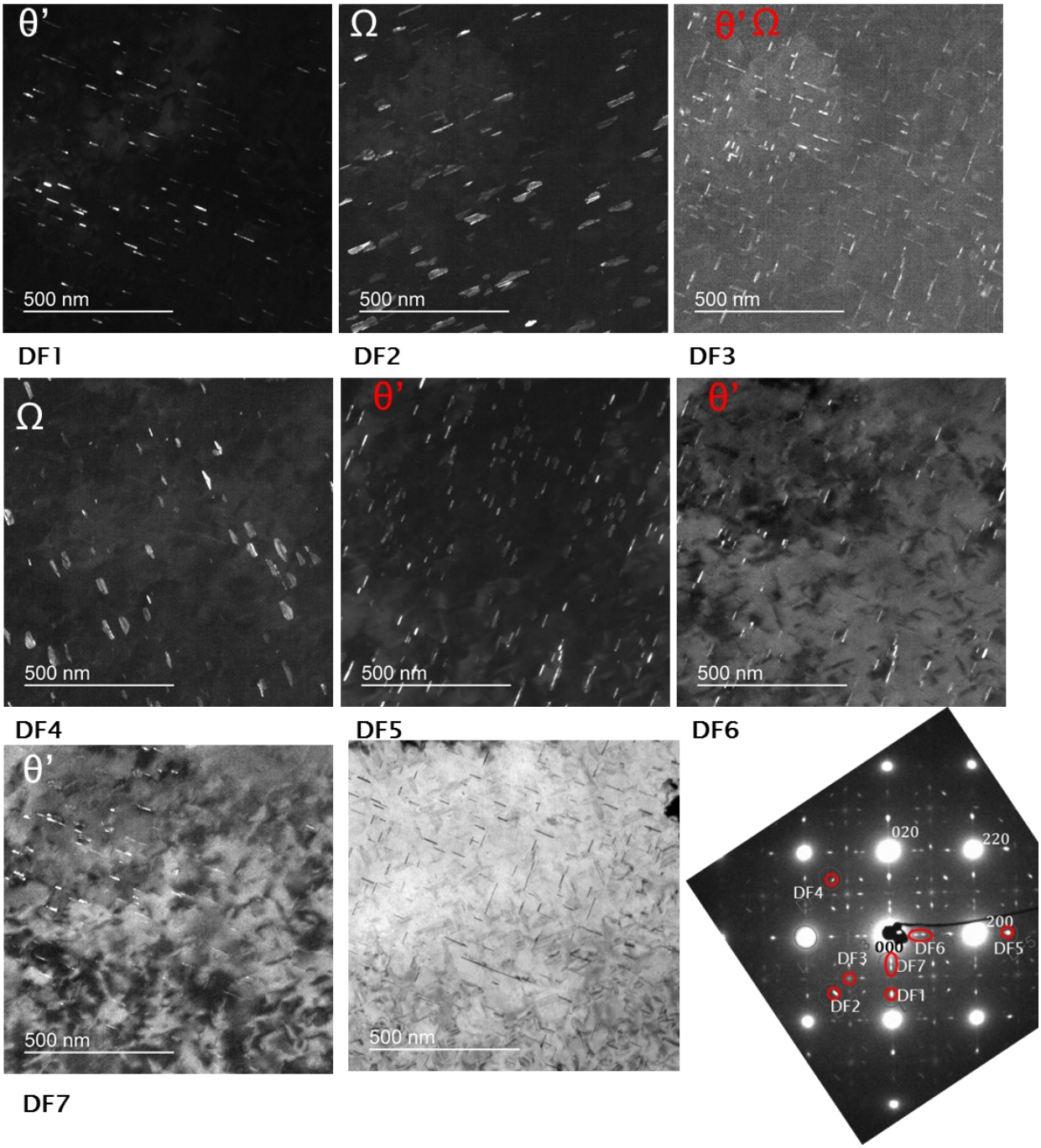

Figure A.2. TEM photomicrographs of the unwelded AA2139-T8 depicting the θ' and the Ω phases in the <100> zone axis. Dark field (DF) photomicrographs are indicated in the first seven images, while the last photomicrograph indicates the BF photomicrograph.

APPENDIX B

SIMULATED SELECTED AREA DIFFRACTION PATTERNS

This section contains the simulated selected area diffraction patterns for the θ' and Ω precipitate phases. Simulations were made using the CrystalMaker® software. The simulations show the allowed and forbidden diffraction spots in the <100>, <110>, and <111> zone axes. First, each of the three variants of the $<100>_{\theta'}$ diffraction patterns were overlaid on top of the simulated diffraction pattern of the [001] α-matrix (FCC Al) zone axis. Then, all of the variant orientations were overlaid (i.e. on top of each other) to provide the resultant diffraction pattern. Next, the resultant simulated diffraction pattern was compared to the experimental diffraction pattern. Lastly, the precipitate diffraction spots were labelled on the experimental diffraction pattern. The same was done for the <110> and <111> zone axes. All steps were repeated for the Ω precipitate phase.

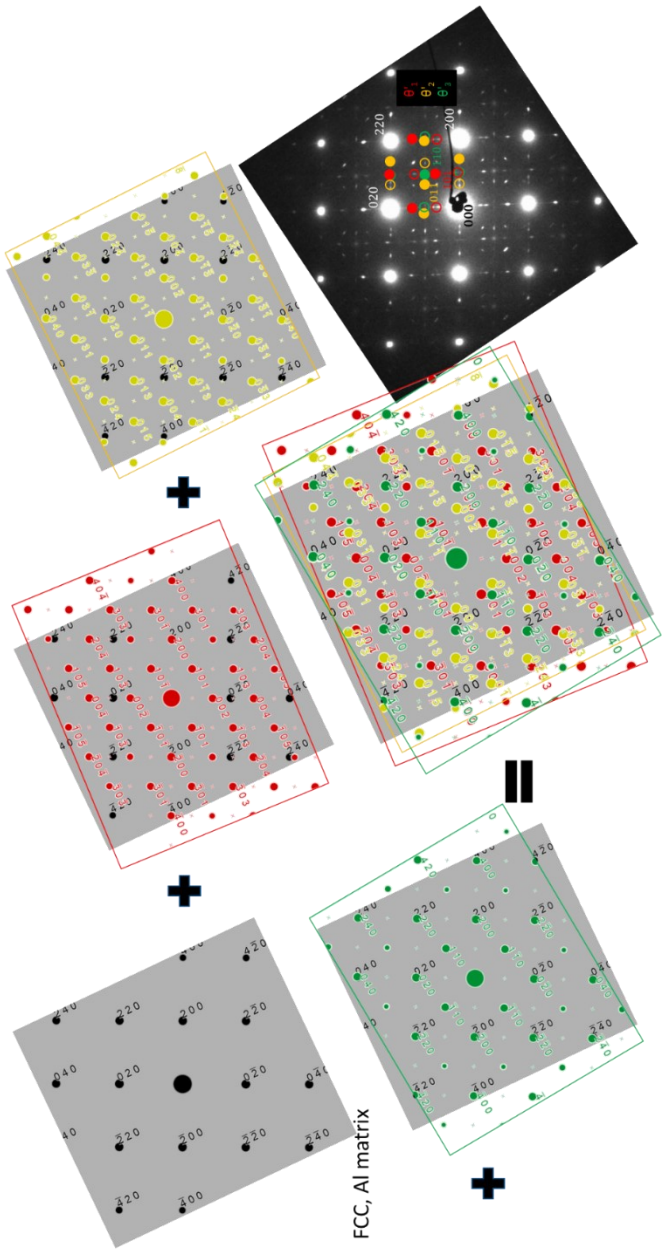

Figure B.1. Simulated diffraction patterns of three <100> variants for the θ’ precipitate phase. The θ’ precipitate diffraction spots are labelled on the experimental selected area diffraction pattern for the <100> Al-matrix zone axis.

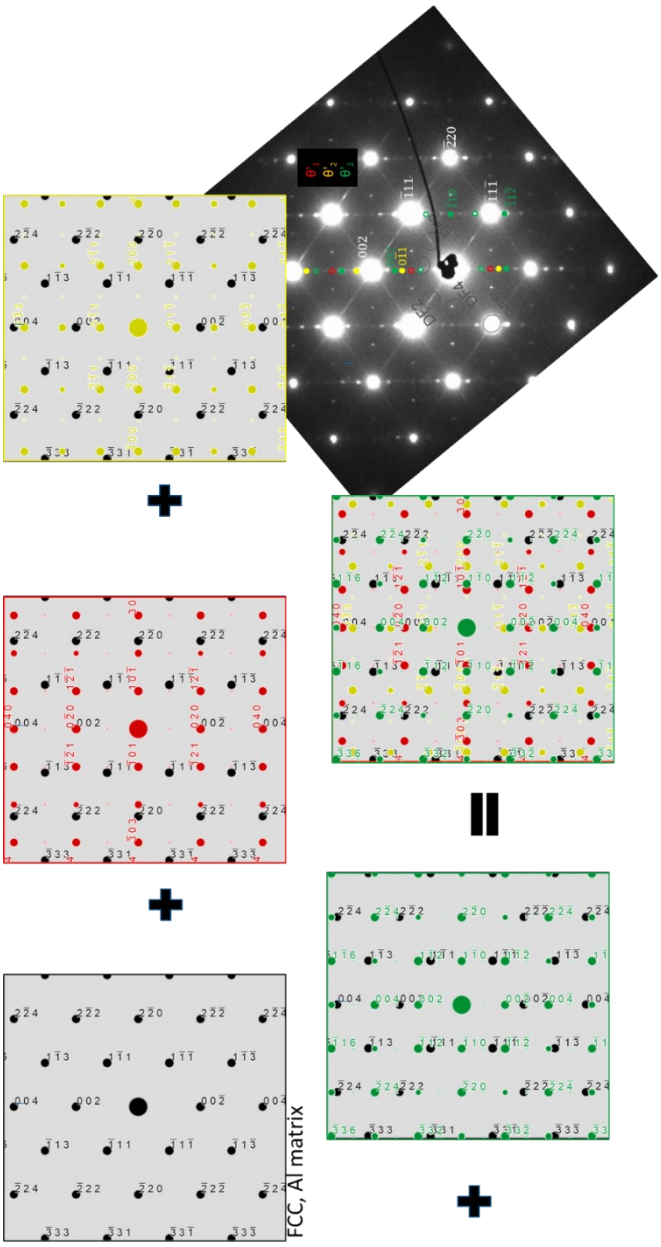

Figure B.2. Simulated diffraction patterns of three <110> variants for the θ’ precipitate phase. The θ’ precipitate diffraction spots are labelled on the experimental selected area diffraction pattern for the <110> Al-matrix zone axis.

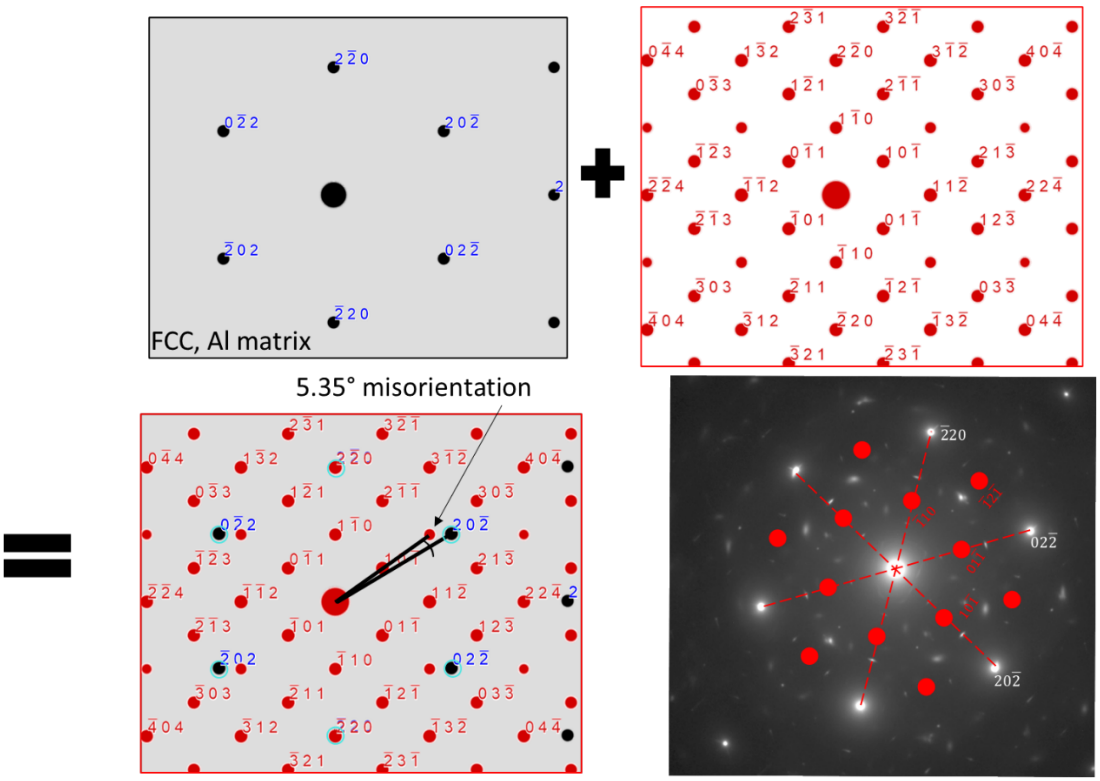

Figure B.3. Simulated diffraction patterns of <111> orientations for the θ' precipitate phase. The θ' precipitate diffraction spots are labelled on the experimental selected area diffraction pattern for the <111> Al-matrix zone axis.

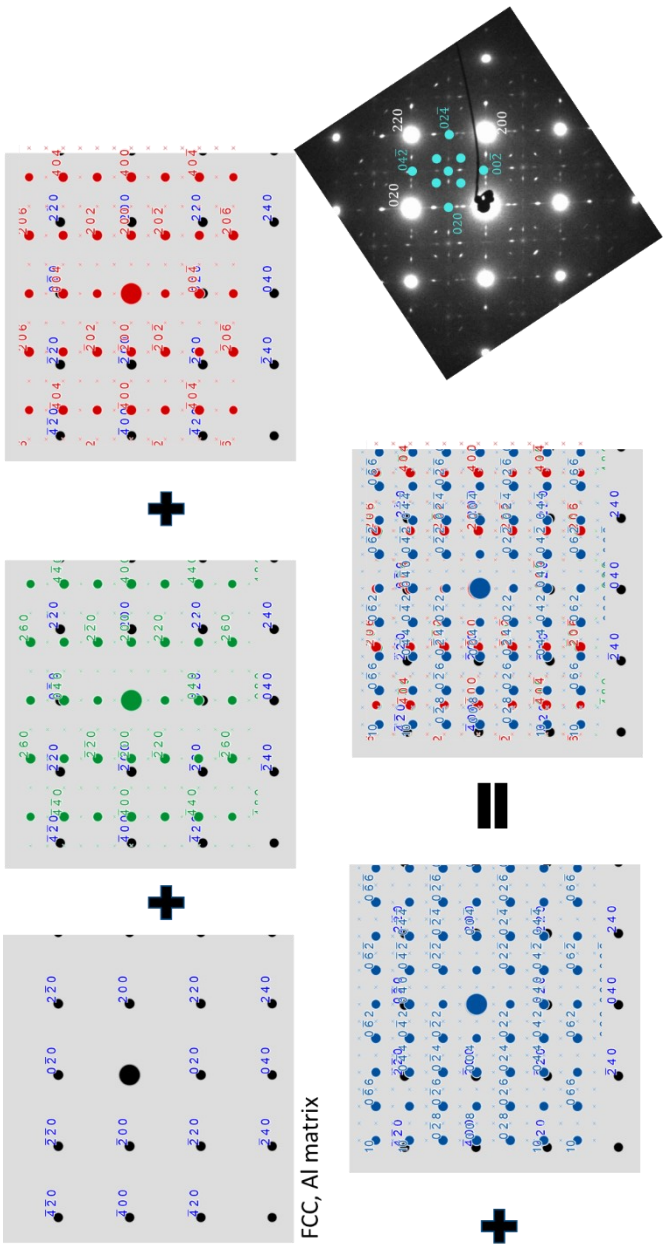

Figure B.4. Simulated diffraction patterns of three <100> variants for the Ω precipitate phase. The omega precipitate diffraction spots are labelled on the experimental selected area diffraction pattern for the <100> Al-matrix zone axis.

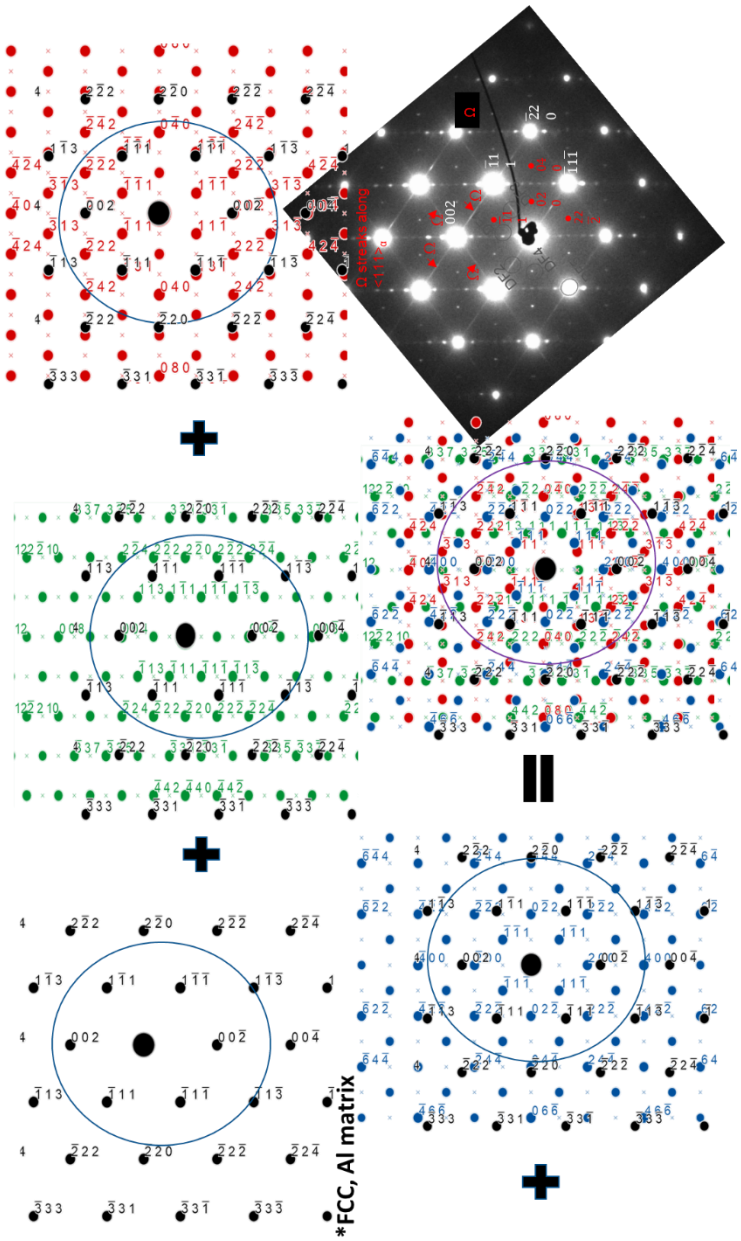

Figure B.5. Simulated diffraction patterns of three <110> variants for the Ω precipitate phase. The omega precipitate diffraction spots are labelled on the experimental selected area diffraction pattern for the <110> Al-matrix zone axis.

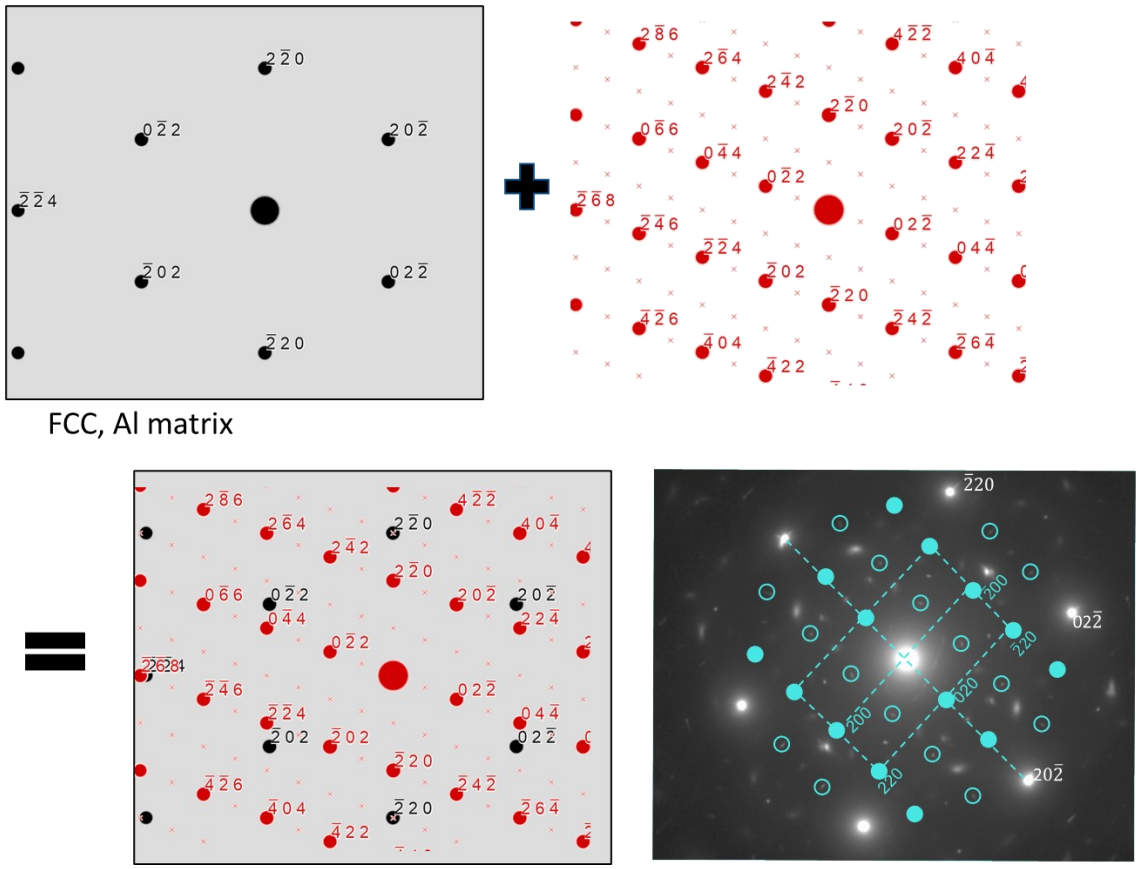

Figure B.6. Simulated diffraction patterns of the <111> variants for the Ω precipitate phase. The omega precipitate diffraction spots are labelled on the experimental selected area diffraction pattern for the <111> Al-matrix zone axis.

APPENDIX C

IN SITU TENSILE BEHAVIOR FOR THE AS-RECEIVED AA2139-T8

C.1 *In Situ* Testing Procedure

Smaller dogbone-shaped samples, see Figure 3.16, were used for the *in situ* tensile and creep experiments performed in the SEM. The small dogbone-shaped specimens were EDM machined and sliced through the thickness of the plate. The gage section width and thickness were machined to 3 mm and 1.8 mm, respectively, see Figure C.1.

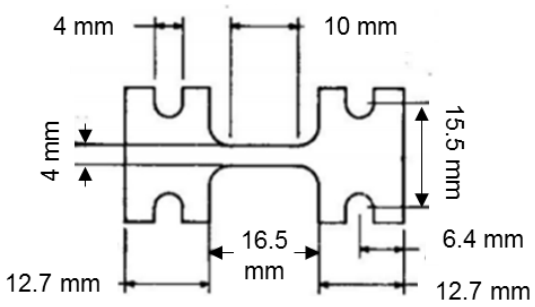

Figure C.1. Schematic representing the specimens used for the *in situ* tensile and creep experiments.

Standard metallurgical grinding and final polishing, as described in section 3.1.3, were performed on the *in situ* samples. To enhance the imaging quality, some samples were chemically polished using 100mL of methanol, 12 mL of HCl, 8 mL of nitric acid for approximately 10 seconds. They were then rinsed with ethanol and dried with a warm stream of air. If samples were not immediately analyzed or tested, then they were stored in a vacuum chamber to delay excessive oxidation.

The smaller dogbone-shaped samples were tensile tested using an Ernest F. Fullam, Inc.

(Lantham, NY[9]) tensile stage placed inside the TESCAN Mira3 SEM. This stage is screw-driven and can perform monotonic, segmented, and cyclic (load, displacement, and strain) controlled experiments via the MTESTW version F3.3e data acquisition and control software (Admet, Inc., Norwood, MA). A fiducial mark was placed on the samples to more easily track the microstructural area of interest during the deformation. These samples were imaged prior to deformation. EBSD maps were acquired before and after the deformation in the same area.

The *in situ* tensile tests were conducted at RT and 300°C at a constant displacement rate of 0.004 mm-s^{-1}, which corresponds to a strain rate of 10^{-3} s^{-1}. The temperature was controlled using a resistive heating unit, located under the sample, and a constant voltage power supply. The temperature was monitored using thermocouples on the sample and was manually recorded. Data output included time, load, and displacement. The displacement data was not isolated to the gage section and incorporated both the gage section and grip sections. To determine the strain of the sample, local strain measurements on the sample surface were made during the deformation. This was accomplished by measuring the distance in the tensile direction between two chosen reference precipitates, which were identified using SE SEM images. This measurement was assisted using the ImageJ software (National Institute of Health). The samples were tensile tested in both the TD and the RD.

C.2 *In Situ* Tensile Test Results

In situ tensile testing was performed in the TD and RD at room temperature (RT) and 300°C for the as-received AA2139-T8. The engineering stress-displacement plots are represented in Figure

[9] Ernest F. Fullam, Inc was originally located in Lantham, NY. It was later acquired by MTI Instruments (Albany, NY)

C.2 and the YS and UTS are summarized in

Table 5.1. The stress drops in the curves occurred when the test was paused for imaging. The YS of the TD is higher than the RD at both temperatures. At 300°C, the UTS of the TD is less than the RD.

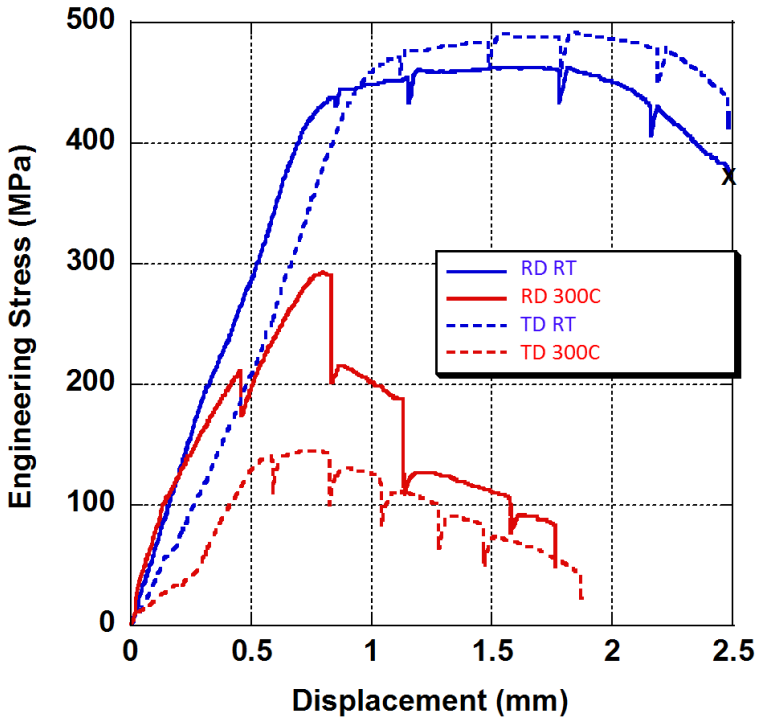

Figure C.2. Stress vs. displacement plot for the base metal tested at room temperature and 300C in the rolling direction (RD) and the transverse direction (TD). "X" indicates samples taken to failure. Displacement values include displacement in the sample grip. Sudden decreases in stress indicate where the testing was paused for imaging.

Table 5.1. AA2139-T8 base metal *in situ* tensile property comparison.

	BM RD, RT	BM TD, RT	BM RD, 300°C	BM TD, 300°C
YS (MPa)	418	470	110	140
UTS (MPa)	460	486	292	144

The progression of the surface deformation at RT and 300°C in the RD and TD are shown in Figures C.3 to C.6. The numbered areas on the plot correlate to the photomicrograph numbers and the calculated strain is shown beneath each photomicrograph. Grain boundary (GB) topography was first observed at RT in the RD at 2.3% strain, Figure C.3 and 3.1% strain in the TD, Figure C.5. At 7% strain in the TD, the fiducial mark that crossed a grain was displaced at the grain boundary. This suggests that grain boundary sliding (GBS) likely occurred. Slip traces were first detected at 3.1% in the TD at RT. At 300°C, grain boundary relief was first observed in the RD at 7% strain, Figure C.4, and 3.7% in the TD, Figure C.6. Slip traces were first detected at 7% strain and 12% strain in the RD and TD, respectively. Cracks at the GBs and triple junctions were observed in the TD at room temperature, Figure C.5 (4). GB cracks were also detected at 300°C in the RD, Figure C.4 (5).

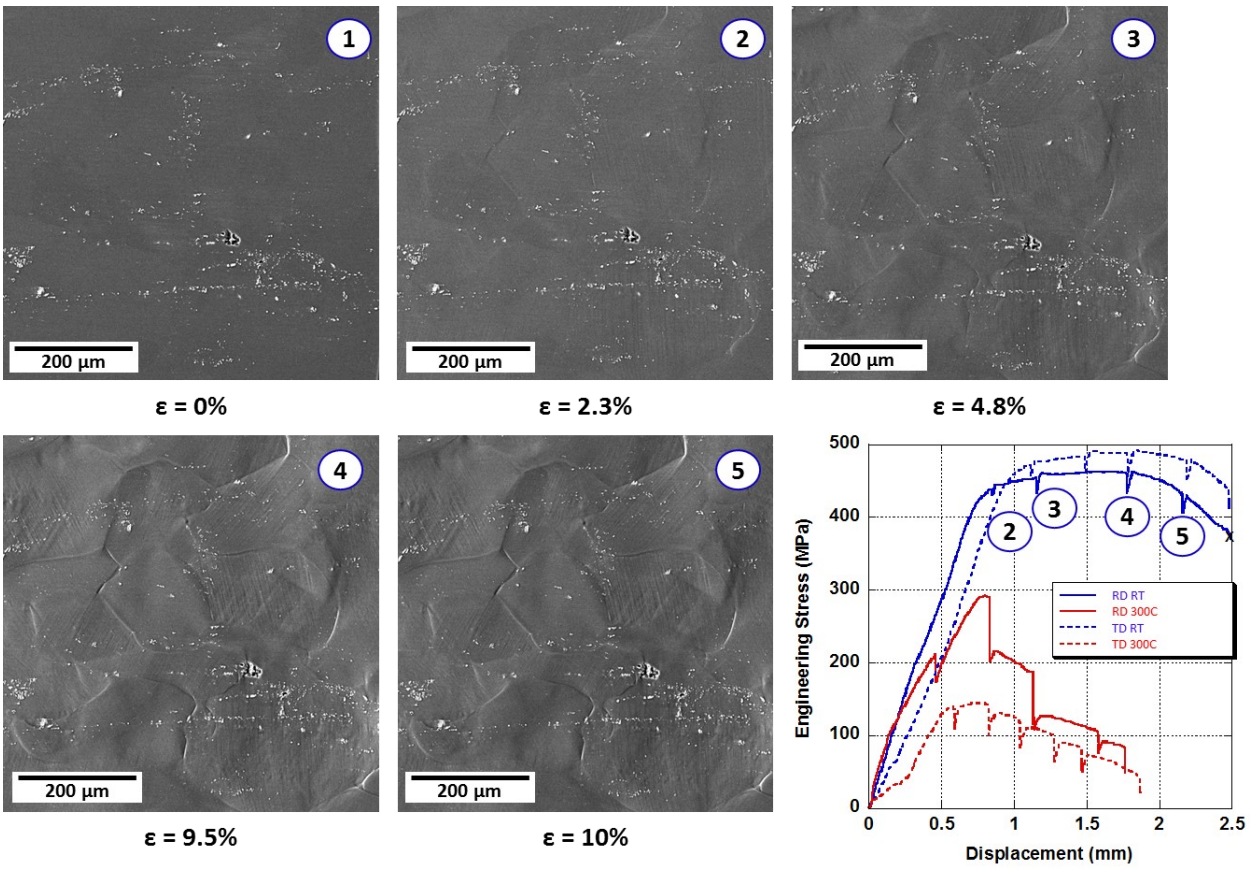

Figure C.3. Sequential SE SEM micrographs for AA2139-T8 *in situ* tensile tested at room temperature (RT) in the rolling direction (RD). Strain at time of loading is indicated below the photomicrograph. Numbered micrographs). The engineering strain is indicated below the photomicrograph. Numbered micrographs correspond to the numbers on the stress-displacement curve. The tensile axis is horizontal.

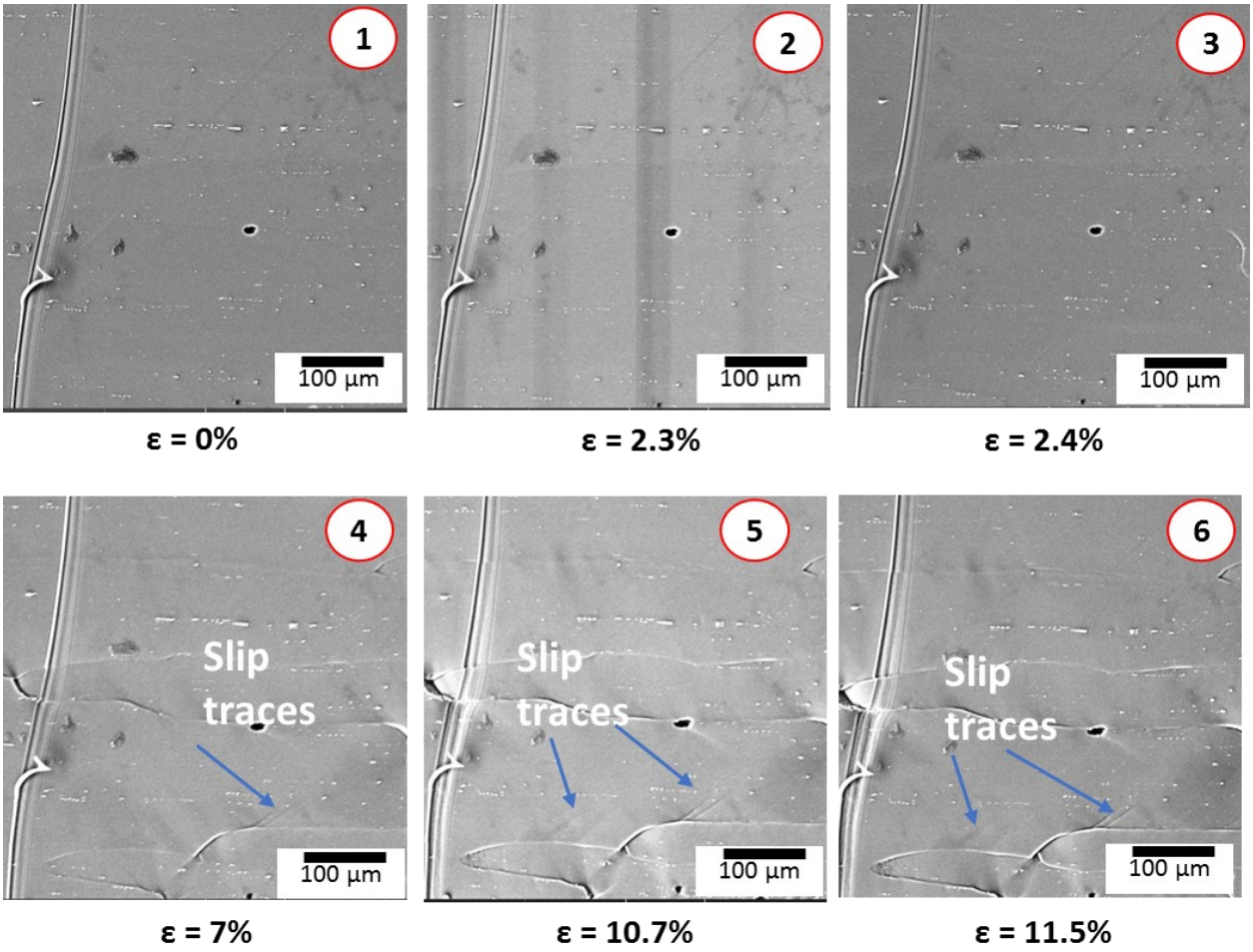

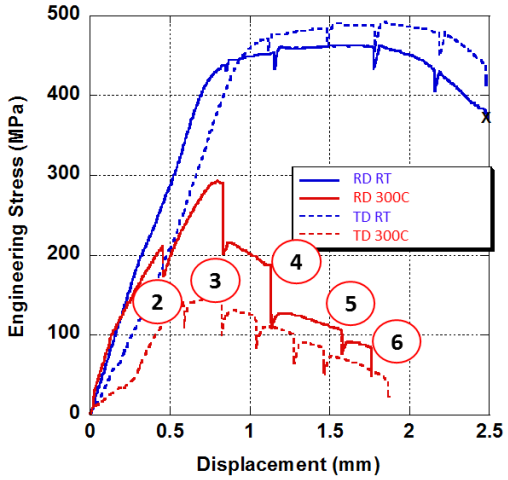

Figure C.4. Sequential SE SEM photomicrographs for AA2139-T8 *in situ* tensile tested at 300°C in the rolling direction (RD). The engineering strain is indicated below the photomicrograph. Numbered photomicrographs correspond to the numbers on the stress-displacement curve. The tensile axis is horizontal.

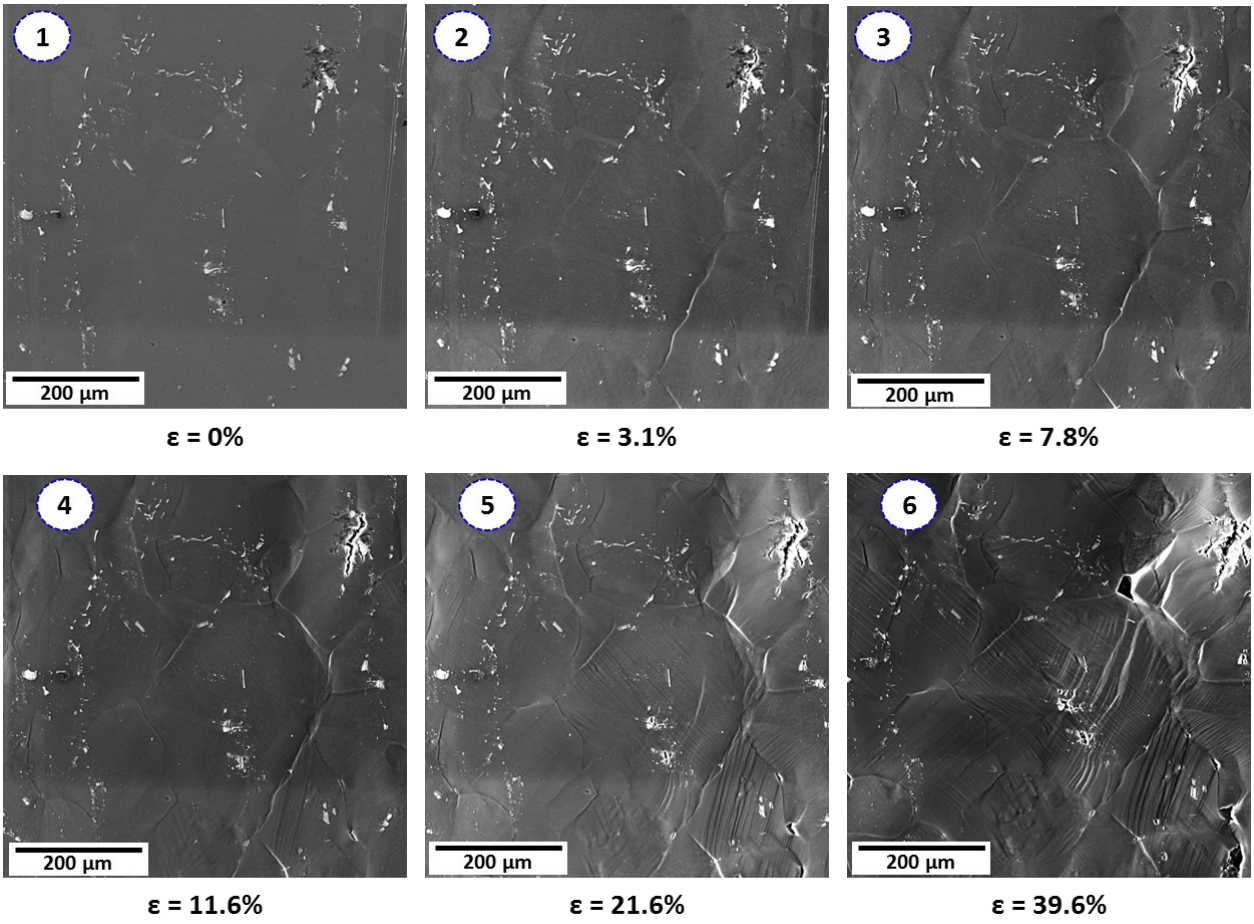

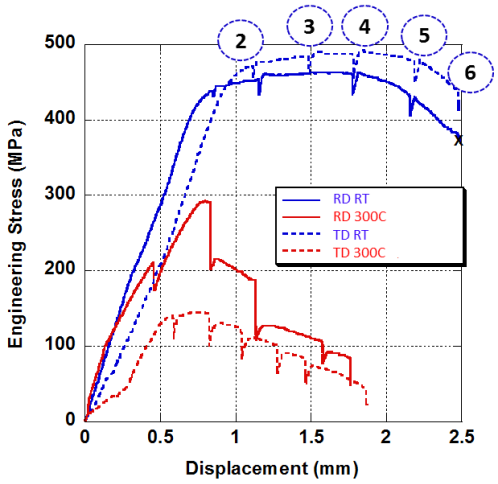

Figure C.5. Sequential SE SEM photomicrographs for AA2139-T8 *in situ* tensile tested at RT in the TD. The engineering strain is indicated below the micrograph. The numbered photomicrographs correspond to the numbers on the stress-displacement curve. The tensile axis is horizontal.

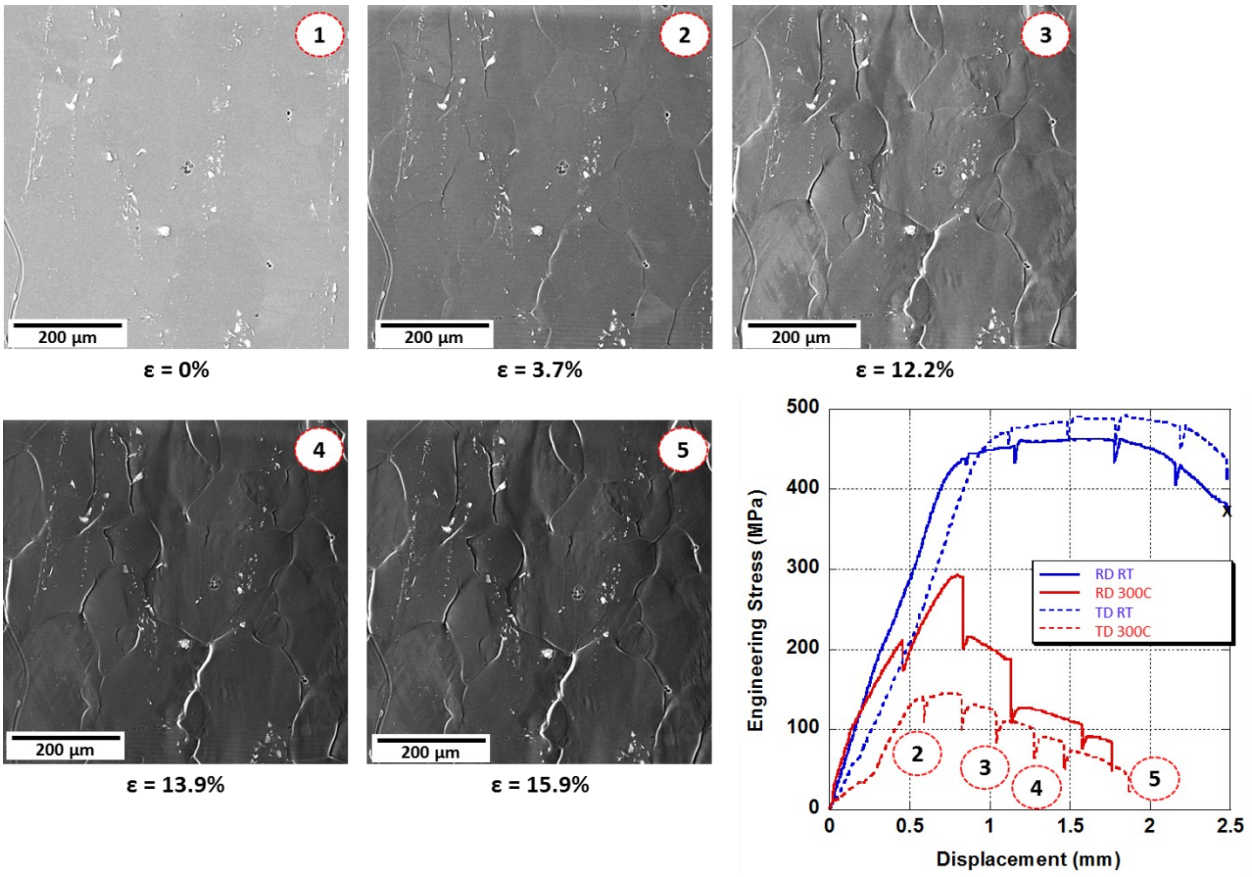

Figure C.6. Sequential SE SEM photomicrographs for AA2139-T8 *in situ* tensile tested at 300°C in the TD. The engineering strain is indicated below the photomicrograph. The numbered photomicrographs correspond to the numbers on the stress-displacement curve. The tensile axis is horizontal.

APPENDIX D

IN SITU TENSILE BEHAVIOR FOR THE CONSTANT-SPEED FSW

In situ tensile testing was performed on the constant-speed FSW in the TD and RD. Testing was conducted at RT and 300°C. The engineering stress-displacement plots are shown in Figure D.1 and the tensile properties are shown in Table D.1. Local decreases in the stress curves occurred when the test was paused for imaging. Samples taken to failure are marked with an 'X' on the stress-displacement curves. At RT, the YS and UTS were slightly higher in the RD than in the TD. Both directions were taken to failure, in which the RD exhibited a higher elongation-to-failure. At 300°C, the RD exhibited a higher YS (91 MPa) compared to the TD (68 MPa), however, the TD (117 MPa) exhibited a higher UTS than the RD (97 MPa), see Table D.1.

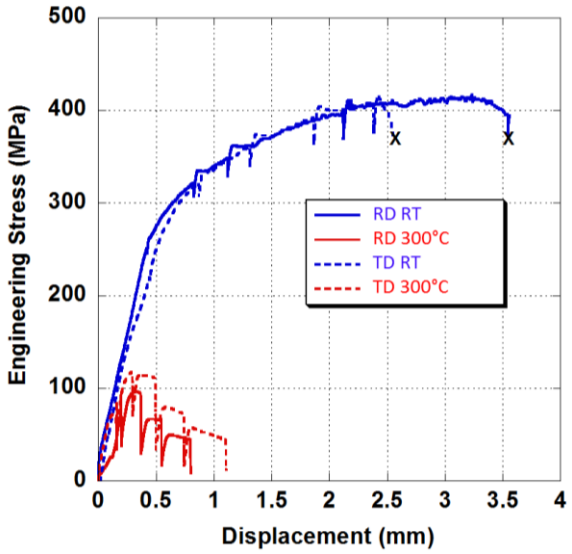

Figure D.1. Stress vs. displacement plot for the constant-speed friction stir welded samples tested at room temperature and 300°C in the RD and the TD. "X" indicates samples taken to failure. Displacement values include displacement in the sample grips.

Table D.1. Tensile properties of the *in situ* tensile tested constant-speed FSW.

	FSW RD, RT	FSW TD, RT	FSW RD, 300°C	FSW TD, 300°C
YS (MPa)	277	270	91	68
UTS (MPa)	413	410	97	117

The tests were paused periodically to image the *in situ* deformation behavior. The progression of the surface deformation in the RD at RT is shown in Figure D.2. Grain boundary relief was first observed in the RD at 2.6% strain and triple junction cracking was observed at 9.6% strain. Slip traces were not observed in the imaged area. In the TD at RT, as shown in Figure D.3, GB relief and cracks were first observed at 3.4% strain. Slip traces were initially observed at 6.6% strain.

In the RD at 300°C, see Figure D.4, cracks were observed before testing began. Grain boundary relief was observed at 2.6% strain. Slip traces were not observed in the imaged area. In the TD at 300°C, see Figure D.5, GB relief and cracks were observed at 3.9% strain. Slip traces were initially observed at 15.3% strain.

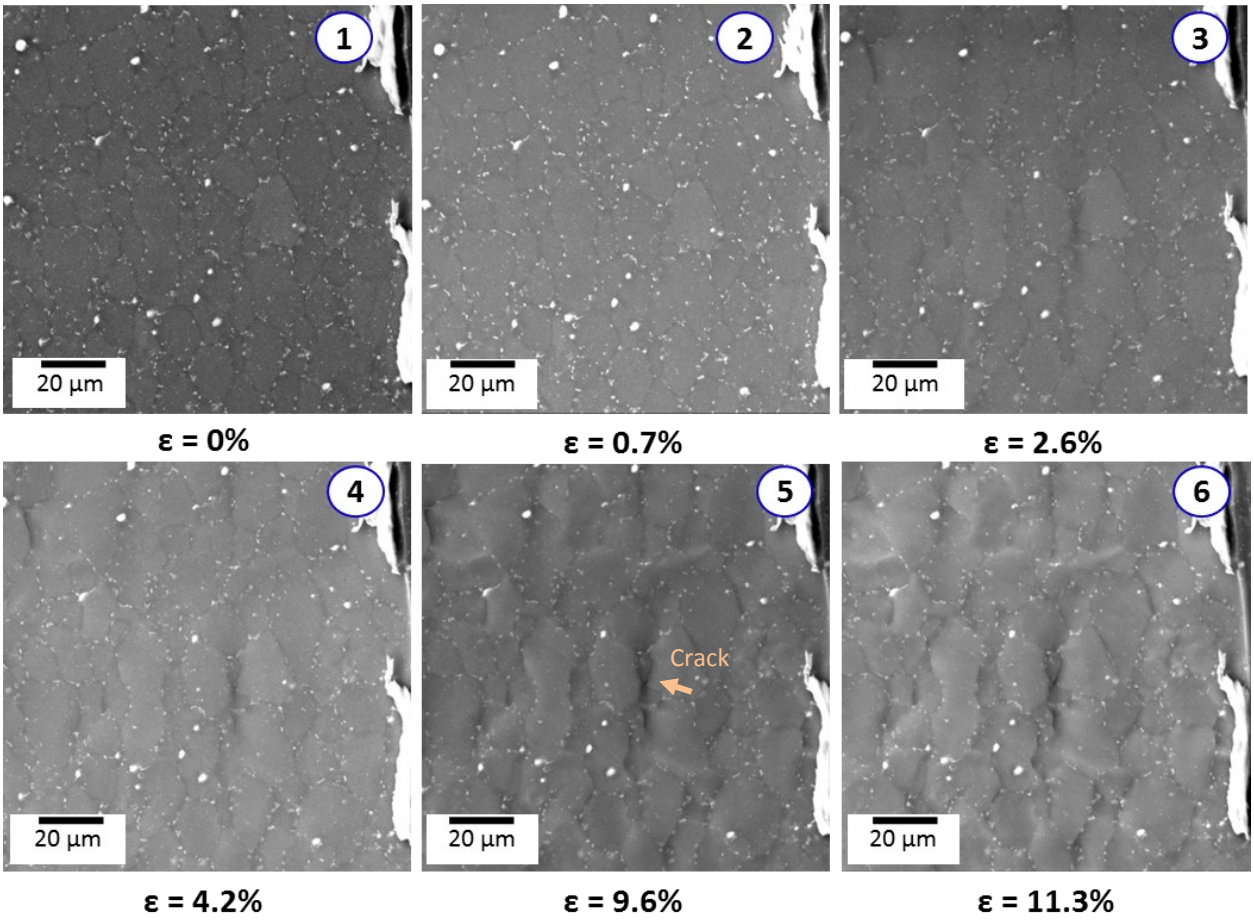

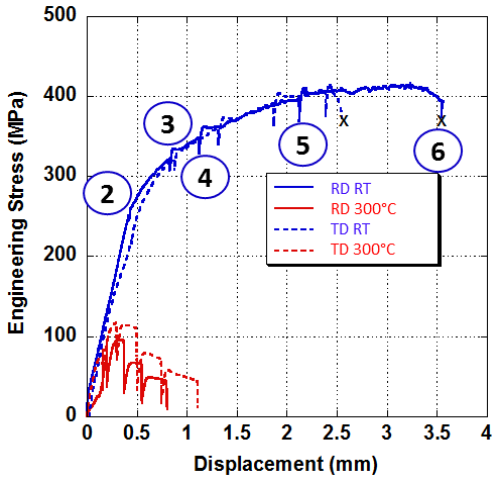

Figure D.2. Sequential SE SEM photomicrographs for constant-speed FSW *in situ* tensile tested at RT in the RD. The engineering strain is indicated below the micrograph. The numbered photomicrographs correspond to the numbers in the stress-displacement curve. The tensile axis is horizontal.

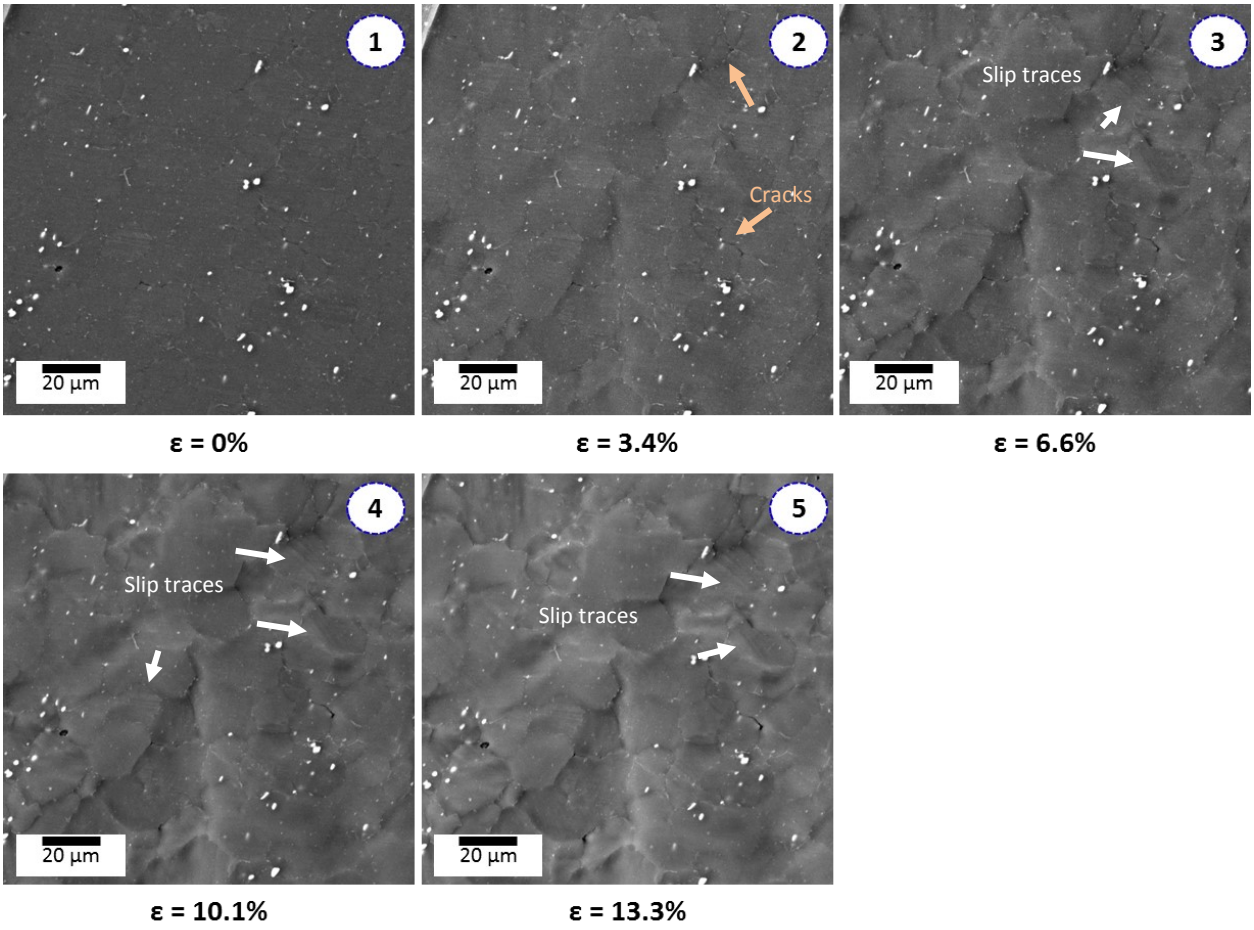

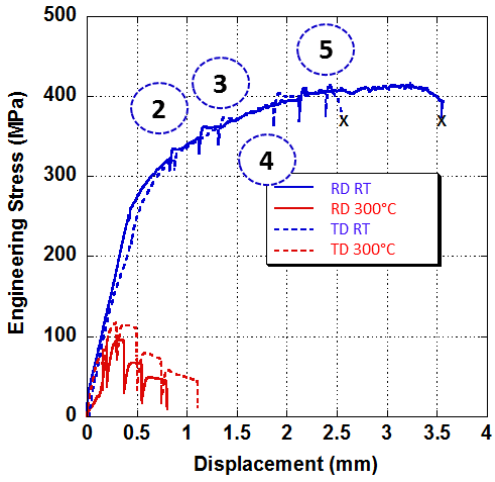

Figure D.3. Sequential SE SEM photomicrographs for constant-speed FSW *in situ* tensile tested at RT in the TD. The engineering strain is indicated below the micrograph. The numbered photomicrographs correspond to the numbers on the stress-displacement curve. The tensile axis is horizontal.

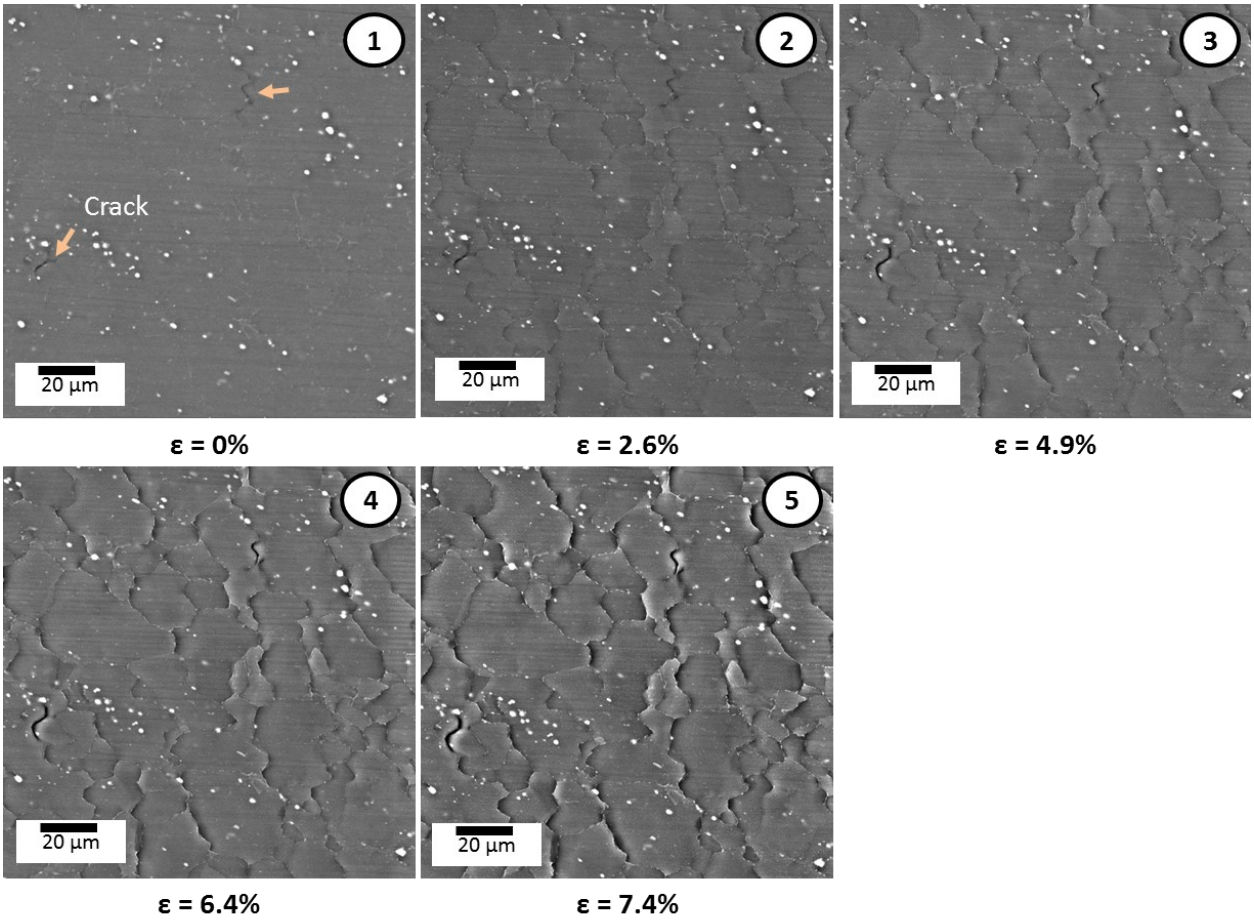

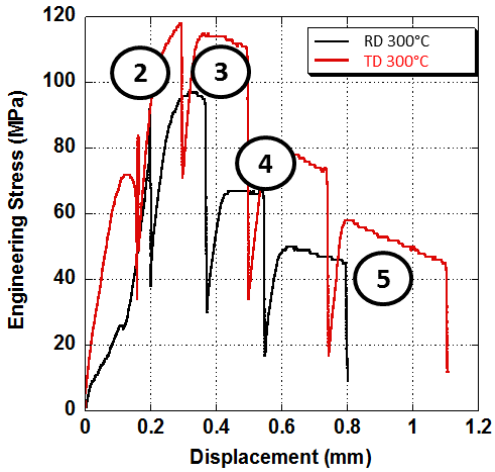

Figure D.4. Sequential SE SEM photomicrographs for constant-speed FSW *in situ* tensile tested at 300°C in the RD. The engineering strain is indicated below the photomicrograph. The labelled numbers in each photomicrograph corresponds to those instress-displacement curve. The tensile axis is horizontal.

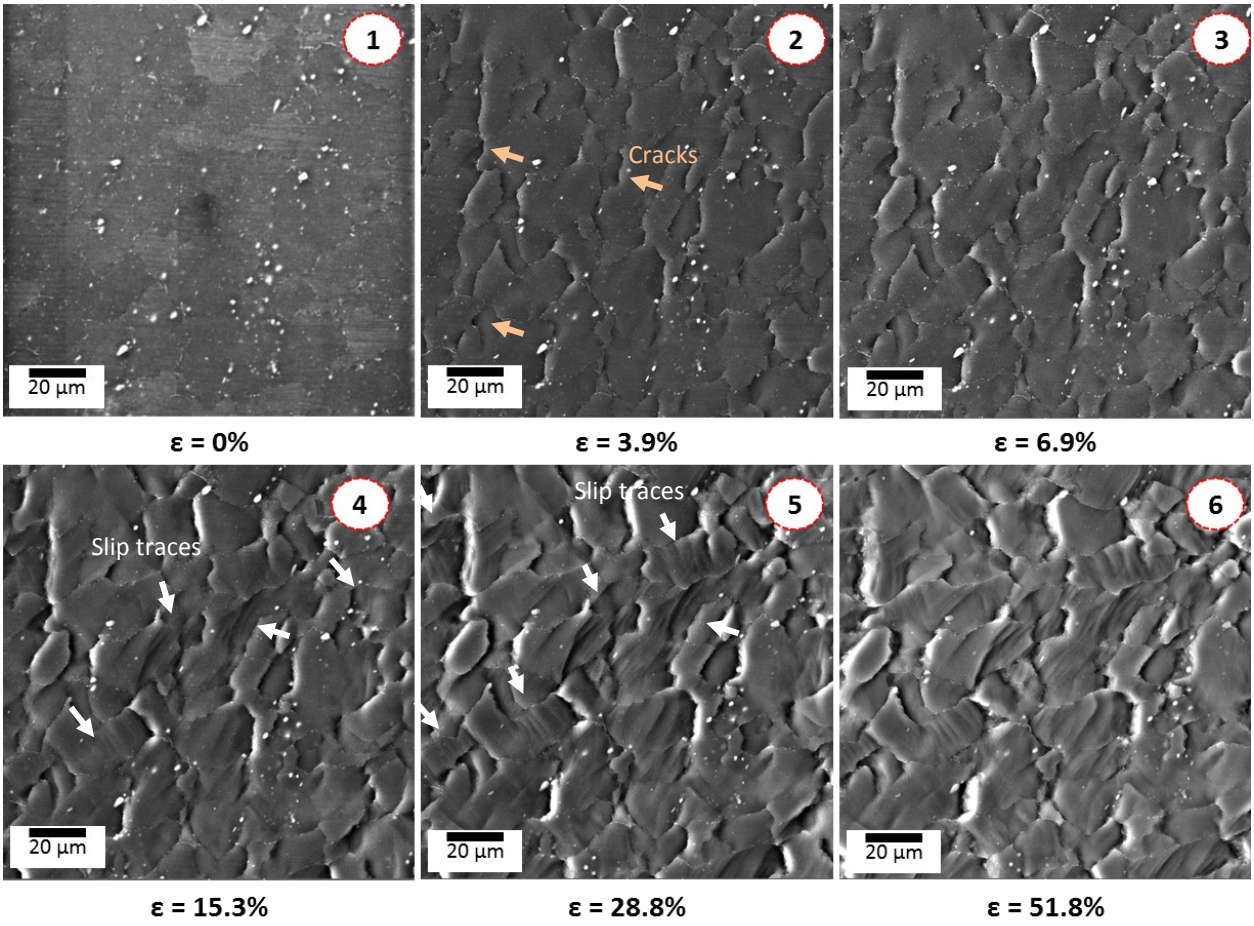

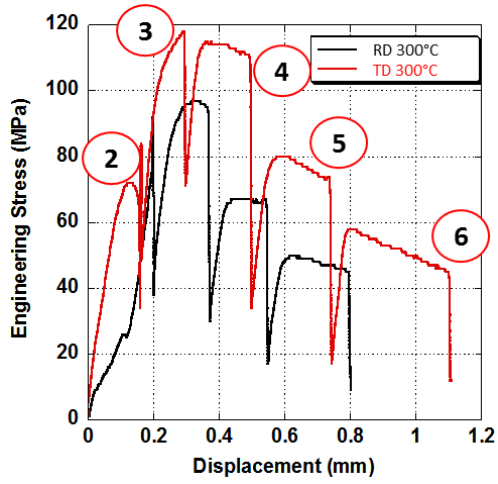

Figure D.5. Sequential SE SEM micrographs for constant-speed FSW *in situ* tensile tested at 300°C in the TD. The engineering strain is indicated below the photomicrograph. The numbered photomicrographs correspond to the numbers onthe stress-displacement curve. Tensile axis is horizontal.

APPENDIX E

CREEP

E.1 Creep Background

Creep is the sustained deformation of a material under a constant load and temperature over time [84,95]. It is critically important in applications where high temperatures and applied tensile stresses are occur during the service life of a component. In order to determine a material's resistance to creep, a number of experiments are performed at constant temperature and constant applied tensile loads, with each successive experiment incrementally changing one of the variables. Upon which, changes in the time-to-fracture, t_f, failure strain, ε_f, and creep rates are documented to understand the creep behavior of the material.

These variables can be determined from a creep curve, shown in Figure E.1 [84,95,96]. The initial strain is labelled as ε_0. The minimum creep rate, $d\varepsilon/dt$ or $\dot{\varepsilon}$, is the slope of the curve. The primary creep stage begins upon initial loading from which ε_0 is measured. During this stage, the creep rate is decreasing until a constant creep rate, or steady-state creep, is obtained. This marks the secondary creep stage. During secondary creep, the dislocation generation due to strain hardening and recovery are balanced; thus, the dislocation density is constant, which yields an apparently constant creep rate. Much of the focus will be on the secondary creep as this is where the minimum creep rate needed for analysis is obtained. The tertiary creep stage is marked by the increasing creep rate until fracture as a result of microstructural (recrystallization, grain growth, and precipitate coarsening) and mechanical (necking, voids, and cracks) instabilities [84].

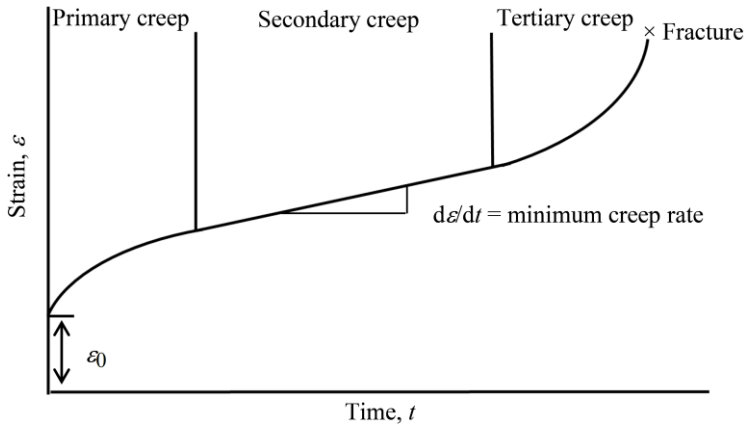

Figure E.1. A schematic of the strain versus time plot typically obtained for high-temperature creep under constant load and temperature. The different stages of creep (primary, secondary, and tertiary) are labelled. [84,95,96]

E.1.1 Effects of Microstructural on Creep Resistance

The temperature and stress applied is dependent on the material, particularly its microstructure. The precipitates and grain size can significantly affect the creep behavior.

In alloys that are precipitation hardened, dislocation motion is impeded and grain boundaries are pinned [95]. However, the microstructure must be stable. The precipitates must be insoluble, fine in size and distribution, and they cannot coarsen rapidly. If the precipitates are too large or if the distribution is too coarse, then the dislocations can move around them. Coarsening increases the average precipitate size and interparticle spacing and occurs as a result of prolonged times at elevated temperatures. Equally, if the precipitates are soluble, then the dislocations and grain boundaries can regain movement.

When $T > 0.4T_m$ and diffusional creep processes are dominant, the creep resistance is dependent on the average grain diameter [95]. Equation (E.1) expresses the relationship between the average grain size, *d,* and diffusion creep processes, *m*. As the grain size decreases, the secondary creep rate increases.

$$\dot{\varepsilon} \propto \left(\frac{1}{d}\right)^m \tag{E.1}$$

The various microstructures in FSW AA2139-T8 present an opportunity to explore the creep behavior as a function of creep temperature and stress through the thickness of the weld.

E.1.2 Temperature and Stress Dependence of Creep

Creep behavior occurs at all temperatures above absolute zero; however, in service, excessive creep is generally observed at temperatures above 0.3-0.4T_m, where T_m is the absolute melting point. At this temperature, atomic diffusion occurs [95,97]. When the temperature is increased, while holding the applied stress constant, the secondary creep rate, or steady-state creep rate, increases exponentially. The relationship between the secondary creep rate and rate of diffusion can be expressed as [95]

$$\dot{\varepsilon} \propto \exp -\frac{Q_c}{RT} \quad , \tag{E.2}$$

where Qc is the activation energy [J-mol^{-1}], R is the universal gas constant (8.31 J-mol^{-1}K^{-1}), and T is the temperature [K]. The equation infers that the temperature dependence of creep conforms to Arrhenius' Law [95]. In high temperature creep of pure metals around 0.4T_m, Qc is often equivalent to the activation energy of self-diffusion, Q_{SD}. For alloys, this may not hold true as diffusion of the other alloying elements must be considered.

Equally, the stress dependence of the secondary creep rate can be determined by varying the applied stresses at the same constant temperature over a series of experiments [95]. This relationship is expressed as

$$\dot{\varepsilon} \propto \sigma^n \, , \tag{E.3}$$

where σ is the applied stress and n is the stress exponent.

The failure time for a creep experiment can range from hours to years depending on the testing temperature and stresses. In addition, several samples are needed to acquire reliable data.

Therefore, stress increase and temperature increase experiments were performed for the dissertation in order to reduce time and the number of samples required. These experiments are explained below.

E.2 Creep Testing Procedure

For the creep experiments, large rectangular dogbones were used in accordance with ASTM E8, see Figure 3.16. Samples were EDM sliced through the thickness of the plate. A schematic drawing of these samples is shown in Figure 3.17. For the creep experiments, a ¼" pin hole was drilled in the grip section of the dogbone samples.

Tensile-creep experiments were performed at constant loads for applied stresses ranging from 25 to 125 MPa and at temperatures ranging from 225°C to 275°C, see Table E.1. The tests were conducted on Applied Tests Systems (Butler, PA) lever-arm creep machines. Data were recorded using LabVIEW® VI software. All tests were conducted using two general steps: temperature ramp up and creep loading. During the ramp up procedure, the temperature was increased to the target temperature within an hour. A low stress (between 3-8 MPa) was applied during heating to prevent compression of the sample due to thermal expansion of the grip assembly. When the target temperature was achieved, the samples were held at temperature for approximately 15 minutes to ensure through thickness temperature uniformity before applying the creep load. The time, temperature, load, and displacement were recorded throughout the tests.

Table E.1. List of creep experiments performed in this dissertation.

Region	Temp (°C)	Stress (MPa)
HAZ	250-275	50
Mid-Bottom-1	250-275	50
HAZ	225	50-75-100
Mid-Bottom-2	225	50-75
Bottom	250	25-35-50
Mid-Bottom-3	250	25-35-50

E.3 Creep Results of the HAZ and SZ

Room temperature (RT) tensile tests were conducted on the HAZ and SZ in the transverse direction to provide insights about the creep properties. To provide a basis for comparison, the tensile properties of the constant-speed FSW SZ and BM are provided in Table 4.9 and Table 4.5**,** respectively.

Increases in the stress (for stress increase tests) and the temperature (for temperature increase tests) occurred after the creep rate versus time plot indicated that a secondary creep stage was reached. Figure E.2 shows the creep rate versus time plot for the creep strain versus time plots in Figure E.3, Figure E.4, and Figure E.8. In Figure E.3 and Figure E.4, the creep strain versus time plot of the HAZ is compared to that of the SZ. Figure E.4 shows the result from the stress increase test for the HAZ and SZ Mid Bottom-2. The applied stresses ranged from 50-125 MPa, in increments of 25 MPa. Samples were tested at a constant temperature of 225°C. The SZ Mid Bottom-2 failed after the stress increased to 75 MPa and approximately 350 hrs of testing. The HAZ sample failed after the stress increased to 125 MPa and approximately 700 hrs of testing. The secondary creep rates for SZ Mid Bottom-2 were faster than the HAZ by approximately one order of magnitude. The transverse cross section of the SZ Mid Bottom-2 in Figure E.4b shows a

refined, equiaxed microstructure with some coarsened precipitates at the grain boundaries. The precipitate volume fraction, V_p, Table E.2, was 3.5%, which was approximately half that of FSW SZ Mid Bottom-2 (6.3%). Analysis of the SZ Mid Bottom-2 fracture surface in Figure E.5 revealed dimples towards the lateral ends of the gage section which is indicative of a ductile fracture. The center exhibited angular intergranular features which is indicative of a brittle fracture.

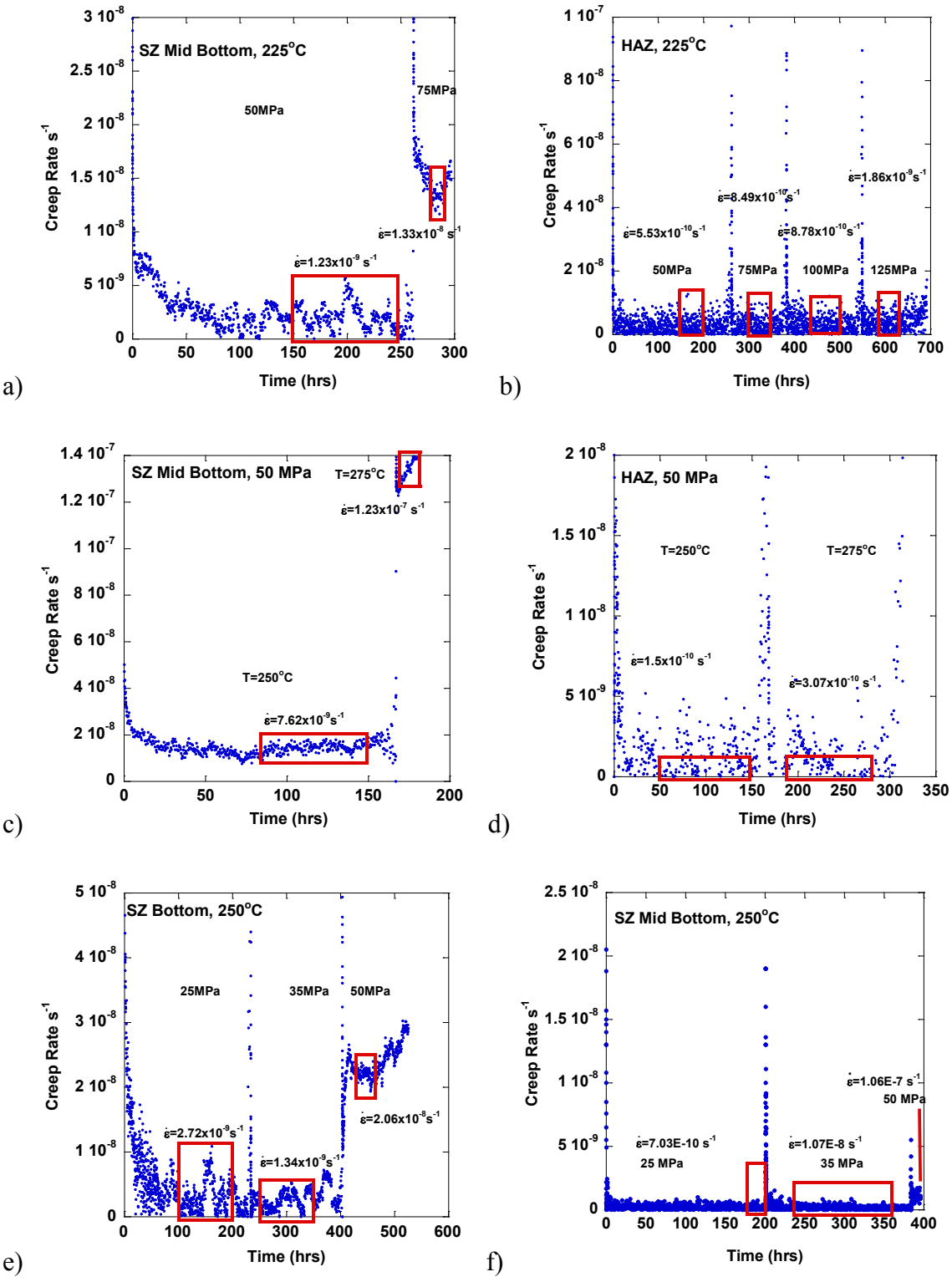

Figure E.2. Creep rate versus time plots for the creep strain versus time plots in Figs. Polynomial functions were fit to derive the secondary creep rates. Plots a) and b) correspond to Figure E.3. Plots c) and d) correspond to Figure E.4. Plots e) and f) correspond to Figure E.8.

The post-test microstructure of the HAZ exhibited intragranular and intergranular precipitate coarsening, as seen in Figure E.3c. The V_p was measured to be 4.3% which was approximately twice that of the untested BM (2.1%). The fracture surface of the HAZ exhibited ductile and brittle features, as well. In Figure E.6, the right side of the fracture surface exhibited intergranular cracking and the left side exhibited dimples. Similar features were made for the samples which underwent the temperature increase experiments.

The SZ Mid Bottom-1 and HAZ were tested at temperatures of 250°C and 275°C and an applied stress of 50 MPa, see Figure E.4a. The SZ Mid Bottom sample failed after the temperature increase to 275°C and approximately 200 hrs of testing. The HAZ sample failed after the temperature increase to 275°C and approximately 320 hrs of testing. The transverse cross section of the HAZ in Figure E.4c shows intergranular and intragranular precipitate coarsening. The precipitate V_p was 3.8% which was greater than the precipitate V_p of the BM. The transverse cross section of SZ Mid Bottom-1 in Figure E.4b reveals a refined, equiaxed microstructure with intergranular and intragranular coarsened precipitates. The precipitate V_p was 7.3%, which was greater than the precipitate V_p of the FSW SZ Mid Bottom-1, see Table E.2. Dimples were observed on the lateral sides of the SZ Mid Bottom-1 fracture surface which suggests a ductile fracture. The center of the sample demonstrated intergranular fracture, see Figure E.7.

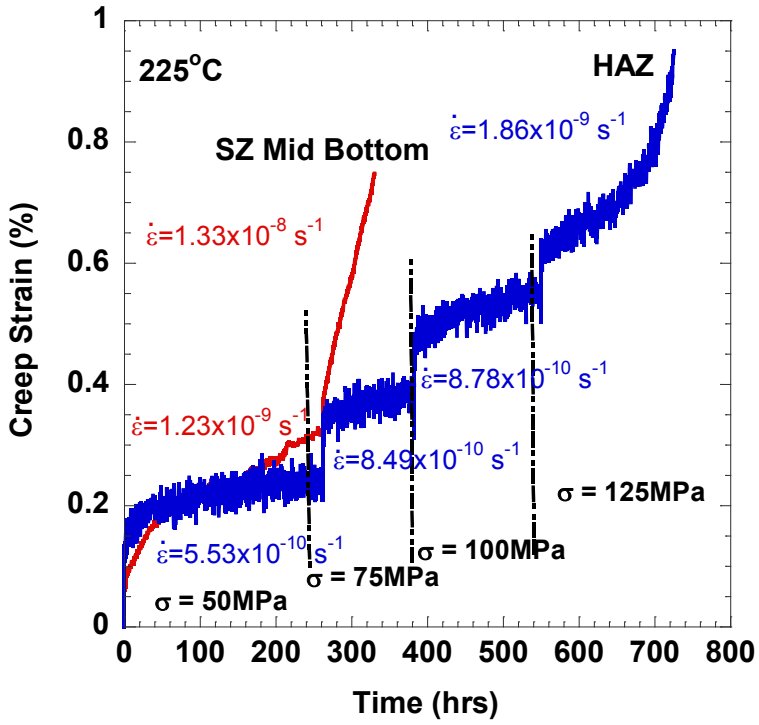

a)

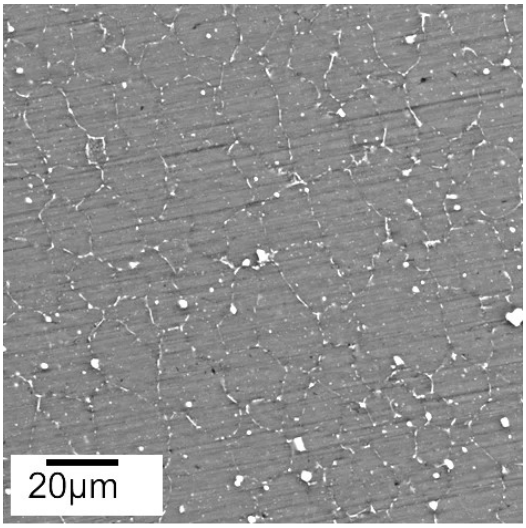

b)

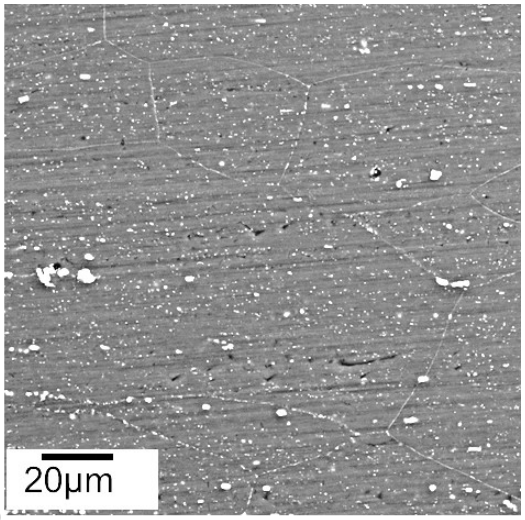

c)

Figure E.3. (a) Creep strain versus time plot for SZ Mid Bottom-2 and HAZ samples at 225°C and stresses ranging between 50-75-100-125 MPa. BSE SEM photomicrographs for (b) SZ Mid Bottom-2 (0.75% creep strain) and (c) HAZ (0.95% creep strain).

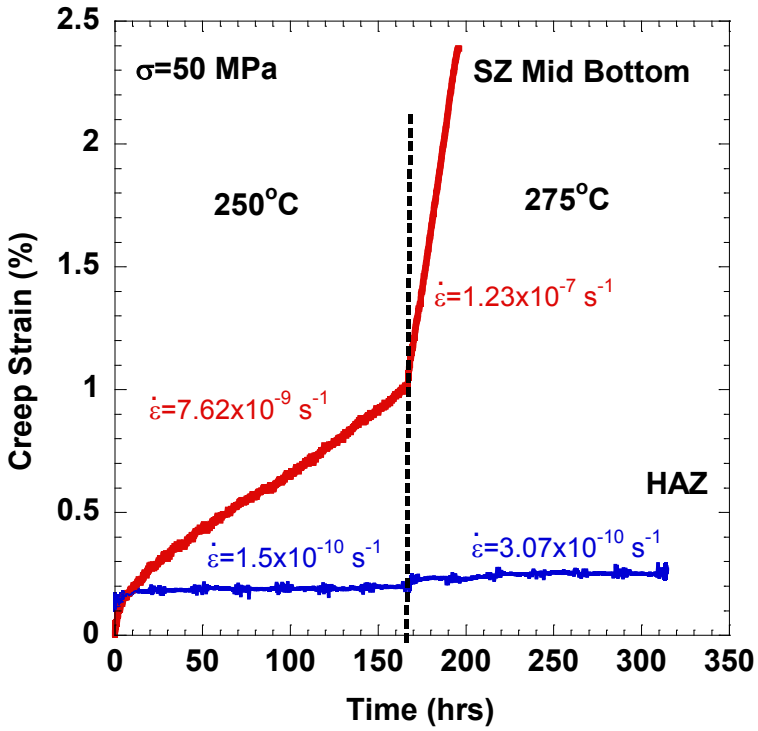

a)

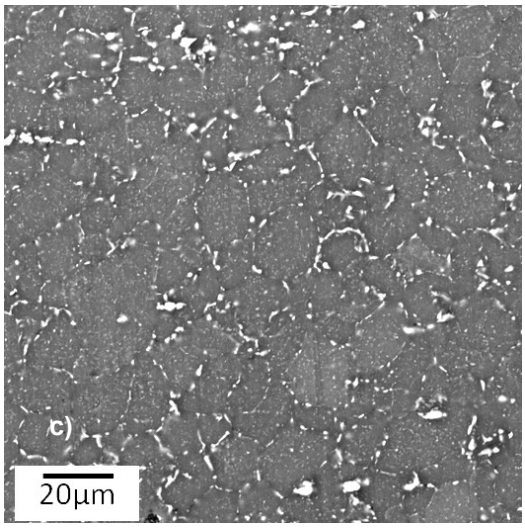

b)

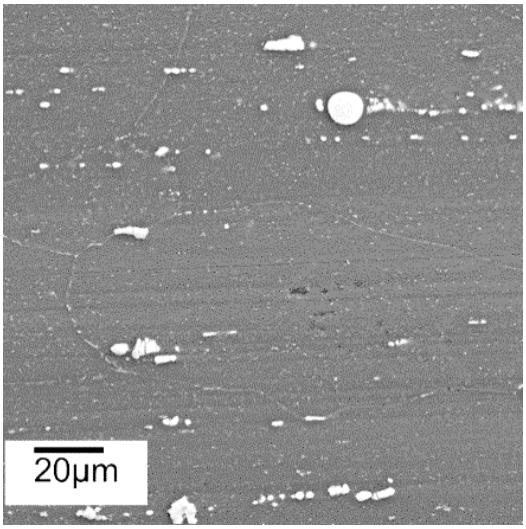

c)

Figure E.4. a) Creep strain versus time plot for SZ and HAZ samples at temperatures ranging between 250-275°C and at stress of 50 MPa. BSE SEM photomicrographs of the b) SZ Mid Bottom-1 (2.4% creep strain) and c) HAZ (0.25% creep strain).

(a)

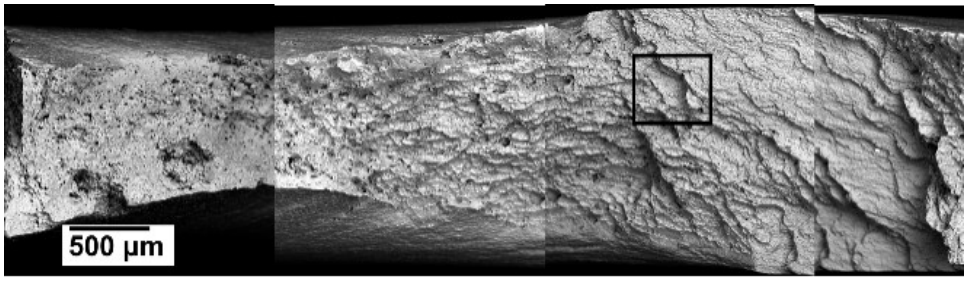

(b)

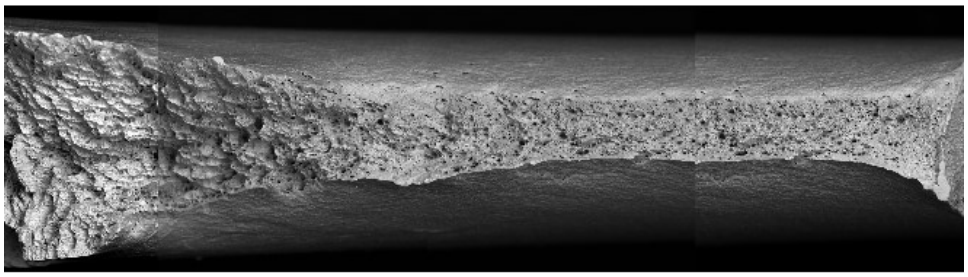

(c)

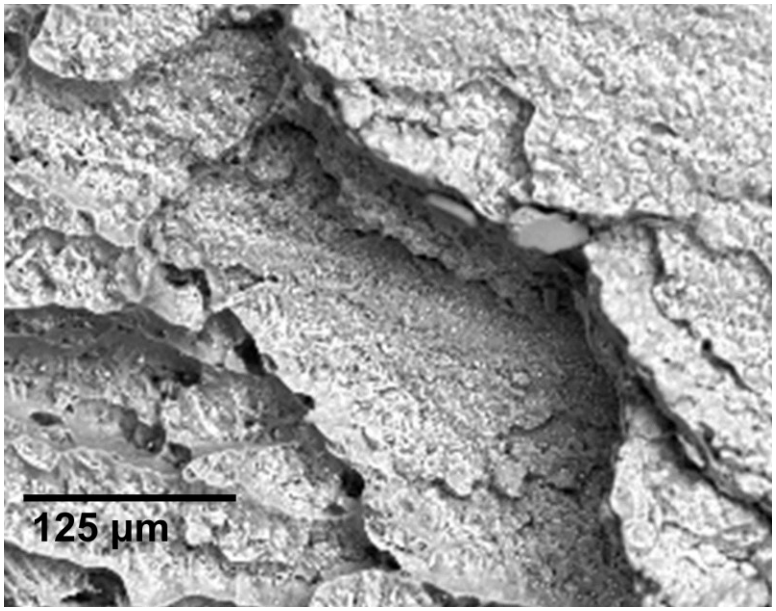

Figure E.5. a-b) SE SEM photomicrographs of the fractured sample SZ Mid Bottom-2 creep tested at 225°C and 50-75 MPa. Lateral sides of the sample have dimples. c) Intergranular features were observed at the center. The creep strain to failure was 0.75%.

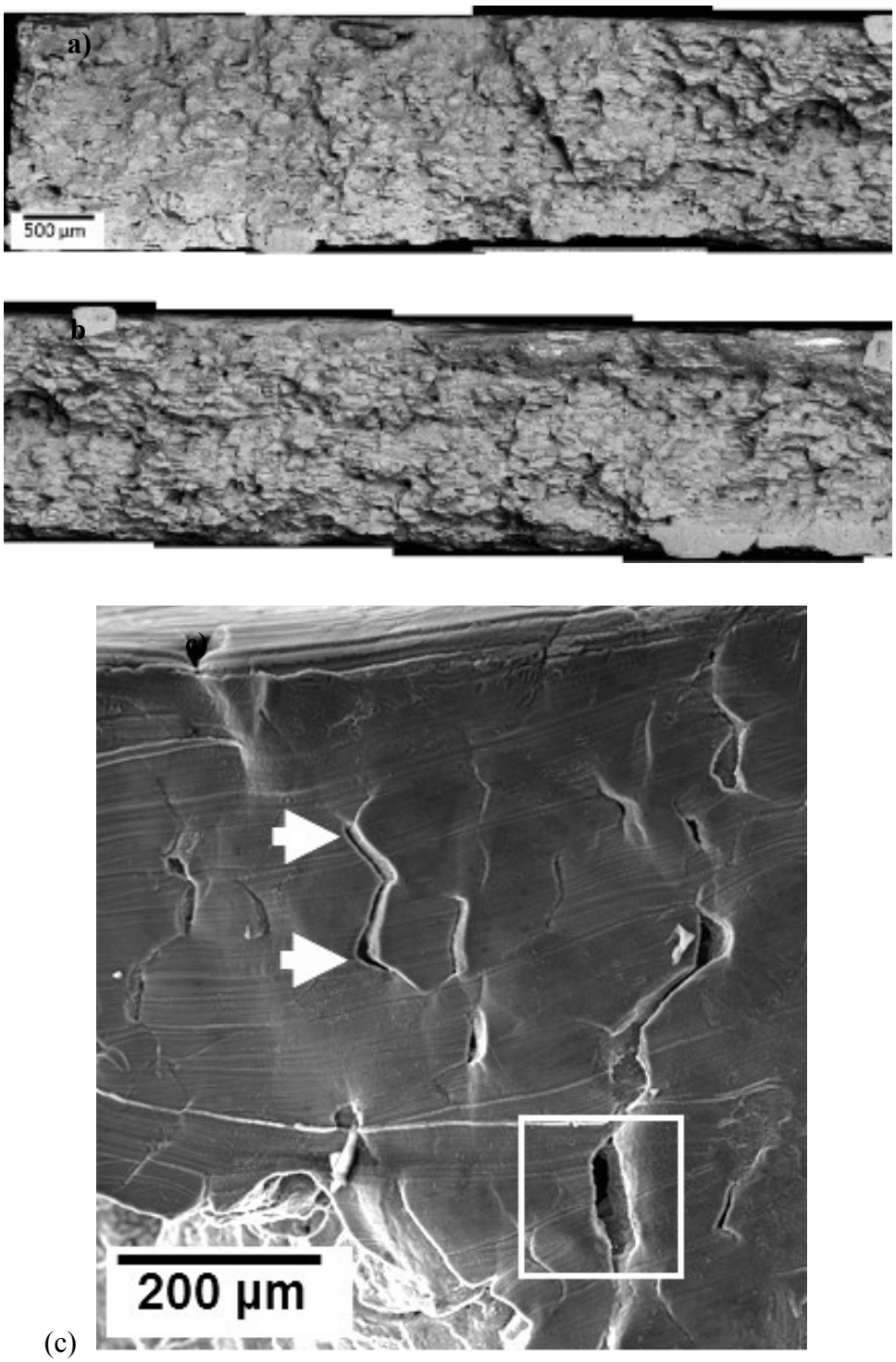

Figure E.6. SE SEM photomicrographs of the fractured sample HAZ creep tested at 225°C and 50-125 MPa. a) Left half (which contained dimples). b) Right half (which exhibited intergranular cracking. c) higher-magnification image showing cracking at triple junctions (arrows) and along GBs (boxed area). The creep strain-to-failure was 0.95%.

(a)

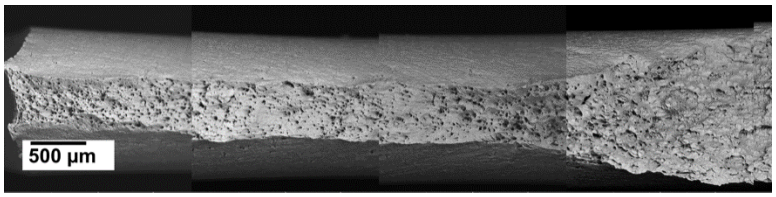

(b)

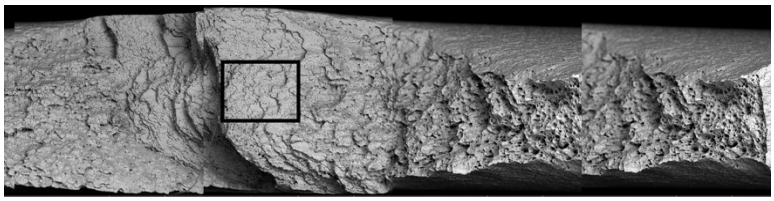

(c)

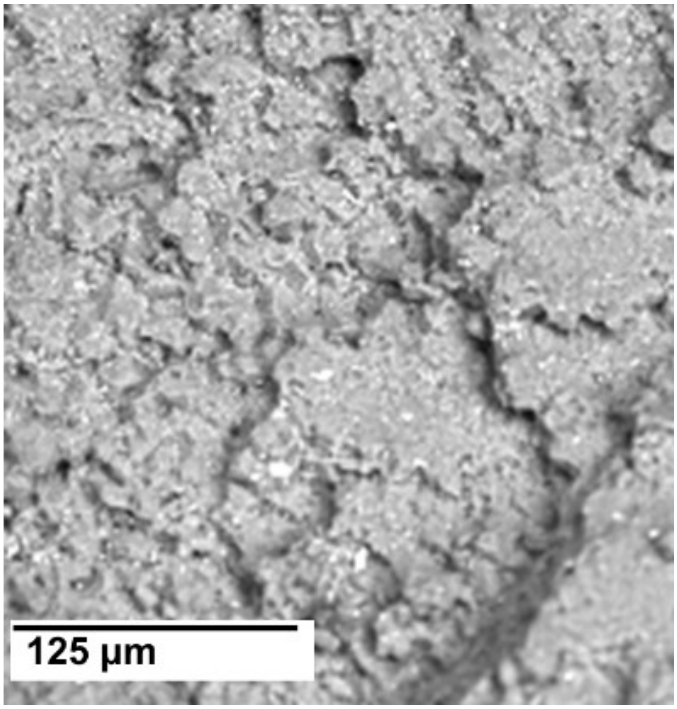

Figure E.7. a-b) SE SEM photomicrographs of fractured sample SZ Mid Bottom-1 which underwent a temperature increase creep test at 250-275°C and 50 MPa. c) Higher-magnification image of the boxed region in (b indicating intergranular cracking. The creep strain-to-failure was 2.4%.

Table E.2. Precipitate V_p of the creep tested samples and the center of the SZ through the depth of the weld.

Sample	Stress (MPa)	Temp. (°C)	V_p (%)
SZ Mid Bottom-2	50-75	225	3.5
HAZ	50-75-100-125	225	4.3
SZ Bottom	25-35-50	250	12.5
SZ Mid Bottom-3	25-35-50	250	11.3
HAZ	50	250-275	3.8
SZ Mid Bottom-1	50	250-275	7.2
BM	--	--	2.1
FSW SZ Top	--	--	2.4
FSW SZ Mid Top	--	--	2.9
FSW SZ Mid	--	--	3.6
FSW SZ Mid Bottom	--	--	6.3
FSW SZ Bottom	--	--	10.6

E.4 Creep through the SZ Depth

Two SZ samples were tensile-creep tested at a temperature of 250°C and at applied stresses of 25, 35, and 50 MPa. Although both samples were from the SZ, they exhibited different creep behavior, as evident in Figure E.8a.

The observed maximum creep strain for SZ Bottom at failure was 2.4% at 560 hrs. The creep rate did not change significantly when the stress was increased to 35 MPa. Sample SZ Mid Bottom-3 experienced significant increases in creep rate from $7.0\text{x}10^{-10}$ s^{-1} to $1.1\text{x}10^{-8}$ s^{-1} to $1.1\text{x}10^{-7}$ s^{-1} at 25, 35, and 50 MPa, respectively. The observed maximum creep strain at failure was 1.6% after approximately 400 hrs. SZ Bottom had a higher creep strain by almost 0.5% than SZ Mid Bottom-3 at 25 MPa and the creep rate was approximately four times faster. SZ Mid Bottom-3

continued to increase in creep rate at 50 MPa which was greater than SZ Bottom. In general, SZ Bottom exhibited a lower creep rate and higher creep strain values than SZ Mid Bottom-3.

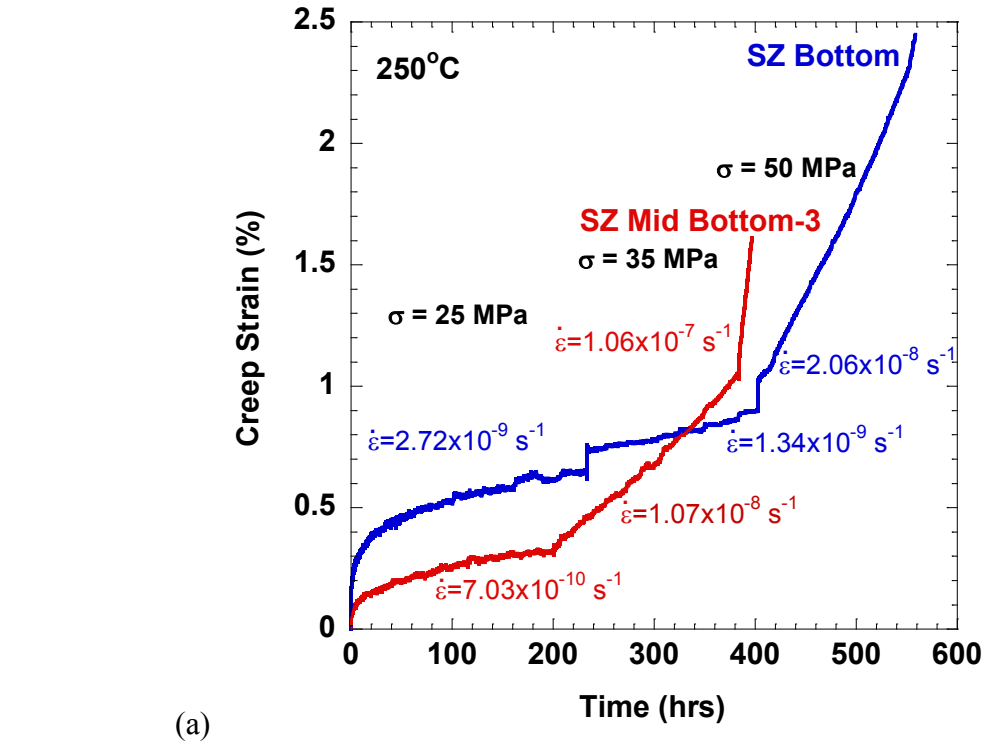

(a)

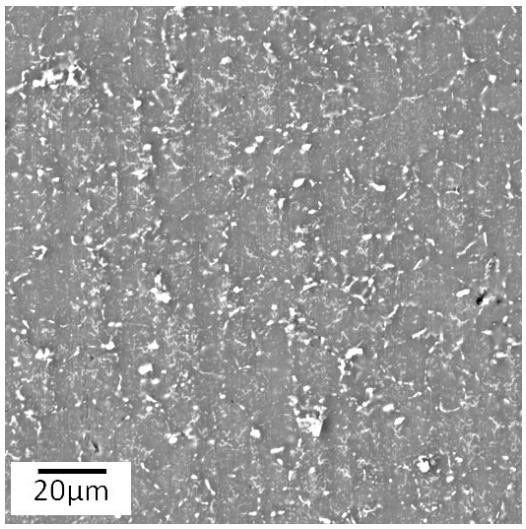

(b)

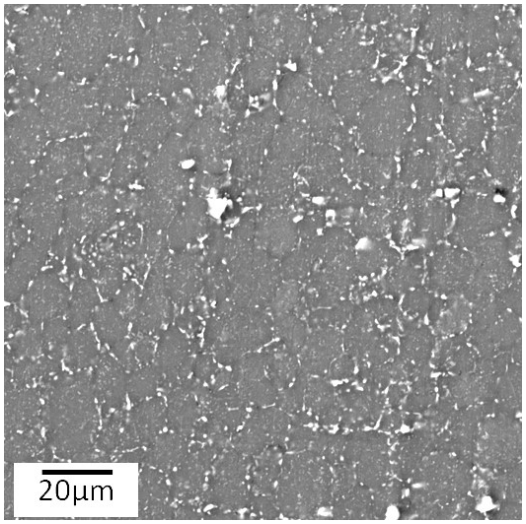

(c)

Figure E.8. (a) Creep strain versus time plot of a stress-jump test for a sample tested at 250°C and at stresses ranging between 25-35-50 MPa. BSE SEM photomicrographs of b) SZ Bottom (2.4% creep strain) and c) SZ Mid Bottom-3 (1.6% creep strain).

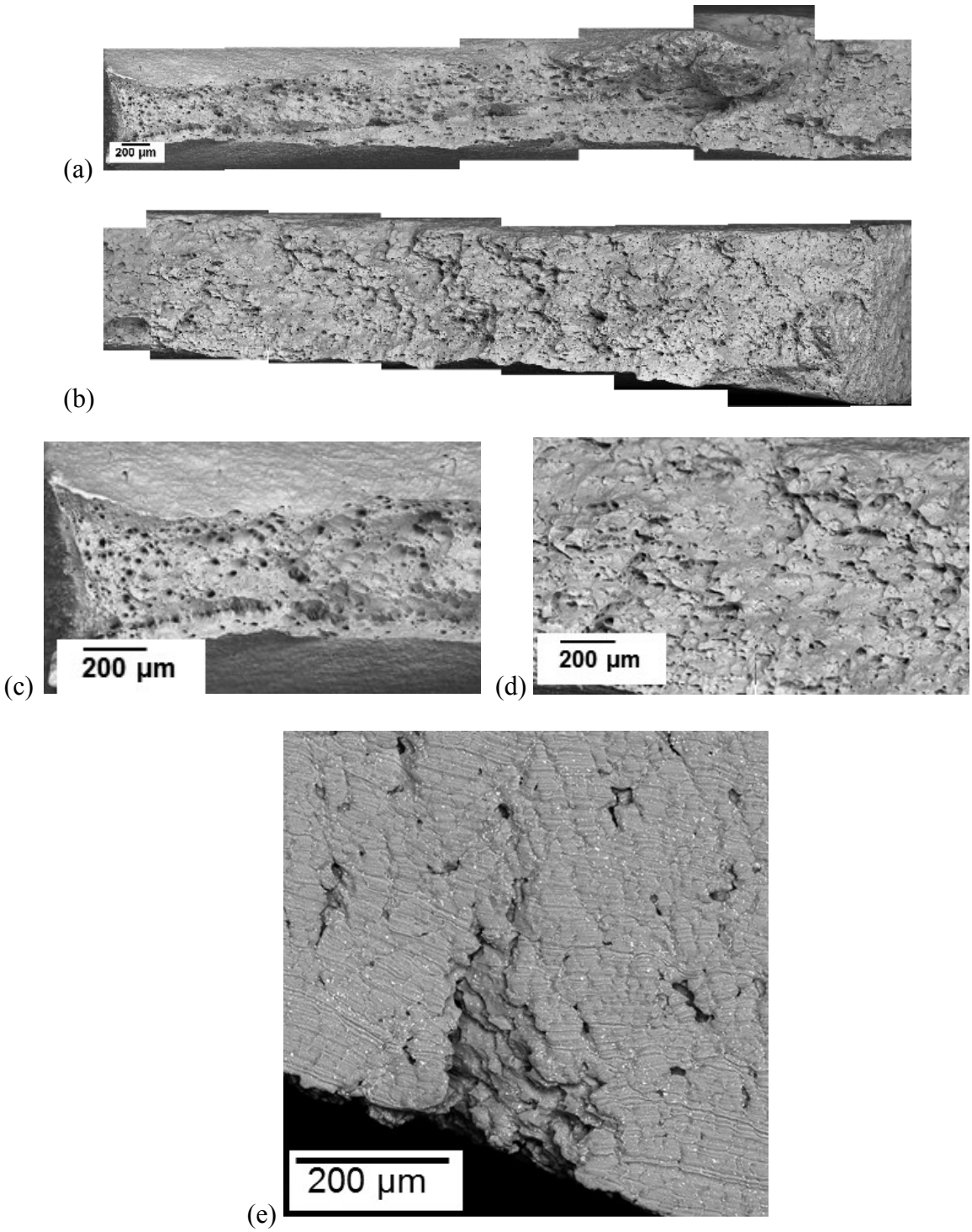

Figure E.9. a-b) Low-magnification SE SEM photomicrographs of a fractured sample SZ Bottom which underwent a stress increase creep test at 250°C and 25-35-50 MPa. Dimples are present on the fracture surface are shown in greater detail in (c) and (d). (e) Cracks and voids are observed. The creep strain to failure was 2.4%

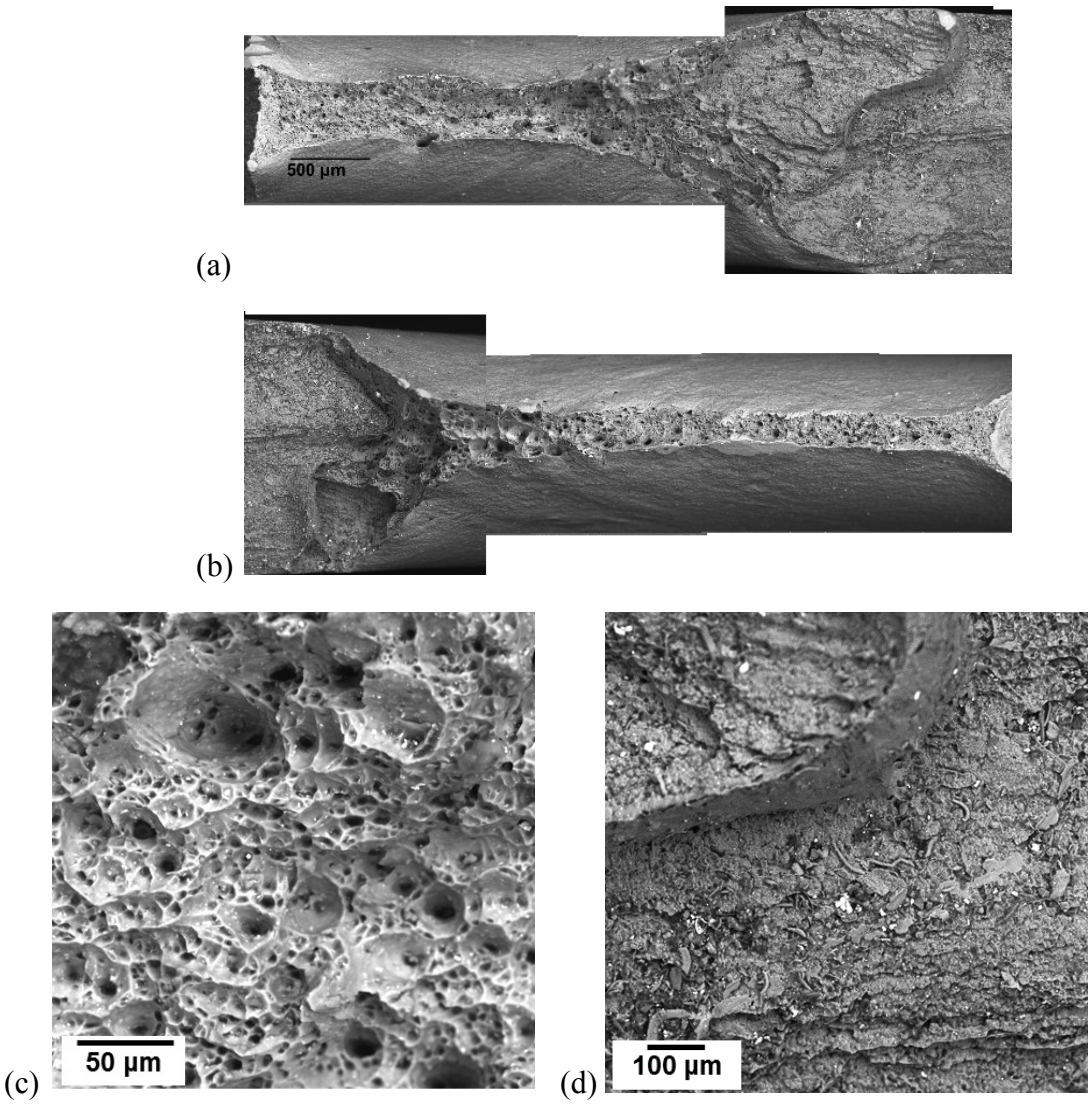

Figure E.10. a-b) Low-magnification SE SEM photomicrographs of SZ Mid Bottom-3 creep tested at 250°C and 25-35-50 MPa. Lateral sides exhibited dimples as shown in (c). The center contains evidence of intergranular fracture shown in (d). The creep strain to failure was 1.6%. Higher magnification of worm-like features in (d) are shown in (e)-(g), which demonstrate that they are a part of the material and contain secondary phases. (g) is a high magnification image of the precipitates on the fracture surface.

Figure E.10 (continued)

(e) 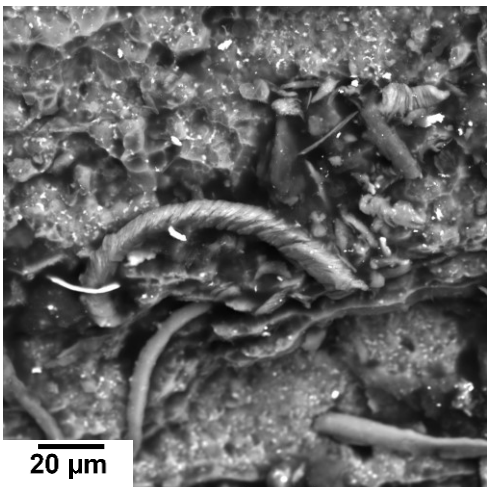

(f) 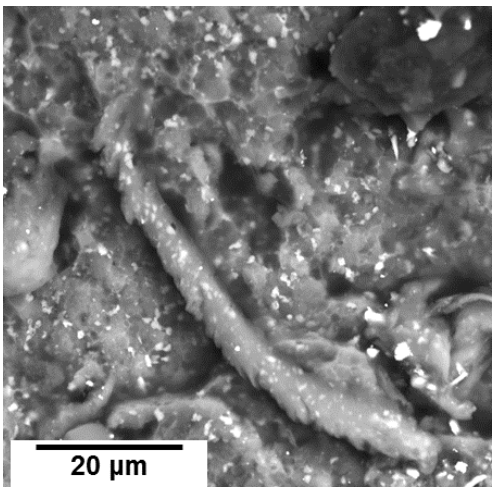

(g) 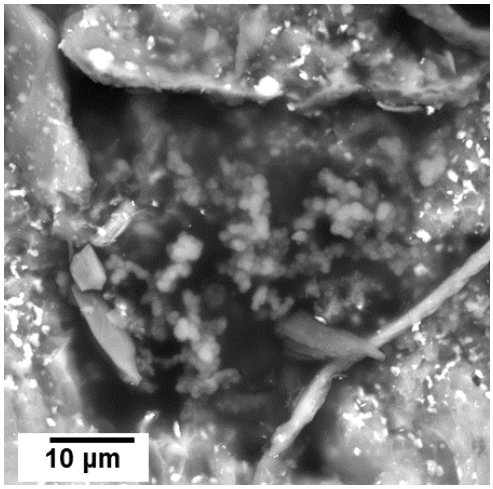

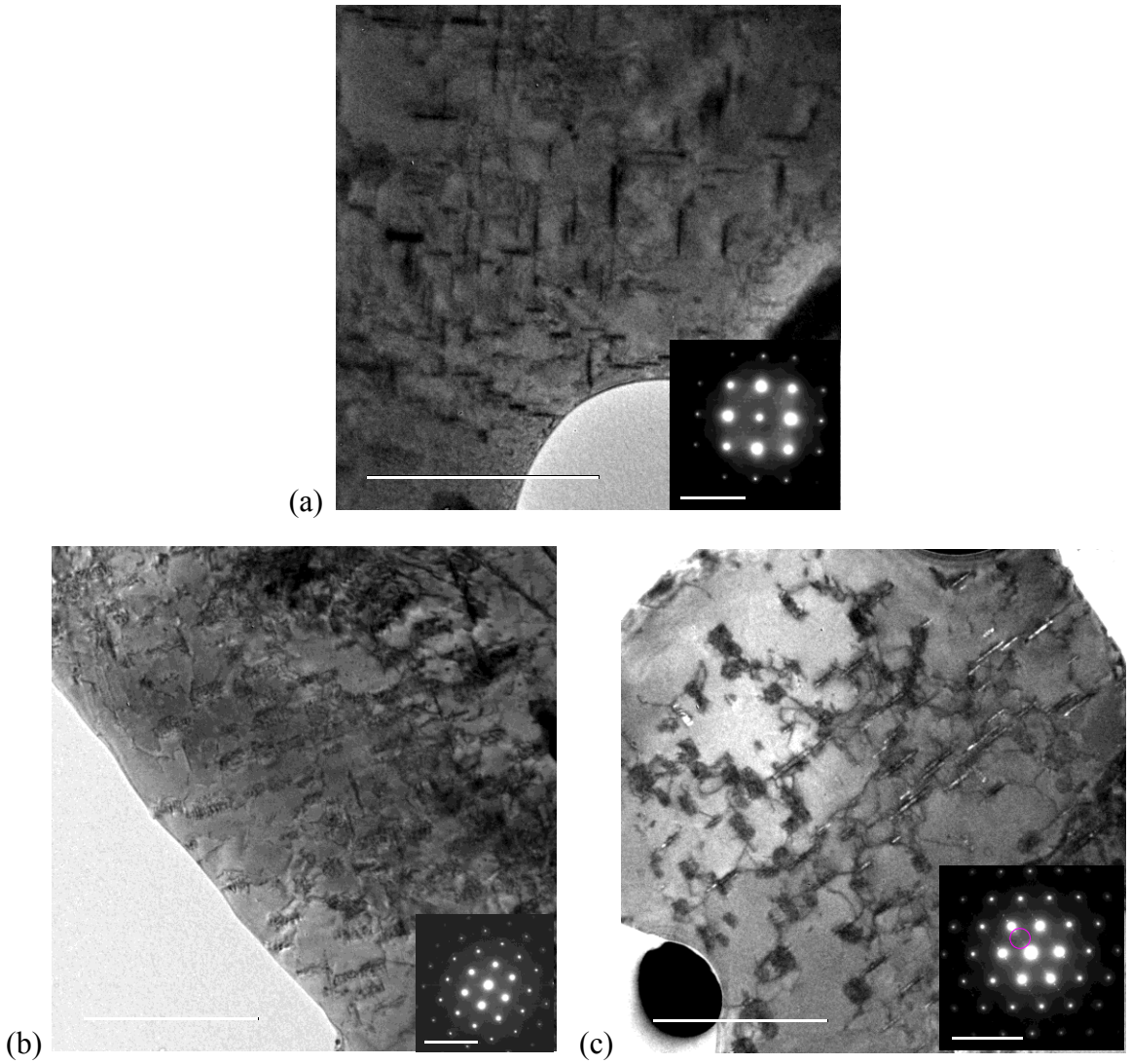

Figure E.11. a-b) Bright field TEM photomicrographs and their associated <100> and <110> zone axes of SZ Bottom and c) SZ Mid Bottom-3 in the <110> (bottom) creep tested at a temperature of 250°C and stresses of 25-35-50 MPa.

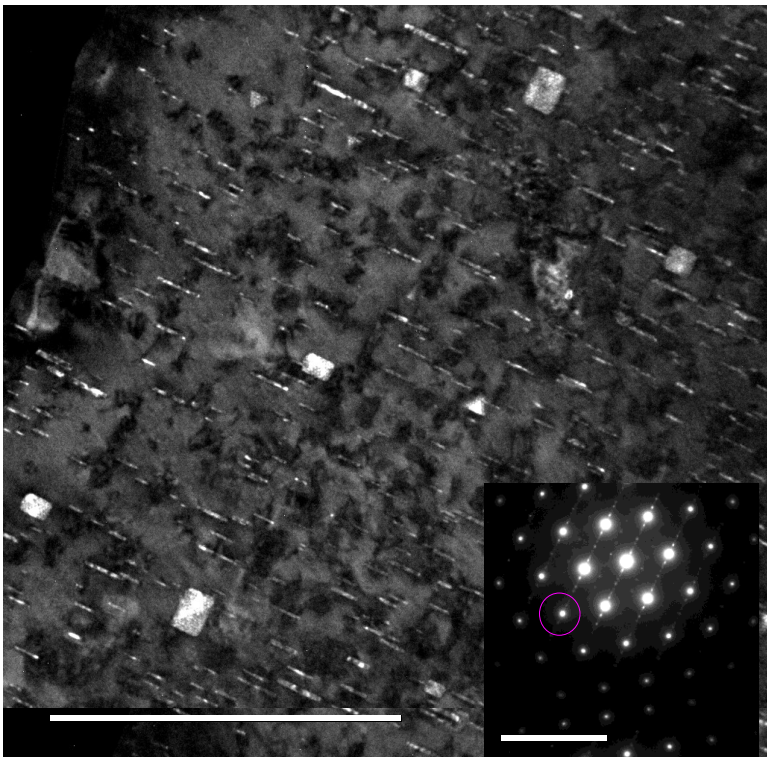

Figure E.12. Dark field TEM photomicrograph and the associated <110> zone axis of the HAZ creep tested at a temperature of 225°C and stresses of 50-125 MPa showing the θ' and σ (cuboidal) phases.

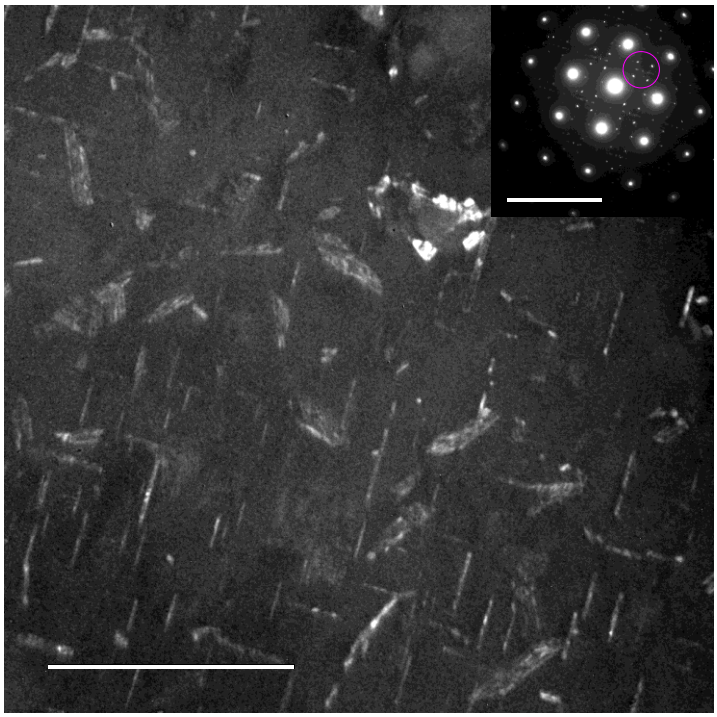

(a)

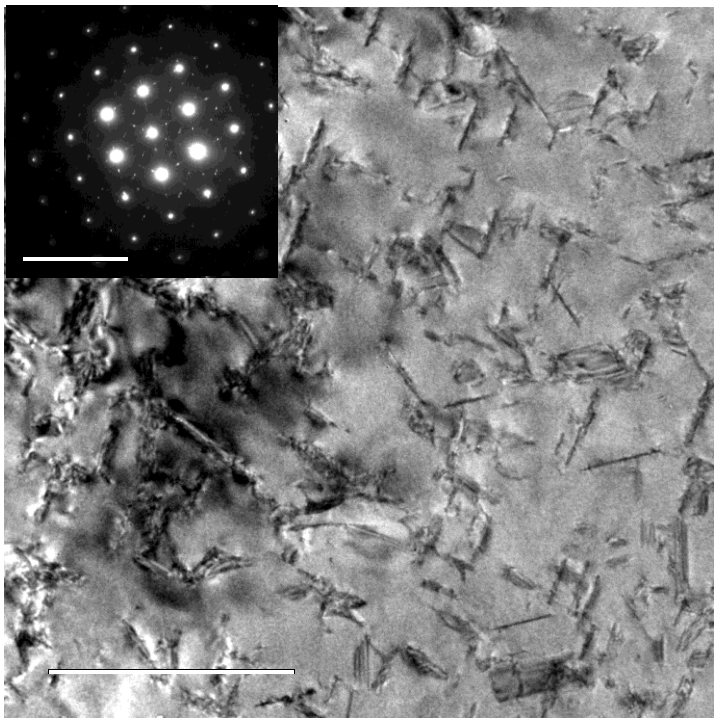

(b)

Figure E.13. a) Dark field photomicrograph associated with the circle points represented in the <100> zone axis insert and b) bright field photomicrograph (with the <110> zone axis insert) of the SZ Mid Bottom-2 creep tested at a temperature of 225°C and stresses of 50-125 MPa. Stress increases were done in 25 MPa increments. The Ω and θ' phases coarsened during the creep experiment.

The transverse cross section of SZ Bottom and SZ Mid Bottom-3, see Figure E.8b-c, show a refined, equiaxed microstructure with coarsened precipitates, especially at the grain boundaries, for both samples. However, the SZ Bottom appears to have slightly more precipitate coarsening. Table E.2 and Figure 4.11 demonstrate that there is a gradient in the microstructure in the SZ. When the precipitate V_p of the bottom and mid bottom? are compared to their corresponding as-welded conditions, SZ Bottom and SZ Mid Bottom-3 exhibited higher V_p values (12.5% and 11.3%, respectively compared to 10.6% and 6.3%, respectively).

Analysis of the SZ Bottom fracture surface revealed dimples (see left side and right half of Figure E.9). Cracks and voids at grain boundaries were observed on the sample surface. Microvoids are a preliminary step in the ductile failure process.

The SZ Mid Bottom-3 fracture surface exhibited dimples on the lateral sides, whereas, the center of the fracture exhibited brittle, intergranular cracking, see Figure E.10 and Figure E.8b-c show SEM photomicrographs of the post-creep microstructure for the SZ Bottom and SZ Mid Bottom-3 samples, which had a refined microstructure and coarsened precipitates.

TEM analysis in Figure E.11 shows that SZ Bottom had coarsened θ' and Ω. The dissolution of the Ω phase, the coarsening of the θ' phase, and the precipitation of the σ phase occurred in the SZ Mid Bottom-3. Another phase was detected in the creep tested HAZ at 225°C and 50-125 MPa. Based on the DF TEM photomicrograph in Figure E.12, this additional phase is most likely the σ precipitate phase. The sigma phase was reported in Mondolfo's Al alloy reference book [19], as having a chemical composition of $Al_5Cu_6Mg_2$, a cubic crystal structure, a cuboid appearance, and inhabiting the $\{100\}_\alpha$ planes.

According to the TEM photomicrographs and diffraction patterns of the base metal in Chapter 4, Figures 4.13 to 4.15 and Figure 4.22, the as-welded SZ at Mid-Bottom only contained

the coarsened Ω phase. Figure E.13 illustrates that during the stress increase creep test, the Ω phase coarsened. This is indicated by the transition of the <111> streaks in the <110> zone axis in Figure 4.4 into dots. This is evident of a change in precipitate shape, or in this case, the precipitate platelet orientation to the electron beam [98]. Some of the θ' orientation variants have precipitated during the creep test as they were not present in the as-welded condition.

APPENDIX F

XRD PEAKS COMPARING THE BASE METAL TO THE CONSTANT-TEMPERATURE FSW

This section contains a comparison of the X-ray diffraction peaks for all constant-temperature friction stir welds and the as-received base metal.

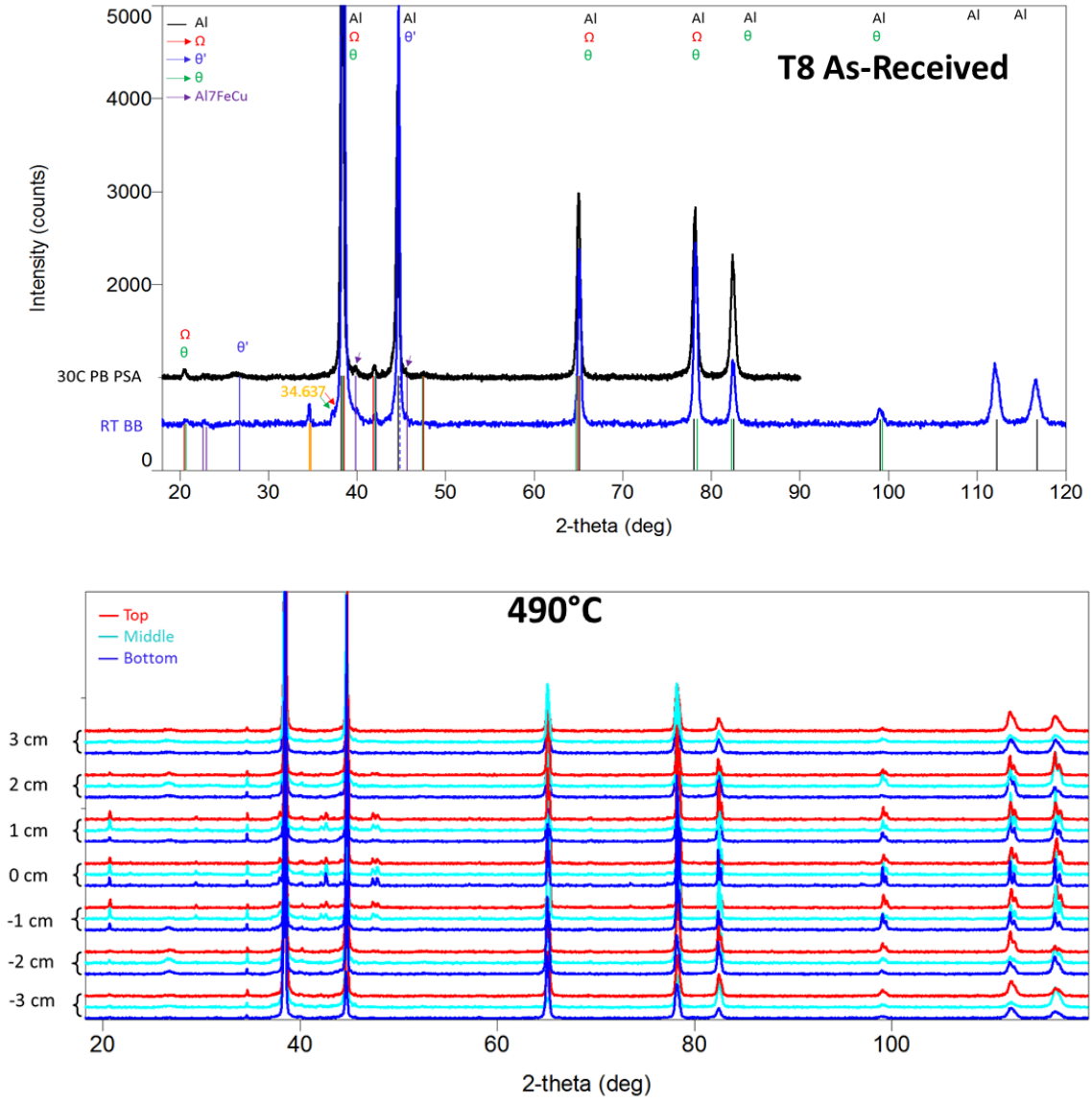

Figure F.1. Comparison of the XRD intensity versus 2-theta peaks for the as-received base metal and the constant-temperature FSWs at 490°C, 500°C, and 510°C.

Figure F.1 (continued)

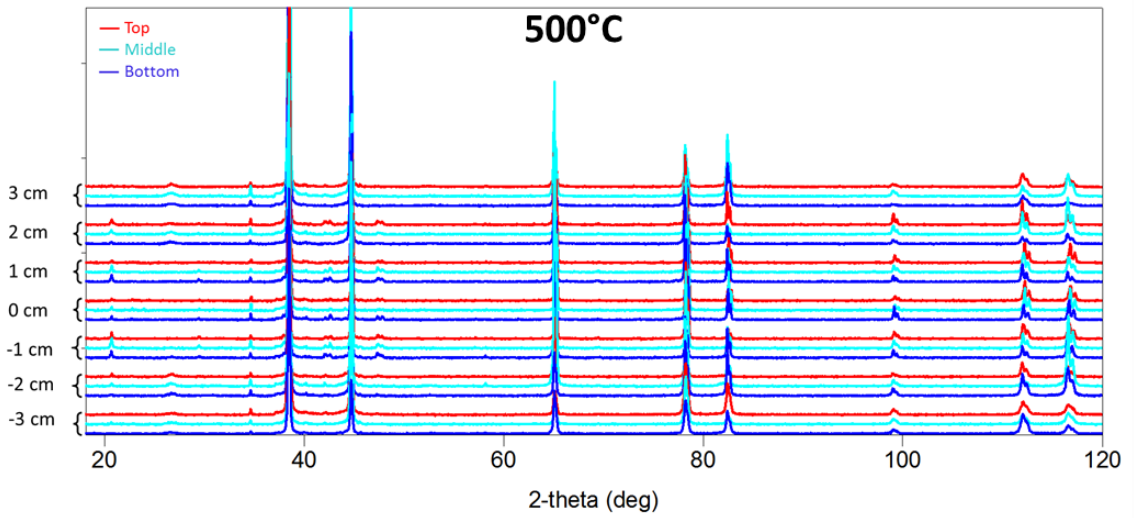

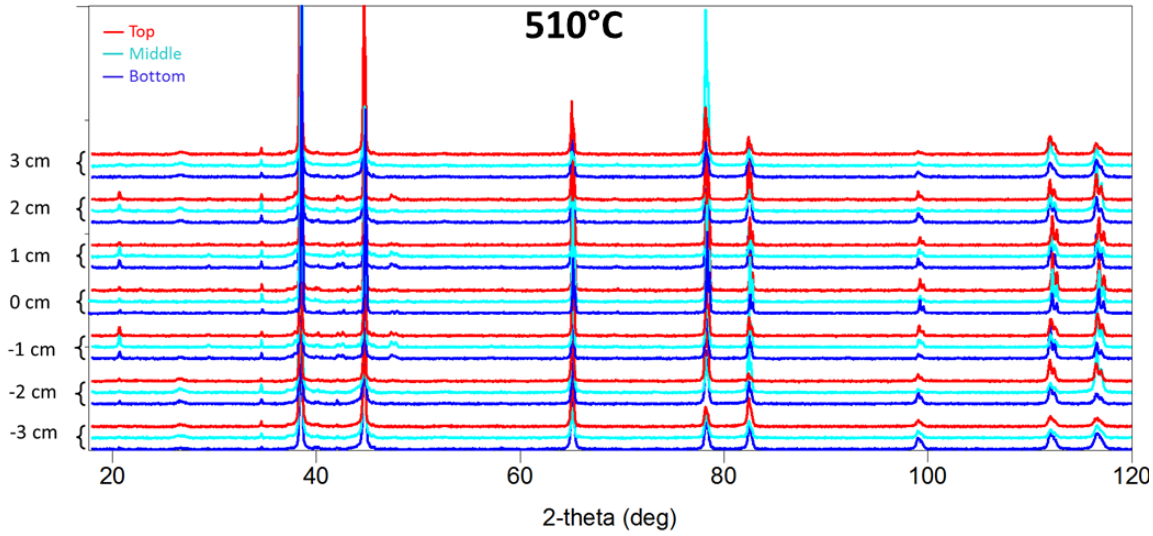

APPENDIX G

XRD PEAKS OF THE CONSTANT-TEMPERATURE FSW BY DISTANCE FROM THE WELD CENTER

This section contains the X-ray diffraction data for the constant-temperature friction stir welds at 490°C, 500°C, and 510°C. Data were acquired at the center of the weld and 30 mm from the center of the weld in 10 mm increments. Data were also acquired through the depth of the weld at the top, middle, and bottom locations, where the top and bottom were 10 mm from the middle.

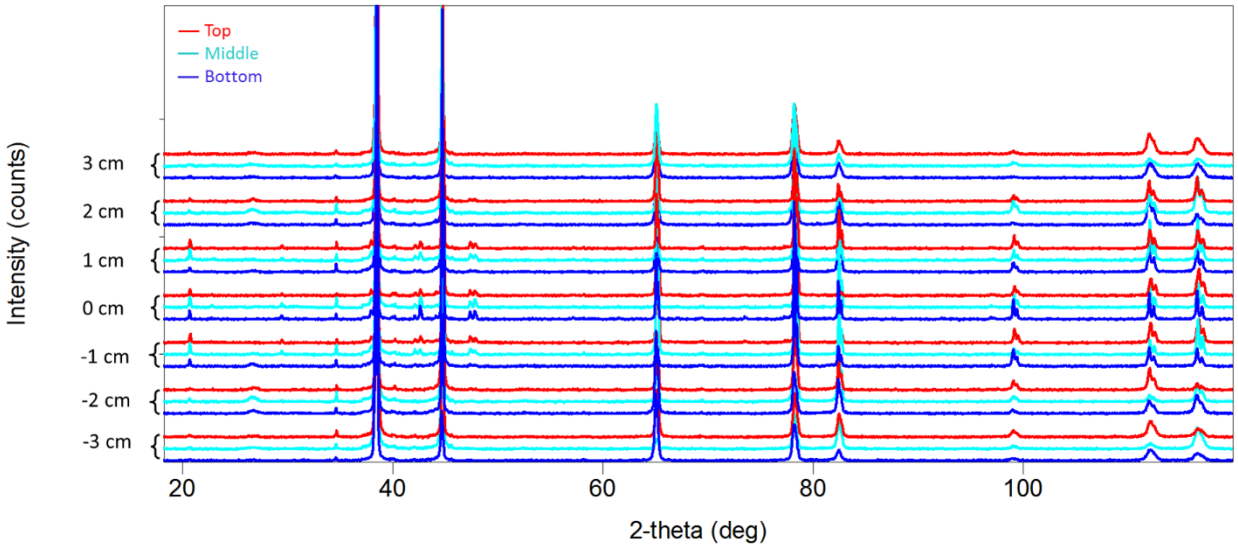

Figure G.1. XRD intensity versus 2-theta plots for constant-temperature FSW at 490°C at all distances from the center of the weld and throughout the depth of the weld.

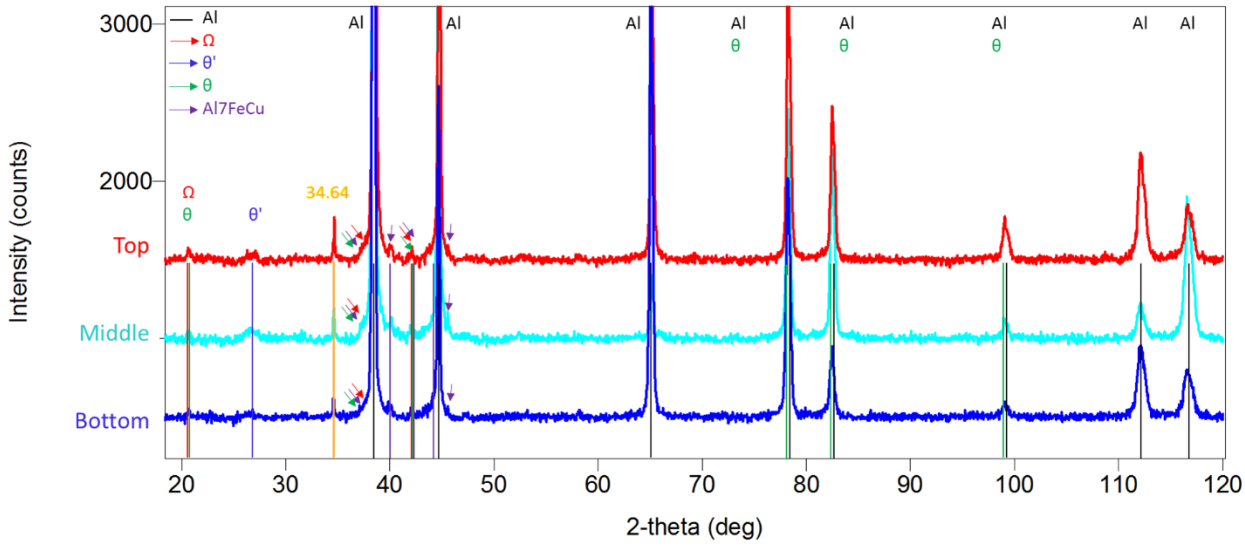

Figure G.2. XRD intensity versus 2-theta plots for constant-temperature FSW at 490°C and at -30 mm (the advancing side) throughout the depth of the weld (top, middle, and bottom).

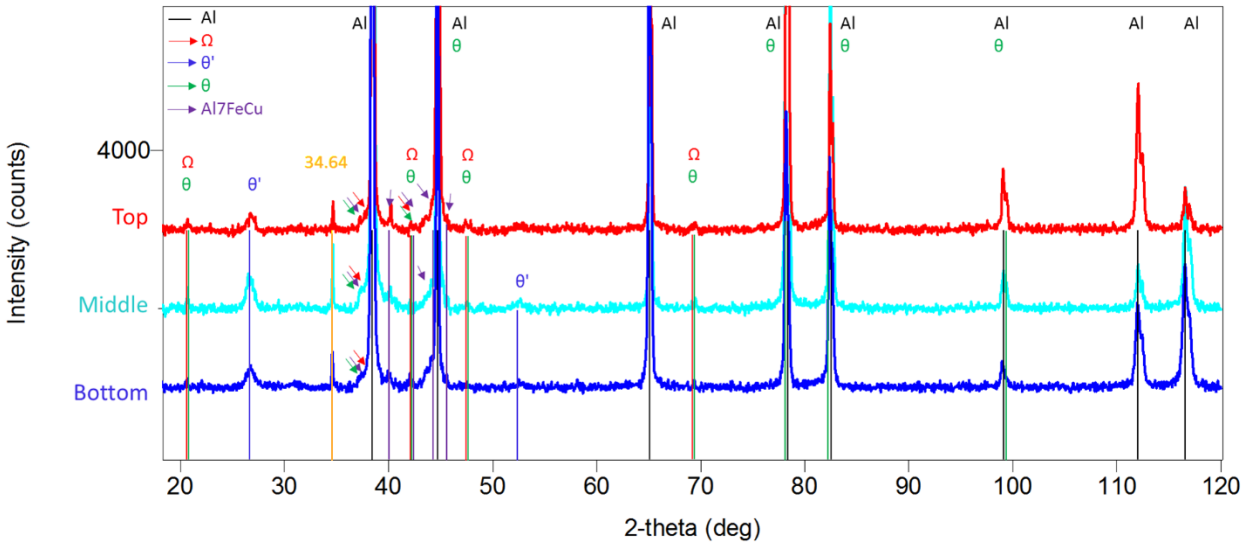

Figure G.3. XRD intensity versus 2-theta plots for constant-temperature FSW at 490°C and at -20 mm (the advancing side) throughout the depth of the weld (top, middle, and bottom).

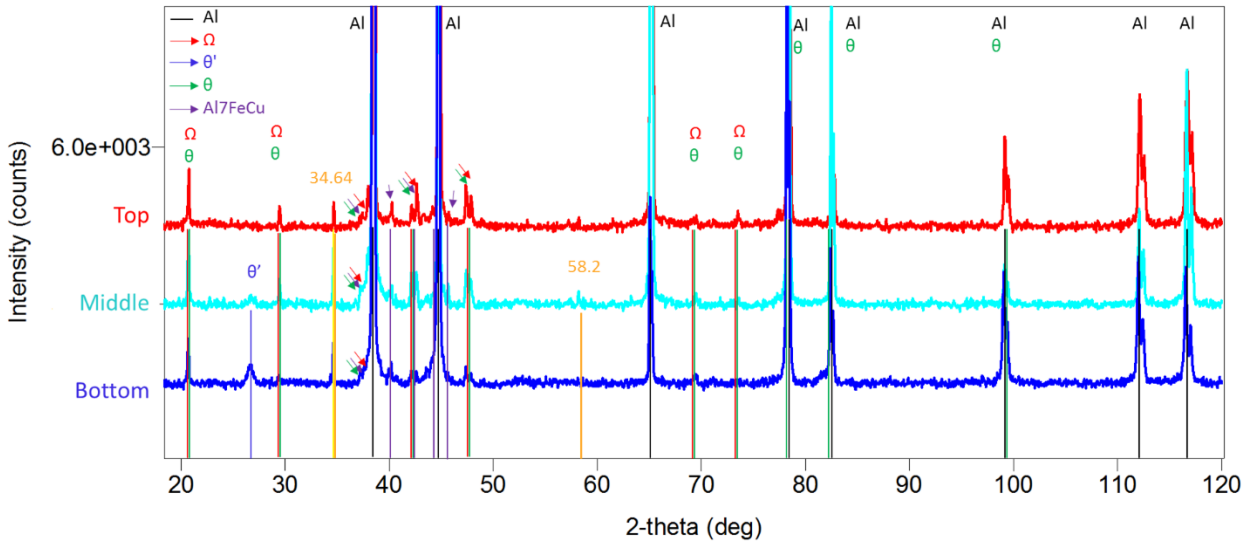

Figure G.4. XRD intensity versus 2-theta plots for constant-temperature FSW at 490°C and at -10 mm (the advancing side) throughout the depth of the weld (top, middle, and bottom).

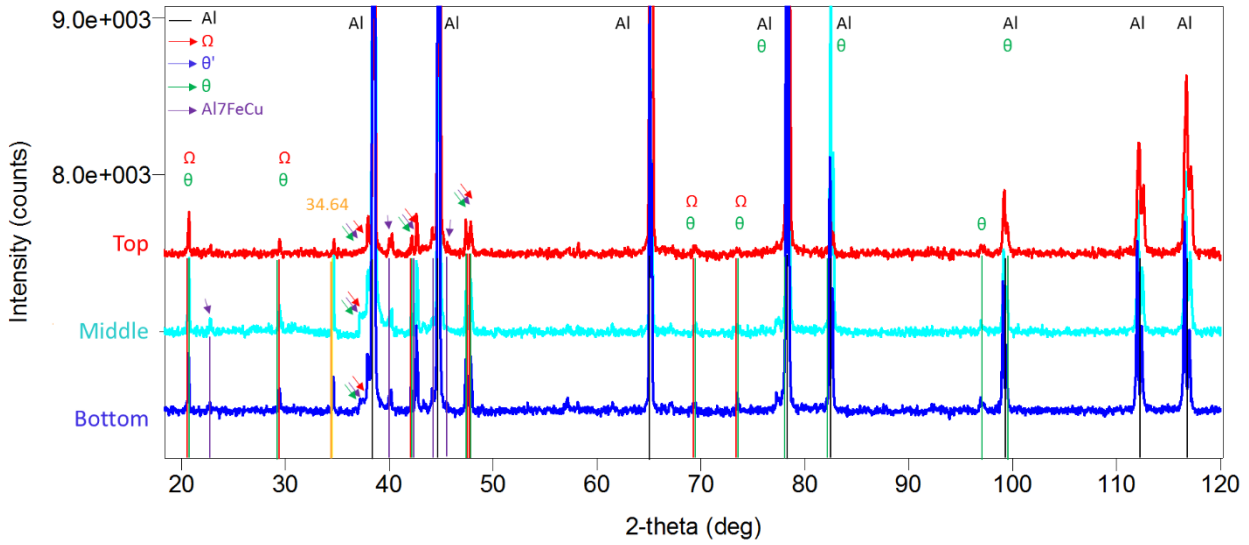

Figure G.5. XRD intensity versus 2-theta plots for constant-temperature FSW at 490°C and at 0 mm throughout the depth of the weld (top, middle, and bottom).

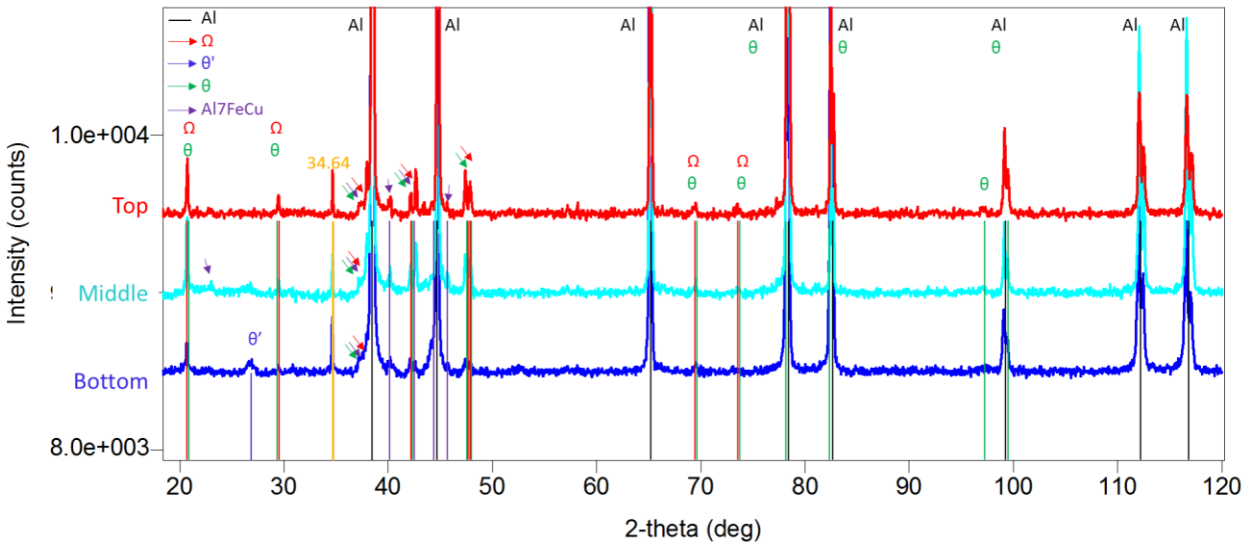

Figure G.6. XRD intensity versus 2-theta plots for constant-temperature FSW at 490°C and at +10 mm (the retreating side) throughout the depth of the weld (top, middle, and bottom).

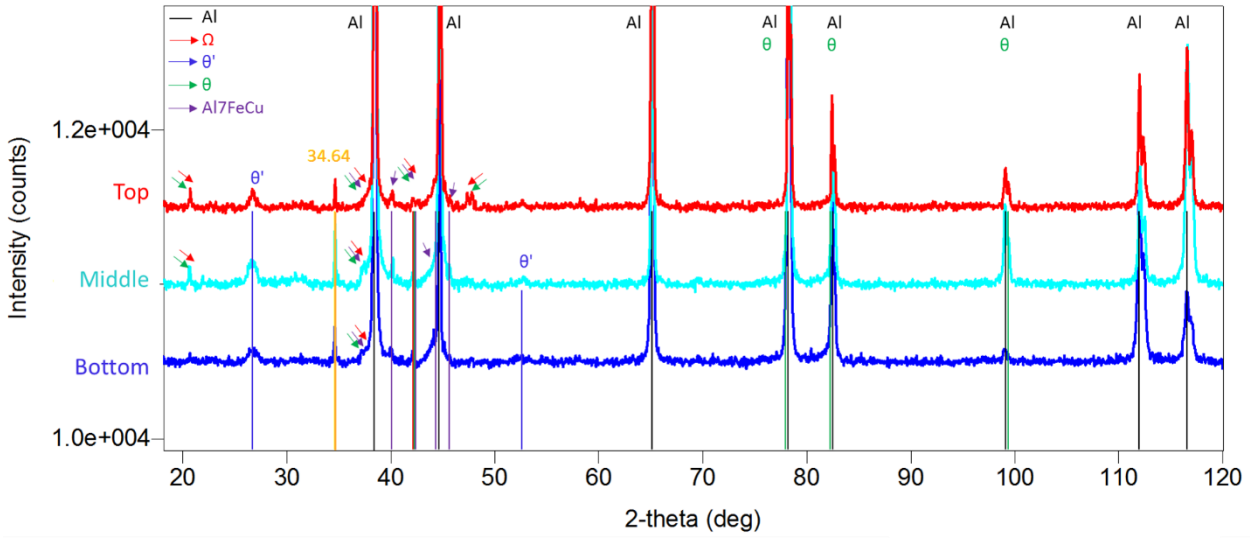

Figure G.7. XRD intensity versus 2-theta plots for constant-temperature FSW at 490°C and at +20 mm (the retreating side) throughout the depth of the weld (top, middle, and bottom).

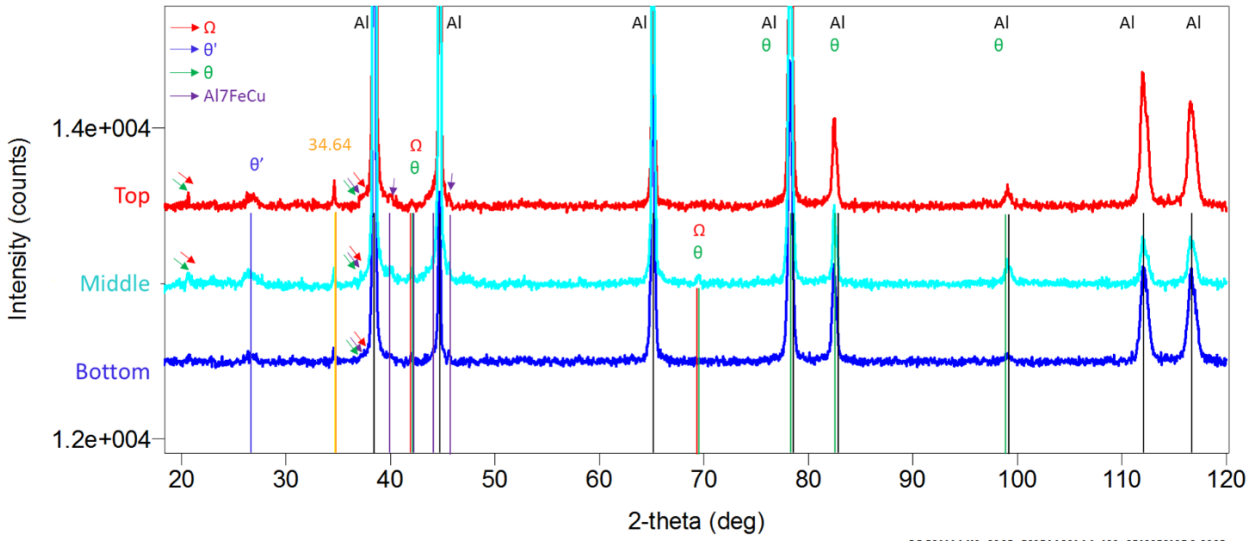

Figure G.8. XRD intensity versus 2-theta plots for constant-temperature FSW at 490°C and at +30 mm (the retreating side) throughout the depth of the weld (top, middle, and bottom).

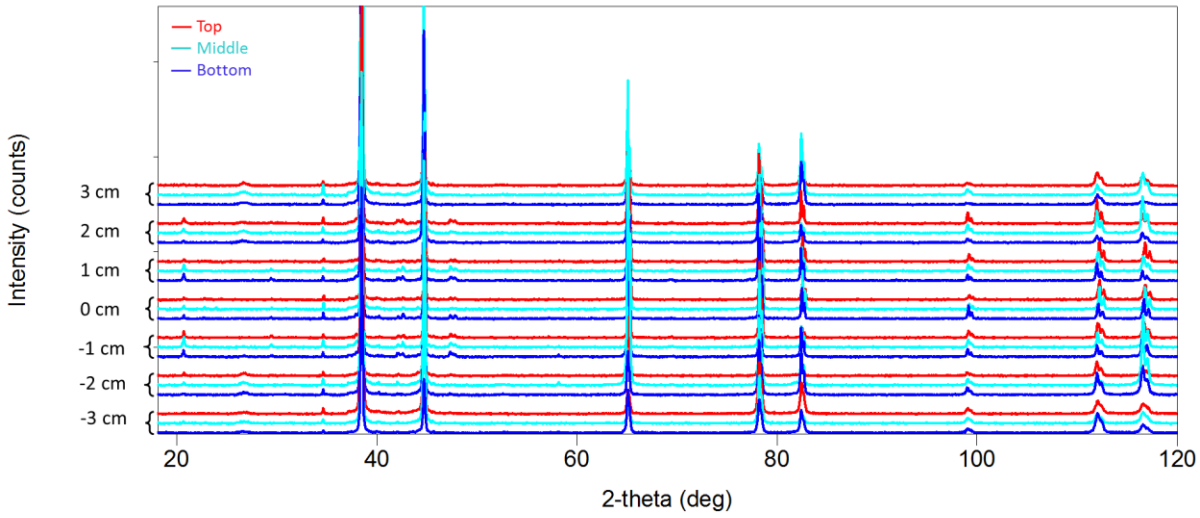

Figure G.9. XRD intensity versus 2-theta plots for constant-temperature FSW at 500°C at all distances from the center of the weld and throughout the depth of the weld.

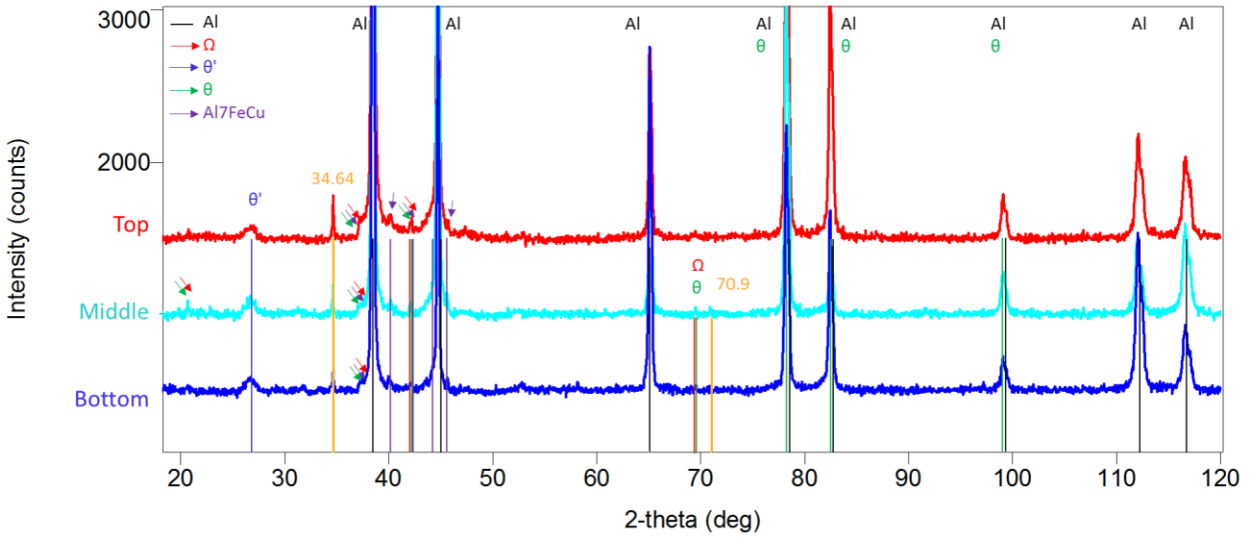

Figure G.10. XRD intensity versus 2-theta plots for constant-temperature FSW at 500°C and at -30 mm (the advancing side) throughout the depth of the weld (top, middle, and bottom).

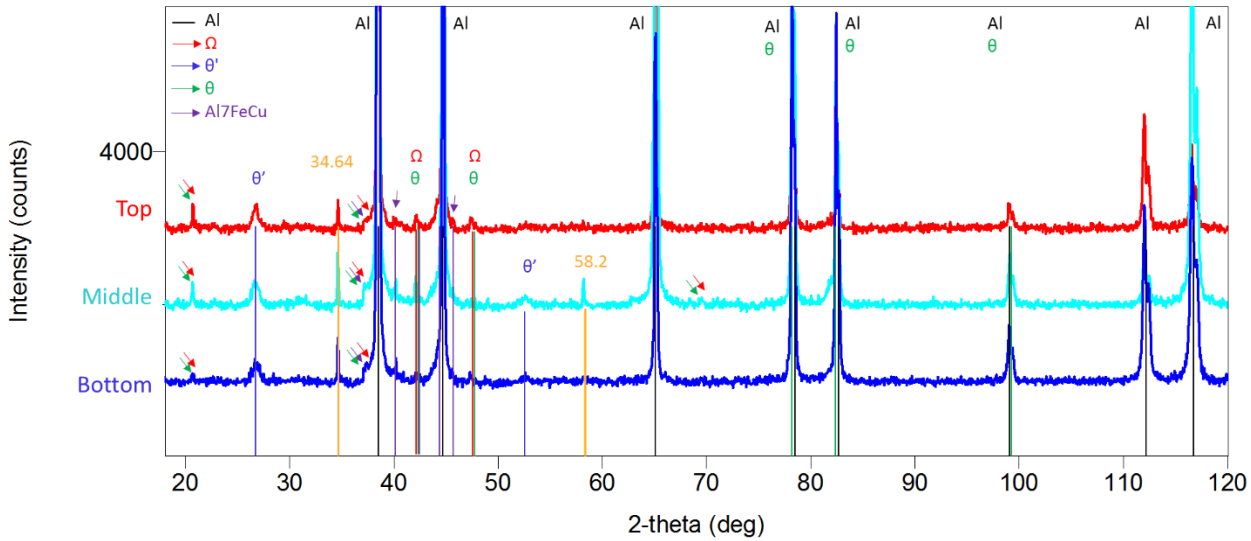

Figure G.11. XRD intensity versus 2-theta plots for constant-temperature FSW at 500°C and at -20 mm (the advancing side) throughout the depth of the weld (top, middle, and bottom).

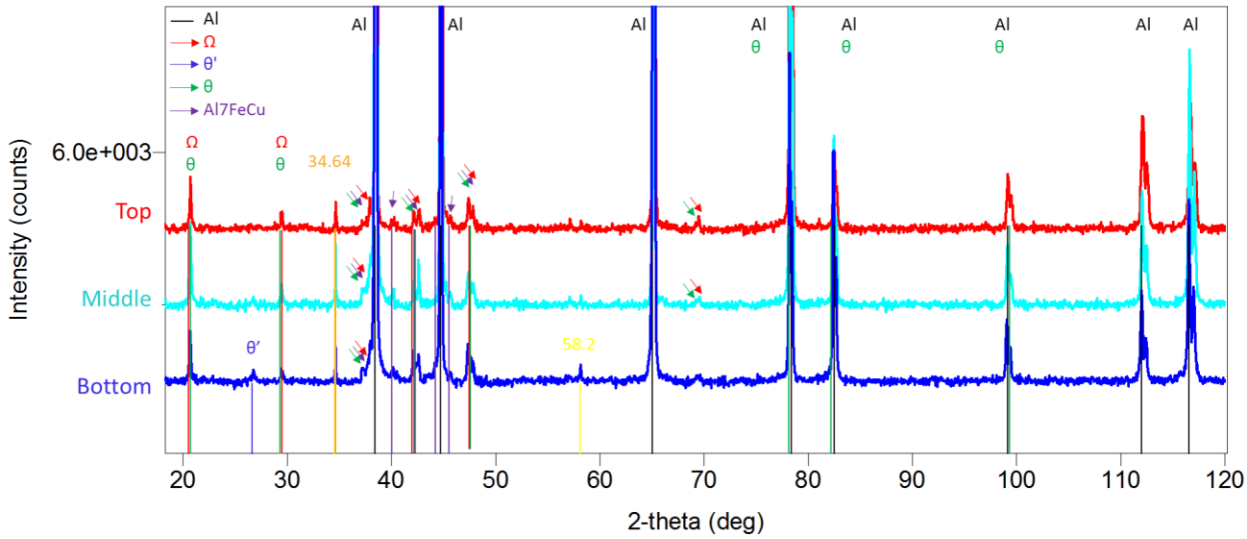

Figure G.12. XRD intensity versus 2-theta plots for constant-temperature FSW at 500°C and at -10 mm (the advancing side) throughout the depth of the weld (top, middle, and bottom).

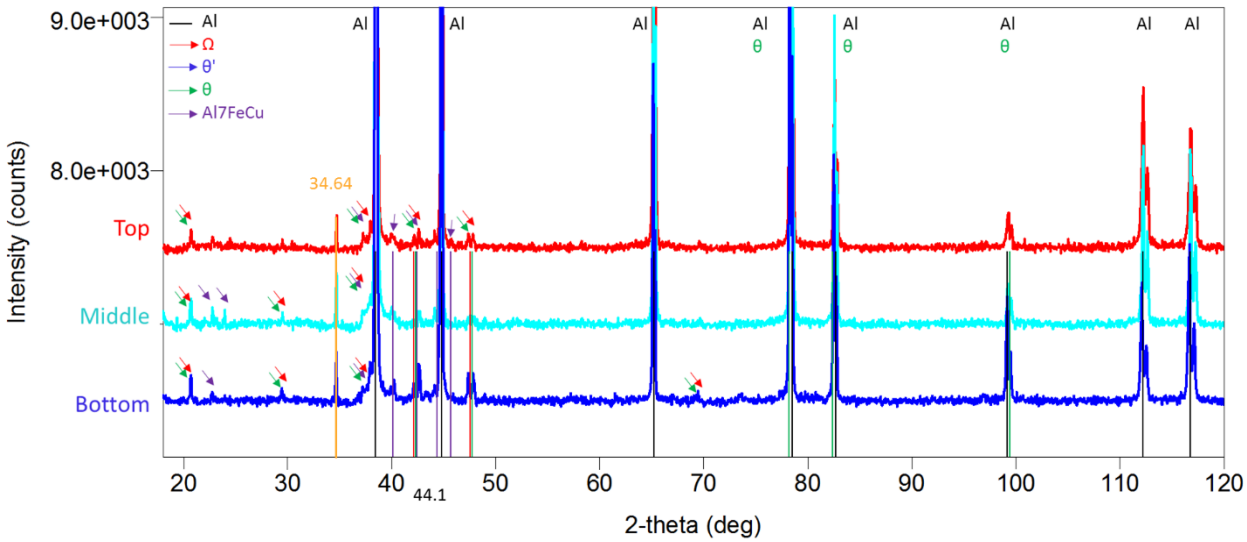

Figure G.13. XRD intensity versus 2-theta plots for constant-temperature FSW at 500°C and at 0 mm throughout the depth of the weld (top, middle, and bottom).

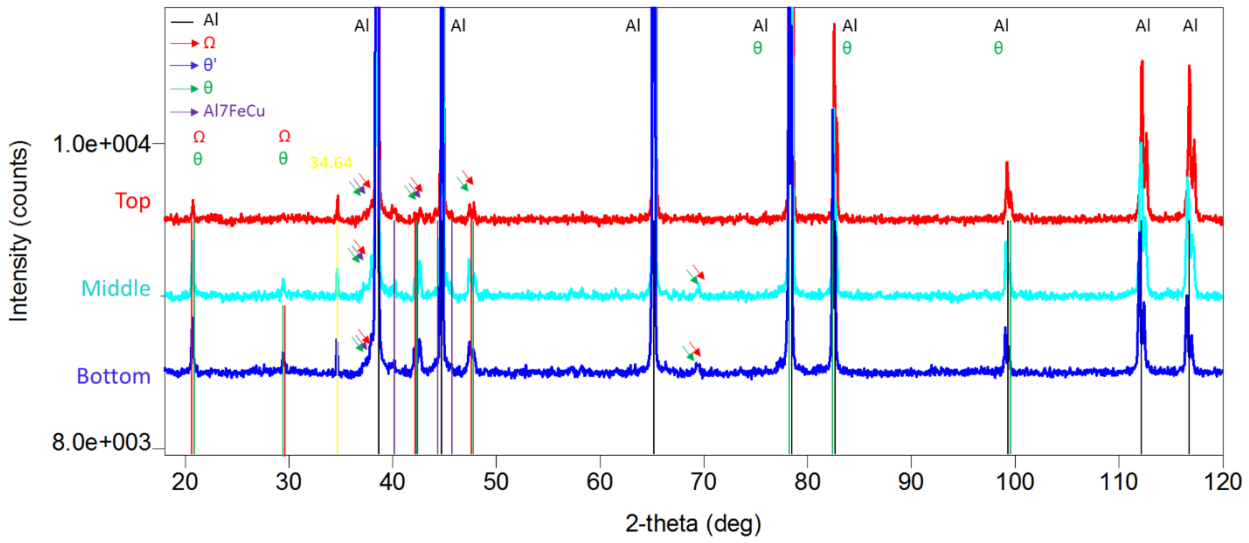

Figure G.14. XRD intensity versus 2-theta plots for constant-temperature FSW at 500°C and at +10 mm (the retreating side) throughout the depth of the weld (top, middle, and bottom).

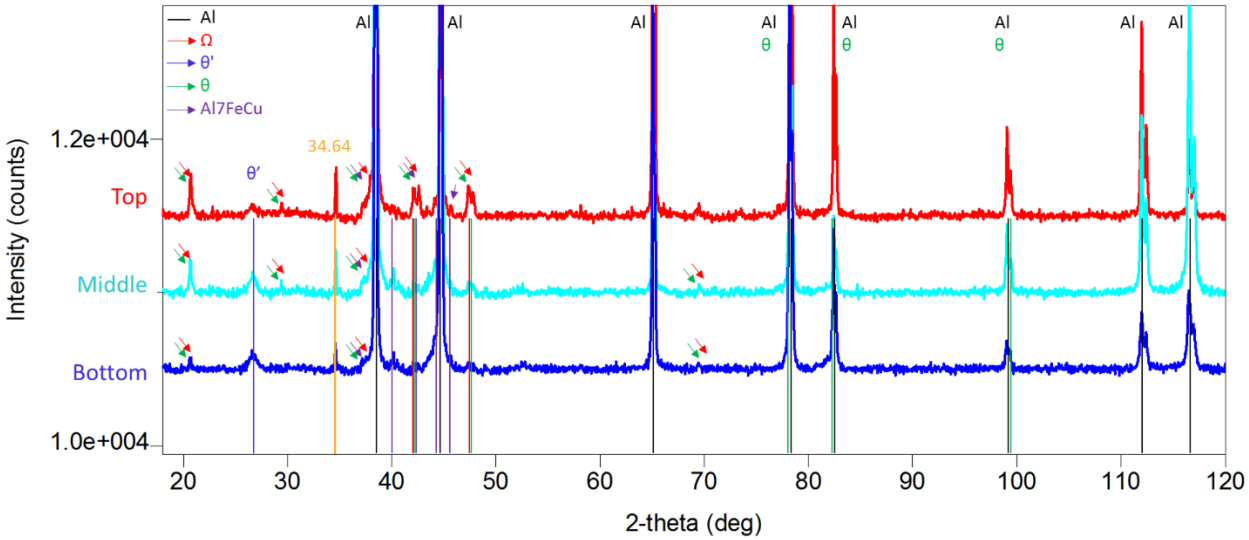

Figure G.15. XRD versus 2-theta plots for constant-temperature FSW at 500°C and at +20 mm (the retreating side) throughout the depth of the weld (top, middle, and bottom).

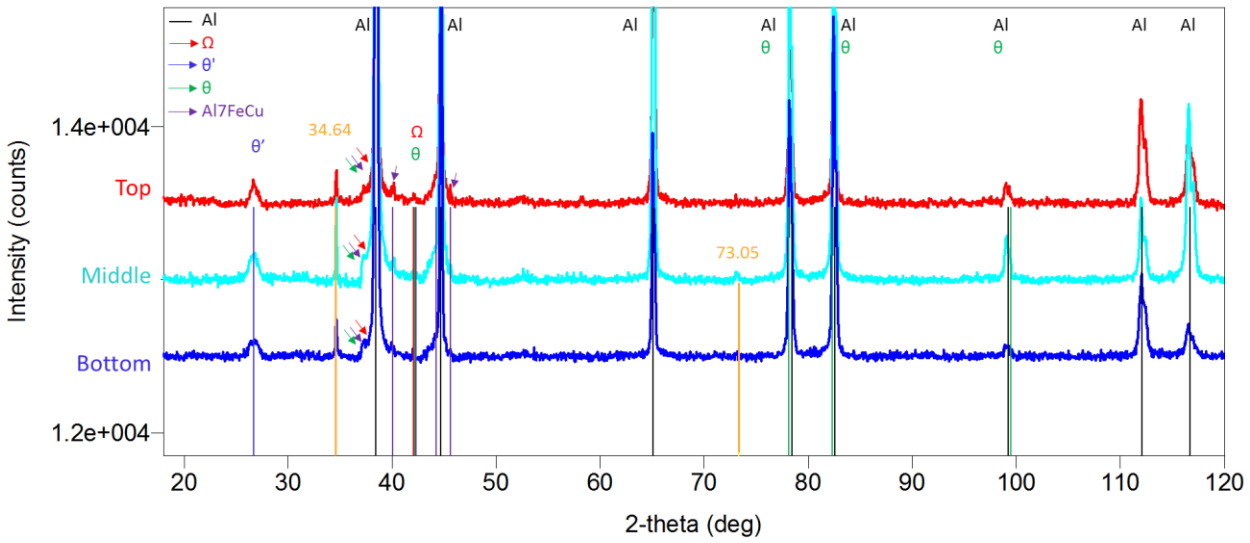

Figure G.16. XRD intensity versus 2-theta plots for constant-temperature FSW at 500°C and at +30 mm (the retreating side) throughout the depth of the weld (top, middle, and bottom).

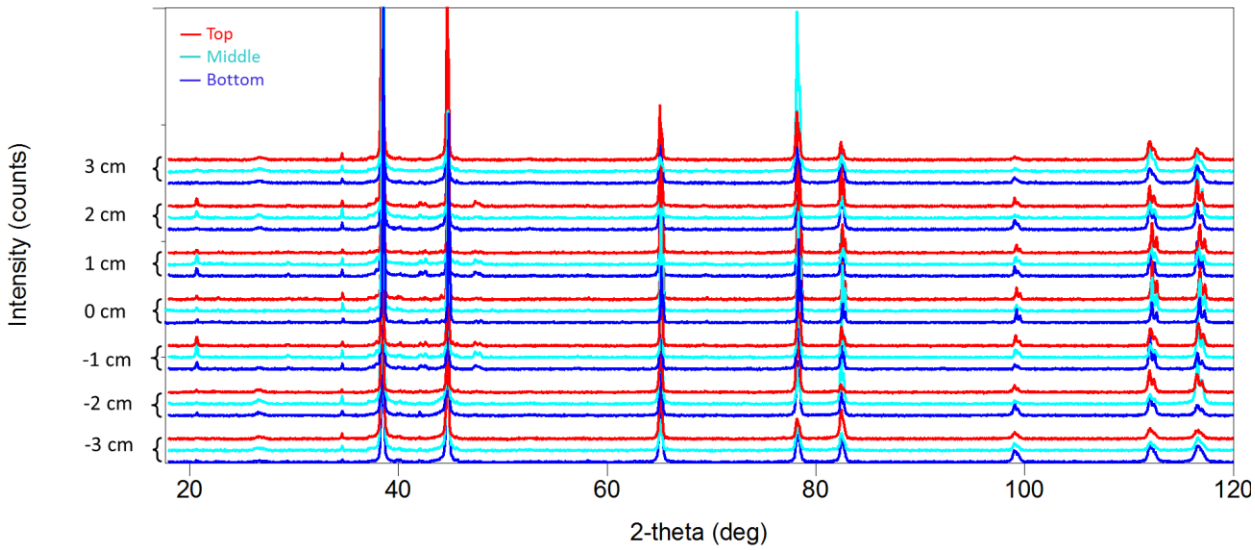

Figure G.17. XRD versus 2-theta plots for constant-temperature FSW at 510°C at all distances from the center of the weld and throughout the depth of the weld.

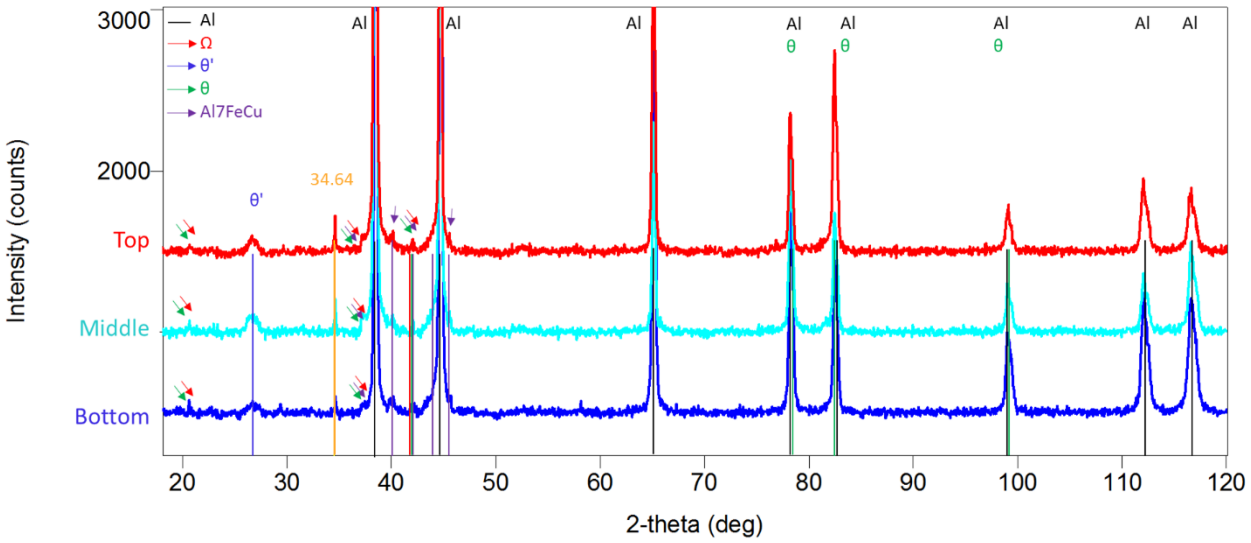

Figure G.18. XRD intensity versus 2-theta plots for constant-temperature FSW at 510°C and at -30 mm (the advancing side) throughout the depth of the weld (top, middle, and bottom).

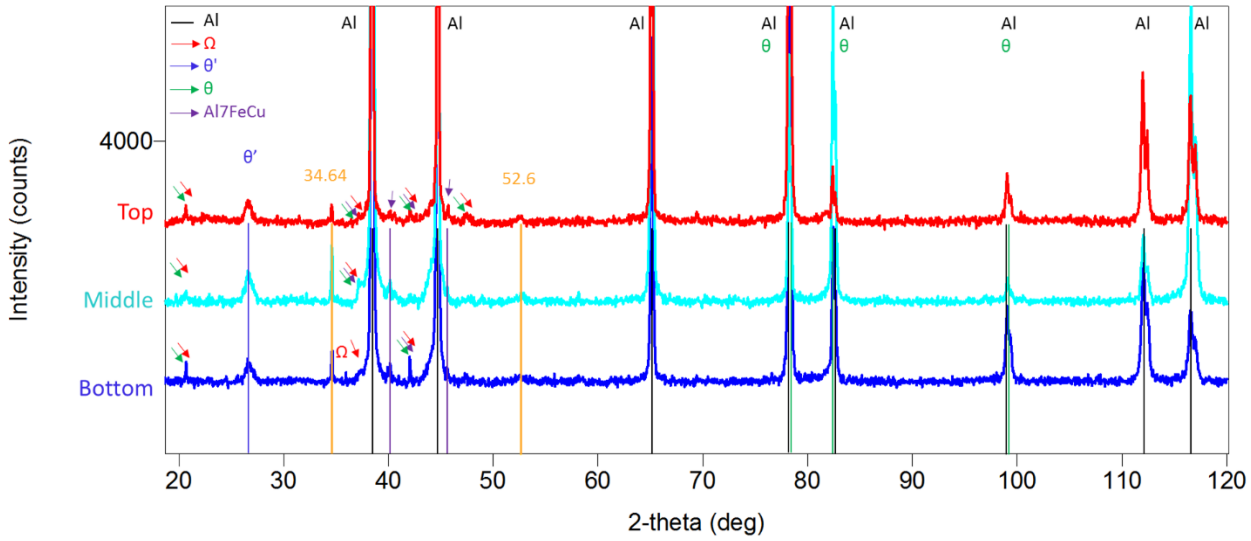

Figure G.19. XRD intensity versus 2-theta plots for constant-temperature FSW at 510°C and at -20 mm (the advancing side) throughout the depth of the weld (top, middle, and bottom).

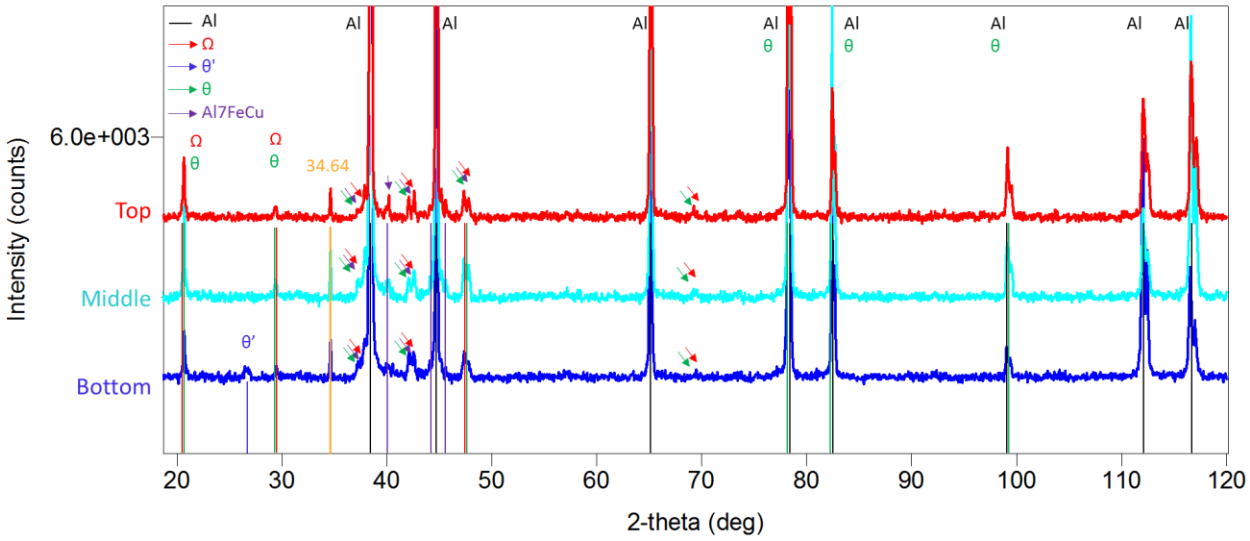

Figure G.20. XRD intensity versus 2-theta plots for constant-temperature FSW at 510°C and at -10 mm (the advancing side) throughout the depth of the weld (top, middle, and bottom).

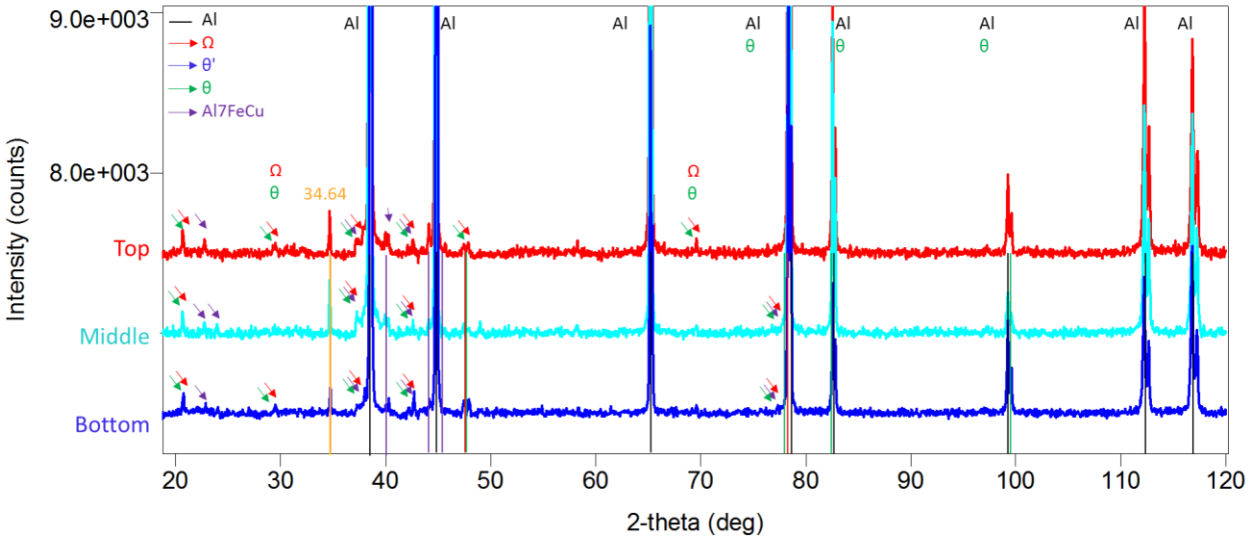

Figure G.21. XRD intensity versus 2-theta plots for constant-temperature FSW at 510°C and at 0 mm throughout the depth of the weld (top, middle, and bottom).

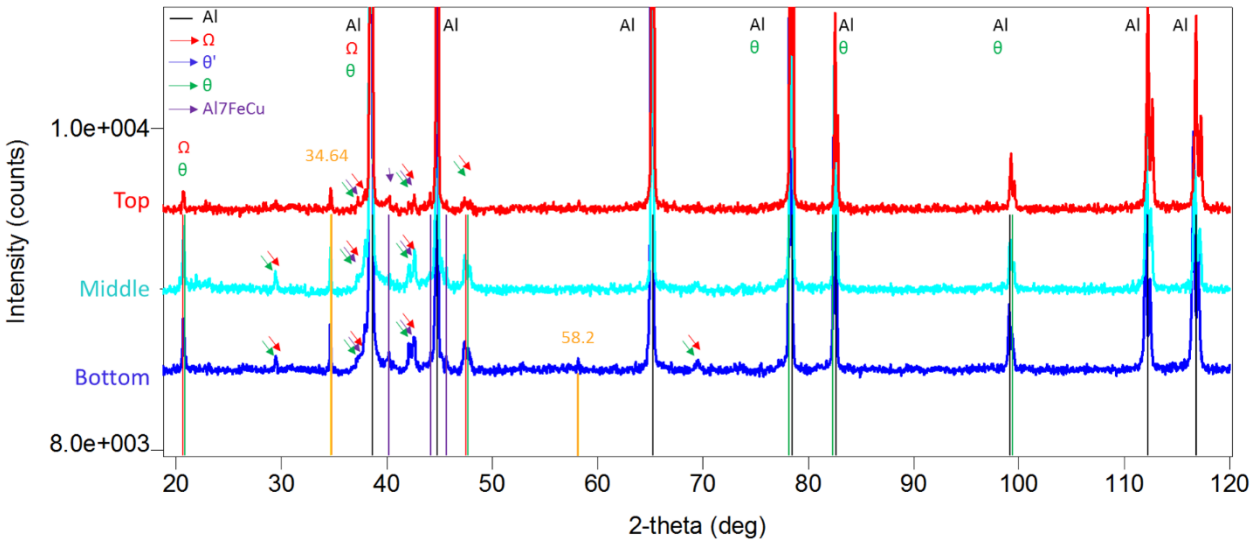

Figure G.22. XRD intensity versus 2-theta plots for constant-temperature FSW at 510°C and at +10 mm (the retreating side) throughout the depth of the weld (top, middle, and bottom).

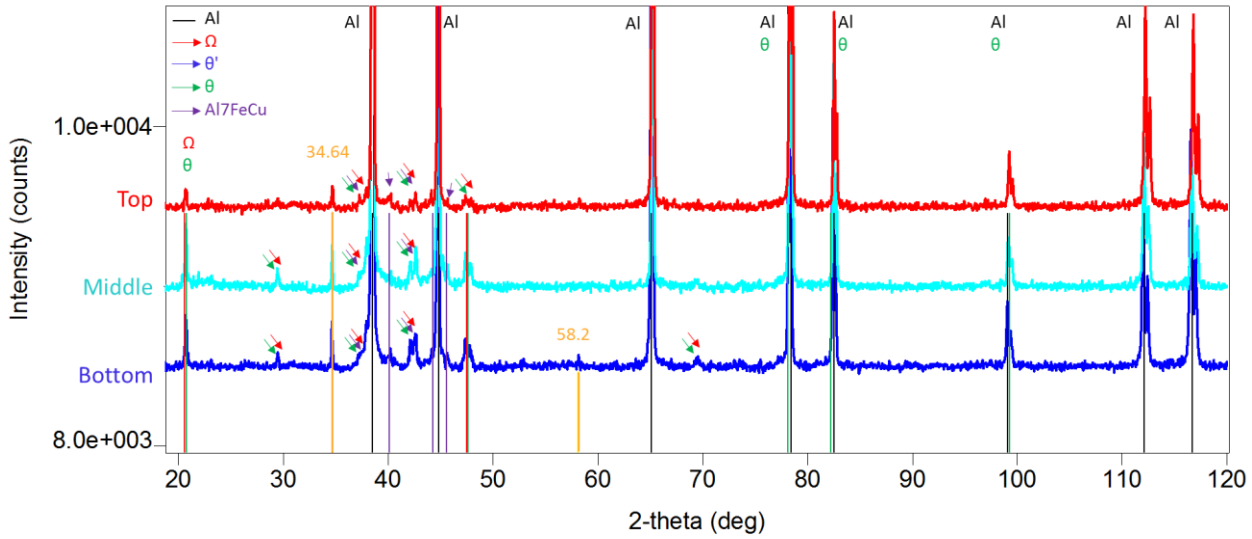

Figure G.23. XRD intensity versus 2-theta plots for constant-temperature FSW at 510°C and at +20 mm (the retreating side) throughout the depth of the weld (top, middle, and bottom).

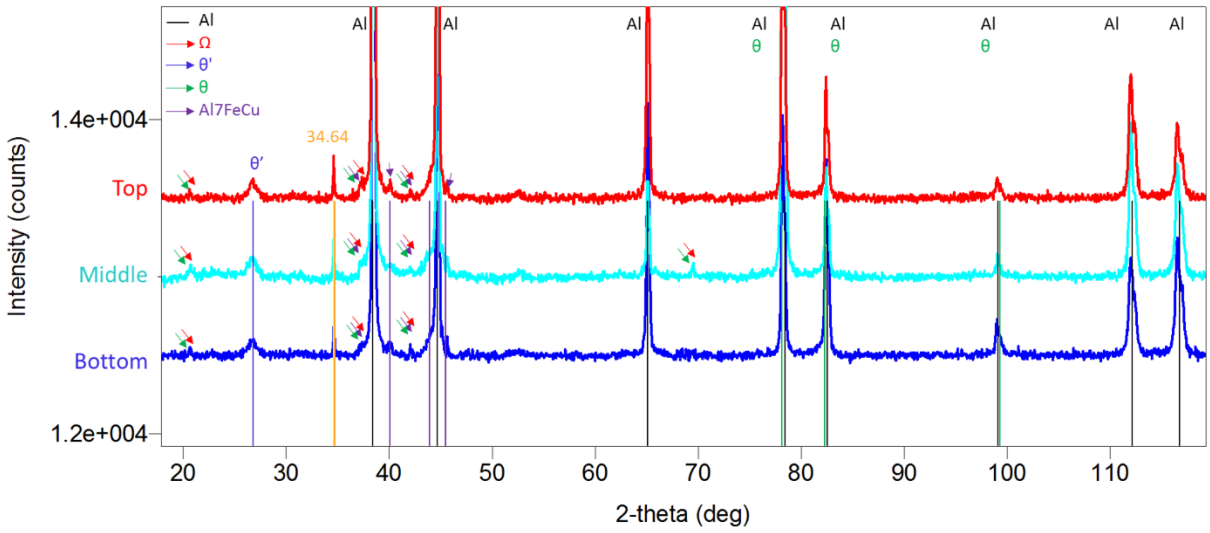

Figure G.24. XRD intensity versus 2-theta plots for constant-temperature FSW at 510°C and at +30 mm (the retreating side) throughout the depth of the weld (top, middle, and bottom).

.

BIBLIOGRAPHY

BIBLIOGRAPHY

[1] W.D. Callister, D.G. Rethwisch, Materials Science and Engineering: An Introduction, 8th ed., Wiley, Hoboken, NJ, 2011.

[2] ASM International Handbook Committee, ASM Handbook, Volume 02 - Properties and Selection: Nonferrous Alloys and Special-Purpose Materials, ASM International, [S.l.], 1990. http://www.knovel.com/knovel2/Toc.jsp?BookID=3106 (accessed November 6, 2014).

[3] J.C. Williams, E.A. Starke Jr., Progress in structural materials for aerospace systems, Acta Mater. 51 (2003) 5775–5799. https://doi.org/10.1016/j.actamat.2003.08.023.

[4] J.C. Williams, E.A. Starke Jr., Progress in structural materials for aerospace systems, Acta Mater. 51 (2003) 5775–5799. https://doi.org/10.1016/j.actamat.2003.08.023.

[5] D. Sivolella, To orbit and back again: how the space shuttle flew in space, Springer/Praxis Pub, Chichester, UK : New York, 2014.

[6] Corporate Average Fuel Economy (CAFE) Standards | US Department of Transportation, (n.d.). https://www.transportation.gov/mission/sustainability/corporate-average-fuel-economy-cafe-standards (accessed February 23, 2020).

[7] F. Ford, REVIEW: The all-aluminum F-150, what you need to know about the new body | Friendly Ford, (n.d.). https://www.friendlyfordny.com/blog/2016/may/10/review-the-allaluminum-f150-what-you-need-to-know-about-the-new-body.htm (accessed February 19, 2020).

[8] What is aluminium on the Ford F-150?, Team Ford. (2018). https://www.teamford.ca/2018/01/02/aluminium-ford-f-150/ (accessed February 19, 2020).

[9] A. Cho, B. Bes, Damage Tolerance Capability of an Al-Cu-Mg-Ag Alloy (2139), Mater. Sci. Forum. 519–521 (2006) 603–608. https://doi.org/10.4028/www.scientific.net/MSF.519-521.603.

[10] R.S. Mishra, H. Sidhar, Friction stir welding of 2xxx aluminum alloys including Al--Li alloys, Butterworth-Heinemann, Oxford, 2017. http://search.ebscohost.com/login.aspx?direct=true&scope=site&db=nlebk&db=nlabk&AN=1145018 (accessed June 5, 2020).

[11] R.S. Mishra, Z.Y. Ma, Friction stir welding and processing, Mater. Sci. Eng. R Rep. 50 (2005) 1–78. https://doi.org/10.1016/j.mser.2005.07.001.

[12] K. Ross, G. Grant, J. Darsell, D. Catalini, Simultaneous Independent Control of Tool Axial Force and Temperature in Friction Stir Processing, Frict. Stir Weld. Process. IX. (2017) 269–275. https://doi.org/10.1007/978-3-319-52383-5_26.

[13] K. Ross, B. Sutton, G. Grant, G. Cannell, G. Frederick, R. Couch, Development of Friction Stir Processing for Repair of Nuclear Dry Cask Storage System Canisters, Frict. Stir Weld. Process. IX. (2017) 39–46. https://doi.org/10.1007/978-3-319-52383-5_5.

[14] Erik Polsen, Lynne Krogsrud, Robert Carter, William Oberle, Christopher Haines, Andrew Littlefield, Lightweight Combat Vehicle S&T Campaign, U.S. Army TARDEC/Ground System Survivability, Warren, MI, 2014. https://apps.dtic.mil/sti/pdfs/AD1010791.pdf (accessed July 5, 2021).

[15] M. Green, J.D. Brown, M2/M3 Bradley at war, Zenith Press, St. Paul, Minn, 2007.

[16] N.N. Greenwood, A. Earnshaw, Chemistry of the elements, 2nd ed, Butterworth-Heinemann, Oxford ; Boston, 1997.

[17] F. Cardarelli, Materials handbook: a concise desktop reference, Springer, Berlin; London, 2008.

[18] L.P.H. Jeurgens, W.G. Sloof, F.D. Tichelaar, E.J. Mittemeijer, Structure and morphology of aluminium-oxide films formed by thermal oxidation of aluminium, Thin Solid Films. 418 (2002) 89–101. https://doi.org/10.1016/S0040-6090(02)00787-3.

[19] L.F. Mondolfo, Aluminum alloys: structure and properties, Butterworths, London ; Boston, 1976.

[20] S. Li, X. Yang, J. Hou, W. Du, A review on thermal conductivity of magnesium and its alloys, J. Magnes. Alloys. 8 (2020) 78–90. https://doi.org/10.1016/j.jma.2019.08.002.

[21] J. Carvill, Thermodynamics and heat transfer, in: Mech. Eng. Data Handb., Elsevier, 1993: pp. 102–145. https://doi.org/10.1016/B978-0-08-051135-1.50008-X.

[22] A. O'Brien, K. Sinnes, eds., Welding Handbook: Materials and Applications, Part 2, 9th Edition, American Welding Society, Miami, FL, 2015.

[23] K. Anderson, J. Weritz, J.G. Kaufman, eds., Aluminum Alloy Nomenclature and Temper Designations[1], in: Alum. Sci. Technol., ASM International, 2018: pp. 3–30. https://doi.org/10.31399/asm.hb.v02a.a0006482.

[24] Iris De Graeve, Jurgen Hirsch, Wrought, AluMATTER. (2001). http://www.aluminium.matter.org.uk/content/html/eng/default.asp?catid=214&pageid=2144417044 (accessed November 6, 2014).

[25] D.A. Porter, K.E. Easterling, M.Y. Sherif, Phase transformations in metals and alloys, 3rd ed, CRC Press, Boca Raton, FL, 2009.

[26] J.M. Silcock, T.J. Heal, H.K. Hardy, Structural ageing characteristics of binary aluminium-copper alloys, J Inst Met. Vol: 82 (1954) 239–249.

[27] S.P. Ringer, W. Yeung, B.C. Muddle, I.J. Polmear, Precipitate stability in Al-Cu-Mg-Ag alloys aged at high temperatures, Acta Metall. Mater. 42 (1994) 1715–1725. https://doi.org/10.1016/0956-7151(94)90381-6.

[28] S.P. Ringer, K. Hono, I.J. Polmear, T. Sakurai, Nucleation of precipitates in aged AlCuMg(Ag) alloys with high Cu:Mg ratios, Acta Mater. 44 (1996) 1883–1898. https://doi.org/10.1016/1359-6454(95)00314-2.

[29] Q. Li, R.N. Shenoy, DSC and TEM characterizations of thermal stability of an Al–Cu–Mg–Ag alloy, J. Mater. Sci. 32 (1997) 3401–3406. https://doi.org/10.1023/A:1018664515422.

[30] C. Laird, H. Aaronson, STRUCTURES AND MIGRATION KINETICS OF ALPHA.. THETA PRIME BOUNDARIES IN AL-4 PCT CU. PT. 1. INTERFACIAL STRUCTURES, TRANS MET SOC AIME. 242 (1968).

[31] S.C. Wang, M.J. Starink, Two types of S phase precipitates in Al–Cu–Mg alloys, Acta Mater. 55 (2007) 933–941. https://doi.org/10.1016/j.actamat.2006.09.015.

[32] S.C. Wang, M.J. Starink, Precipitates and intermetallic phases in precipitation hardening Al–Cu–Mg–(Li) based alloys, Int. Mater. Rev. 50 (2005) 193–215. https://doi.org/10.1179/174328005X14357.

[33] Y.C. Lin, Y.-C. Xia, Y.-Q. Jiang, H.-M. Zhou, L.-T. Li, Precipitation hardening of 2024-T3 aluminum alloy during creep aging, Mater. Sci. Eng. A. 565 (2013) 420–429. https://doi.org/10.1016/j.msea.2012.12.058.

[34] Y.C. Lin, Y.-Q. Jiang, Y.-C. Xia, X.-C. Zhang, H.-M. Zhou, J. Deng, Effects of creep-aging processing on the corrosion resistance and mechanical properties of an Al–Cu–Mg alloy, Mater. Sci. Eng. A. 605 (2014) 192–202. https://doi.org/10.1016/j.msea.2014.03.055.

[35] Silcock, J. M., The structural ageing characteristics of Al-Cu-Mg alloys with copper-magnesium weight ratios of 7:1 and 2.2:1, J. Inst. Met. 89 (1961) 203–210.

[36] K.M. Knowles, W.M. Stobbs, The structure of {111} age-hardening precipitates in Al–Cu–Mg–Ag alloys, Acta Crystallogr. B. 44 (1988) 207–227. https://doi.org/10.1107/S0108768187012308.

[37] B.C. Muddle, I.J. Polmear, The precipitate Ω phase in Al-Cu-Mg-Ag alloys, Acta Metall. 37 (1989) 777–789. https://doi.org/10.1016/0001-6160(89)90005-9.

[38] J.M. Silcock, T.J. Heal, The θ' structure in aluminium–copper alloys, Acta Crystallogr. 9 (1956) 680–680. https://doi.org/10.1107/S0365110X56001820.

[39] M.-W. Park, J.-S. Lee, D.-G. Lim, Y.-G. Choi, D.-J. Kwak, Y.-M. Sung, Transmission electron microscopy characterization of Al2Cu precipitate growth kinetics by in situ heat treatment, Vacuum. 83 (2008) 107–112. https://doi.org/10.1016/j.vacuum.2008.03.049.

[40] I.J. Polmear, M.J. Couper, Design and development of an experimental wrought aluminum alloy for use at elevated temperatures, Metall. Trans. A. 19 (1988) 1027–1035. https://doi.org/10.1007/BF02628387.

[41] S.P. Ringer, K. Hono, Microstructural Evolution and Age Hardening in Aluminium Alloys: Atom Probe Field-Ion Microscopy and Transmission Electron Microscopy Studies, Mater. Charact. 44 (2000) 101–131. https://doi.org/10.1016/S1044-5803(99)00051-0.

[42] J.A. Taylor, B.A. Parker, I.J. Polmear, Precipitation in Al-Cu-Mg-Ag casting alloy, Met. Sci. 12 (1978) 478–482. https://doi.org/10.1179/030634578790433341.

[43] B.M. Gable, G.J. Shiflet, E.A. Starke Jr., The effect of Si additions on Ω precipitation in Al–Cu–Mg–(Ag) alloys, Scr. Mater. 50 (2004) 149–153. https://doi.org/10.1016/j.scriptamat.2003.09.004.

[44] L. Reich, M. Murayama, K. Hono, Evolution of Ω phase in an Al–Cu–Mg–Ag alloy—a three-dimensional atom probe study, Acta Mater. 46 (1998) 6053–6062. https://doi.org/10.1016/S1359-6454(98)00280-8.

[45] I.S. Suh, J.K. Park, Influence of the elastic strain energy on the nucleation of Ω phase in Al-Cu-Mg(-Ag) alloys, Scr. Metall. Mater. 33 (1995) 205–211. https://doi.org/10.1016/0956-716X(95)00133-G.

[46] K. Hono, T. Sakurai, I.J. Polmear, Pre-precipitate clustering in an Al-Cu-Mg-Ag alloy, Scr. Metall. Mater. 30 (1994) 695–700. https://doi.org/10.1016/0956-716X(94)90184-8.

[47] K. Hono, N. Sano, S.S. Babu, R. Okano, T. Sakurai, Atom probe study of the precipitation process in Al-Cu-Mg-Ag alloys, Acta Metall. Mater. 41 (1993) 829–838. https://doi.org/10.1016/0956-7151(93)90016-L.

[48] L. Sun, D.L. Irving, M.A. Zikry, D.W. Brenner, First-principles investigation of the structure and synergistic chemical bonding of Ag and Mg at the Al | Ω interface in a Al–Cu–Mg–Ag alloy, Acta Mater. 57 (2009) 3522–3528. https://doi.org/10.1016/j.actamat.2009.04.006.

[49] S.P. Ringer, B.C. Muddle, I.J. Polmear, Effects of cold work on precipitation in Al-Cu-Mg-(Ag) and Al-Cu-Li-(Mg-Ag) alloys, Metall. Mater. Trans. A. 26 (1995) 1659–1671. https://doi.org/10.1007/BF02670753.

[50] L. Del Castillo, E.J. Lavernia, Microstructure and Mechanical Behavior of Spray-Deposited Al-Cu-Mg(-Ag-Mn) Alloys, Met. Mater Trans Phys Met. Mater Sci. 31 (2000) 2287–2298.

[51] Kristina Morrow, 95--Aluminum Alloy 2139 Plates. Solicitation Number: W91CRB-10-T-0096, (2010). https://www.fbo.gov/index?s=opportunity&mode=form&tab=core&id=bfc8cbf52d05d361f32fd14337d37b48.

[52] B. Justusson, Microstructural Investigation and Evaluation of Mechanical Properties in Friction Stir Welded Joints, U.S. Army Research Laboratory, U.S. Army Research Labortory, WMRD, RDRL-WMM-B, Aberdeen Proving Ground, MD, 2011. file:///C:/Users/Uchechi/Documents/01%20MSU/01%20MSE/01%20Readings/Aluminum/ADA558384.pdf (accessed November 7, 2017).

[53] W.M. Lee, M.A. Zikry, Microstructural Characterization of a High-Strength Aluminum Alloy Subjected to High Strain-Rate Impact, Metall. Mater. Trans. A. 42 (2011) 1215–1221. https://doi.org/10.1007/s11661-010-0476-z.

[54] T. Sano, U. Okeke, J. Yu, C. Boehlert, C.-F. Yen, Tms, Analysis of the Microstructure and Properties of Friction Stir Weld Zones in the Al 2139-T8 Alloy, in: TMS 2014 Suppl. Proc., John Wiley & Sons, Inc., 2014: pp. 545–555. http://onlinelibrary.wiley.com/doi/10.1002/9781118889879.ch66/summary (accessed October 30, 2014).

[55] T. Sano, J. Yu, J. Medintz, C.-F. Yen, K. Doherty, The Effect of Friction Stir Welding on the Microstructure and Tensile Properties of Al 2139-T8 Alloys, in: C.E. Suarez (Ed.), Light Met. 2012, John Wiley & Sons, Inc., 2012: pp. 497–501. http://onlinelibrary.wiley.com/doi/10.1002/9781118359259.ch84/summary (accessed April 4, 2014).

[56] J.B. Zhang, Y.A. Zhang, B.H. Zhu, R.Q. Liu, F. Wang, Q.M. Liang, Characterization of microstructure and mechanical properties of Al–Cu–Mg–Ag–(Mn/Zr) alloy with high Cu:Mg, Mater. Des. 49 (2013) 311–317. https://doi.org/10.1016/j.matdes.2013.01.044.

[57] D. Bakavos, P.B. Prangnell, B. Bes, F. Eberl, The effect of silver on microstructural evolution in two 2xxx series Al-alloys with a high Cu:Mg ratio during ageing to a T8 temper, Mater. Sci. Eng. A. 491 (2008) 214–223. https://doi.org/10.1016/j.msea.2008.03.014.

[58] J. Yu, Property Mapping of Friction Stir Welded Al-2139 T8 Plate using Site Specific Shear Punch Testing, Acta Mater. (2016).

[59] U. Okeke, H. Yilmazer, S. Sato, C.J. Boehlert, Strength enhancement of an aluminum alloy through high pressure torsion, Mater. Sci. Eng. A. 760 (2019) 195–205. https://doi.org/10.1016/j.msea.2019.05.102.

[60] J. Dudas, F. Collins, Preventing Weld Cracks in High-Strength Aluminum Alloys, Weld. J. 45 (1966) S241-.

[61] W. M. Thomas, E. D. Nicholas, J. C. Needham, M. G. Murch, P. Temple-Smith, C. J. Dawes, Friction stir butt welding, 9125978–8, 1991.

[62] W. M. Thomas, E. D. Nicholas, J. C. Needham, M.G. Murch, P. Temple-Smith, C. J. Dawes, Improvements relating to friction welding, 5460317, 1991.

[63] P.L. Threadgill, A.J. Leonard, H.R. Shercliff, P.J. Withers, Friction stir welding of aluminium alloys, Int. Mater. Rev. 54 (2009) 49–93. https://doi.org/10.1179/174328009X411136.

[64] V.T. Saccon, B.S. Parra, C.W. Olea, J.F. dos Santos, N.G. de Alcântara, Microstructural characterization and mechanical behavior of an AA2139 T3 and T8 aluminum alloy joined by friction stir welding (FSW), Soldag. Amp Insp. 15 (2010) 289–297. https://doi.org/10.1590/S0104-92242010000400006.

[65] H.R. Shercliff, M.J. Russell, A. Taylor, T.L. Dickerson, Microstructural modelling in friction stir welding of 2000 series aluminium alloys, Mech. Ind. 6 (2005) 25–35. https://doi.org/10.1051/meca:2005004.

[66] L. E. Murr, G. Liu, J. C. McClure, J. Mater. Sci. 33 (1998) 1243–1251.

[67] G. J. Bendszak, T. H. North, C. B. Smith, in: Proc 2nd Int Symp 'Friction Stir Welding,' TWI, Gothenburg, Sweden, 2000.

[68] M. W. Mahoney, C. G. Rhodes, J. G. Flintoff, R. A. Spurling, W. H. Bingel, Metall. Mater. Trans. A. 29A (1998) 1955–1964.

[69] Matthew Zaluzec, Light-Weight Materials in Automobiles: Designing the Ford Fusion, Past, Present and Future (unpublished research), (2014).

[70] National Aeronautics and Space Administration, Space Shuttle Technology Summary: Friction Stir Welding, Pub 8-1263. FS-2001-03-60-MSFC (n.d.). http://www.nasa.gov/centers/marshall/pdf/104835main_friction.pdf.

[71] M. Reza-E-Rabby, Quantification of the effect of tool geometric features on aspects of friction stir welding, Ph.D., University of South Carolina, 2015. http://search.proquest.com/docview/1728146800/abstract/DE5A2E7FF95A469APQ/1 (accessed June 20, 2018).

[72] C.J. Dawes, TWI Bull. 41 (2000) 51–55.

[73] K. Lindner, Z. Khandkar, J. Khan, W. Tang, A. P. Reynolds, in: Proc 4th Int Symp 'Friction Stir Welding,' TWI, Park City, UT, USA, 2003.

[74] K. Ross, Md. Reza-E-Rabby, M. McDonnell, S.A. Whalen, Advances in dissimilar metals joining through temperature control of friction stir welding, MRS Bull. 44 (2019) 613–618. https://doi.org/10.1557/mrs.2019.181.

[75] W. Xu, J. Liu, G. Luan, C. Dong, Temperature evolution, microstructure and mechanical properties of friction stir welded thick 2219-O aluminum alloy joints, Mater. Des. 30 (2009) 1886–1893. https://doi.org/10.1016/j.matdes.2008.09.021.

[76] K. Ross, Temperature control in friction stir welding for industrial and research applications, in: Proc. 10th Int. Symp. Frict. Stir Weld., TWI, Cambridge, 2014.

[77] B.C. Hornbuckle, H.A. Murdoch, A.J. Roberts, L.J. Kecskes, M.A. Tschopp, K.J. Doherty, J.H. Yu, K.A. Darling, Property mapping of friction stir welded Al-2139 T8 plate using site specific shear punch testing, Mater. Sci. Eng. A. 682 (2017) 192–201. https://doi.org/10.1016/j.msea.2016.11.032.

[78] R.S. Mishra, M.W. Mahoney, eds., Friction stir welding and processing, ASM International, Materials Park, Ohio, 2007.

[79] K. Elangovan, V. Balasubramanian, Influences of post-weld heat treatment on tensile properties of friction stir-welded AA6061 aluminum alloy joints, Mater. Charact. 59 (2008) 1168–1177. https://doi.org/10.1016/j.matchar.2007.09.006.

[80] J. R. Davis & Associates, ASM International, eds., Aluminum and aluminum alloys, ASM International, Materials Park, OH, 1993.

[81] C.A. Schneider, W.S. Rasband, K.W. Eliceiri, NIH Image to ImageJ: 25 years of image analysis, Nat. Methods. 9 (2012) 671–675. https://doi.org/10.1038/nmeth.2089.

[82] Kathryn A. Dannemann, Sidney Chocron, Arthur E. Nicholls, Darryl L. Wagar, Mechanical Characterization of Aluminum 2139-T8 for Determination of Johnson-Cook Constitutive Constants, Southwest Research Institute (prepared for U.S. Army RDECOM-TARDEC), San Antonio, TX, 2009.

[83] V. Radmilovic, R. Kilaas, U. Dahmen, G.J. Shiflet, Structure and morphology of S-phase precipitates in aluminum, Acta Mater. 47 (1999) 3987–3997. https://doi.org/10.1016/S1359-6454(99)00259-1.

[84] G.E. Dieter, Mechanical metallurgy, McGraw-Hill, New York, 1961.

[85] S. Kalpakjian, S.R. Schmid, Manufacturing engineering and technology, Seventh edition, Pearson, Upper Saddle River, NJ, 2014.

[86] R.W. Fonda, J.F. Bingert, K.J. Colligan, Development of grain structure during friction stir welding, Scr. Mater. 51 (2004) 243–248. https://doi.org/10.1016/j.scriptamat.2004.04.017.

[87] P. Kosky, R. Balmer, W. Keat, G. Wise, Chapter 12 - Mechanical Engineering, in: P. Kosky, R. Balmer, W. Keat, G. Wise (Eds.), Explor. Eng. Third Ed., Academic Press, Boston, 2013: pp. 259–281. https://doi.org/10.1016/B978-0-12-415891-7.00012-1.

[88] ASM Material Data Sheet, (n.d.). http://asm.matweb.com/search/SpecificMaterial.asp?bassnum=MA2024T4 (accessed September 12, 2020).

[89] ASM Material Data Sheet, (n.d.). http://asm.matweb.com/search/SpecificMaterial.asp?bassnum=MA2219T81 (accessed September 12, 2020).

[90] N. Martinez, N. Kumar, R.S. Mishra, K.J. Doherty, Microstructural variation due to heat gradient of a thick friction stir welded aluminum 7449 alloy, J. Alloys Compd. 713 (2017) 51–63. https://doi.org/10.1016/j.jallcom.2017.04.147.

[91] Kh.A.A. Hassan, A.F. Norman, D.A. Price, P.B. Prangnell, Stability of nugget zone grain structures in high strength Al-alloy friction stir welds during solution treatment, Acta Mater. 51 (2003) 1923–1936. https://doi.org/10.1016/S1359-6454(02)00598-0.

[92] 1501 - E118 - Welding Technology and Codes - 03a - Welding Metallurgy, (2012). https://www.nrc.gov/docs/ML1215/ML12157A580.html (accessed July 3, 2021).

[93] A. O'Brien, ed., Welding Handbook - Welding processes, Part 1, 9. ed., 2. print, American Welding Society, Miami, Fla, 2007.

[94] Piyush Upadhyay, Reza-E-Rabby, Scott Whalen, Martin McDonnell, Private communication with research personnel at the Pacific Northwest National Laboratory, (2020).

[95] R.W. Evans, B. Wilshire, Introduction to Creep, The Institute of Materials, London, 1993.

[96] Zhe Chen, A Study of the Effects of Processing and Alloying on the Microstructure and Deformation Behavior of Wrought Magnesium Alloys, PhD, Michigan State University, 2012.

[97] D. Bakavos, Microstructural interactions during creep ageforming of aerospace aluminium alloys, Ph.D., The University of Manchester (United Kingdom), 2006. https://search.proquest.com/docview/2071876560/abstract/C4FC1CA81A1D47B8PQ/1 (accessed February 24, 2021).

[98] D.B. Williams, C.B. Carter, Transmission electron microscopy: a textbook for materials science, 2nd ed, Springer, New York, 2008.